

**UCGE Reports  
Number 20261**

Department of Geomatics Engineering

**A Dynamic Geoid Model for Canada**

(URL: <http://www.geomatics.ucalgary.ca/research/publications/GradTheses.html>)

**by**

**Elena Veselinova Rangelova**

**November 2007**



UNIVERSITY OF CALGARY

A Dynamic Geoid Model for Canada

by

Elena Veselinova Rangelova

A THESIS

SUBMITTED TO THE FACULTY OF GRADUATE STUDIES  
IN PARTIAL FULFILMENT OF THE REQUIREMENTS FOR THE  
DEGREE OF DOCTOR OF PHILOSOPHY

DEPARTMENT OF GEOMATICS ENGINEERING

CALGARY, ALBERTA

November, 2007

© Elena Veselinova Rangelova 2007

# Abstract

The main objective of this research is to develop a methodology that can be used to optimally combine geodetic data for empirical modelling of the temporal variations of the geoid caused by the slow dynamic process of glacial isostatic adjustment of the Earth. A dynamic geoid model is needed for establishing a modern dynamic geoid-based vertical datum for Canada. By correcting the geoid for the secular temporal variations, a reference surface for orthometric heights free from systematic effects due to geodynamics will be maintained. To provide a centimetre level of accuracy for precise surveying activities, corrections should be applied generally at a ten-year time interval. Models of the temporal variations of orthometric heights are another important outcome required for ensuring consistency between the dynamic vertical reference surface and gravity related heights.

The sub-objectives of this research are (i) developing a general framework for combining terrestrial and space-borne data including GRACE, GPS, tide gauge/altimetry, and absolute gravimetry data, (ii) implementing data-driven statistical approaches for modelling temporal variations of the geoid and heights, and (iii) delineating practical considerations for implementing the dynamic geoid model as a dynamic vertical reference surface.

The developed methodology is applied, for the first time, to combine GRACE-observed rates of vertical deformation with terrestrial data. The modeled temporal variations of the geoid agree within 0.1 - 0.2 mm/yr with glacial isostatic model predictions based on the ICE-4G model in the areas with a peak geodynamic signal. Making use of robust least-squares procedures combined with variance component estimation, reliable constraints for geodynamic modelling free from the influence of erroneous observations and reliably estimated error bounds of the empirical rates of crustal displacement are provided. An important outcome of this research is the use of the developed statistical tools as a necessary step towards combining geodynamic modelling of glacial isostatic adjustment with the empirical statistical approach in a rigorous dynamic-based procedure.

# Preface

This is an unaltered version of the author's Doctor of Philosophy thesis of the same title. This thesis was accepted by the Faculty of Graduate Studies in November, 2007. The faculty supervisor of this work was Dr. M.G. Sideris, and the other members of the examining committee were Dr. N. Sneeuw, Dr. P. Wu, Dr. C. Valeo, and Dr. S. Pagiatakis.

# Acknowledgements

I would like to express my appreciation and thank my supervisor, Dr. M.G. Sideris, for his support and guidance throughout my graduate studies at the University of Calgary. His continuous encouragement and advice is highly appreciated. I also thank the other members of my supervisory committee, Dr. P. Wu and Dr. N. Sneeuw, for the discussions on postglacial rebound, geodynamics, and satellite gravimetry and for their comments on my thesis.

I am very grateful to Dr. G. Fotopoulos (University of Toronto) for many useful comments and suggestions during my research and thesis preparation. Also, I would like to thank Dr. R. Peltier for giving me the excellent opportunity to visit the Department of Physics at the University of Toronto during the first years of my graduate studies.

Joe Henton, Marc Véronneau, and Jianliang Huang from Geodetic Survey Division at NRCAN are thanked for providing the Canadian data. Tony Lambert is thanked for making available the North-American Tilt Project Data. Funding for my PhD studies was provided from NSERC and GEOIDE NCE, the Department of Geomatics Engineering, Schulich School of Engineering at the University of Calgary, and the University of Architecture, Civil Engineering, and Geodesy, Sofia, Bulgaria.

My friends and colleagues, Dr. Rossen Grebenitcharsky (Technical University of Delft) and Wouter van der Wal (University of Calgary) are also thanked for our endless and very helpful discussions and for their constant help. I would like to thank my friends from the gravity field and geodynamics research group in the Department of Geomatics Engineering Dr. Matthias Weigelt, Dr. Mohamed El-Habiby, Dr. Chen Xu, Balaji Devaraju, and Dr. Bihter Erol for their support and friendship.

Finally, I would like to thank my family for their love, endless support, and encouragement during my PhD studies.

# Table of Contents

Approval Page.....	ii
Table of Contents.....	vi
List of Tables.....	ix
List of Figures.....	x
List of Symbols and Abbreviations.....	xv
CHAPTER ONE: INTRODUCTION.....	1
1.1 Background.....	1
1.2 Thesis Objectives.....	5
1.3 Thesis Outline.....	6
1.4 Assumptions and Limitations.....	7
CHAPTER TWO: VERTICAL DATUM PROBLEM AND DYNAMIC GEOID.....	9
2.1 Geoid as a vertical datum for orthometric heights.....	9
2.1.1 Definition and realization of the vertical datum.....	10
2.1.2 Definition of orthometric and ellipsoidal heights.....	13
2.1.3 Relationship of ellipsoidal, orthometric, and geoid heights.....	14
2.2 Glacial isostatic adjustment.....	17
2.2.1 Forward problem.....	17
2.2.2 Inverse problem.....	19
2.3 Relationship of temporal changes of ellipsoidal, orthometric, and geoid heights.....	22
2.4 Geodetic constraints on geodynamic, tectonic, and other processes in North America.....	27
2.4.1 GRACE-observed temporal changes of the gravity field.....	27
2.4.2 Absolute and relative terrestrial gravimetry.....	30
2.4.3 Continuous and episodic GPS measurements.....	31
2.4.4 Combination of tide gauge records and satellite altimetry data.....	33
2.4.5 Precise re-levelling.....	35
2.4.6 Collocation of geodetic techniques.....	36
2.4.7 Gravity-to-height ratio.....	39
2.5 Geodetic approaches for modelling temporal variations of geoid and heights.....	42
2.5.1 Analysis of GRACE time series.....	42
2.5.2 Time-variable boundary value problem. Geodetic integrals.....	43
2.5.3 Least-squares collocation approach.....	45
2.6 Summary.....	47
CHAPTER THREE: APPROXIMATION OF VERTICAL DISPLACEMENT DATA USING RADIAL BASE FUNCTIONS.....	48
3.1 Definition and properties of radial base functions.....	49
3.2 Radial base function interpolator. Scaling of base functions.....	51
3.2.1 Definition and properties.....	51
3.2.2 Optimal scale of base functions.....	54
3.3 Radial base function approximator. Selecting base functions locations.....	55

3.3.1 Definition.....	55
3.3.2 Algorithms for selecting optimal locations of base functions.....	57
3.4 Numerical case studies .....	60
3.4.1 Interpolation of noise-free vertical displacement data .....	61
3.4.2 Approximation of noise-free vertical displacement data.....	68
3.4.3 Approximation of noisy vertical displacement data.....	70
3.4.4 Applications of the inverse multiquadric approximator.....	73
3.5 Relation between inverse multiquadric base functions and a mass flow model.....	76
3.6 Summary.....	77
CHAPTER FOUR: RATES OF CHANGE OF GEOID AND HEIGHTS OBTAINED FROM TERRESTRIAL DATA .....	79
4.1 General least-squares collocation with parameters approach.....	79
4.1.1 Mathematical model.....	80
4.1.2 Statistical testing.....	82
4.2 Optimal combination of heterogeneous terrestrial data.....	86
4.2.1 Modelling the trend component.....	88
4.2.2 Modelling the signal component .....	88
4.2.3 Description of the computational algorithm.....	91
4.2.4 Validation of predicted rates .....	95
4.3 Models of the rates of change of the terrestrial gravity, geoid, and heights.....	96
4.3.1 Description of the terrestrial gravity and GPS velocity data.....	96
4.3.2 Signal auto- and cross- covariance functions .....	99
4.3.3 A priori threshold value for selecting optimal locations of base functions...	101
4.3.4 Effect of the threshold value on the trend surface.....	102
4.3.5 Empirical models of the rates of the terrestrial gravity, geoid, and heights..	105
4.3.6 Validation of predicted rates of change of terrestrial gravity and ellipsoidal height .....	114
4.4 Summary.....	116
CHAPTER FIVE: GRACE-OBSERVED RATES OF CHANGE OF THE GEOID HEIGHT AND ABSOLUTE VERTICAL DISPLACEMENT.....	118
5.1 Error propagation.....	119
5.2 Methodology of post-processing of GRACE data and error analysis .....	120
5.2.1 De-correlation filter .....	120
5.2.2 Smoothing filters .....	123
5.2.3 Uncertainties in the secular geoid rate from the continental hydrology correction .....	129
5.3 PC/EOF analysis of GRACE-observed geoid changes .....	133
5.3.1 Mathematical background .....	134
5.3.2 Selecting a subset of principal components .....	136
5.3.3 Rotation of principal components .....	137
5.3.4 GRACE-observed geoid changes in North America.....	139
5.3.5 Validation of the PC/EOF geoid rate and summary.....	148
5.4 Optimal combination of GRACE, terrestrial gravity, and GPS data.....	150
5.4.1 Mathematical model.....	150
5.4.2 Combined models for rates of the vertical displacement and the geoid height	152

5.5 Summary .....	156
<b>CHAPTER SIX: PRACTICAL ASPECTS OF MODELLING RATES OF VERTICAL DISPLACEMENT AND GEOID HEIGHT .....</b>	
6.1 Problem statement .....	160
6.2 Combined least-squares adjustment model .....	162
6.3 Approximation of a single velocity data set .....	165
6.4 Combined model for vertical displacement rates .....	172
6.4.1 Outlier detection .....	174
6.4.2 Variance component estimation and a posteriori accuracy .....	175
6.5 Summary .....	181
<b>CHAPTER SEVEN: IMPLEMENTING THE DYNAMIC GEOID MODEL AS A VERTICAL DATUM .....</b>	
7.1 Definition of the dynamic geoid .....	182
7.2 Role of the dynamic geoid in the vertical datum problem.....	186
7.2.1 Combined adjustment of ellipsoidal, geoid, and orthometric heights .....	187
7.2.2 Effect of geodynamics on the parametric surface .....	189
7.2.3 Analysis of results .....	196
7.3 Summary .....	198
<b>CHAPTER EIGHT: CONCLUDING REMARKS .....</b>	
8.1 Conclusions.....	200
8.2 Outlook for future research.....	203
8.3 Recommendations for establishing a geoid-based, dynamic vertical datum for Canada .....	205
8.3.1 A dynamic geoid model .....	205
8.3.2 A dynamic vertical datum .....	206
<b>BIBLIOGRAPHY .....</b>	<b>209</b>
<b>APPENDIX A: SIGNAL AUTO- AND CROSS-COVARIANCE FUNCTIONS .....</b>	
A.1. Auto-covariance functions.....	233
A.2. Cross-covariance functions.....	234
<b>APPENDIX B: OUTLIERS AND CALIBRATED ERRORS OF GPS AND TIDE GAUGE/ALTIMETRY DATA .....</b>	
B.1. Results from Baarda's data snooping in the combined case.....	237
B.2. Calibrated errors for GPS vertical velocities .....	238
B.3. Calibrated errors for tide gauge/altimetry data .....	241

# List of Tables

Table 2.1: Estimates and predictions of gravity-to-height ratio .....	40
Table 2.2: Summary of the formal errors of the rates of change of gravity and heights .....	41
Table 3.1: Comparison of the interpolators for noise free data on a $5^\circ \times 5^\circ$ grid.....	62
Table 3.2: Comparison of the performance of the interpolators for interpolating noise-free irregularly distributed data.....	65
Table 4.1: Standard deviations of the terrestrial gravity rates and GPS velocities.....	98
Table 4.2: Parameters of the covariance kernels defined by Eq. (4.50) .....	99
Table 4.3: Variance ratio computed for the PGR models by the Monte Carlo simulation.	102
Table 4.4: Standard deviations of the predicted rates of the ellipsoidal height, in mm/yr .	106
Table 4.5: Standard deviations of the predicted rates of the terrestrial gravity, in $\mu\text{Gal}/\text{yr}$	109
Table 4.6: Standard deviations of the predicted rates of the geoid height, in mm/yr .....	113
Table 5.1: Effect of the radius of the Gaussian filter on the geoid rate .....	125
Table 5.2: Uncertainties in the GRACE-observed postglacial rebound geoid rate .....	133
Table 5.3: Data variance (in percentage) explained by the principal components .....	141
Table 5.4: Accuracy of predicted rates of vertical displacement and geoid height, mm/yr	154
Table 5.5: Estimated variance factors and a posteriori standard deviations, in mm/yr .....	156
Table 6.1: Effect of outliers on the approximated surface.....	168
Table 6.2: Statistics of the a priori (not scaled) standard deviations .....	174
Table 6.3: Estimated variance factors and a posteriori standard deviations in mm/yr .....	176
Table 7.1: Temporal effects in the geoid model .....	185
Table 7.2: Statistics of the errors of the ellipsoidal, geoid, and orthometric heights, in mm .....	192

# List of Figures

Figure 1.1: GRACE-observed rates of change of the geoid height derived in this thesis from the Center for Space Research (CSR) RL-01 data. ....	4
Figure 2.1: Relation between ellipsoidal, orthometric, and geoid heights. ....	15
Figure 2.2: Factors contributing to the discrepancies among ellipsoidal, orthometric, and geoid heights. ....	16
Figure 2.3: Rate of change of the geoid height as a function of viscosity for a spherically symmetric incompressible Earth and the ICE-4G model. ....	22
Figure 2.4: Temporal changes of the gravity field and heights at a point P of the topographic surface. ....	23
Figure 2.5: Relationship between the apparent and levelled crustal displacement and the changes in the geoid and sea level. ....	34
Figure 2.6: CGSN gravity rates, CBN vertical velocities, levelling data, and Mid-continent tilt project data. ....	37
Figure 2.7: A general framework for combining geodetic data constraints. ....	38
Figure 2.8: “Collocated” CGSN gravity sites and CBN GPS stations for estimating the gravity-to-height ratio. ....	40
Figure 2.9: Gravity-to-height ratio estimated from the “collocated” CGSN absolute gravity rates and the CBN GPS vertical velocities. ....	41
Figure 3.1: IMQ base functions: (a) a cone-like function and (b) a bowl-like function. ....	51
Figure 3.2: Modified Gram-Schmidt algorithm. ....	60
Figure 3.3: RMS error as a function of the shape parameter for noise-free data given on a $5^\circ \times 5^\circ$ grid. ....	63
Figure 3.4: Condition number of the coefficient matrix as a function of the shape parameter for noise-free data given on a $5^\circ \times 5^\circ$ grid. ....	63
Figure 3.5: RMS error as a function of the shape parameter for noise-free irregularly distributed data. ....	65
Figure 3.6: Condition number of the coefficient matrix as a function of the shape parameter for noise-free irregularly distributed data. ....	66

Figure 3.7: (a) Reference surface; (b) interpolated surface from noise-free irregularly distributed data with IMQ base functions and $c^2 = 0.230$ ; and (c) differences between the interpolated and reference surfaces. ....	67
Figure 3.8: Differences between the reference and approximated (with 24 base functions) surfaces: (a) forward CV with $c^2 = 0.230$ and RMS error of 1.2 mm/yr, (b) forward CV with adaptive $c^2$ and RMS error of 0.9 mm/yr; (c) modified GS with $c^2 = 0.230$ , and RMS error of 0.9 mm/yr; (d) backward CV with adaptive $c^2$ and RMS error of 0.8 mm/yr.....	69
Figure 3.9: Number of base functions as a function of noise variance for different thresholds (tolerances). ....	71
Figure 3.10: RMS error as a function of noise variance for different thresholds (tolerances).....	71
Figure 3.11: Condition number as a function of noise variance for different thresholds (tolerances).....	72
Figure 3.12: Differences between the approximated and reference surfaces by the modified GS selection algorithm ( $\sigma^2 = 1.00 \text{ mm}^2/\text{yr}^2$ and $c^2 = 0.06$ ). The RMS error is 1.4 mm/yr. ....	73
Figure 3.13: (a) Simulated bowl-like surface, (b) approximated surface, (c) simulated surface plus noise (note the different scale of the z-axis), and (d) smoothed surface. .	74
Figure 3.14: (a) Approximated surface – base functions tend to group along the discontinuity present in the data, (b) simulated surface plus noise (note the different scale of the z-axis), and (c) smoothed surface. ....	75
Figure 3.15: Effect of the approximation errors on the rate of change of geoid height, in mm/yr.....	77
Figure 4.1: Flowchart of the computational procedure.....	92
Figure 4.2: (a) Rates of the terrestrial gravity (the CGSN sites are plotted in red) and (b) GPS velocities (the CBN stations are plotted in blue).....	98
Figure 4.3: Signal cross-covariance function of $\dot{h}$ and $\dot{H}$ . ....	100
Figure 4.4: Signal auto- and cross-covariance functions.....	100
Figure 4.5: (a) Adjusted coefficient of determination and (b) condition number of the normal matrix as a function of the threshold value.....	104
Figure 4.6: Predicted rates of change of ellipsoidal height for the three solutions: (a) total rate, (b) predicted signal, and (c) accuracy of prediction. Red and yellow stars denote the CGSN sites and CBN stations, respectively.....	108

Figure 4.7: Rates of change of the terrestrial gravity from the three solutions: (a) total rate, (b) predicted signal, and (c) accuracy of prediction. Red and yellow stars denote the CGSN sites and CBN stations, respectively. ....	110
Figure 4.8: (a) Predicted total rates of change of the geoid height (b) predicted signal of the rate of geoid height, and (c) predicted rate of the orthometric height. Red and yellow stars denote the CGSN sites and CBN stations, respectively. ....	113
Figure 4.9: Comparison of the geoid rates along north-south and west-east profiles: outputs from the PGR model simulations are plotted in blue, Solution (1) is plotted in dotted red line, Solution (2) is plotted in dashed red line, and Solution (3) is in solid red line.....	114
Figure 4.10: Predicted rates of change of (a) the terrestrial gravity and (b) the ellipsoidal height (absolute vertical displacement) compared with the Mid-continent tilt project data.....	115
Figure 5.1: Distortions in the rate of change of the geoid height: (a) after a de-correlation filter is applied and (b) smoothed with a Gaussian filter.....	122
Figure 5.2: Error degree amplitudes in mm of the geoid height.....	123
Figure 5.3: Effect of the Gaussian smoothing on the simulated GIA geoid rate. A filter with half-width $r$ of (a) 400 km, (b) 600 km, (c) 750 km, and (d) 1000 km is used. Differences are plotted in mm/yr. ....	126
Figure 5.4: Effect of the stochastic-based smoothing on the GIA-induced geoid rates: (a) reference geoid rates; (b) differences between the reference and filtered rates. ..	128
Figure 5.5: Formal errors of the geoid rates from least-squares fitting to the four-year time series of GRACE SH coefficients smoothed with: (a) a de-correlation filter and (b) a de-correlation filter and Gaussian filter with $r = 400$ km.....	128
Figure 5.6: Pattern of the water mass increase that interferes with postglacial rebound signal. Least-squares fitting to the time series of the SH coefficients of the GLDAS model is applied. ....	130
Figure 5.7: GRACE-observed rates of change of the geoid height obtained with (a) a Gaussian filter with $r = 400$ km, (b) stochastic smoothing, (c) and (d) the same, but a correction for the hydrology signal is applied.....	132
Figure 5.8: Principal components for (a) Case 1 and (b) Case 2. ....	140
Figure 5.9: EOF and REOF loading patterns for Case 1. ....	144
Figure 5.10: PC and rotated PC time series for Case 1 (a and b) and Case 2 (c and d).....	145
Figure 5.11: EOF and REOF loading patterns for Case 2. ....	147

Figure 5.12: Rate of change of the geoid height derived from (a) the first three principal components in Case 2, (b) a least-squares fit of the GRACE SH time series, and (c) the smoothed ICE-5G (VM2) model. ....	149
Figure 5.13: An iterative estimation procedure including VCE and outlier detection. ....	153
Figure 5.14: Estimated rates of the terrestrial gravity and GPS velocities. ....	153
Figure 5.15: Predicted rates of the vertical displacement and the rate of change of the geoid height for Canada: (a) and (b) GRACE-observed rates, (c) and (d) modelled trend component, and (e) and (f) the trend plus the signal components. The gravity sites and GPS stations are plotted with red and yellow stars, respectively.....	155
Figure 5.16: Comparison of the geoid rates computed by least-squares (LS) fitting and PC/EOF analysis of the GRACE-observed geoid changes and a combination of terrestrial and GRACE data along north-south and west-east profiles. The smoothed with a Gaussian filter (400 km) ICE-5G (VM2) model is also given. ....	157
Figure 6.1: Iterative re-weighting least-squares (IRLS) adjustment.....	166
Figure 6.2: (a) Test surface sampled by means of 50 point velocity observations (red stars) and 12 base functions (black squares), (b) approximated surface with two random scattered outliers, (c) approximated surface with two random adjacent outliers, and (d) approximated surface with five jointly influential outliers. ....	167
Figure 6.3: Effect of (a) a single random and (b) jointly influential outliers on the approximated velocity surface with a data gap.....	169
Figure 6.4: Weights of the observations for the cases of random scattered outliers and jointly influential outliers computed by the Fair-MAD estimator, (a) and (b), and by the Fair-sigma estimator, (c) and (d). ....	171
Figure 6.5: Rates of vertical displacement from (a): GRACE, (b) PGR model with a four-layer approximation of the VM2 model and the ICE-4G de-glaciation history, (c) GPS measurements (red stars), and (d) an optimal combination of water tide gauge records and TOPEX/Poseidon altimetry water surface heights (yellow stars). ....	173
Figure 6.6: Combined model using least-squares adjustment (no outliers removed). A priori (black) and a posteriori (red) standard deviations of the GPS vertical velocities and TGA vertical displacement rates are given in the upper and lower plots, respectively. ....	177
Figure 6.7: Combined model using least-squares adjustment with Baarda's data snooping. A priori (black) and a posteriori (red) standard deviations of the GPS vertical velocities and TGA vertical displacement rates are given in the upper and lower plots, respectively. ....	178

Figure 6.8: Combined model using IRLS adjustment with the Fair-sigma estimator. A priori (black) and a posteriori (red) standard deviations of the GPS vertical velocities and TGA vertical displacement rates are given in the upper and lower plots, respectively. ....	179
Figure 6.9: Combined model using IRLS adjustment with the Fair-MAD estimator. A priori (black) and a posteriori (red) standard deviations of the GPS vertical velocities and TGA vertical displacement rates are given in the upper and lower plots, respectively. ....	180
Figure 7.1: GPS on first order levelling benchmarks for the three regions and modelled rates of change of the geoid height. ....	191
Figure 7.2: Left: parametric surfaces for the three regions; right: total dynamic effect on the parametric surfaces. ....	193
Figure 7.3: Effect of dynamic components and relative errors from diagonal error covariance matrices: (a) change in geoid height and (b) change in geoid and orthometric heights. The vertical axis shows relative variables. ....	194
Figure 7.4: Effect of the dynamic components and relative errors from fully-populated error covariance matrices: (a) change in geoid height and (b) change in geoid and orthometric heights. The vertical axis shows relative variables. ....	195
Figure 7.5: Effect of the temporal change in the geoid height for a 10-year time period as a function of the mean standard deviation of the three height data components....	198
Figure 7.6: Effect of the temporal changes in the geoid and orthometric heights over 10 years. Vertical axis shows relative variables. ....	199
Figure 8.1: A general scheme for computing a dynamic geoid model. ....	206
Figure 8.2: Steps for establishing a dynamic geoid-based vertical datum.....	208

# List of Symbols and Abbreviations

$\mathbf{a}$	column vector (regressor) of the coefficient matrix $\mathbf{A}$
$\mathbf{A}$	coefficient matrix
$\mathbf{A}_{\dot{g}}$	coefficient matrix for rates of change of terrestrial gravity
$\mathbf{A}_{\dot{h}}$	coefficient matrix for rates of change of ellipsoidal height
$\mathbf{A}_p$	coefficient matrix of predicted points
$B$	linear operator
$c^2$	shape parameter of the (inverse) multiquadric function
$c^T$	terrain correction
$C_P$	geopotential number of a point P
$\mathbf{C}_{\dot{g}}$	signal auto-covariance matrix for rates of change of terrestrial gravity
$\mathbf{C}_{\dot{h}}$	signal auto-covariance matrix for rates of change of ellipsoidal height
$\mathbf{C}_{\dot{g}\dot{h}}$	signal cross-covariance matrix of rates of terrestrial of gravity and ellipsoidal height
$\mathbf{C}_l$	data covariance matrix
$\mathbf{C}_s$	covariance matrix of given signals
$\mathbf{C}_{\bar{s}}$	signal covariance matrix
$\mathbf{C}_{s_p}$	covariance matrix of predicted signals
$(\mathbf{C}_v)_{\dot{g}}$	error covariance matrix of rates of change of terrestrial gravity
$(\mathbf{C}_v)_{\dot{h}}$	error covariance matrix of rates of change of ellipsoidal height
$\mathbf{C}_v$	error covariance matrix
$\mathbf{C}_h$	error covariance matrix of ellipsoidal height
$\mathbf{C}_H$	error covariance matrix of orthometric height
$\mathbf{C}_N$	error covariance matrix of geoid height

$\mathbf{C}_{\delta N}$	error covariance matrix of GRACE-observed temporal change in the geoid
$\mathbf{C}_{\hat{\mathbf{s}}}$	error covariance matrix of estimated signals
$\mathbf{C}_{\hat{\mathbf{s}}_p}$	error covariance matrix of predicted signals
$\mathbf{C}_{\hat{\mathbf{x}}}$	error covariance matrix of estimated parameters
$\mathbf{C}_{\hat{\mathbf{x}}\hat{\mathbf{s}}_p}$	error cross-covariance matrix of estimated parameters and predicted signals
$\mathbf{C}_{\hat{\mathbf{v}}}$	covariance matrix of estimated residuals
$\mathbf{C}_{\hat{\boldsymbol{\theta}}}$	covariance matrix of estimated variance components
$d\sigma$	surface element of the sphere
$dH$	distance between two equipotential surfaces measured along the plumb line
$\mathbf{D}$	data matrix in PC analysis
${}_m\mathbf{D}$	rank $m$ approximation matrix of the data matrix $\mathbf{D}$
$\mathbf{e}$	vector of errors
$f$	degrees of freedom of a model
$g$	absolute gravity
$\mathbf{g}$	absolute gravity vector
$g_a$	average gravity of the Earth
$\dot{g}$	rate of change of terrestrial gravity
$\bar{g}$	mean gravity along the plumb line
$\dot{g}/\dot{h}$	gravity-to-height ratio
${}_1F_1$	confluent hypergeometric function of the first kind
$G$	gravitational constant
$\tilde{G}$	perturbation of the geoid
$h$	ellipsoidal height
$\dot{h}$	rate of change of ellipsoidal height
$\mathbf{h}$	vector of vertical displacements
$H$	orthometric height
$\dot{H}$	rate of change of orthometric height; also, rate of levelled uplift/subsidence

$\dot{H}^a$	rate of apparent uplift/subsidence
$\dot{H}_o$	rate of change of orthometric height of the fundamental datum point
$J_o(\phi r)$	zero order Bessel function
$k$	subset of base functions
$k_j, j = 1, \dots, 5$	trend, annual, and semi-annual components of a spherical harmonic coefficient $K_{lm}$
$k_l$	elastic Love number of degree $l$
$K_{lm}$	spherical harmonic coefficient
$\ell_{ij}$	Euclidean distance between points $i$ and $j$
$l_{max}$	maximum spherical harmonic degree of a geopotential model
$l_p$	height misclosure at a point P of the topographic surface
$LT$	gravity functional
$\tilde{L}$	ice/water load
$\mathbf{I}_p$	vector of predicted data
$\mathbf{I}_{AG}$	vector of rates of change of terrestrial gravity
$\mathbf{I}_{GPS}$	vector of GPS vertical velocities
$\mathbf{I}_{GRACE}$	vector of GRACE-observed rates of absolute vertical displacement
$\mathbf{I}_{TGA}$	vector of TGA rates of absolute vertical displacement
$M$	mass of the Earth
$n^i$	random error of a spherical harmonic coefficient
$N$	geoid height
$\dot{N}$	rate of change of the geoid height
$\tilde{N}$	non-linear temporal change in geoid height
$N_o$	shift of the geoid
$N^{stat}$	static geoid
$N^I$	indirect effect on the geoid from topography

$N^{\text{GM}}$	geoid height from a global geopotential model
$N^{\Delta g}$	geoid height from residual gravity anomalies
$O$	ocean function
$p(y^1, y^2)$	polynomial base function
$P_l(\cos\psi)$	Legendre polynomial of degree $l$
$\bar{P}_{lm}$	fully normalized Legendre function of degree $l$ and order $m$
$P^M(\Xi)$	polynomial space of degree $M$
$\mathbf{P}$	weight matrix
$\mathbf{P}_\alpha$	matrix with polynomial base functions
$\mathbf{Q}$	cofactor matrix
$\tilde{\mathbf{Q}}$	orthogonal matrix from Gram-Schmidt decomposition of $\mathbf{A}$
$\mathbf{Q}_\alpha$	orthogonal matrix from QR factorization of the matrix $\mathbf{P}_\alpha$
$\mathbf{Q}_1$	column space of the matrix $\mathbf{P}_\alpha$
$\mathbf{Q}_2$	null space of the matrix $\mathbf{P}_\alpha^{\text{T}}$
$r$	half-width of an isotropic Gaussian filter
$r_h$	roughness parameter
$R$	mean radius of the Earth
$\tilde{R}$	perturbation of the radius of the solid Earth
$\mathbf{r}$	position vector
$\mathbf{R}$	upper triangular matrix from QR factorization of the matrix $\mathbf{P}_\alpha$
$\tilde{\mathbf{R}}$	upper triangular matrix from Gram-Schmidt decomposition of the coefficient matrix $\mathbf{A}$
$\Re^2$	space of real numbers
$s_l^2$	signal degree variances
$\dot{s}$	rate of change of absolute sea level
$S$	relative sea level
$S(\psi)$	Stokes kernel

$S^L(\psi)$	spheroidal Stokes kernel of degree $L$
$\mathbf{s}$	vector of signal components
$\mathbf{s}_p$	vector of predicted signals
$\bar{\mathbf{s}}$	signal vector
$\mathbf{S}$	data matrix in PC/EOF analysis
$t$	time
$T$	anomalous potential
$T_{00}$	zero degree harmonic of the anomalous potential
$\mathbf{T}$	matrix with principal component time series
$U$	normal gravity potential
$U_0$	potential at the reference ellipsoid
$\mathbf{U}, \mathbf{V}$	orthonormal matrices from singular value decomposition
$\mathbf{v}$	vector of residuals
$W$	geopotential
$W_0$	potential of the geoid
$W_l$	degree-dependent coefficient of an isotropic smoothing filter
$W_{lm}$	degree and order-dependent coefficient of a non-isotropic smoothing filter
$\dot{W}$	rate of change of geopotential
$\dot{W}_{1,2}$	components of rate of change of geopotential
$\mathbf{W}$	weight matrix in iterative re-weighting least-squares adjustment
$\bar{\mathbf{W}}$	equivalent weight matrix in iterative re-weighting least-squares adjustment
$y^1, y^2$	Euclidean coordinates
$\hat{\mathbf{x}}$	vector of estimated parameters
$\hat{\mathbf{x}}'$	vector of estimated parameters using orthogonal least-squares
$\partial/\partial r$	radial derivative at a sphere
$\partial/\partial z$	vertical derivative
$\partial\gamma/\partial h$	normal gravity gradient
$\hat{\mathbf{a}}$	vector of estimated polynomial coefficients

$\beta_l$	degree-dependent transfer coefficient
$\Gamma^L$	viscoelastic surface load Green function for radial displacement
$\delta\bar{C}_{lm}$	temporal change in the cosine SH coefficient of degree $l$ and order $m$
$\delta\hat{C}_{lm}$	cosine spherical harmonic coefficients for the surface load
$\delta g$	temporal change in gravity
$\delta h$	temporal change in ellipsoidal height
$\delta H$	temporal change in orthometric height
$\delta H_o$	temporal change in orthometric height of the fundamental datum point
$\delta I$	change in ice thickness
$\delta M$	difference of the masses of the geoid and ellipsoid
$\delta N$	temporal change in geoid height
$\delta N^{\text{GRACE}}$	GRACE-observed temporal change in the geoid height
$\delta N^{\text{commission}}$	GRACE commission error
$\delta N^{\text{omission}}$	GRACE omission error
$\delta N^{\text{leakage}}$	GRACE leakage error
$\delta \mathbf{r}$	change in the position vector
$\delta S$	change in relative sea level
$\delta\bar{S}_{lm}$	temporal change in the sine harmonic coefficient of degree $l$ and order $m$
$\delta\hat{S}_{lm}$	sine spherical harmonic coefficients for the surface load
$\delta_{lm}^{C,S}$	errors of the GRACE-determined spherical harmonic coefficient
$\delta t$	change in time epoch
$\delta W$	change in geopotential
$\delta W'$	temporal change in geopotential at the deformed Earth's surface
$\delta W_o$	change in geopotential at the displaced fundamental vertical datum point
$\delta W_1$	change in the position of the geocenter
$\delta\mu$	mass element
$\Delta g$	free air gravity anomaly

$\Delta g_{ij}$	gravity difference between points $i$ and $j$
$\Delta g_{00}$	zero degree harmonic of gravity anomaly
$\Delta g^F$	Faye gravity anomaly
$\Delta g^{GM}$	gravity anomaly from a global geopotential model
$\Delta h$	ellipsoidal height difference
$\Delta H$	orthometric height difference
$\Delta n_i$	differential height
$\Delta N$	geoid height difference
$\Delta T$	laplacian of the anomalous potential
$\Delta W$	vertical datum parameter
$\Delta \lambda$	error of the eigenvalue $\lambda$
$\Delta \Phi$	mass conservation term
$\varepsilon$	threshold
$\gamma$	normal gravity
$\varphi$	geodetic latitude
$\Phi^L$	viscoelastic surface load Green function for potential perturbation
$\Phi(r)$	radial base function
$\hat{v}$	standardized residual
$\lambda$	geodetic longitude
$\lambda_i$	eigenvalues of the data covariance matrix $\mathbf{S}$
$\theta$	co-latitude
$\boldsymbol{\theta}$	vector of unknown variance components
$\rho$	planar distance
$\rho_a$	average density of the Earth
$\rho_m$	density of mantle
$\rho_I$	density of ice
$\rho_W$	density of water
$\sigma$	standard deviation

$\sigma_{C_{lm}}, \sigma_{S_{lm}}$	standard deviation of cosine and sine spherical harmonic coefficients
$\sigma_0^2$	variance of unit weight
$\sigma_l^2$	error degree variances
$\hat{\sigma}_{AG}$	standard deviation of rate of change of the terrestrial gravity
$\hat{\sigma}_{GPS}$	standard deviation of GPS vertical velocity
$\hat{\sigma}_{GRACE}$	standard deviation of GRACE-observed rates of absolute vertical displacement
$\hat{\sigma}_{TGA}$	standard deviation of the TGA absolute vertical displacement
$\sigma_{\delta N}$	standard deviation of the temporal change in geoid height
$\hat{\sigma}_{\hat{\theta}_i}$	standard deviation of the variance component $\hat{\theta}_i$
$\omega$	frequency of one cycle per year
$\Omega$	quadratic form
$\dot{\zeta}$	sea level rise
$\Xi$	finite set of points in real numbers space
$\psi$	spherical distance
$\Psi$	influence function

AG	Absolute Gravimetry
BIFROST	Baseline Inferences for Fennoscandian Rebound Observations, Sea-level and Tectonics
BIQUE	Best Invariant Quadratic Unbiased Estimation
BVP	Boundary Value Problem
CBN	Canadian Base Network
CGADB	Canadian Gravity Anomaly Data Base
CGG05	Canadian Gravimetric Geoid 2005
CGSN	Canadian Gravimetric Standardization Network
CGVD28	Canadian Geodetic Vertical Datum of 1928
CHAMP	Challenging Minisatellite Payload
CPV	Cumulative Percentage Variance
CSR	Center for Space Research in Texas
CV	Cross-validation
DInSAR	Differential Interferometric SAR
EGM96	Earth Geopotential Model 1996
EOF	empirical orthogonal functions
EVRS2000	European Vertical Reference System 2000
GIA	Glacial Isostatic Adjustment
GGM02S	Global Geopotential Model 02 Satellite
GNSS	Global Navigation Satellite System
GOCE	Gravity Field and Steady-state Ocean Circulation Explorer
GPS	Global Positioning System
GRACE	Gravity Recovery and Climate Experiment
GS	Gram-Schmidt
IERS	International Earth Rotation and Reference Systems Service
IMQ	Inverse Multiquadric
InSAR	Interferometric SAR
IRLS	Iterative Re-weighting Least-Squares
ITRF2000	International Terrestrial Reference Frame 2000
LGM	Last Glacial Maximum

MQ	Multiquadric
MSL	Mean Sea Level
MSST	Mean Sea Surface Topography
NAREF	North American Reference Frame
PC	principal component
PGR	Post Glacial Rebound
PREM	Preliminary Reference Earth Model
RMS	Root Mean Square
RSL	Relative Sea Level
SH	Spherical Harmonic
SLR	Satellite Laser Ranging
SNARF	Stable North American Reference Frame
SST	Sea Surface Topography
SVD	Singular Value Decomposition
TGA	Tide gauge/Altimetry
TPS	Thin Plate Spline
VCE	Variance Component Estimation
VLBI	Very Long Baseline Interferometry

# Chapter One: Introduction

## 1.1 Background

Canada's official vertical datum is the Canadian Geodetic Vertical Datum of 1928 (CGVD28) accessible at a control network of more than 80,000 benchmarks over 150,000 km (Véronneau, 2002). The vertical reference surface (datum) is constrained to the mean sea level of five tide gauges on the Pacific and Atlantic coasts. As a result, large east-west tilting in the orthometric heights across the country is observed. In addition to the large distortion of the reference surface, the height system is outdated and with limited coverage. Also, large regional systematic errors of up to 1 m, a consequence of the piece-wise manner of developing the network over the last 100 years, exist. Moreover, the significant vertical displacements caused by glacial isostatic adjustment of the crust, the local motion of benchmarks, the high cost, and the harsh environmental conditions for maintenance of the network have urged the need for a modernized vertical datum (Véronneau *et al.*, 2006). This new datum should be compatible with the GNSS positioning technique and easily accessible even in the northern parts of Canada, where a vertical control network does not exist. This opens the problem of re-definition of the vertical datum in terms of an accurate model for the regional geoid, which would allow one to replace the conventional spirit levelling by *GNSS/levelling* in order to determine the orthometric height at any point of the topographic surface.

An accurate model for the geoid will be based on the new geopotential models provided by the GRACE (Gravity Recovery and Climate Experiment) satellite mission. These models have two orders of magnitude smaller errors of the long wavelengths compared to the best geopotential models before GRACE. For example, the satellite only models GGM02S (Tapley *et al.*, 2005) and EIGEN-GRACE02S (Reigber *et al.*, 2005) have a cumulative

error of 1 cm for the spatial half-wavelength of 280 km. A significant improvement in the accuracy of the medium and short wavelengths is expected after the completion of the GOCE satellite mission. According to Visser *et al.* (2002), the static gravity field will be recovered with accuracy of 1 cm in terms of the geoid height for half-wavelengths of 75 km. Thus, the computational one-centimetre accuracy of the geoid will become realizable in the very near future (Tscherning *et al.*, 2000). The present-day theory for computing the regional geoid for Canada also assures the one-centimetre error (Vaníček *et al.*, 1999). Therefore, the problem of accounting for the secular temporal changes in the geoid height in Canada emerges. Over a time period of 5 to 10 years, the temporal changes in the geoid height become comparable with the desirable accuracy of the regional geoid model.

Geodynamic processes, such as land subduction, plate tectonics, mantle convection, orogeny, and episodic seismic events cause temporal variations of the Earth's gravity field and heights. However, their contribution to the temporal variations of the future geoid-based vertical datum is much smaller than the effect of *glacial isostatic adjustment* (GIA), also called *postglacial rebound* (PGR). While the latter is responsible for secular changes in the geoid at a rate of approximately 1 mm/yr, the former can contribute by as much as  $10^{-2}$  mm/yr (Dickey *et al.*, 1997). Therefore, only GIA will be of importance for the modernization of the vertical datum in Canada.

With the ice de-loading at the end of the last ice age approximately 21 000 years before present, the Earth has been experiencing continuous viscous adjustment driven by the disequilibrium caused by the mass imbalance in the previously ice-covered areas (e.g., Cathles, 1975). While the Earth's crust under the ice load is rebounding, the area in the periphery of the ice load is now subsiding and moving towards the centre of rebound. Consequently, the shape of the Earth and its potential are changing with time until a new equilibrium state is reached. The process of GIA is identified by geological observations and geodetic data such as observations of relative sea levels during the Late Pleistocene and Holocene, tilts of ancient strandlines, postglacial faults, moments of rebound-induced earthquakes, the polar wander, secular trends in tide gauge records of sea/lake level changes, changes in levelled heights, changes in the relative and absolute gravity, and free-

air anomalies over the de-glaciated areas. These constraints comprise the “truth” for the numerical GIA model outputs.

When the nontidal acceleration of the Earth’s rotation became observable from the  $J_2$  perturbation of the LAGEOS orbit three decades ago (Wu and Peltier, 1984; Peltier, 1985), opportunities for using the space techniques in the GIA modelling arose. The glacial isostatic adjustment, characterized by significant redistributions of masses, perturbs the moment of inertia tensor and induces anomalies in the Earth’s rotation. After subtracting the contribution of the tidal friction from the observed  $J_2$  harmonic time series, a strong negative rate corresponding to an acceleration of the Earth’s rotation is estimated. This secular rate is superimposed by a climate signal associated with the present-day melting of the polar ice sheets and sub-polar glaciers. The latter induces an increase in the  $J_2$  harmonic through the sea level rise and counteracts the negative GIA trend. The  $\dot{J}_2$  signal is an important constraint on the Earth’s viscosity profile, but the contribution of the melting of the present-day polar ice sheets in Antarctica and Greenland needs to be corrected for. Inverse procedures have been developed that allow for inferences about the mantle viscosity profile and a separation of the polar areas signal at the same time (Tosi *et al.*, 2005).

Historically, very long baseline interferometry (VLBI) and satellite laser ranging (SLR) enabled studies of the Earth crustal dynamics including the GIA process on a global scale. VLBI data were used for constraining ice history and Earth rheology in a number of works including Mitrovica *et al.* (1993), James and Lambert (1993), and Peltier (1995). Today, GPS provides the opportunity to create and maintain denser networks (compared to VLBI and SLR) over de-glaciated regions for constraining the GIA process. GPS compensates for the technique’s lower precision by the large amount of data collected at permanent and campaign stations. The reported achievable accuracy of the vertical velocities reaches 1mm/yr after five years of continuous measurements (e.g., Larson and van Dam, 2000).

For the first time, the dedicated gravity missions CHAMP and GRACE have determined a homogeneous and accurate gravity field and its temporal variations (Reigber *et al.*, 2003; Tapley *et al.*, 2004a); see Figure 1.1. Thus, they have provided new constraints for the GIA

studies. The GRACE mission provides time series of monthly gravity field solutions from which the mass redistribution in the Earth's interior and exterior can be computed (Tapley *et al.*, 2004b). Velicogna and Wahr (2002) have showed that, in principle, the GIA signal can be resolved from the GRACE data after 5 years of the mission's lifetime. This is particularly important for constraining the largest in magnitude and spatial scale signal in North America because the accurately GPS-derived crustal displacements are sparsely distributed.

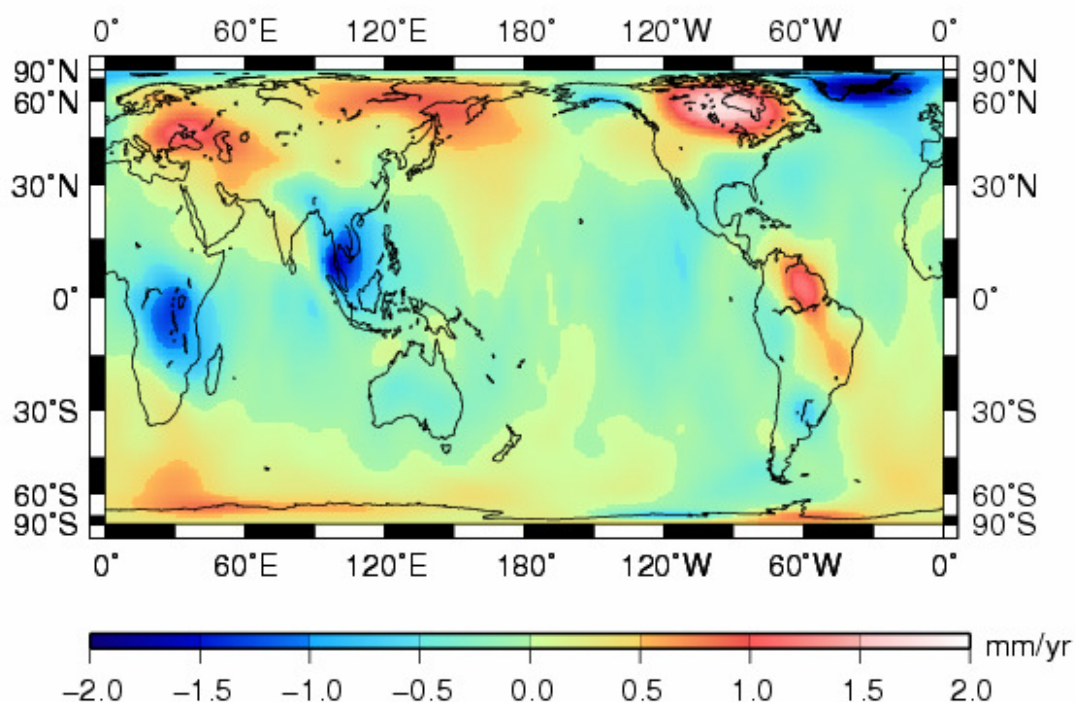


**Figure 1.1:** GRACE-observed rates of change of the geoid height derived in this thesis from the Center for Space Research (CSR) RL-01 data.

The rates of change of the geoid height and the absolute vertical displacement have been provided by the numerical GIA models since Peltier's development of the normal mode theory (1974). These models are subject to uncertainties of the input in terms of an Earth body model and an ice de-loading model. In parallel with the GIA modelling, empirical models based on geodetic observations have also been developed. A list of recent models would include the following:

- *Fennoscandia*: Ekman (1996), Kakkuri (1997), Mäkinen and Saaranen (1998), Mäkinen *et al.* (2000), Danielsen (2001), and Vestøl (2006);
- *North America*: Carrera *et al.* (1991), Pagiatakis and Salib (2003), Mainville and Craymer (2005).

Traditionally, the empirical models for the crustal uplift in Fennoscandia have been based on precise re-levelling data and tide gauge records with longer than one century history. Because of the excellent data coverage and the long time span of the measurements, the empirical models have provided valuable constraints on the Fennoscandian uplift for decades. The permanent GPS observations (e.g., Scherneck *et al.*, 1998) have provided an absolute datum for the tide gauges and the re-levelling data and made possible the direct comparison of the measured rates of the absolute vertical displacement with the radial displacement outputs from the GIA model simulations.

In North America, scattered (in space and time) re-levelling data and tide gauge records provided the sole spatial information for the crustal uplift and subduction until the first GPS-based constraints were published (Henton *et al.*, 2006; Sella *et al.*, 2007). The latter, combined with the rates of the absolute terrestrial gravity, which virtually cover all of Canada (Pagiatakis and Salib, 2003), provide a means for estimating the geoid change as an alternative to the GRACE observations. Alternatively, gravity rates estimated from GRACE data can be converted to uplift rates and compared to GPS velocities (see Chapter 2).

## 1.2 Thesis Objectives

The purpose of this thesis is to contribute to the *definition* and *realization* of a dynamic geoid-based vertical datum for Canada through modelling temporal variations of the gravimetric geoid and heights. The dynamic geoid model will serve as a reference surface for orthometric heights that also change with time. The main objective of this research is to develop and test a methodology for optimally combining the available geodetic constraints for modelling the temporal variations of the geoid and heights. The data include, but are not limited to, the GRACE-observed rates of change of the geoid height and absolute vertical displacement, rates of the absolute terrestrial gravity, GPS vertical velocities, and combined

tide gauge and satellite altimetry data. For the first time, terrestrial gravity and vertical displacement data are combined in empirical models to provide homogeneous in space temporal variations of the geoid height as a result of the glacial isostatic adjustment of the Earth and its geopotential.

To accomplish the objectives of this research, the following key issues should be resolved:

- To assess the available methods for an optimal combination of deformation data with regard to the spatial scales of the modelled temporal changes, the possibility for heterogeneous input, error propagation, and updating the empirical models whenever new data are available.
- To select appropriate base functions for modelling the spatial trend of the vertical crustal deformation field and to ensure the existence of a physically meaningful relationship between the rates of the vertical displacement and the rates of change of the geoid.
- To apply appropriate stochastic models and to resolve the relative weighting between the heterogeneous data.

### **1.3 Thesis Outline**

Chapter 2 introduces the vertical datum problem in the context of the time-variable gravity field and heights. Theoretical relationships among the temporal variations of the ellipsoidal, orthometric, and geoid heights are established. A critical review of the geodetic data constraints and their accuracy and the existing methods for modelling the temporal variations of the geoid and heights is presented. GIA modelling is reviewed briefly as the outputs are used for validation of the empirical models.

Chapter 3 deals with the approximation of vertical displacement rates by means of radial base functions. Critical issues including the optimal number, location, and shape of the base functions are resolved. In addition, an analytical relationship between the rates of the absolute vertical displacement and the rates of change of the geoid height is established in terms of inverse multiquadric base functions.

A methodology for empirical modelling of heterogeneous data is developed in Chapter 4. The methodology is based on the least-squares collocation with parameters approach combining the analytical representation of the smooth spatial trend surfaces in terms of radial base functions and a signal stochastic model with analytical signal covariance functions. Special attention is paid to the statistical testing and the proper relative weighting of the heterogeneous data input.

Chapter 5 is devoted to modelling the GRACE-observed rates of change of the geoid height. In particular, the capabilities of the principal component method for analysing the spatio-temporal variability of the geoid height are studied in depth. It is shown that the principal component analysis and the least-squares fitting of the time series give identical results, but the advantages of applying the former are emphasized. Furthermore, the GRACE-observed rates of vertical displacement are combined with the GPS and terrestrial gravity data for estimating the rates of change of the geoid height.

Chapter 6 deals with some practical aspects of the vertical displacement modelling using radial base functions. The emphasis is on the developed robust procedure for detecting erroneous observations in the heterogeneous data and the proper relative weighting of data.

In Chapter 7, the possibilities for implementing the dynamic geoid as a reference surface for orthometric heights in Canada are studied.

Finally, in Chapter 8, the achievements of this research are summarized together with the conclusions and outlook for future research. Recommendations and practical consideration for establishing the geoid-based dynamic vertical datum are given.

#### **1.4 Assumptions and Limitations**

The following assumptions and limitations have been adopted for this research:

- The developed methodology assumes slow deformation processes related to the viscoelastic response of the Earth to surface unloading. These processes are associated with secular rates of crustal displacement and mass redistribution.

- The testing areas are confined to the continental scale GIA deformation. This research does not focus on areas with tectonically driven deformations or areas affected by present-day glacier melting.
- The value of the gravity-to-height ratio, which defines the relative contributions of the mass redistribution and vertical crustal displacement to the change in gravity, is assumed constant over the whole of Canada. Although no justification for a laterally varying gravity-to-height ratio has been provided by glacial isostatic models, modelling with lateral heterogeneities is capable of predicting such variations. However, the present-day data quality and the accuracy of the estimated rates of the terrestrial gravity and the GPS vertical velocities impose certain limitations on such inferences.
- The developed methodology is limited to local and regional applications. Global implementations are not visible because of the lack of globally distributed terrestrial gravity and GPS data.
- The procedure deals only with the vertical component of the crustal deformation and does not include estimation of horizontal crustal displacements and velocities. Horizontal velocities comprise about 30% of the magnitude of vertical crustal velocities. Predicted horizontal velocities in Laurentide using a spherically symmetric self-gravitating and rotating Earth range from 0.5 mm/yr to 2 mm/yr (Mitrovica *et al.*, 2001). Neglected horizontal displacement introduces a maximum error of 0.1 mm in the empirically modelled vertical crustal displacement at distances of 100 km.
- A homogeneous and isotropic residual deformation field is assumed, while, in fact, it could be inhomogeneous and anisotropic, especially in tectonic areas. While this issue deserves a future investigation, results in this research are not affected by this assumption because the residual signal (1.5 - 2.0 mm/yr at most) is a small fraction of the observed vertical rates of 12 mm/yr.

## Chapter Two: Vertical datum problem and dynamic geoid

This chapter introduces and discusses the vertical datum problem in the context of the time-dependent gravity field and heights. Because glacial isostatic adjustment (GIA) is the dominant signal in the temporal variations of the geoid and heights in North America (see e.g., Sella *et al.*, 2007), the forward and inverse GIA modelling is presented briefly. It is shown that depending on the variations of the mantle viscosity profile, a wide range of geoid rates can be predicted. The significant deviations of the model predictions have further strengthened the idea to optimally combine the available geodetic constraints for empirical modelling of the rates of change of the geoid. For this purpose, the necessary theoretical relationships among the temporal variations of the ellipsoidal, orthometric, and geoid heights are established. In addition, a critical review of the available geodetic data in North America, data accuracy, and modelling approaches is presented.

### 2.1 Geoid as a vertical datum for orthometric heights

This section deals with the geoid as a vertical datum for orthometric heights. Two definitions for vertical datum are presented namely, the geodetic “Gauss-Listing” and the boundary value problem definitions, together with various options for realization of the vertical datum. The inconsistencies among ellipsoidal, orthometric, and geoid heights are discussed briefly. The contribution of the geodynamic phenomena to the vertical datum problem is discussed at the end of this section.

### 2.1.1 Definition and realization of the vertical datum

The *vertical (height) datum* is defined as “the coordinate surface to which heights, taken as vertical coordinates of points, are referred” (Vaníček, 1991). There exist three different types of vertical datum:

1. the geoid, an equipotential surface of the Earth gravity field, is a reference surface for orthometric heights;
2. the quasi-geoid, not an equipotential surface (except over the oceans), is a local reference surface for normal heights; and
3. the reference ellipsoid, a simple mathematical surface, is a reference surface for ellipsoidal (geodetic) heights.

The vertical datum (vertical reference surface) and the gravity related heights adopted for a country or a region form the *height system*.

The geoid can be defined by means of different approaches extensively described by Heck and Rummel (1989). Two of the definitions related to the objectives of this thesis are introduced in the following section.

#### ***Geodetic “Gauss-Listing” definition***

The geodetic “Gauss-Listing” definition of the geoid leads to a *levelling-based vertical datum*. The geoid is the particular equipotential surface of the gravity field that coincides with the mean sea level (MSL). Traditionally, MSL is computed by averaging tide gauge records of sea level variations over a sufficiently long time period to define a conventional “zero” (origin at the geoid). Orthometric heights are then determined and propagated by spirit levelling starting at the datum origin(s) to establish a vertical control network through which the vertical datum is accessible (Vaníček and Krakiwsky, 1986).

This definition of the vertical datum disregards the fact that the MSL is not an equipotential surface of the gravity field. Besides the short-period variations that can be filtered out from the measurements of the instantaneous sea level, there exist water variations originating from density changes, currents, and low frequency changes from atmospheric forcing and wind. In addition, large scale water oscillations due to seasonal solar heating, deviations of

the long-period tides from the equilibrium state, and sea level rise are present. All these effects characterize MSL as a quasi-stationary surface that is in departure from the geoid by values of 1 to 2 m. The difference between MSL and the geoid is called mean dynamic sea surface topography (MSST), which is determined by oceanographic methods and/or combining satellite altimetry sea level data, tide gauge records, and geoid models. If the geopotential of MSST at the datum origin is not accounted for, the orthometric heights will be biased with respect to the geoid. For countries of a continental scale, the vertical datum was traditionally realized by fixing the height of the mean sea level at several tide gauges to zero. For example, the CGVD28 is constrained to the mean sea level at five tide gauges on the Atlantic and Pacific coasts (e.g., Véronneau, 2001). As a consequence, the vertical reference surface is not an equipotential surface and may be subject to large distortions (Kearsley *et al.*, 1993).

### ***Boundary value problem (BVP) definition***

The boundary value problem provides the theoretical framework for computing the geoid, and, as a result, a *geoid-based vertical datum* can be defined. The geoid is found from the solution of the global, single boundary value problem (BVP), which, in spherical approximation, is defined as follows (Heiskanen and Moritz, 1967):

$$\left\{ \begin{array}{l} \Delta T = 0 \\ -\frac{\partial T}{\partial r} - \frac{2}{R}T = \Delta g - \frac{2}{R}\Delta W \end{array} \right. \quad (2.1)$$

The anomalous potential  $T$  is defined as the difference between the geopotential  $W$  and the normal gravity potential  $U$  of a reference ellipsoid, i.e.,  $T = W - U$ . The anomalous potential is a harmonic function outside the boundary surface (geoid). On the geoid, gravity anomalies  $\Delta g = g - \gamma$  ( $g$  is the gravity at the geoid and  $\gamma$  is the normal gravity at the ellipsoid) are corrected for the vertical datum parameter  $\Delta W = W_o - U_o$ , where  $W_o$  is the potential of the geoid and  $U_o$  is the potential at the ellipsoid. In Eq. (2.1),  $R$  is a mean radius of the Earth and  $\partial/\partial r$  is the radial derivative at the sphere with a radius  $R$ .

The geoid height (undulation),  $N$ , is computed using the Stokes integral as follows:

$$N = N_0 + \frac{R}{4\pi\gamma_\sigma} \iint \Delta g S(\psi) d\sigma, \quad (2.2)$$

where  $S(\psi)$  is the Stokes kernel,  $\psi$  is the spherical distance, and  $d\sigma$  is the surface element of the sphere.  $N_0$  is the shift of the geoid with respect to the level surface for which  $W_0 = U_0$  and is expressed as follows:

$$N_0 = \frac{G\delta M}{R\gamma} - \frac{\Delta W}{\gamma}, \quad (2.3)$$

where  $G$  is the gravitational constant, and  $\delta M$  is the difference of the masses of the geoid and ellipsoid. Usually  $\delta M = 0$  is assumed. This condition reads as follows: the zero degree harmonic of the anomalous potential has a vanishing at infinity zero degree harmonic, i.e.,  $T_{00} \rightarrow 0$ , when  $r \rightarrow \infty$ . Under this condition, the vertical datum parameter  $\Delta W$  is expressed as

$$\Delta W = \frac{R}{2} \Delta g_{00} = \frac{R}{8\pi} \iint \Delta g d\sigma, \quad (2.4)$$

where  $\Delta g_{00}$  is the zero degree gravity anomaly.

The global single BVP is classified as a single vertical (height) datum problem (Sansó and Venuti, 2002). Because the integral in Eq. (2.4) cannot be evaluated,  $\Delta W$  is assumed zero.

### ***Vertical datum realization***

Several options for vertical datum realization exist (see e.g., Vaníček, 1991 and Kearsley *et al.*, 1993) and are summarized as follows:

1. The vertical datum that is constrained to (i) one tide gauge for which an accurate model for MSST is available. The reference surface will be equipotential and biased with respect to the geoid, however, unification in a global vertical datum is possible; (ii) several tide gauges with modelled MSST. The reference surface will be distorted by possible errors of MSST models; (iii) a weighted mean of a set of tide gauges, but MSL at the different tide gauges will have orthometric heights different from zero.

2. The vertical datum that is constrained to an independent GPS station or a SLR site with an accurately estimated orthometric height as a difference between the ellipsoidal and geoid heights. At that fundamental benchmark, the vertical reference surface will coincide with the geoid. The orthometric heights can be propagated by *GNSS levelling*; however, due to errors in the geoid model and limitations in the accuracy of ellipsoidal heights, the orthometric heights will deviate from their true values. For large countries, such a realization is impossible and the vertical datum can be constrained to several fundamental benchmarks by a combined adjustment of ellipsoidal, orthometric, and geoid heights. This approach is followed by Fotopoulos (2003 and 2004) who also includes sea surface topography at tide gauges in the adjustment model.
3. The vertical datum is defined as a world height system by assuming that  $W_o = U_o$  and realized by the potential of one tide gauge as in option 1. An example of such a realization is EVRS2000 (Ihde and Augath, 2001).

### 2.1.2 Definition of orthometric and ellipsoidal heights

Orthometric height is defined as the distance along the plumb line between the point P on the topographic surface of the Earth and the geoid; it is computed as follows:

$$H_P = \frac{C_P}{\bar{g}_P}, \quad (2.5)$$

where  $C_P$  is the geopotential number and  $\bar{g}_P$  is the mean gravity along the plumb line at the point P. Since the crustal density is known only approximately, the computation of the mean gravity is based on assumptions. Therefore, orthometric heights are also approximately known. The geopotential number is defined as the difference between the constant potential of the geoid and the potential at the point P as follows:

$$C_P = W_o - W_P. \quad (2.6)$$

The geopotential number can be computed by means of the integral

$$C_P = \int_{P_0}^P g dH, \quad (2.7)$$

where  $dH$  is the distance between every two equipotential surfaces measured along the plumb line between the point P on the topographic surface and  $P_0$  on the geoid, and  $g$  is gravity for that increment. The integral is evaluated by the sum of the products of the differential height  $\Delta n_i$  and gravity  $g_i$  for small sections (between two rods)  $i$  along the levelling line as follows:

$$C_P = \sum_{i=1}^n g_i \Delta n_i. \quad (2.8)$$

Ellipsoidal height,  $h$ , is defined as the distance between the point P and the surface of the reference ellipsoid measured along the outer normal to the ellipsoid. The ellipsoidal height can be obtained by space-borne positioning techniques, including satellite laser ranging (SLR), very long baseline interferometry (VLBI), and GNSS (Seeber, 2003).

### 2.1.3 Relationship of ellipsoidal, orthometric, and geoid heights

The geometric relation of the ellipsoidal, geoid, and orthometric heights is illustrated in Figure 2.1. The small angle between the normal to the ellipsoid and the plumb line (the deflection of the vertical) at the point P is ignored and the following relationship along the normal to the ellipsoid holds (Heiskanen and Moritz, 1967):

$$h - N - H = 0. \quad (2.9a)$$

The relationship

$$H = h - N \quad (2.9b)$$

represents the basic idea of GNSS/levelling. The orthometric height can be computed by differencing the ellipsoidal height and the geoid height at any point at the topographic surface. For practical purposes, this relationship is given as follows:

$$\Delta H = \Delta h - \Delta N, \quad (2.9c)$$

where  $\Delta h$  is the ellipsoidal height difference,  $\Delta H$  is the orthometric height difference, and  $\Delta N$  is the geoid height difference.

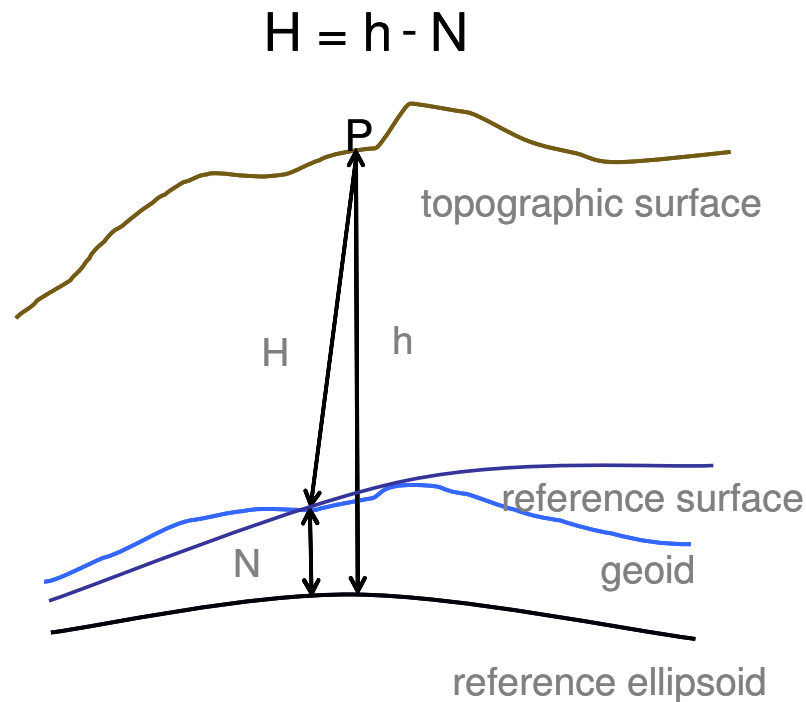


**Figure 2.1:** Relation between ellipsoidal, orthometric, and geoid heights.

The link between the traditional levelling-based vertical datum and the geoid is realized by means of GNSS positioning at the benchmarks of the vertical control network. Discrepancies among ellipsoidal, orthometric, and geoid heights are usually greater than the measurement and computational accuracy imply. Apart from the conceptually different definitions of the geoid given in Section 2.1.1, other important factors (see Figure 2.2) are horizontal datum inconsistencies of the geoid and ellipsoidal heights, systematic errors in the levelling network, and limitations in the measurement accuracy of the vertical component by GNSS (Kotsakis and Sideris, 1999). The geoid model may contain long-wavelength errors inherited from the geopotential model as well as short-wavelength errors from the digital terrain models employed (see Section 7.2). Also, biases present in gravity

anomalies as a result of gravity, vertical, and horizontal datum inconsistencies in addition to systematic distortions and short-wavelength errors caused by theoretical assumptions in the computation of the vertical gravity gradient may affect the geoid (Heck, 1990; Featherstone, 1995).

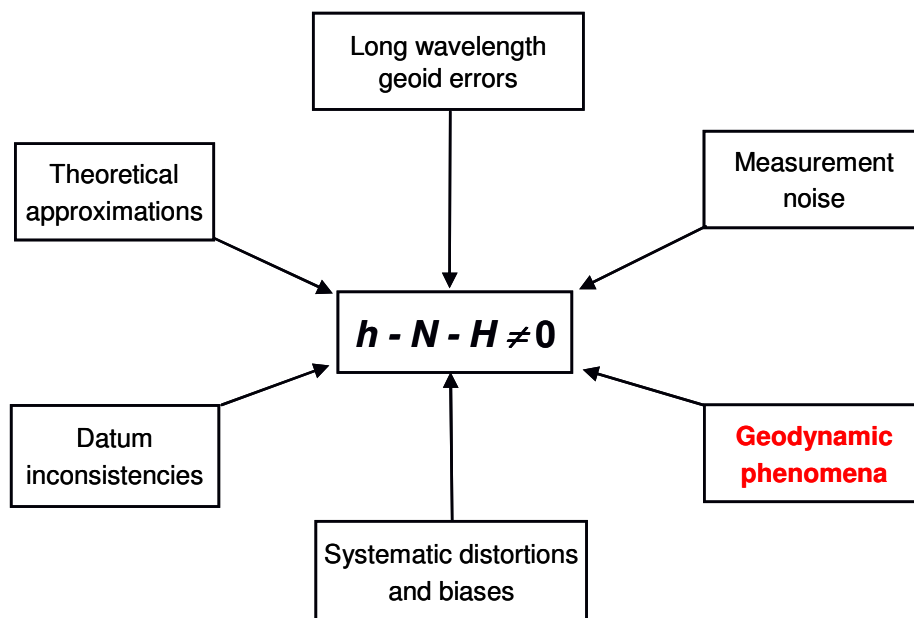


**Figure 2.2:** Factors contributing to the discrepancies among ellipsoidal, orthometric, and geoid heights.

Due to the combined effect of all of the factors, Eq. (2.9a) can be rewritten as follows:

$$h_p - N_p - H_p = l_p, \quad (2.10)$$

where  $l_p$  is the height misclosure at the benchmark P of the levelling network.

As shown in Figure 2.2, the geodynamic phenomena comprise one of the causes of height misclosures through the temporal changes of ellipsoidal, orthometric, and geoid heights. The secular glacial isostatic adjustment of the Earth's potential and crust dominates the temporal changes of the geoid and heights in North America. Therefore, GIA modelling is presented in the following section.

## 2.2 Glacial isostatic adjustment

This section starts with a description of the sea level equation that explains the interaction of the solid Earth and its gravitational potential with the ice and water load throughout the ice accumulation and melting during the ice age cycles. The section continues with an overview of the ice models in use and inferences of mantle viscosity in the studies that involve inversion of geological and geodetic data in the Hudson Bay region. This is followed by a description of the GIA simulation outputs used for validation of the empirical models developed in this thesis by means of an optimal combination of geodetic data.

### 2.2.1 Forward problem

The theory of glacial isostatic adjustment, or postglacial rebound (PGR), predicts the gravitational response of a viscoelastic Earth body to the surface ice load. Usually, the Earth's rheology is assumed Maxwell for which a linear relation between stress and strain exists. According to the normal mode theory (Peltier, 1974; Wu and Peltier, 1982), the solution of the field equations of Newton's law of momentum conservation and the Poisson equation is obtained by the "correspondence principle" (Cathles, 1975) from the solution of the equivalent elastic problem in the Laplace transform domain. Spherical harmonic expansions of the field equations and boundary conditions lead to a system of first order differential equations, from the solution of which the impulse response Green functions are obtained. Multiplication with the ice load spectrum results in a spectral solution that is transformed to the space-time domain. The outputs of the described "forward modelling" are relative sea level changes, radial and horizontal displacements, geoid and gravity changes and their rates.

The geoid changes are caused by change in ice/water load and internal mass redistributions from the viscoelastic response of the Earth body to the change in the load. Therefore, the relationship among changes in the sea level, the geoid, and the solid Earth is treated in a "gravitationally self-consistent" manner by solving the so-called "sea level equation" (Farrell and Clark, 1976; Peltier *et al.*, 1978). The "gravitational self-consistency" implies that the calculated ocean surface (which is an equipotential surface of the perturbed gravity

field, i.e., the geoid) is consistent with the internal and external mass redistributions. The basic form of the sea level equation is as follows:

$$S(\theta, \lambda, t) = O(\theta, \lambda, t)[\tilde{G}(\theta, \lambda, t) - \tilde{R}(\theta, \lambda, t)], \quad (2.11)$$

where  $S$  is the relative sea level (RSL) with respect to the perturbed geoid,  $\tilde{G}$  and  $\tilde{R}$  are the perturbations of the geoid and radius of the solid Earth, respectively, and  $O$  is the ocean function;  $\theta$  and  $\lambda$  are the geocentric co-latitude and longitude, respectively, and  $t$  is the time epoch. To the first order perturbation, the sea level equation is the space-time convolution (see, e.g., Mitrovica and Peltier, 1991):

$$\delta S(\theta, \lambda, t) = O(\theta, \lambda, t) \left\{ \int_{-\infty}^t dt' \int_{\sigma} d\sigma \tilde{L}(\theta', \lambda', t') \left[ \frac{\Phi^L(\psi, t-t')}{g_a} - \Gamma^L(\psi, t-t') \right] + \frac{\Delta\Phi(t)}{g_a} \right\}, \quad (2.12)$$

where  $\tilde{L}$  is the time-dependent load convolved with the viscoelastic surface load Green functions for the potential perturbation  $\Phi^L(\psi, t)$  and the radial displacement  $\Gamma^L(\psi, t)$ . The last term  $\Delta\Phi(t)/g_a$  in Eq. (2.12) is the time-dependent mass conservation term. It includes the contribution of the eustatic sea level rise from the disintegration of the ice sheets.

Since the unknown sea level is a part of the load

$$\tilde{L}(\varphi, \lambda, t) = \rho_I \delta I(\varphi, \lambda, t) + \rho_W \delta S(\varphi, \lambda, t), \quad (2.13)$$

the sea level equation is solved iteratively. In this equation,  $\delta I$  and  $\delta S$  are changes in the ice thickness and relative sea level, and  $\rho_I$  and  $\rho_W$  are the densities of the ice and water, respectively.

The so-called ‘‘pseudo-spectral algorithm’’ (Mitrovica and Peltier, 1991) is currently widely applied to solve the sea level equation. The improvements of the original Farrell and Clark theory include (i) the effect of the changing rotational potential due to GIA on the sea level (e.g., Milne and Mitrovica, 1998), (ii) the ‘‘near-field hydro-isostasy’’ (Milne *et al.*, 1999), and (iii) a time-dependent coast line (Peltier, 1994).

### 2.2.2 Inverse problem

The pattern and amplitude of the GIA model outputs depend on the radially and laterally stratified viscoelastic model of the Earth and the ice model adopted. The two model inputs are interrelated; in principle, this requires iterative inferences based on geological and geodetic constraints. In the so-called “inverse modelling”, one model is assumed to represent the truth while inferring either the ice model or the viscosity structure of the mantle (e.g., Peltier, 1998). For example, if the ice de-glaciation history is to be modelled, the assumed viscosity profile is kept unchanged while the ice history is modified until the required fit with the data is found. Then, based on the inferred ice model, the viscosity profile can be improved. In the following section, a short review of the ice models and the inferred viscosity profiles is presented with an emphasis on those obtained from data constraints in North America. The Earth is assumed radially symmetric, self-gravitating and viscoelastic, with density stratification and elastic parameters according to PREM (Dziewonski and Anderson, 1981).

#### *Ice models*

The ICE-3G model of Tushingham and Peltier (1991) has been widely used in postglacial rebound studies. It is constrained by RSL histories and is accepted to be independent of geodetic constraints. The following assumptions hold: (i) the last glacial maximum (LGM) was 18,000 years before present; (ii) the Laurentide ice sheet was melting fastest 9,000 years before present; (iii) a time discretization of 1,000 years is assumed; and (iv) a constant ocean function is used. The ICE-3G model was constructed based on the following viscosity profile: a lithosphere thickness of 120 km, an upper mantle viscosity of  $1 \times 10^{21}$  Pa·s, and a lower mantle viscosity of  $2 \times 10^{21}$  Pa·s, which is inferred by the ICE2 model of Wu and Peltier (1983).

The ice thickness of Peltier’s ICE-4G model (1994, 1996) also is derived by inverting postglacial RSL histories with new  $^{14}\text{C}$  calibration. A simple viscosity profile was used as follows: a lithosphere thickness of 120.6 km, an upper mantle, a transition zone with

viscosity of  $10^{21}$  Pa·s, and a lower mantle viscosity of  $2 \times 10^{21}$  Pa·s. In difference with the ICE-3G model, a time- dependent ocean function was used.

The ICE-5G model (*ibid.*) is the latest ice sheet model in use. The main difference in geometry from its predecessors is the multi-dome structure of the Laurentide ice sheet complex, which has been debatable for a long time. The early reconstructions of the ice sheet complex account for a multidome structure with ice domes located over Keewatin and northern Quebec (Tushingham and Peltier, 1991). These are replaced by a one-dome ice sheet in the ICE-3G and ICE-4G models. The newest ICE-5G model returns to the multidome structure and includes a very thick and large dome over Keewatin, centered close to Yellowknife, a smaller dome in southeastern Hudson Bay, and a third dome in the Foxe basin (Peltier, 2004). Another important difference is the much smaller ice thickness over Hudson Bay compared to the ICE-4G model due to the fast flow of ice through the Hudson Bay Strait. The ICE-5G (VM2) model simultaneously fits a large set of RSL histories, a VLBI vertical displacement rate over Yellowknife, and the gravity rates along the traverse of the North American Mid-continental tilt project (Section 2.4.2).

### ***Inferences of mantle viscosity***

Traditionally, the inferences of the mantle viscosity are based on an inversion of RSL histories. The optimal viscosity values are obtained from the best fit to the RSL time curves. In North America, the negative free-air gravity anomaly, believed to indicate the remaining isostatic compensation of the Earth (Peltier and Wu, 1982), was also used to constrain the longer wavelengths of the GIA deformation. Using the conventional two-layer parameterization of the mantle with a discontinuity at the 670 km depth, Peltier and Andrews (1983) inferred upper and lower mantle viscosities of  $1 \times 10^{21}$  and  $(1-3) \times 10^{21}$  Pa·s, respectively. Using only RSL histories, Nakada and Lambeck (1991) obtained estimates of  $(0.4-0.6) \times 10^{21}$  Pa·s and  $(20-50) \times 10^{21}$  Pa·s, respectively. In the Han and Wahr (1995) study, the best fit to both RSL histories and gravity anomaly is obtained for an upper mantle viscosity of  $(0.6-1.0) \times 10^{21}$  Pa·s and a lower mantle viscosity of  $(30-50) \times 10^{21}$  Pa·s. As Mitrovica (1997) and Simons and Hager (1997) argued, the gravity low is partially

related to the mantle convection. From the joint inversion of mantle convection and GIA data (including the RSL histories in Hudson Bay), Mitrovica and Forte (2004) showed that the mantle profile exhibits a three orders of magnitude increase from the upper mantle with a mean viscosity value of  $4 \times 10^{20}$  Pa·s to a high viscosity peak of  $10^{23}$  Pa·s located at the 2000 km depth. Further studies showed that the postglacial RSL data in North America cannot be fitted simultaneously by a single Earth model within their uncertainties; see, e.g., (Mitrovica and Peltier, 1995) and (Cianetti *et al.*, 2002). Recently, from a joint inversion of RSL data in the Hudson Bay region, the present-day relative sea level from the tide gauge record at Churchill, the absolute vertical displacement, and the rate of change of the terrestrial gravity at the same site, and using the ICE-3G model, Wolf *et al.* (2006) obtained estimates of  $3.2 \times 10^{20}$  Pa·s for the upper mantle viscosity and  $1.6 \times 10^{22}$  Pa·s for the lower mantle viscosity. The authors pointed out that lower mantle viscosities larger than  $5 \times 10^{21}$  Pa·s are also supported by the data constraints.

The review of the ice models and mantle viscosity profiles demonstrates that large variations in the input models exist, which presupposes large variations in the spatial pattern and amplitude of the simulation outputs. Figure 2.3 shows the range of the predicted rates of change of the geoid height in Laurentide using different viscosity profiles and the ICE-4G model (van der Wal *et al.*, 2006). The geoid rate varies significantly with the mantle viscosity profile adopted. The highest amplitudes are obtained for an upper mantle viscosity of  $0.7 \times 10^{21}$  Pa·s and a lower mantle viscosity of  $20 \times 10^{21}$  Pa·s, while the lowest geoid rate is predicted by  $0.4 \times 10^{21}$  Pa·s and  $2-4 \times 10^{21}$  Pa·s (close to the VM2 values of Peltier (2004)), respectively. The rates of the geoid height will be used for validation of the empirical models in Chapter 4 computed by means of terrestrial geodetic data.

The outputs from postglacial rebound simulations used in this thesis are obtained with a radially symmetric, incompressible Earth model using the pseudo-spectral algorithm to solve the sea level equation. Recent advances in GIA modelling account for lithospheric and upper mantle lateral variations; see, e.g., Latychev *et al.* (2005), Spada *et al.* (2006), and Wang and Wu (2006).

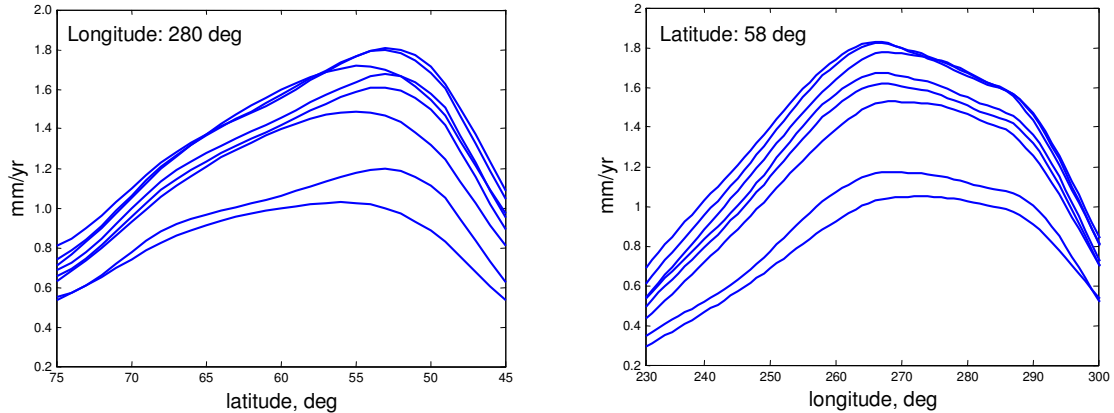


**Figure 2.3:** Rate of change of the geoid height as a function of viscosity for a spherically symmetric incompressible Earth and the ICE-4G model (see text).

### 2.3 Relationship of temporal changes of ellipsoidal, orthometric, and geoid heights

In this section, the basic concepts of the temporal changes of the geoid and heights are introduced. No assumptions regarding the spatial scale (global, regional, or local) and the processes (elastic or viscoelastic) responsible for the temporal changes in the gravity field and vertical crustal displacement are made.

In Figure 2.4, a point P on the topographic surface of the Earth is positioned in an Earth fixed coordinate system through a vector  $\mathbf{r}_p$  (Biró, 1983 and Biró *et al.*, 1986). The point P can be a collocated GPS station and an absolute gravity site. It is assumed that the GPS positions and gravity are corrected for ocean loading, solid Earth tides, pole tide, rotational deformation due to polar motion, as well as atmospheric loading (IERS conventions 2003; Boedecker, 1991). In addition, gravity is corrected for soil moisture and variations of the local ground water table. The soil moisture correction applies to the GPS positions also. The permanent tidal component will be discussed later in this section; for now it is assumed that there is consistency between the geoid and the crust, being a zero tidal geoid and crust. It is assumed that secular geodynamic, tectonic, and episodic processes are superimposed and affect the gravity field and crust.

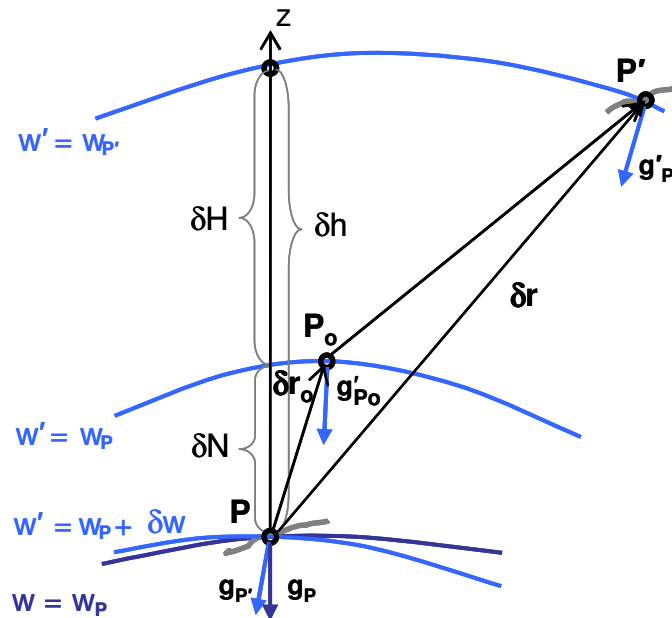


**Figure 2.4:** Temporal changes of the gravity field and heights at a point P of the topographic surface (adopted after Biró *et al.*, 1986).

The equipotential surface through the point P at the time epoch  $t$  is given by  $W = W_P$ . It is assumed that at epoch  $t' = t + \delta t$  the geopotential changes by the constant value  $\delta W$  so that the equipotential surfaces of the new gravity field are defined by the equation  $W' = W + \delta W$ . The surface  $W = W_P$  is displaced to its new position through the point  $P_0$ , for which the change in geopotential can be expressed by a Taylor expansion including only linear terms as follows (Moritz, 1980, p. 340):

$$\delta W = W'_{P_0} - W_P = W_P - (W_P + \text{grad}W \delta \mathbf{r}_0) = -\mathbf{g} \delta \mathbf{r}_0, \quad (2.14)$$

where  $\mathbf{g}^T = (W_x, W_y, W_z)$  and  $\mathbf{r}_0^T = (r_{0x}, r_{0y}, r_{0z})$  in a topocentric coordinate system  $xyz$  at the point P.

From Eq.(2.14), with  $W_x = W_y = 0, W_z = -g$ , and  $\delta r_{0z} = \delta N$ , it follows that the displacement of the equipotential surface is the change in the geoid height

$$\delta N = \frac{\delta W}{g_a}, \quad (2.15)$$

where, without loss of accuracy,  $g$  is substituted by the average gravity  $g_a$ .

Let  $\delta \mathbf{r}^T = (\delta r_x, \delta r_y, \delta r_z)$  define the new position of the station at the point  $P'$  in the topocentric coordinate system of the point  $P$ . The difference

$$\delta H = \frac{W'_{P'} - W'_P}{g_a} = \frac{\delta W'}{g_a} \quad (2.16)$$

is the relative (levelled) change in the position of  $P$  with respect to the displaced geoid and represents the change in the orthometric height.

The change in the gravity vector at  $P'$  can be expressed as follows:

$$\mathbf{g}'_{P'} = \mathbf{g}_P + \text{grad} \delta W. \quad (2.17)$$

At epoch  $t$ , the gravity vector at the point  $P'$  can be obtained from the gravity vector at the point  $P$  as

$$\mathbf{g}_{P'} = \mathbf{g}_P + (\text{grad} \mathbf{g})_P \delta \mathbf{r}, \quad (2.18)$$

with the tensor of the second order derivatives of the gravity potential (Moritz, 1980, p.235)

$$\text{grad} \mathbf{g} = \begin{bmatrix} W_{xx} & W_{xy} & W_{xz} \\ W_{yx} & W_{yy} & W_{yz} \\ W_{zx} & W_{zy} & W_{zz} \end{bmatrix}. \quad (2.19)$$

With Eqs. (2.17), (2.18), and (2.19), the change in the gravity vector,

$\delta \mathbf{g}^T = (\delta g_x, \delta g_y, \delta g_z)$ , is expressed as follows:

$$\delta \mathbf{g} = \mathbf{g}'_{P'} - \mathbf{g}_P = \text{grad} \mathbf{g} \delta \mathbf{r} + \text{grad} \delta W. \quad (2.20)$$

An absolute gravimeter located at  $P$  measures the vertical component of gravity. Therefore, the change in gravity in the vicinity of the point  $P$  is

$$\delta g_z = \delta g = W_{zx} \delta r_x + W_{zy} \delta r_y + W_{zz} \delta r_z + \frac{\partial \delta W}{\partial z}. \quad (2.21)$$

If the horizontal gravity gradients are assumed equal to zero, i.e.,  $W_{zx} = W_{zy} = 0$ , Eq.(2.21) is further simplified to

$$\delta g = \frac{\partial g}{\partial z} \delta r_z + \frac{\partial \delta W}{\partial z}. \quad (2.22)$$

Eq.(2.22) shows that the change in gravity at the point P is a sum of two components, namely, a change due to the absolute vertical displacement of the point and a change due to the redistributed masses. In this thesis, the measured change in gravity on the topographic surface will be called change in the terrestrial gravity, while the mass component will be called change in gravity.

From Figure 2.4, the absolute vertical displacement of the point P,  $\delta h$ , is determined as follows:

$$\delta h = \delta N + \delta H. \quad (2.23a)$$

Provided that the change in the geoid height is modelled, the levelled vertical displacement can be determined by measuring the absolute vertical displacement by means of GPS and using Eq.(2.23a) as follows:

$$\delta H = \delta h - \delta N. \quad (2.23b)$$

Analogously, the following relation can be written for the rates of change of the ellipsoidal, orthometric, and geoid heights:

$$\dot{H} = \dot{h} - \dot{N}. \quad (2.23c)$$

As in Section 2.1.3, the deflection of the vertical at the point P has been neglected.

In the discussion above, it has been assumed that the terrestrial gravity, geoid, and absolute and levelled crustal displacement refer to a zero tidal system. Under the luni-solar tidal forces, an elastic Earth's body experiences a change in potential that consists of a direct attraction component, a deformation part, and change in potential due to the vertical shift of the crust (Torge, 2001). The tidal potential contains a time dependent (periodic) component

and a time independent (permanent) component called a *permanent tidal potential*. A point P on the topographic surface undergoes permanent displacement (called permanent crustal deformation) as a result of the permanent tide. Three different concepts exist regarding the tidal components removed from the geodetic measurements (e.g., Ekman, 1989; Poutanen *et al.*, 1996; Sun and Sjöberg, 2001). The measurements refer to a *non-tidal* geoid and crust if they are corrected for the total tidal potential and displacement including the periodic and permanent tide; the measurements refer to a *mean tidal* geoid and crust if the permanent tidal potential and deformation are restored; and the measurements refer to a *zero tidal* geoid if the permanent tidal potential is removed but the permanent tidal deformation is included. The zero and mean crusts are identical because the Earth's crust is not affected by the permanent tidal potential.

The consistency with respect to the permanent tidal correction is important when secular vertical displacements are estimated from measurements of different time epochs. A typical example is the levelled postglacial uplift/subsidence derived from precise levellings with different epochs (Ekman, 1989). Also, if different data sets are combined in a least-squares adjustment procedure, the consistency of the tidal corrections should be ensured. If this is not the case, systematic errors larger than the standard error of the vertical crustal displacement can introduce distortions (of a north-south orientation) in the estimated displacements (*ibid.*). However, if rates of change derived independently from different data sets are compared, provided that the permanent tide is treated consistently within each data set, the rates are free from distortions.

Inconsistencies among the tidal corrections for gravity, geoid height, and orthometric height can introduce large systematic distortions in the vertical datum. The local  $W_0$  value is affected both by the change in the potential of the geoid and the crustal displacement of the fundamental benchmark of the vertical datum. Practical aspects of this problem are discussed by Jekeli (2000). Using an example for the Nordic countries, Ekman (1989) has shown that the permanent tide can introduce a decimetre error in the orthometric height differences obtained by means of GPS positioning and a geoid model. In addition, the systematic errors in gravity and heights due to the inconsistencies of the tidal corrections may propagate into the geoid model through the gravity corrections. Therefore, if the

vertical datum is defined by means of a geoid model and accessed at the fundamental benchmarks, it is important that the ellipsoidal, orthometric, and geoid heights refer to the same tidal system.

## **2.4 Geodetic constraints on geodynamic, tectonic, and other processes in North America**

This section presents a review of the existing geodetic data constraints on the GIA signal and other local processes in North America. It starts with the rates of change of the geoid height estimated from an analysis of GRACE time series of geopotential and proceeds with terrestrial measurements including rates of the terrestrial gravity from absolute gravimetry, absolute vertical displacement from GPS measurements and from combining tide gauge records and satellite altimetry sea level data, relative vertical displacements and tilts from precise re-levelling data, and estimates of the gravity-to-height ratio. The emphasis is on the accuracy with which different geodetic techniques provide measurements of the time-dependent heights, gravity, and geoid. This is a necessary step towards the optimal combination of the heterogeneous geodetic observations in Chapters 4, 5, and 6.

### **2.4.1 GRACE-observed temporal changes of the gravity field**

GRACE provides maps of large scale gravity field variations that are homogeneous both in space and time and are independent of crustal displacements. “Static” gravity field solutions averaged over approximately one month are used to construct time series of the change in the geoid height analyzed subsequently in order to estimate seasonal, annual, inter-annual, and long-term variability. Each GRACE solution is relative to the background models of the mean gravity field and the de-aliasing models of short-term variability of the atmosphere and oceans employed in the processing of the GRACE measurements (see, Tapley *et al.*, 2005). Thus, the time series of the monthly gravity field solutions contain (i) unmodelled geophysical signals over the continents and oceans and mass variations in the Earth’s interior, (ii) aliased errors in the long-period variations of the atmosphere and ocean models, and (iii) errors of the GRACE measurements and data processing strategies.

Estimates of the GRACE gravity field errors are provided in the form of calibrated standard deviations of the geopotential coefficients for every month.

GRACE observes changes in gravity that are integrated in a vertical column and spatially averaged at distances of hundreds to thousands of kilometres. A separation of the gravity signal from different sources is impossible without a priori information available in terms of models of mass variability (see, e.g., Ramillien *et al.*, 2004 and 2005). As shown by Rangelova *et al.* (2007a), in the previously glaciated areas in North America, the GIA signal can interfere with the hydrology model variability, which, over the duration of the GRACE time series, appears as a trend. Thus, to estimate the GIA geoid rate, the hydrology signal from the available continental water storage models should be removed. Conversely, the improvement of the same models relies on the knowledge gained from GRACE to constrain the GIA models.

The true temporal change of the geoid height can be represented as follows:

$$\begin{aligned} \delta N(\varphi, \lambda, t)^{\text{true}} = & \delta N(\varphi, \lambda, t)^{\text{GRACE}} + \delta N(\varphi, \lambda, t)^{\text{commission}} + \dots \\ & + \delta N(\varphi, \lambda, t)^{\text{omission}} + \delta N(\varphi, \lambda, t)^{\text{leakage}} \end{aligned} \quad (2.24)$$

The first term on the right hand side, i.e.,  $\delta N(\varphi, \lambda, t)^{\text{GRACE}}$ , is the change in the geoid height with respect to the long-term mean (or the first epoch of the time series) computed with GRACE geopotential spherical harmonic (SH) coefficients  $\delta \bar{C}_{lm}(t)$  and  $\delta \bar{S}_{lm}(t)$  of maximum degree and order  $l_{\text{max}}$  as follows:

$$\delta N(\varphi, \lambda, t)^{\text{GRACE}} = R \sum_{l=2}^{l_{\text{max}}} \sum_{m=0}^l \bar{P}_{lm}(\sin \varphi) \left[ \delta \bar{C}_{lm}(t) \cos(m\lambda) + \delta \bar{S}_{lm}(t) \sin(m\lambda) \right], \quad (2.25)$$

where  $R$  stands for the mean radius of the Earth,  $\varphi$  and  $\lambda$  are the latitude and longitude, respectively, and  $\bar{P}_{lm}(\sin \varphi)$  are the fully normalized Legendre functions. The second term in Eq. (2.24) is the commission error  $\delta N(\varphi, \lambda, t)^{\text{commission}}$  that is due to the noise present in the GRACE SH coefficients. The omission error  $\delta N(\varphi, \lambda, t)^{\text{omission}}$  is due to the truncation of the geoid changes at the maximum spherical degree  $l_{\text{max}}$ .

The accuracy of the GRACE SH coefficients becomes worse with increasing the spherical degree. One way to decrease the effect of the GRACE error is to truncate the series in Eq.(2.25) at a lower degree, which increases the omission error. Instead, the SH coefficients are weighted according to

$$\delta N(\varphi, \lambda, t) = R \sum_{l=2}^{l_{\max}} \sum_{m=0}^l W_l \bar{P}_{lm}(\sin \varphi) \left[ \delta \bar{C}_{lm}(t) \cos(m\lambda) + \delta \bar{S}_{lm}(t) \sin(m\lambda) \right], \quad (2.26)$$

where  $W_l$  are the coefficients of an isotropic smoothing filter per degree. In fact, the geoid change is averaged within an area with a certain radius and the random errors cancel out. The geoid changes computed from the GRACE gravity field solutions exhibit significant spatial correlation evident as a north-south striping effect as shown by Chen *et al.* (2005a). This effect is attributable to the correlations of the even and odd order coefficients (taken as a function of degree) and is observed for the coefficients above degrees 5-8 (Swenson and Wahr, 2006). Different filtering techniques and their effect on the rate of change of the geoid height are discussed in Chapter 5.

The last term  $\delta N(\varphi, \lambda, t)^{\text{leakage}}$  in Eq.(2.24) is the contribution of the signals outside of the area of interest that leak into the area because of the smoothing filter applied (e.g., Swenson and Wahr, 2002). The leakage error increases with the increase in the radius of the smoothing filter. For the Hudson Bay region, the signals of interest are the present-day melting of the Greenland ice sheet and Alaska glaciers as well as the ocean signal in Hudson Bay. According to van der Wal *et al.* (2007), the leakage of Greenland and Alaska signals is between -0.4 and -0.2 mm/yr for the northern areas of Hudson Bay for various decreasing smoothing radii. Another source of uncertainty is the sea level rise due to recent melting of polar ice sheets and mountain glaciers, which in Hudson Bay has a similar pattern to the GIA signal. According to Wahr and Davis (2002), in the presence of sea level rise, the GIA signal can be recovered with an error of approximately 5%. For rate of change of the geoid height of 1.5 mm/yr, the sea level error is less than 0.1 mm/yr.

### 2.4.2 Absolute and relative terrestrial gravimetry

According to Groten and Becker (1995), the basic benefit from the terrestrial gravimetry, in combination with satellite or traditional surveying techniques, is "... in its "integrating effect", which means that height and gravity changes together enable, at least in principle, the solution of a four-dimensional boundary value problem,...". The "integrating" effect contains the local uplift or subsidence together with a local and/or regional potential change caused by mass redistributions in the Earth's interior.

The accuracy of the absolute gravity (AG) measurements is defined as the level of certainty with which measurements can be considered representative of the true (unknown) value of absolute gravity at the site (CIRES, 1993). According to Faller (2002), the present day level of accuracy approaches 1  $\mu\text{Gal}$ , which corresponds to accuracy of 3 mm of the measured height if there is no redistribution of masses. If a vertical crustal displacement and a mass redistribution are of interest, the absolute gravity measurements have to be corrected for all known geophysical signals and environmental noise including tides, periodic and non-periodic ocean loading, atmospheric effects, ground water table, microseism. These corrections are based on models whose uncertainties can introduce in a single absolute gravity measurement errors of several  $\mu\text{Gal}$ . For example, the uncertainty in the modelled ground water table can reach 10  $\mu\text{Gal}$  (CIRES, 1993).

#### *North American Mid-continent tilt project*

For the purpose of postglacial rebound studies, a traverse of absolute gravity stations collocated with continuously-operating GPS receivers has been established (e.g., Larson and van Dam, 2000; Lambert *et al.*, 2001 and 2006). The traverse starts from an area of significant uplift on the west coast of the Hudson Bay and continues southward to the subsiding area southwest of the Great Lakes (see Figure 2.6). The reported accuracy of the estimated rate of change of the terrestrial gravity from 20 measurements within one decade at Churchill is approximately 0.1  $\mu\text{Gal/yr}$  (Lambert *et al.*, 2006). A gravity-to-height ratio of  $-0.18 \pm 0.03$   $\mu\text{Gal/mm}$  has been obtained from a weighted least-squares fit to the ratio values computed for the four sites. The estimates of gravity rates and vertical crustal

displacements have been used in local improvements of the postglacial rebound models in the Nelson drainage basin (Lambert *et al.*, 2005).

### ***Canadian Gravity Standardization Network***

The Canadian Gravity Standardization Network (CGSN) is designed to provide gravimetric control and to support geophysical exploration in Canada (Pagiatakis and Salib, 2003). The network is not optimally designed for geodynamics monitoring; nor are gravity observations regularly repeated in time. As a consequence, the relative gravity observations are not consistent in space and time; however, they span more than four decades, which allows for estimating the temporal changes in gravity. Five absolute gravity stations re-observed at least three times provide constraints for the adjustment of the observed gravity differences. The covariance matrix of observations is obtained from a detailed analysis of the observation procedures assessing factors that include experience of the observer, means of transportation, vibrations (seismicity, traffic, transportation, etc.), atmosphere conditions (wind and temperature), quality of calibration, magnetic fields, and instrumental levelling biases (*ibid.*). CGSN consists of about 1500 primary and secondary gravity reference stations; 64 of them are classified as “primary gravity control” sites with rates of change of the terrestrial gravity parameterized in the least-squares adjustment model. The epoch of the adjustment is 2000.0. The estimated standard deviations of the rates vary from 0.06 to 0.9  $\mu\text{Gal}/\text{yr}$ .

### **2.4.3 Continuous and episodic GPS measurements**

GPS measurements have been used in postglacial rebound studies for approximately one decade. One of the earliest published results was obtained from the Permanent Finnish GPS Network for the time span of 1995 to 1999 (Mäkinen *et al.*, 2000). The computed rates of change of the ellipsoidal height from weekly solutions relative to one station were compared to the levelled uplift computed from three levelling campaigns in Finland and corrected for the rates of change of the geoid. The derived slopes agreed at the 95% confidence level. In the BIFROST-related study, Johansson *et al.* (2002) provided 1.3 mm/yr as a conservative estimate of the uncertainty in the vertical velocity component. A

large part of this value is due to correlated errors related to systematic errors in the satellite orbits and/or terrestrial reference frames. Other sources of errors include regionally correlated errors due to errors in the atmosphere and the ocean loading models and site-specific errors (multipath, antenna phase center variations, and rapid snow accumulation).

### ***Stable North American Reference Frame (SNARF)***

GPS vertical velocities in North America have been provided in the Stable North American Reference Frame (SNARF) since 2005. SNARF is a selection of “datum sites” representing the tectonically stable interior of the North American plate that facilitates the derivation and geophysical interpretation of the relative crustal displacements along the North American-Pacific plate boundary and the GIA signal (Blewitt *et al.*, 2005).

The North American Reference Frame (NAREF) is a densification of the ITRF using continuously operating GPS stations in Canada and the US. The station coordinates and their velocities are obtained from combining weekly solutions in a single multi-epoch solution. Accuracy of better than 1 mm/yr of the rate of the absolute vertical displacement is expected after accumulation of several years of data (*ibid.*).

### ***Canadian Base Network (CBN)***

The Canadian Base Network (CBN) provides velocity estimates by combining more than 10 years of permanent and episodic GPS measurements and 36 individual solutions for the time period of 1994 to 2004 (Henton *et al.*, 2006; personal communication Henton, 2006). The CBN is connected to ITRF2000.0 by aligning all regional solutions to the IGS stations. The vertical GPS velocities are obtained from a cumulative solution of the weighted regional solutions with single station constraints. The preliminary velocities have a spatial pattern and magnitude consistent with GIA model predictions for North America. The formal standard deviations of the CBN vertical velocities are between 0.1 and 5 mm/yr.

#### 2.4.4 Combination of tide gauge records and satellite altimetry data

Long-term tide gauge records of sea level (more than 60 years continuous recording is required; see Douglas, 2001) provide estimates of the vertical crustal displacement (with respect to the sea level) in the de-glaciated areas of Fennoscandia and North America. Using water levels of 55 tide gauges, Mainville and Craymer (2005) have determined the postglacial rebound tilting of the crust in the Great Lakes region. Being attached to the deformable crust, tide gauges measure the sea/water level relative to the crust. As shown by Kuo (2006), the change in sea level is characterized by significant geographical variations caused by the steric (salinity and heat) component, the water mass redistribution of the present-day glaciers and polar ice sheets melting as a result of the self-gravitation of the ocean, and the change in the geoid due to GIA. In the following, the rate of change of sea level from both steric and mass redistribution signals is denoted by  $\dot{\zeta}_P$ , while the rate of change of geoid is  $\dot{N}_P$ .

The negative of the change in the relative sea level is a measure for the so-called apparent vertical crustal displacement (Ekman, 1989). The rate of the apparent displacement at point P,  $\dot{H}_P^a$ , corrected for the rate of change of sea level gives the rate of the levelled displacement  $\dot{H}_P$  with respect to the geoid, i.e.,

$$\dot{H}_P = \dot{H}_P^a + \dot{\zeta}_P. \quad (2.27)$$

The rate of the absolute vertical displacement  $\dot{h}_P$  is obtained after the rate of change of the geoid is added in Eq.(2.27) as follows:

$$\dot{h}_P = \dot{H}_P^a + \dot{\zeta}_P + \dot{N}_P. \quad (2.28)$$

In order to estimate the absolute vertical displacement, the height of the sea level at (at least) one tide gauge must be accurately determined in a geocentric reference frame by GPS measurements. Then, using precise re-levelling data and the rate of change of the geoid, the absolute vertical displacement can be obtained at all tide gauges. An alternative approach involves extrapolation of the absolute sea surface level measured by satellite altimetry to

the tide gauge locations. Under the assumption that the altimeter and tide gauge measure the same sea level signal, the absolute vertical crustal displacement is obtained by differencing the rate of change of the absolute sea level,  $\dot{s}_p$ , and the rate of change of the relative sea level,  $(-\dot{H}_p^a)$ , at the tide gauge location as follows (see Figure 2.5):

$$\dot{h}_p = \dot{s}_p - (-\dot{H}_p^a) = \dot{\zeta}_p + \dot{N}_p + \dot{H}_p^a. \quad (2.29)$$

For implementations of this approach, the reader can refer to Cazenave *et al.*, (1999), Clark *et al.*, (2000), Lin (2000), Nerem and Mitchum (2002), Shum *et al.*, (2002), Kuo *et al.*, (2004), and Jekeli and Dumrongchai (2003). Kuo (2006) has developed algorithms based on a Gauss-Markov model with stochastic constraints for estimating rates of postglacial uplift/subsidence in the Baltic Sea and Great Lakes regions as well as a post-seismic non-linear vertical deformation in the tectonically active regions such as the Alaska region.

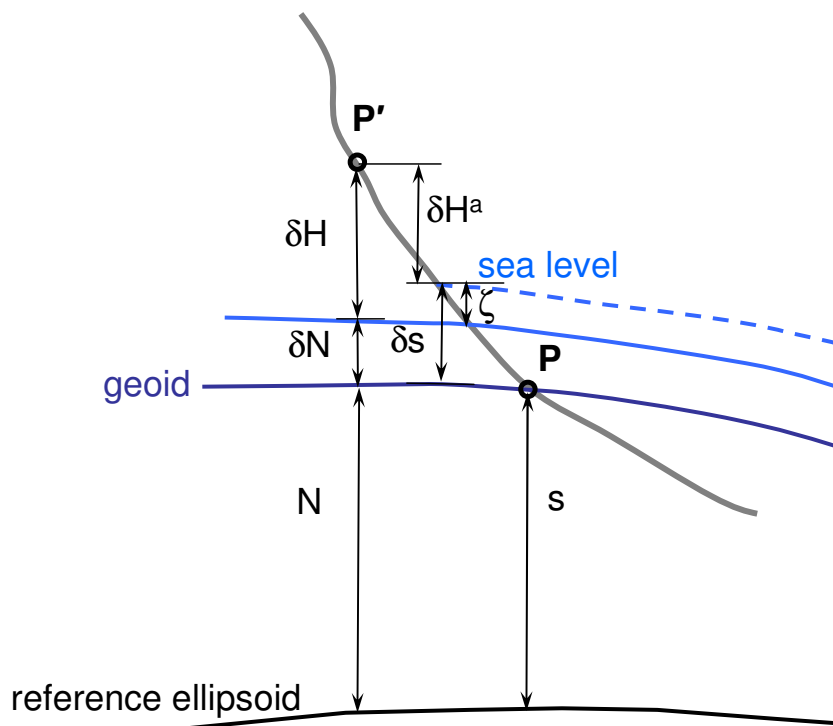


**Figure 2.5:** Relationship between the apparent and levelled crustal displacement and the changes in the geoid and sea level.

The uncertainties of the estimated vertical displacement rates depend mainly on the accuracy with which tide gauges and satellite altimetry measure the sea level, the errors with which the sea level is extrapolated, and the presence of sea level currents along the coast and river discharge that can affect the tide gauge records. Factors responsible for systematic effects in tide gauge sea level records are the instrumental drift, atmospheric pressure variations, temporal variations of sea currents, long-period components of wind stress, thermohaline changes, river discharge fluctuations, bathymetry configuration, glacio-eustasy (generally defined by the loss and gain of water related to glaciers), and shelf subsidence due to oceanic lithosphere cooling and sediment/water loading. The accuracy of the altimetric measurements depends on orbital errors, altimeter drift and lag, sea state bias, troposphere refraction, ionosphere effects, and atmosphere pressure loading.

#### **2.4.5 Precise re-levelling**

Repeated precise levelling provides relative vertical displacement rates and tilts from re-levelled primary control networks in the territories experiencing crustal uplift or subsidence. Examples exist in a series of maps of the contemporary postglacial uplift in Fennoscandia, including Ekman (1996), Kakkuri (1997), Mäkinen and Saaranen (1998), Danielsen (2001), and Vestøl (2006), among others. In contrast to Fennoscandia, where re-levelled lines cover the whole uplifting territory, in North America, the territories with the largest uplift in the Hudson Bay region are not covered by a vertical control network. In the populated areas south of the Hudson Bay region, scattered in space and time re-levelling segments exist. Traditionally, vertical displacement rates are approximated by low degree bi-variate polynomials fitted to the re-levelled height differences and differences in the relative sea level at a set of tide gauges (Vaníček and Christodulidis, 1974; Vaníček and Nagy, 1981; Carrera *et al.*, 1991). This approach has been adopted because of the poor quality of the levelling data for geodynamics studies in Canada as shown by Devaraju (2006). The accuracy of the vertical displacement rates modelled in these studies remains unknown. Based on the quality of the re-levelling data, it could be accepted that the errors are larger than the errors of the vertical displacement rates computed from the Fennoscandian primary levelling networks. According to Mäkinen and Saaranen (1998),

the accuracy of the relative vertical displacement rates is 0.15 mm/yr over distances of 50 km (the distance of 1mm/yr tilt).

#### **2.4.6 Collocation of geodetic techniques**

Refinements of GIA models rely considerably on the geodetic constraints in North America since the Laurentide signal is the largest in magnitude and spatial scale. Sites that are spatially well distributed across Canada and the northern parts of the US are required to accurately sample the complex (due to the multi-dome structure of the North American ice sheet) GIA signal. In principle, collocated permanent GPS stations and absolute gravity sites can provide the required information in terms of rates of the absolute vertical displacement and rates of change of the terrestrial gravity. In addition, these sites can provide “ground-truth” for validation of the GRACE-observed geoid rates.

The first step towards providing consistent in space and time information for constraining GIA models and validating GRACE-observed mass changes is undertaken in Fennoscandia. Across Norway, Sweden, Denmark, and Finland, thirty absolute gravity sites observed periodically by FG5 instruments are collocated with permanent GPS stations (Timmen *et al.*, 2005). Currently, in North America, no information of this kind is available on a regional scale. Figure 2.6 shows the CGSN primary control sites, the CBN stations, and the primary control network in Canada. The figure depicts the irregularly distributed data mostly concentrated in the populated areas to the south of the Hudson Bay region. The CGSN sites are sparse, but as it will be demonstrated in Chapter 3, they are able to sample the characteristic wavelengths of the postglacial rebound signal. The GPS sites are clustered in the southern Canada with few exceptions to the north of the degree 60 parallel. The CGSN sites and the CBN stations are not collocated. In addition to the different topology, the measurements of the two networks have different time spans. Despite these deficiencies, the methodology proposed in Chapter 4 is tested based on the available rates of the terrestrial gravity and GPS velocities as the only alternative for Canada at present.

The requirements for integrated in space and time gravity and vertical crustal displacement information has led to proposals for modernizing the CGSN. Absolute gravity

measurements will be collocated with CBN stations, thus providing not only data constraints for GIA modelling but also a basis for a new “gravity-based height system” (Henton *et al.*, 2005). Preliminary results exist for northern Quebec, where absolute gravity sites collocated with a set of permanent CBN stations are established for the purpose of local studies of postglacial rebound (Henton *et al.*, 2004). For the sake of completeness, the collocated networks for local geodynamic and tectonic studies in Canada are described, as well. In the northern Cascadia subduction zone, the “episodic tremor and slip” superimposed on the trends related to the convergence of North American and Juan de Fuca plates are studied by means of repeat gravity and permanent GPS measurements (Lambert *et al.*, 2006). In southeastern Alaska, collocated absolute gravity and continuous GPS measurements (Miura *et al.*, 2006) provide geodetic data for a refinement of the viscoelastic models of the “world’s fastest” isostatic uplifting of approximately 30 mm/yr as a response to the glacial retreat after the Little Ice Age (Larsen *et al.*, 2004).

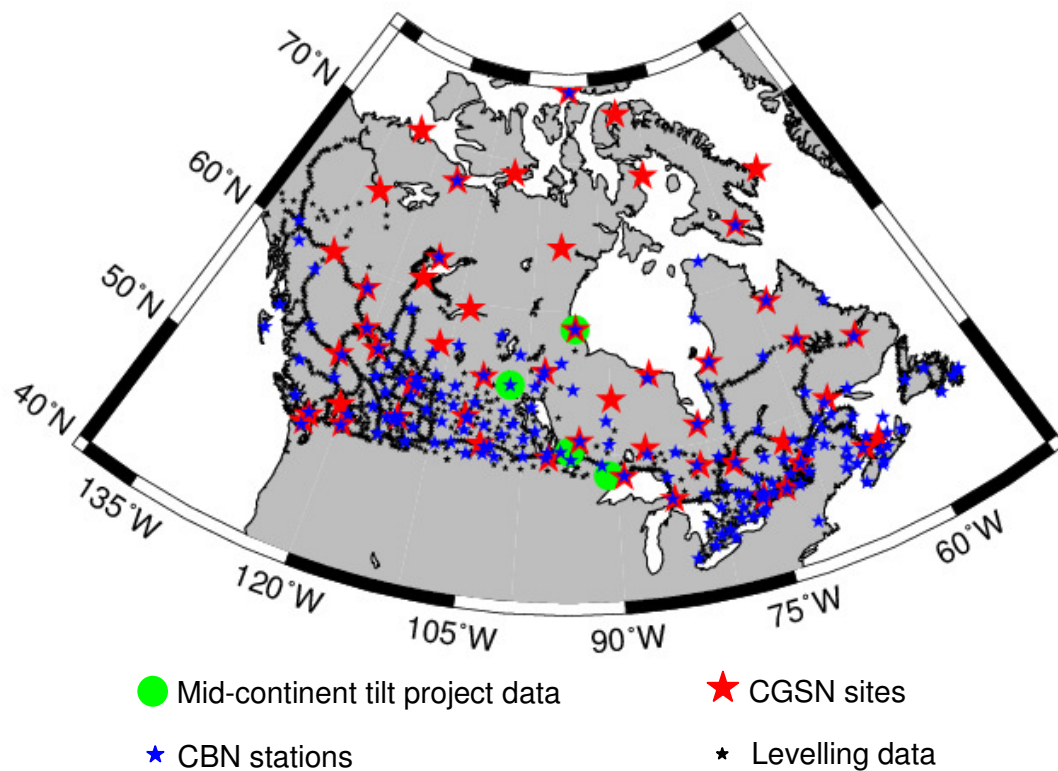


**Figure 2.6:** CGSN gravity rates, CBN vertical velocities, levelling data, and Mid-continent tilt project data.

Figure 2.7 summarizes the contemporary geodetic techniques that can serve the time-variable vertical datum through measuring the changes in ellipsoidal, orthometric, and geoid heights. Permanent and episodic GPS measurements, SLR and VLBI (Argus *et al.*, 1999), a combination of tide gauges and satellite altimetry (TGA) sea level measurements, as well as InSAR/DInSAR (e.g., Bürgmann *et al.*, 2006) data provide rates of absolute vertical crustal displacements. Precise re-levelling data and tide gauge records provide levelled uplift/subsidence relative to the geoid. Changes in the latter are obtained from an analysis of GRACE time series of the geopotential. Both absolute and levelled crustal displacements in combination with gravity rates from absolute and relative gravimetry provide rates of change of the geoid. The link between the mass change component, i.e., the change in the geoid height, and the geometrical component is provided by the gravity-to-height ratio defined in the next section.

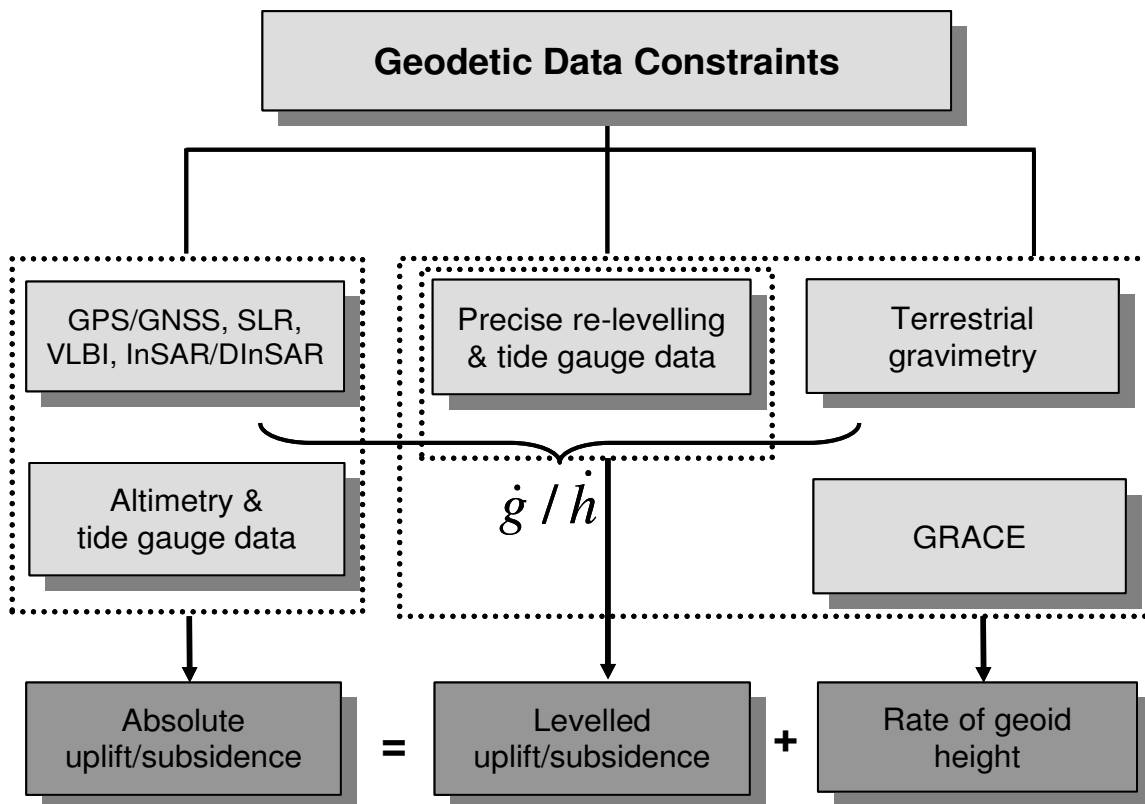


**Figure 2.7:** A general framework for combining geodetic data constraints.

### 2.4.7 Gravity-to-height ratio

Estimates of gravity-to-height ratio,  $\dot{g}/\dot{h}$ , have been used to infer the upper mantle mass inflow accompanying the postglacial rebound process (see, e.g., Ekman and Mäkinen, 1996). Two simple models were used to set limits for the gravity-to-height ratio obtained from gravity and height measurements. The “free-air” ratio

$$\frac{\dot{g}}{\dot{h}} = \frac{dg/dt}{dh/dt} = \frac{dg}{dh} \approx \frac{d}{dR} \left( \frac{GM}{R^2} \right) = \frac{-2g_a}{R} = -0.31 \mu\text{Gal/mm} \quad (2.30)$$

accounts for a vertical motion without mass redistribution, while the “Bouguer” ratio

$$\frac{\dot{g}}{\dot{h}} = \frac{-2g_a}{R} + 2\pi G\rho_m = -0.17 \mu\text{Gal/mm} \quad (2.31)$$

accounts for a viscous inflow of masses from the upper mantle into the rebounding crust (Honkasalo and Kukkamäki, 1964). In Eqs.(2.30) and (2.31),  $g_a$  is the average gravity value of 981 Gal,  $R$  is the mean radius of the Earth, and  $\rho_m$  is the density of the upper mantle assumed to be  $3.30 \text{ g}\cdot\text{cm}^{-3}$ . It is believed that the gravity-to-height ratio that characterizes postglacial rebound is close to the Bouguer ratio. Some physical processes have a gravity-to-height ratio quite different from the free-air and Bouguer values. For example, the elastic compression or extension induces values of approximately  $0\div 3.0 \mu\text{Gal/mm}$  (Tanner and Lambert, 1987). The magma injection can be characterized by values of  $-3.0\div 0.5 \mu\text{Gal/mm}$  (*ibid.*). Exploitation of natural resources (oil, gas and geothermal fields) can lead to decrease in gravity due to fluid extraction, but rapid subsidence is also observed (see e.g., Allis and Hunt, 1986; Fielding *et al.*, 1998). Table 2.1 summarizes some empirically-derived and theoretically-predicted  $\dot{g}/\dot{h}$  values for postglacial rebound.

Since the CGSN sites and the CBN stations are not collocated, the gravity-to-height ratio cannot be estimated rigorously. Nevertheless, the  $\dot{g}/\dot{h}$  value can be computed by means of a simple procedure. Thirteen GPS stations and gravity sites (five repeated absolute gravity

sites) located within a radius of 100 km are assumed to be “collocated” (Figure 2.8). By means of weighted least-squares adjustment of the gravity-to-height ratios computed at these sites, a value of  $-0.18 \pm 0.02 \mu\text{Gal}/\text{mm}$  is estimated (Figure 2.9). This value matches the result of Lambert *et al.* (2006) estimated from the Mid-continent tilt project data and is close to the theoretical values in Table 2.1.

**Table 2.1:** Estimates and predictions of gravity-to-height ratio

Source	Region/Earth model	$\frac{\dot{g}}{h}$ , $\mu\text{Gal}/\text{mm}$
Ekman and Mäkinen (1996)	Fennoscandia (relative gravity and levelling)	$-0.20 \pm 0.06$
Lambert <i>et al.</i> (2006)	Laurentide (absolute gravity and GPS)	$-0.18 \pm 0.03$
Wahr <i>et al.</i> (1995)	empirical for a large range of viscosity profiles and lithosphere thicknesses	$-0.154$
James and Ivins (1998)	elastic response	$\approx -0.27$
	viscoelastic response	$\approx -0.16$
Fang and Hager (2001)	$-2g_a / R + 2\pi G \langle \tilde{\rho} \rangle^1$ (an incompressible Earth)	$-0.16$

$^1 \langle \tilde{\rho} \rangle \approx 3.50 \text{ g} \cdot \text{cm}^{-3}$  is the average of the pseudo surface density for PREM.

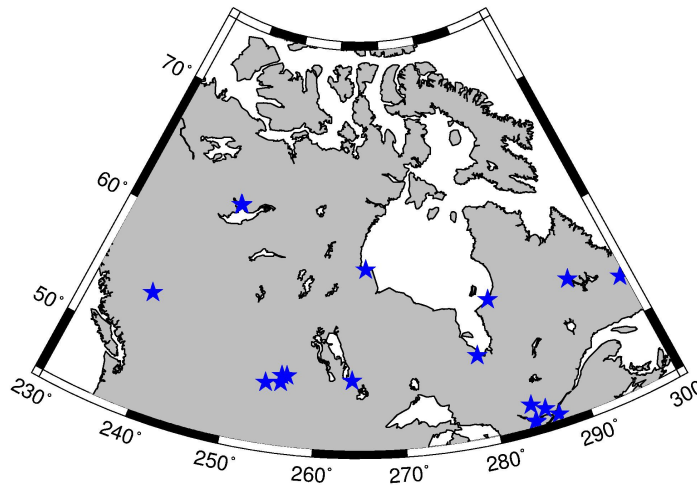


**Figure 2.8:** “Collocated” CGSN gravity sites and CBN GPS stations for estimating the gravity-to-height ratio.

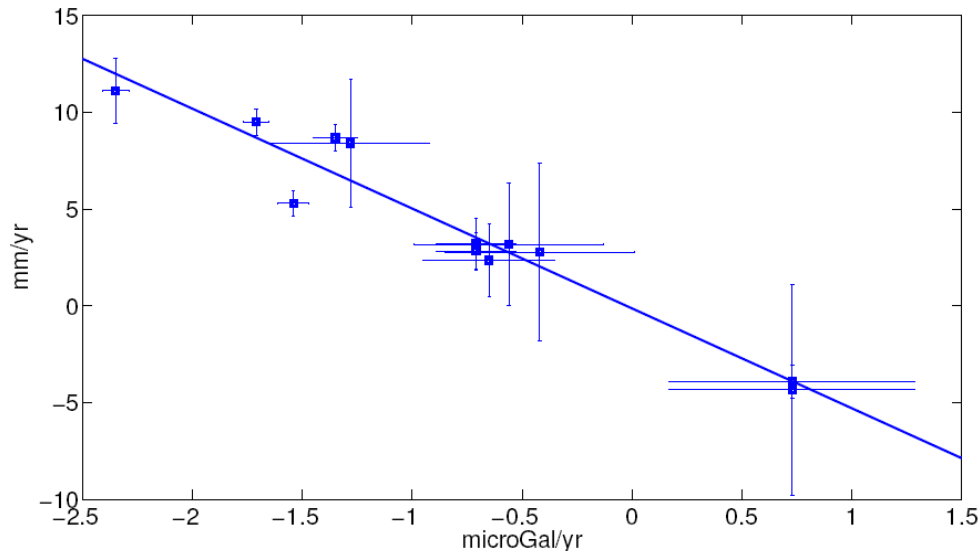


**Figure 2.9:** Gravity-to-height ratio estimated from the “collocated” CGSN absolute gravity rates and the CBN GPS vertical velocities.

Table 2.2 summarizes the formal errors of the rates of the geoid height, terrestrial gravity, and absolute vertical displacement. All rates are expressed in mm/yr. A gravity-to-height ratio of  $-0.18 \mu\text{Gal}/\text{mm}$  is used to convert the error of the terrestrial gravity rates to an error of the vertical displacement rates. As it can be observed, GRACE and absolute gravimetry can provide vertical displacement rates with an accuracy level of 1 mm/yr, which is identical to the accuracy of the rates obtained by means of GPS measurements and by combining tide gauge and satellite altimetry.

**Table 2.2:** Summary of the formal errors of the rates of change of gravity and heights

Technique	Formal error	Source
GRACE	1.4 mm/yr	Chapter 5 of this thesis
AG	$0.2 \mu\text{Gal}/\text{yr} \rightarrow 1.1 \text{ mm}/\text{yr}^*$	(Lambert <i>et al.</i> , 2006)
CBN	$0.1 \div 5 \text{ mm}/\text{yr}$	(Henton, personal communication)
CGSN	$0.06 \div 0.9 \mu\text{Gal}/\text{yr} \rightarrow 0.3 \div 5.0 \text{ mm}/\text{yr}^*$	(Pagiatakis and Salib, 2003)
TGA	$0.5 \div 1.6 \text{ mm}/\text{yr}$	(Kuo, 2006)

\* a gravity-to-height ratio of  $-0.18 \mu\text{Gal}/\text{mm}$  is assumed.

## 2.5 Geodetic approaches for modelling temporal variations of geoid and heights

Global gravity field models in the form of geopotential spherical harmonic (SH) coefficients are conventionally used for estimating GRACE-observed mass changes (e.g., Tapley *et al.*, 2004a). The main disadvantages of this approach include the limited spatial resolution due to the truncation of the spherical harmonics to a certain degree and the required smoothing of random errors. The temporal resolution is limited to one month required for providing global gravity field solutions from GRACE inter-satellite measurements. To improve the spatial and temporal resolution of mass change estimates several approaches have been implemented: the use of GRACE satellite-to-satellite tracking data (Han *et al.*, 2005a), the mascons technique (Rowlands *et al.*, 2005; Luthcke *et al.*, 2006), and the wavelet representation of the geopotential (Schmidt *et al.*, 2007; Fengler *et al.*, 2007). These techniques have been applied for estimating semi-annual and annual continental water mass redistributions. The rates of change of the geoid height in this thesis are obtained using the conventional spherical harmonic representation of the geopotential.

### 2.5.1 Analysis of GRACE time series

The rate of change of any gravity functional  $LT(\theta, \lambda, t)$  can be computed by means of the time derivatives of the geopotential coefficients  $\dot{\bar{C}}_{lm}(t)$  and  $\dot{\bar{S}}_{lm}(t)$  as follows:

$$L\dot{T}(\theta, \lambda, t) = \sum_{l=2}^{\infty} \sum_{m=0}^l \beta_l \bar{P}_{lm}(\cos \theta) \left[ \dot{\bar{C}}_{lm}(t) \cos(m\lambda) + \dot{\bar{S}}_{lm}(t) \sin(m\lambda) \right], \quad (2.32)$$

where  $\beta_l$  are the specific transfer coefficients for the gravity functional. The transfer coefficients for the rates of the geoid height and gravity are  $\beta_l^N = R$  and  $\beta_l^g = \frac{GM}{R^2}(l-1)$ , respectively, provided that the geopotential is assumed to be downward continued to the geoid. A complete list of transfer coefficients can be found in Sneeuw (2000).

The time derivatives (rates) are estimated by least-squares fitting to the time series of the coefficients as follows. Let a SH coefficient  $K_{lm} = \{\bar{C}_{lm}, \bar{S}_{lm}\}$  at epoch  $t_j$  is represented as

$$K_{lm}(t_j) = k_1 t_j + k_2 \cos(\omega t_j) + k_3 \sin(\omega t_j) + k_4 \cos(\omega t_j / 2) + k_5 \sin(\omega t_j / 2) + v(t_j), \quad (2.33)$$

where the mean has been subtracted.  $k_1$  is the trend,  $k_2$  and  $k_3$  are the annual cosine and sine amplitudes, respectively, and  $k_4$  and  $k_5$  are the amplitudes of the semi-annual components;  $v(t_j)$  is the random error, and  $\omega = 2\pi/T$ ,  $T = 1$  year is the frequency of one cycle per year. The unknown parameters  $k_j$ ,  $j = 1, \dots, 5$  are determined by solving the over-determined system of Eq. (2.33).

According to Wahr *et al.* (2000), rates of the absolute vertical crustal displacement due to postglacial rebound can be computed by

$$\dot{h}(\varphi, \lambda, t) = R \sum_{l=2}^{\infty} \frac{2l+1}{2} \sum_{m=0}^l \bar{P}_{lm}(\sin \varphi) \left[ \dot{\bar{C}}_{lm}(t) \cos(m\lambda) + \dot{\bar{S}}_{lm}(t) \sin(m\lambda) \right]. \quad (2.34)$$

Eq. (2.34) uses an approximate relation between the geopotential and absolute vertical displacement given by Wahr *et al.* (1995). This relation is based on the fact that the postglacial rebound geoid change is mainly a result of the mass anomalies associated with the deformation of the lithosphere which results in vertical crustal displacements. Because of this approximate relation, the factor  $R(2l+1)/2$  is not a transfer coefficient.

### 2.5.2 Time-variable boundary value problem. Geodetic integrals

In the presence of interior mass redistributions and crustal deformation, the topographic surface of the Earth, geopotential, and data are time-variable. To account for these temporal effects, a boundary value problem has been formulated as a *geodynamic* BVP (Sansò and Dermanis, 1982), a *Molodensky-like* BVP (Heck, 1982), a *time-dependent* geodetic BVP (Heck and Mälzer, 1983, 1986; Biró *et al.*, 1986), and *gradiometric-geodynamic* BVP (Tóth, 2004). The boundary surface is the deformable solid Earth surface and the boundary data comprise the time-variable gravity and heights. Formulated in this way, the boundary value problem is free from assumptions related to the driving mechanisms of the internal mass redistributions.

In spherical approximation, the time-dependent geodetic BVP is defined as (Biró *et al.*, 1986):

$$\begin{cases} \Delta(\delta W - \delta W_o) = 0 \\ -\frac{\partial(\delta W - \delta W_o)}{\partial r} - \frac{2}{R}(\delta W - \delta W_o) = \delta g - \frac{2}{R}\delta W' \end{cases}, \quad (2.35)$$

where  $\delta W$  is the temporal change in the geopotential,  $\delta W_o = (W_p')_o - (W_p)_o$  is the change in geopotential at the displaced vertical datum point, and  $\delta g$  and  $\delta W'$  are the temporal changes in the terrestrial gravity and geopotential at the deformed Earth's surface as defined in Section 2.3 and Figure 2.4.

If the total mass of the Earth is not time dependent, the solution of Eq.(2.35) is given by (Heck, 1982) as follows:

$$\delta h = -\frac{\delta W'}{g_a} - \frac{\delta W_o}{g_a} + \frac{\delta W_1}{g_a} + \frac{R}{4\pi g_a \sigma} \iint (\delta g - \frac{2\delta W'}{R}) S(\psi) d\sigma, \quad (2.36)$$

where  $\delta H = -\delta W' / g_a$  is the change in the orthometric height,  $\delta H_o = -\delta W_o / g_a$  is the change in the orthometric height of the fundamental datum point, and  $\delta W_1 / g_a$  is the change in the position of the geocenter in a global orthogonal Cartesian coordinates system with origin at the centre of gravity at the initial epoch. The integral term is the change in the geoid height computed with two types of boundary data, i.e.,  $\delta g$  and  $\delta W'$ . If the geocenter motion is assumed zero, Eq.(2.36) can be written as

$$\delta h = \delta H + \delta H_o + \delta N, \quad (2.37)$$

where

$$\delta N = \frac{R}{4\pi g_a \sigma} \iint (\delta g - \frac{2\delta W'}{R}) S(\psi) d\sigma \quad (2.38)$$

The same relationship can be written for the rates of change as follows:

$$\dot{h} = \dot{H} + \dot{H}_o + \dot{N}. \quad (2.39)$$

$\dot{H}_o$  is the rate of the vertical displacement (with respect to the geoid) of the fundamental benchmark of the vertical control network if a single global vertical datum is assumed.

The linear relationship between the rates of change of the terrestrial gravity  $\dot{g}$  and orthometric height  $\dot{H}$  can be used to evaluate the Stokes integral with only one type of boundary data. Using the Stokes integral,  $\dot{g}$ , and  $\dot{g}/\dot{H}$ , the rate of the geoid height can be computed as follows:

$$\dot{N} = \frac{R}{4\pi g_a} \iint_{\sigma} \dot{g} \left[ 1 + \frac{2g_a}{R} \left( \frac{\dot{g}}{\dot{H}} \right)^{-1} \right] S(\psi) d\sigma, \quad (2.40)$$

where  $\dot{g}/\dot{H} \approx \dot{g}/\dot{h}$  can be used. Because  $\dot{g}/\dot{H} = \dot{g}/(\dot{h} - \dot{N}) \approx \dot{g}/(\dot{h} - 0.1\dot{h}) = 1.11\dot{g}/\dot{h}$ , the error introduced in Eq. (2.40), being 10% of the gravity-to-height ratio, is at the level of the error with which the later is obtained (Ekman and Mäkinen, 1996).

The BVP approach benefits from a regular data distribution; however, in the case of local surface measurements with irregular data spacing and coverage, data-driven approaches like least-squares collocation are preferred.

### 2.5.3 Least-squares collocation approach

Generally, different modelling approaches can be used to describe a surface of vertical displacement using irregularly distributed (scattered) data in space and time. These approaches include functional modelling, stochastic signal modelling, hybrid modelling, and dynamic Kalman filtering with variance component estimation (Dermanis, 1985; Liu and Chen, 1998).

In the functional approach, a trend surface is parameterized by simple analytical functions, such as bi-variate polynomials (e.g., Carrera *et al.*, 1991), Chebishev polynomials (e.g., Ishii *et al.*, 1981), and radial base functions (Holdahl and Hardy, 1979). Usually, it is assumed that the functional model describes an area with an identical deformation pattern. In an active tectonic area with faulting or in large areas with different vertical deformation characteristics, a set of blocks can be used with a different functional model assigned to

each block. Such an approach may require imposing continuity conditions along the borders of the blocks (e.g., Koohzare *et al.*, 2006). The advantage of the functional approach is the ease of its implementation. The disadvantage consists in the fact that the modelled vertical displacement surface depends largely on the displacement of a single point as well as on data point density and locations. To a large extent, this applies to bi-variate polynomial surfaces. In Chapter 3, it will be shown that radial base functions exhibit a superior behaviour in comparison with bi-variate polynomials.

In the stochastic signal approach, the rate of the vertical crustal displacement is a zero mean signal defined by a covariance matrix computed from the local empirical signal covariance function. The deformation field is assumed homogeneous and isotropic. The deformation rates at the new point locations are obtained by a simple least-squares prediction (Moritz, 1980). Despite the simplicity of the description of the vertical displacement rates, this approach has a limited implementation in the crustal deformation modelling. The ground for this is the assumption for an isotropic and homogeneous displacement field, which, in reality, may not be fulfilled. In addition, usually the stochastic information is estimated from a small number of data points and is transferred to other areas with similar tectonic characteristics. Nevertheless, the stochastic approach has been successfully implemented in earthquake studies for modelling migrating vertical displacements near convergent plate boundaries (Fujii and Xia, 1993), detecting temporal changes in vertical displacement rates (El-Fiky *et al.*, 1997), and creating common continuous models for temporal changes in gravity and vertical crustal displacements (Kanngieser, 1983).

Often, the stochastic signal modelling is combined with functional modelling in a hybrid approach which is identical with the least-squares collocation with parameters approach (Moritz, 1980). The functional model is assumed to describe a smooth regional displacement field, while the signal component may describe, for example, local vertical displacements or correlated errors in levelling or GPS measurements; see Danielsen (2001) and Vestøl (2006) for modelling the Fennoscandian uplift. Another example is found in the study of Hein and Kistermann (1981) who treat local groundwater table variations as a stochastic signal superimposed on the regional tectonic vertical displacements. One important advantage of the use of stochastic information in the description of the vertical

velocity field is in the introduced regularization. It is well known that the functional approach may lead to numerical instabilities that manifest themselves as oscillations of the smooth displacement surfaces. This effect can be minimized by using stochastic information in terms of signal and noise covariance matrices. Recently, Egli *et al.* (2007) have developed an adaptive least-squares collocation procedure, which accounts for inhomogeneity and anisotropy of the vertical crustal displacements. The proposed approach is stable in abrupt spatial variations in the displacement field, in which case the conventional least-squares collocation usually fails.

The approach applied in this research to model the rate of change of the geoid height, the rate of the vertical crustal displacements and the terrestrial gravity is least-squares collocation with parameters. In addition to the local solutions, this approach provides a means for error propagation and stepwise computations. The most important characteristic, however, from which this research benefits, is the heterogeneous data input and output. In Chapter 4, a procedure for estimation of rates of change of the geoid height using terrestrial gravity rates and GPS vertical velocities is developed and tested.

## **2.6 Summary**

This chapter has discussed the vertical datum problem in the context of the time-dependent gravity field and vertical crustal displacements. A relation among the temporal change in ellipsoidal, orthometric, and geoid heights has been established. This relationship is the basis for the procedures developed and tested in this research. Since the postglacial rebound induces the dominant temporal change in the geoid and heights at a regional scale, it is assumed that it can be modelled as a smooth spatial trend by means of radial base functions. For the purpose of modelling of the postglacial rebound signal, the geodetic constraints in North America have been reviewed at length and compared in terms of the accuracy of the estimated rates.

## **Chapter Three: Approximation of vertical displacement data using radial base functions**

In postglacial rebound studies, rates of vertical crustal displacement can be represented by a smooth surface estimated from repeated precise absolute and/or relative height measurements. For this purpose, least-squares approximators are constructed by means of selected base functions. For example, recently, Vestøl (2006) has used a fifth degree bi-variate polynomial to model the postglacial rebound uplift in Fennoscandia from GPS and tide gauge point vertical velocities and re-levelling data. In contrast with the Fennoscandian signal, the viscoelastic response of the Earth to the multidome North American ice sheet complex is characterized by a vertical displacement surface that cannot be modelled using low-degree bi-variate polynomials.

Another factor that precludes the use of the polynomials in the approximation of the vertical velocities in North America is the fact that the base functions have uniform approximation properties over the domain of data. This can lead to numerical instabilities and oscillating surfaces for irregularly distributed data and large data-free areas if the degree of the polynomial is increased in order to accurately approximate the complex surface. This problem may arise, for example, when the vertical displacement surface is sampled by re-levelling data confined to the levelling lines of the vertical control network in Canada. In addition, as shown in Chapter 2, GPS stations and gravity sites are very irregularly distributed across Canada. Therefore, a need exists to define an approximator that adapts to the varying data density.

Accurate approximators for scattered data can be constructed by means of radial base functions (RBF), which can be located at the data points. Thus, automatically, changes in the density of the data locations are taken into account. Since the RBFs have global support

(Franke, 1982), and the coefficient matrices are fully populated, the use of the RBF approximator is limited to data sets of a small or moderate size. Here global implies that the approximator depends on all data points, and changes in the number, locations, and data point values affect all base functions.

The main problems that need to be resolved when constructing RBF approximators are

1. scaling of the base functions for a given data set,
2. determining the optimal locations of the base functions, and
3. varying the scale with the base function locations.

In this research, the problems are resolved in the context of interpolation and approximation of vertical crustal displacement surfaces. Although the interpolation case is rarely encountered in practice, its implementation in this thesis demonstrates the excellent fitting properties of radial base functions, particularly, in describing the line of zero vertical displacement. A recent example of the application of RBF models in gravity field approximation can be found in the work of Mautz *et al.* (2003).

This chapter starts with a definition and properties of the radial base functions and proceeds with the definitions of the RBF interpolator and approximator. The scaling of the base functions is resolved first in the interpolation case. Next, algorithms for determining the optimal locations of the base functions in the approximation case are developed, and an empirically-based rule for scaling the radial base functions is outlined. Moreover, a relationship between the absolute vertical crustal displacement and the change in the geoid height is established by means of inverse multiquadric base functions.

### 3.1 Definition and properties of radial base functions

In two-dimensional interpolation and approximation problems, the radial base function (kernel),  $\Phi(\rho_j)$ , is defined as a function of the Euclidean distance

$$\rho_j = \sqrt{(y^1 - y_j^1)^2 + (y^2 - y_j^2)^2} \quad (3.1)$$

between the knot  $(y_j^1, y_j^2)$ , also called a node or center, and the current point  $(y^1, y^2)$ . The base function  $\Phi(\rho_j)$  is continuously differentiable, symmetric around the knot, and translation-invariant. Three types of radial base functions are implemented in this study: the thin-plate spline, multiquadric, and inverse multiquadric functions.

The thin-plate spline (TPS) is defined as follows (e.g., Wood, 2003):

$$\Phi(\rho_j) = \rho_j^{2n} \log(\rho_j), n \geq 1. \quad (3.2)$$

The multiquadric (MQ) base function (Hardy, 1971) is

$$\Phi(\rho_j) = \sqrt{\rho_j^2 + c^2}, \quad (3.3)$$

and the inverse (reciprocal) multiquadric (IMQ) (Hardy, 1990) is

$$\Phi(\rho_j) = 1/\sqrt{\rho_j^2 + c^2}. \quad (3.4)$$

The MQ and IMQ base functions are right and inverse hyperboloids, respectively. The parameter  $c$  is interpreted as the perpendicular distance from the  $Y^1Y^2$  plane to the hyperboloid's maximum/minimum; the parameter  $c$  determines the shape of the base function. As  $c \rightarrow 0$ , the hyperboloid turns into a cone, and as  $c$  increases, bowl- and sheet-like surfaces are generated. For the sake of convenience,  $c^2$  will be called the shape parameter.

Figure 3.1 shows two examples of an IMQ base function. The shape parameter  $c^2$  is given in unit distance. By varying  $c^2$ , the shape of the base functions is adapted for the particular interpolation/approximation problem.

The list of the commonly used RBF can be extended to include Gaussian and exponential functions, truncated parabolic functions, Sobolev splines, and cubic functions (see, e.g., Györfi *et al.*, 2002 and Chen *et al.*, 2003).

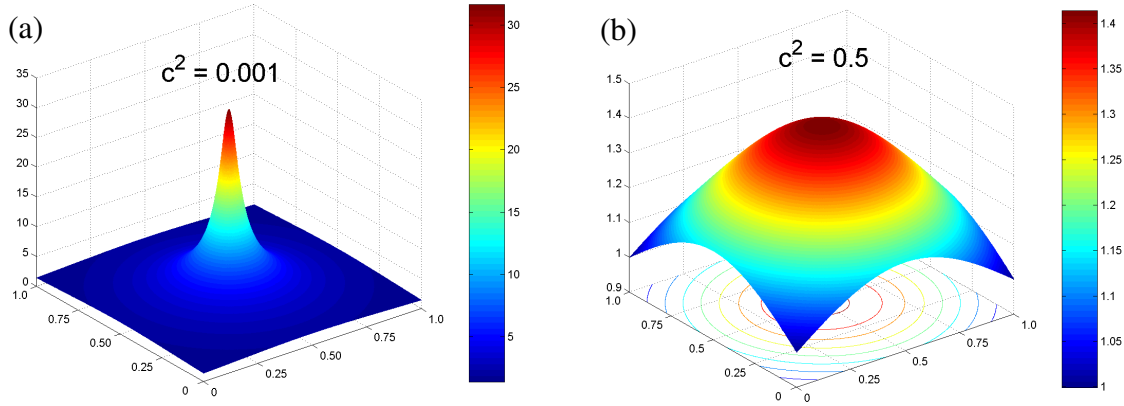


**Figure 3.1:** IMQ base functions: (a) a cone-like function and (b) a bowl-like function.

## 3.2 Radial base function interpolator. Scaling of base functions

### 3.2.1 Definition and properties

Let  $\Xi$  denotes a finite set of distinct points in  $\mathfrak{R}^2$ . Then the RBF interpolator is defined by a linear combination of translated base functions,  $\sum_j x_j \Phi(r_j)$ , where  $x_j \in \mathfrak{R}^{\Xi}$ ,  $j \in \Xi$  are the coefficients (weights) to be determined from the given finite data set  $i \in \Xi$  by solving a linear system of equations (whose number equals the number of the data points  $n$ ) as follows:

$$h(y_i^1, y_i^2) = \sum_{j=1}^n x_j \Phi(\rho_{ij}), \quad i, j \in \Xi. \quad (3.5)$$

$h(y_i^1, y_i^2)$  is the vertical displacement at the location  $(y_i^1, y_i^2)$ ,  $i = 1, \dots, n$ .

If the base function is strictly positive definite, the coefficient matrix  $[\Phi(\rho_{ij})]$  is invertible and the linear system has a unique solution that guarantees the existence of the interpolator (Lodha and Franke, 1997). Examples for positive definite functions are the Gaussian and IMQ functions. According to Micchelli (1986), MQ and TPS are conditionally positive

definite functions of degree  $M$ . The polynomial  $p(y^1, y^2) \in P^M(y^1, y^2)$  is appended in Eq. (3.5) in order to guarantee the invertibility of the coefficient matrix (Buhmann, 2000).

The linear system to be solved is

$$\begin{aligned} \sum_{j=1}^n x_j \Phi(\rho_{ij}) + \sum_{l=1}^m \alpha_l p_l(y_i^1, y_i^2) &= h(y_i^1, y_i^2), \quad i = 1, 2, \dots, n \\ \sum_{j=1}^n x_j p_l(y_j^1, y_j^2) &= 0, \quad l = 1, 2, \dots, m \end{aligned} \quad (3.6)$$

where  $m = M(M+1)/2$  is the number of the base functions  $p_l(y^1, y^2), l = 1, \dots, m$  in the polynomial space  $P^M(\Xi)$ . The extra degrees of freedom gained by adding the polynomial term are removed by the second set of equations which imposes orthogonality of the vector  $\mathbf{x} = [x_1 \ x_2 \ \dots \ x_n]^T$  and the polynomial space  $P_n^M(\Xi)$ , i.e.,  $\mathbf{x} \perp P_n^M(\Xi)$ .

The TPS base function is conditionally positive definite of degree  $M = 2$  and requires a linear term to be added. The MQ base function is conditionally positive definite of degree  $M = 1$  and a constant term is included in the system of equations. The IMQ interpolator can be constructed without appending a polynomial term (Micchelli, 1986). In principle, the minimum degree  $M$  that guarantees the existence of the interpolator should be used (Lodha and Franke, 1997).

The matrix form of Eqs. (3.6) is as follows:

$$\begin{bmatrix} \mathbf{A} & \mathbf{P}_\alpha \\ \mathbf{P}_\alpha^T & \mathbf{0} \end{bmatrix} \begin{bmatrix} \mathbf{x} \\ \boldsymbol{\alpha} \end{bmatrix} = \begin{bmatrix} \mathbf{h} \\ \mathbf{0} \end{bmatrix}, \quad (3.7)$$

where  $\mathbf{A} = [\Phi(\rho_{ij})]$ ,  $i, j = 1, \dots, n$  is the coefficient matrix;  $\mathbf{P}_\alpha$  is a  $(n \times m)$  matrix with elements  $p_l(y_i^1, y_i^2), l = 1, \dots, m$ , where  $m$  is the number of the polynomial base functions; and  $\mathbf{x}$  and  $\boldsymbol{\alpha}$  are  $(n \times 1)$  and  $(m \times 1)$  vectors of the RBF weights and polynomial coefficients, respectively.

According to Billings *et al.* (2002), Eqs. (3.7) can be solved by means of QR factorization of the matrix  $\mathbf{P}_\alpha$  as follows. If  $\mathbf{P}_\alpha = \mathbf{QR}$ , then the first  $m$  columns of  $\mathbf{Q}_\alpha$ , which span the

column space of  $\mathbf{P}_\alpha$ , form  $\mathbf{Q}_1$  so that  $\mathbf{P}_\alpha = \mathbf{Q}_1 \mathbf{R}$ . The  $(n-m)$  columns span the null space of  $\mathbf{P}_\alpha^T$  and form the matrix  $\mathbf{Q}_2$ . The polynomial constraints are satisfied if  $\mathbf{x} = \mathbf{Q}_2 \tilde{\mathbf{x}}$ ,  $\tilde{\mathbf{x}} \in \mathfrak{R}^{n-m}$ . Then, Eqs. (3.7) can be rewritten as follows:

$$\mathbf{C} \tilde{\mathbf{x}} = \tilde{\mathbf{h}}, \quad (3.8)$$

where  $\mathbf{C} = \mathbf{Q}_2^T \mathbf{A} \mathbf{Q}_2$  and  $\tilde{\mathbf{h}} = \mathbf{Q}_2^T \mathbf{h}$ .

Franke (1982) compares the performance of the TPS, MQ, and IMQ interpolators to other scattered data interpolation methods according to the following key criteria: *accuracy*, *stability*, *efficiency*, and *ease of implementation*. He rates TPS, MQ and IMQ among the best methods, which exhibit excellent fitting abilities and accuracy. Although the MQ base function is unbounded, i.e.,  $\Phi(\rho_j) \rightarrow \infty$ ,  $\rho_j \rightarrow \infty$ , the interpolator can outperform the bounded base functions such as IMQ ( $\Phi(\rho_j) \rightarrow 0$ ,  $\rho_j \rightarrow \infty$ ), which intuitively are accepted as more accurate. A physical explanation of this fact is given by Hardy and Nelson (1986) in terms of the *multiquadric-biharmonic* representation of the disturbing potential. They show that the potential function vanishes in infinity provided that  $\sum_j x_j \rightarrow 0$ . This is achieved by appending a constant term in Eqs. (3.6).

Another important criterion for assessing the performance of the base functions is the *sensitivity to the parameter*. According to Franke (1982), sensitivity to the parameter involves two aspects: stability of the interpolator with respect to small changes in the parameter value and independence of the parameter with respect to the approximated function. The numerical experiments in Section 3.4 show that both MQ and IMQ methods satisfy the first requirement. It is shown that the shape parameter can be varied around its optimal value, and the base functions still provide an accurately interpolated velocity surface. The MQ and IMQ functions do not satisfy the second requirement. In fact, the base functions need to be scaled for each data set. Various empirical relations for  $c^2$  are investigated in the following sections. An empirically-based rule for scaling of the IMQ function is given at the end of Section 3.4.

### 3.2.2 Optimal scale of base functions

There is no strict analytical theory developed for the choice of the shape parameter  $c^2$ . The optimal value is defined as the value that minimizes the interpolation error. In practice, values for the shape parameter can be chosen such that interpolated surfaces satisfy certain accuracy requirements. However, care must be taken since the coefficient matrix can easily become ill-conditioned for values of the shape parameter larger than the squared distances between the data point locations because the matrix elements become nearly equal. Different approaches for computing the shape parameter have been suggested, such as an average of distances between data points (Hardy, 1990), a linear function of the number of the knot, i.e.,  $c_j = b_0 + b_1 j, j = 1, \dots, n$  (Hon and Mao, 1997), and a function of the local radius of the curvature of the interpolated surface (Kansa and Hon, 2000). Recently, Sharifi (2006) has implemented genetic algorithms for resolving the scale of radial base functions in gravity field approximation problems.

In the following, two frequently used approaches in the interpolation of smooth surfaces are described. Carlson and Foley (1991) provide the following formula:

$$c^2 = 1/(1+120\sigma^2), \quad (3.9)$$

where  $\sigma^2$  is the variance of the fit of the data to a quadratic bi-variate polynomial. Scaling data to a unit cube is recommended before interpolation to make the results independent of the spatial distances and function values.

The flexibility with respect to the shape of the MQ function has been used by Kansa (1990) to improve the interpolation by decreasing the condition number of the coefficient matrix. The shape parameter is allowed to vary exponentially with the base function number  $j$  as follows:

$$c^2 = c_{\min}^2 (c_{\max}^2 / c_{\min}^2)^{[(j-1)/(n-1)]}, \quad (3.10)$$

where  $n$  is the number of the base functions. Thus, distinct matrix elements are obtained, which improves the condition number of the coefficient matrix. It is shown that the MQ interpolator provides very accurate interpolation for surfaces with moderate to steep

gradients, but it is not so accurate for flat surfaces. Multistage schemes for interpolation, e.g., the Foley-Carlson scheme (see, Carlson and Foley, 1991), in which MQ is the starting interpolator, are developed to successively decrease the error at every stage by using monotonic cubic splines.

### 3.3 Radial base function approximator. Selecting base functions locations

#### 3.3.1 Definition

The least-squares approximation problem is defined as follows:

$$\min \|\mathbf{h} - \mathbf{A}\mathbf{x} - \mathbf{P}_\alpha \boldsymbol{\alpha}\|^2 \quad \text{subject to: } \bar{\mathbf{P}}_\alpha^T \mathbf{x} = 0. \quad (3.11)$$

$\mathbf{A} = [\Phi(\rho_{ij})]$ ,  $i = 1, \dots, n$ ,  $j = 1, \dots, k$ , where  $n$  is the number of data points and  $k$  is the number of knots (base functions);  $\mathbf{P}_\alpha$  is a  $(n \times m)$  matrix with elements  $p_l(y_i^1, y_i^2)$ ,  $l = 1, \dots, m$ ;  $\bar{\mathbf{P}}_\alpha$  is a  $(k \times m)$  matrix with elements  $p_l(y_j^1, y_j^2)$ ; and  $\mathbf{x}$  and  $\boldsymbol{\alpha}$  are  $(k \times 1)$  and  $(m \times 1)$  vectors of the RBF weights and polynomial coefficients, respectively, determined from the solution of Eq. (3.11).

Analogously to the interpolation case, and using matrices  $\bar{\mathbf{Q}}_1$  and  $\bar{\mathbf{Q}}_2$  obtained by means of QR factorization of  $\bar{\mathbf{P}}_\alpha$ , the constrained least-squares problem is transformed to an unconstrained one as follows:

$$\min \|\tilde{\mathbf{h}} - \tilde{\mathbf{C}}\tilde{\mathbf{x}}\|^2, \quad (3.12)$$

where  $\tilde{\mathbf{C}} = \mathbf{Q}_2^T \mathbf{A} \bar{\mathbf{Q}}_2$  and  $\tilde{\mathbf{h}} = \mathbf{Q}_2 \mathbf{h}$ .

For small-size problems (as in this research),  $\tilde{\mathbf{x}}$  is estimated by solving the normal equations

$$\tilde{\mathbf{C}}^T \tilde{\mathbf{C}} \tilde{\mathbf{x}} = \tilde{\mathbf{C}}^T \tilde{\mathbf{h}}, \quad (3.13)$$

where  $\tilde{\mathbf{C}}^T\tilde{\mathbf{C}}$  is a positive definite matrix. The weights of the RBF are determined from the following equation:

$$\mathbf{x} = \bar{\mathbf{Q}}_2\tilde{\mathbf{x}}, \quad (3.14)$$

and the polynomial coefficients are found from the solution of

$$\mathbf{R}\boldsymbol{\alpha} = \mathbf{Q}_1^T(\mathbf{h} - \mathbf{A}\mathbf{x}). \quad (3.15)$$

Determination of the optimal locations of the base functions is a non-linear problem and can be solved rigorously by non-linear optimization. The scale of the base functions should be parameterized together with the unknown locations. The main problem consists in the fact that the initial guess for the shape of the base functions should guarantee convergence of the solution to the global minimum.

Franke *et al.* (1994) have experimented with an adaptive “greedy” algorithm for selection of the knot locations based on the residuals at the data points obtained at every stage of iterated least-squares approximation. They state that the suggested algorithm is “potentially useful for many problems where data subject to error is available and the surface must be approximated using an approximation that is computationally as efficient as possible.” Furthermore, they applied non-linear optimization schemes to determine the optimal locations of the knots and the shape parameter. It is found that variable knot locations can significantly reduce the RMS error and even greater improvement is achieved when the shape parameter is allowed to vary with different knots.

In this research, the base functions are located either on a grid or at a subset of data point locations. The first option is appropriate when the data cover the region of interest homogeneously. The second option is chosen in the case of irregularly distributed data. Thus, not only do the base functions adapt to the data density, but also the characteristics of the vertical displacement surface, i.e., the hinge line, surface gradient, and location of the peak signal, can be modelled accurately. Methods for selection of locations of base functions are designed and presented in the following section.

### 3.3.2 Algorithms for selecting optimal locations of base functions

#### *Backward and forward selection algorithms based on the cross-validation technique*

Generally, the knots in the approximation problem in Eq.(3.13) are correlated. This property can be used to select a subset of knots from the set of data point locations. One efficient statistical tool is the cross-validation (CV) technique (Breiman, 1993; Fotopoulos, 2003), which is based on the RMS error computed as follows:

$$\text{RMS} = \frac{1}{n} \sqrt{\sum_{i=1}^n (h_i - \hat{h}_{k(i)})^2}, \quad (3.16)$$

where  $\hat{h}_{k(i)}$  is the approximation of the data value  $h_i$  obtained by solving Eq.(3.12) with a subsets of base functions  $k$ . The cross-validation algorithm consists of removing one knot at a time from the set of candidate knots and approximating the surface with the knot subset. Next, residuals at the data points are computed, and, using Eq.(3.16), the significance of the removed knot is assessed. The knot that leads to the least RMS error among all of the candidate knots has the least significance and can be deleted. The procedure is repeated to determine the least significant knot from the new subset of knots. This describes the basic algorithm for backward elimination of knots. It starts with all data locations taken as candidate knots and is iterated until the RMS error becomes larger than a defined threshold value. The same procedure can be applied in a forward manner by adding the most significant knots, one at a time, to the subset of knots that initially contained zero knots. The described algorithms use a constant shape parameter, e.g., the optimal value taken from the interpolation case. The algorithms can be modified so that after a knot has been deleted/added, the optimal shape parameter for the particular knot subset is determined and this value is used in the next iteration.

#### *Orthogonal least-squares algorithm*

Despite the simple logic behind the algorithms based on the cross-validation technique, they are computationally intensive and, more importantly, the contribution of each base function/knot to the output is not known. The orthogonal least-squares approach offers a

simple tool for estimating the contribution and number of base functions to assure the desired approximation accuracy. Examples of using orthogonal least-squares in both forward and backward selection procedures can be found in the optimization of the RBF neural networks (see, e.g., Chen *et al.*, 1989 and 1991; Gomm and Yu, 2000). In the following, the forward selection algorithm is presented. The notations are kept consistent with the interpolation case.

Data are represented by the observation equation

$$\mathbf{h} = \mathbf{A}\mathbf{x} + \mathbf{e}, \quad (3.17)$$

where  $\mathbf{A} = [\mathbf{a}_1 \mathbf{a}_2 \cdots \mathbf{a}_k]$  is the coefficient matrix that contains a set of  $k$  base vectors (regressors),  $\mathbf{a}_i$ , of dimension  $(n \times 1)$ ;  $\mathbf{x} = [x_1 \ x_2 \ \cdots \ x_k]^T$  is a vector of unknown coefficients, and  $\mathbf{e}$  is the vector of errors.

Because  $\mathbf{A}\hat{\mathbf{x}}$  is a projection of the data vector  $\mathbf{h}$  onto the space spanned by the regressors  $\mathbf{a}_i$ ,  $[\mathbf{A}\hat{\mathbf{x}}]^2$  is the part of the output variance explained by them. The individual contributions of the regressors are estimated after applying orthogonal least-squares with the coefficient matrix decomposed as follows:

$$\mathbf{A} = \tilde{\mathbf{Q}}\tilde{\mathbf{R}} \quad (3.18)$$

where  $\tilde{\mathbf{R}}$  is a  $(k \times k)$  upper triangular matrix with ones on the main diagonal;  $\tilde{\mathbf{Q}}$  is an  $(n \times k)$  matrix with orthogonal columns  $\tilde{\mathbf{q}}_i, i=1, \dots, k$  such that  $\mathbf{H} = \tilde{\mathbf{Q}}^T \tilde{\mathbf{Q}}$  is a diagonal matrix.

By means of Eq. (3.18), Eq. (3.17) can be rewritten as follows:

$$\mathbf{h} = \tilde{\mathbf{Q}}\mathbf{x}' + \mathbf{e}, \quad (3.19)$$

where  $\mathbf{x}' = \tilde{\mathbf{R}}\mathbf{x}$  is a vector of the new coefficients. The orthogonal least-squares solution is found from

$$\hat{\mathbf{x}}' = \mathbf{H}^{-1} \tilde{\mathbf{Q}}^T \mathbf{h}. \quad (3.20)$$

and  $\hat{\mathbf{x}}$  is computed from the linear system

$$\tilde{\mathbf{R}}\hat{\mathbf{x}} = \hat{\mathbf{x}}' \quad (3.21)$$

by means of backward substitution.

The coefficient matrix  $\mathbf{A}$  can be decomposed by different methods, such as the Gram-Schmidt, modified Gram-Schmidt, or Householder transformation methods (Golub and van Loan, 1996). In this work, the Gram-Schmidt method is implemented.

Because of orthogonality of the base vectors  $\tilde{\mathbf{q}}_i$ , the output variance is expressed as

$$\frac{\mathbf{h}^T \mathbf{h}}{n} = \frac{\sum_{i=1}^k \hat{\mathbf{x}}_i'^2 \tilde{\mathbf{q}}_i^T \tilde{\mathbf{q}}_i}{n} + \frac{\mathbf{e}^T \mathbf{e}}{n}. \quad (3.22)$$

The contribution of the  $i^{\text{th}}$  regressor to the output variance is

$$\frac{\hat{\mathbf{x}}_i'^2 \tilde{\mathbf{q}}_i^T \tilde{\mathbf{q}}_i}{n}. \quad (3.23)$$

Reduction in the error from this regressor is given by

$$err_i = \frac{\hat{\mathbf{x}}_i'^2 \tilde{\mathbf{q}}_i^T \tilde{\mathbf{q}}_i}{(\mathbf{h}^T \mathbf{h})}, \quad 1 \leq i \leq k. \quad (3.24)$$

Based on Eq.(3.24), the Gram-Schmidt algorithm can be modified so that the regressor with the maximum reduction ratio (i.e., the maximum contribution to the output variance among all regressors) is selected at every step of the orthogonalization procedure (Chen *et al.*, 1991); see the flowchart in Figure 3.2. The algorithm can be terminated at the  $\tilde{k}$  step if

$$\left(1 - \sum_{i=1}^{\tilde{k}} err_i\right) < \varepsilon, \quad (3.25)$$

where  $0 < \varepsilon < 1$  is the predefined threshold value being the level of the unexplained output variance. The threshold is an important tool that can be used to control the balance between the accuracy of approximation and the number of selected knots. Also, the threshold can be used to effectively filter out frequencies from the spectrum of the output.

The methods based on the cross-validation technique and orthogonal least-squares are tested and compared in Section 3.4 using the IMQ base functions.

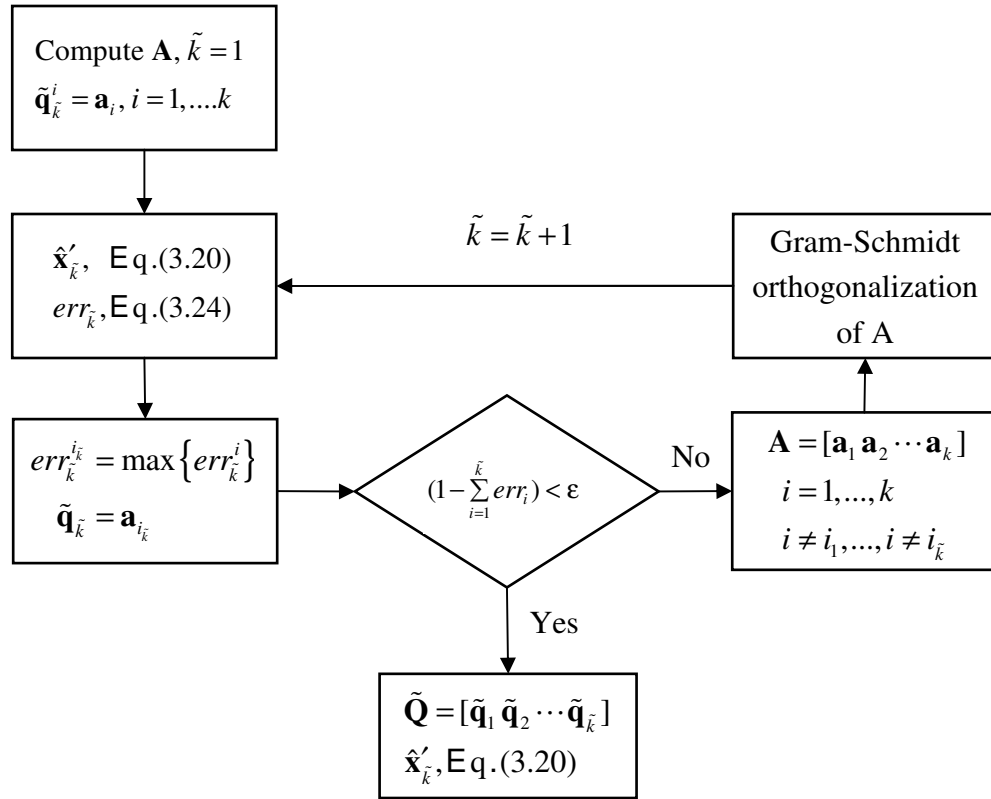


**Figure 3.2:** Modified Gram-Schmidt algorithm.

### 3.4 Numerical case studies

The RBF method will be investigated given a surface of vertical displacement rates over Canada obtained by postglacial rebound modelling. Therefore, the conclusions based on the numerical experiments in this section are valid for PGR surfaces. However, it is demonstrated that the RBF method can be applied also for velocity surfaces related to other processes, e.g., tectonics, or man-made activities, such as fluid extraction. Examples are given in Section 3.4.4.

The surface is assumed not to be discontinuous from faulting, for instance. The simulated rates are given on a grid with resolution  $1^\circ \times 1^\circ$ . The geographical coordinates of the data points are transformed into conformal conic (Lambert) coordinates. To obtain results

independent of the scale of the coordinate axes and data, a scaling to a unit cube is performed. This scaling also allows one to control the shape of the base functions.

Roughness of the surface is expressed by the parameter (Franke *et al.*, 1994)

$$r_h = \int_{y^1 y^2} (h_{y^1 y^1}^2 + 2h_{y^1 y^2}^2 + h_{y^2 y^2}^2) dy^1 dy^2, \quad (3.26)$$

where finite differences are used to compute the derivatives and to evaluate the integral.

The following criteria are used to assess the performance of the RBF interpolator/approximator:

1. the RMS error computed by Eq. (3.16); the target accuracy is 1mm/yr.
2. the condition numbers of the matrix  $\mathbf{C}$ , Eq. (3.8), and the matrix  $\tilde{\mathbf{C}}^T \tilde{\mathbf{C}}$ , Eq. (3.13).
3. the roughness parameter  $r_h$  of the interpolated/approximated surface;  $r_h = 0.037$  for the reference surface.

### 3.4.1 Interpolation of noise-free vertical displacement data

Two cases are investigated: data given on a regular grid and irregularly distributed data. The first case is not encountered in practice; however, the result of the study demonstrates the excellent fitting properties of the base functions if they are properly scaled. The result obtained in the second case demonstrates the capability of the base functions to adapt to the variations of the density of the data point locations.

#### *Study case 1: Data on a grid*

The performance of the interpolators is investigated using data on a  $5^\circ \times 5^\circ$  grid constructed through re-sampling the original  $1^\circ \times 1^\circ$  grid. The total number of data points is 105; the coefficient matrix is of relatively small size and with a moderate condition number.

Table 3.1 summarizes the results for the TPS, MQ, and IMQ interpolators. The optimal shape parameter for the MQ and IMQ interpolators is 0.035 and 0.047, respectively, expressed in terms of unit distance. The optimal shape parameter is determined by

searching in the subinterval from  $10^{-4}$  to 1 in the parameter space. The value for which the minimum RMS error is obtained is taken as optimal (Figure 3.3). An important observation is that both interpolators give identical results when the base functions are optimally scaled. The area of overlap extends approximately from -2 to  $-1.3\log_{10}$ . For cone-like surfaces, the MQ interpolator outperforms the IMQ interpolator. In contrast, for larger shape parameters, the RMS error of the MQ interpolator increases much faster. In the area of overlap, the results are identical with those obtained by the TPS interpolator. However, the coefficient matrix of the latter has a much smaller condition number (see Table 3.1 and Figure 3.4). In fact, the condition number for MQ and IMQ coefficient matrices is very large as a result of the equal distances between the data points given on a grid. The large condition number leads to numerical instabilities and worsens the interpolation accuracy.

The RBF interpolators are compared also to low degree bi-variate polynomial interpolators. Although the condition numbers are small, the RMS errors are far above 1 mm/yr. In particular, the 3<sup>rd</sup> degree polynomial leads to under-parameterization of the surface, which is evident from the large RMS error and very small roughness parameter. In contrast, the 5<sup>th</sup> degree polynomial provides better interpolation, which indicates that if data are distributed regularly over the area of interest, the degree of the bi-variate polynomial can be increased.

**Table 3.1:** Comparison of the interpolators for noise free data on a  $5^\circ \times 5^\circ$  grid

Method	RMS error, mm/yr	Roughness, $r_h$	Condition number
TPS	0.41	0.048	$6.3 \times 10^4$
MQ, $c^2 = 0.035 \sim -1.5\log_{10}$	0.38	0.051	$1.0 \times 10^{11}$
IMQ, $c^2 = 0.047 \sim -1.3\log_{10}$	0.38	0.050	$1.3 \times 10^{10}$
3 <sup>rd</sup> degree polynomial	1.78	0.006	$8.5 \times 10^3$
4 <sup>th</sup> degree polynomial	1.32	0.011	$2.2 \times 10^5$
5 <sup>th</sup> degree polynomial	1.13	0.037	$6.1 \times 10^6$

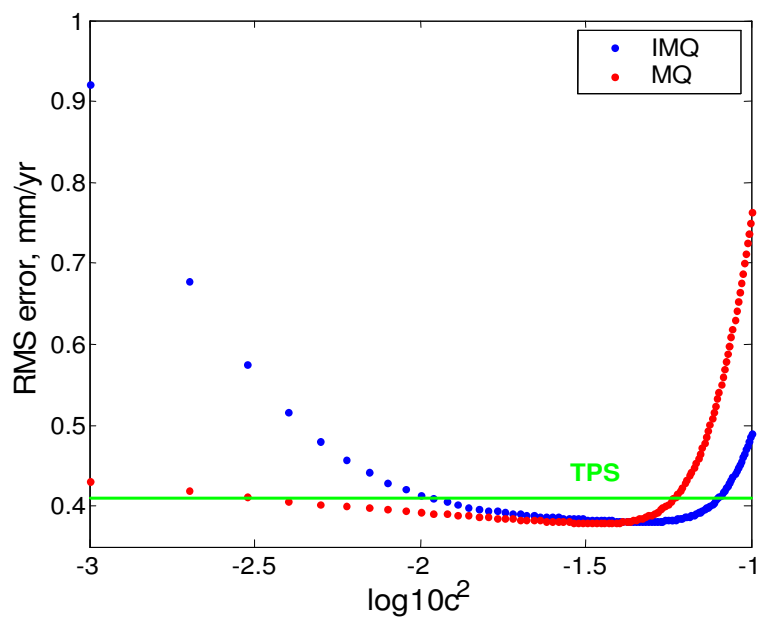


**Figure 3.3:** RMS error as a function of the shape parameter for noise-free data given on a  $5^\circ \times 5^\circ$  grid.

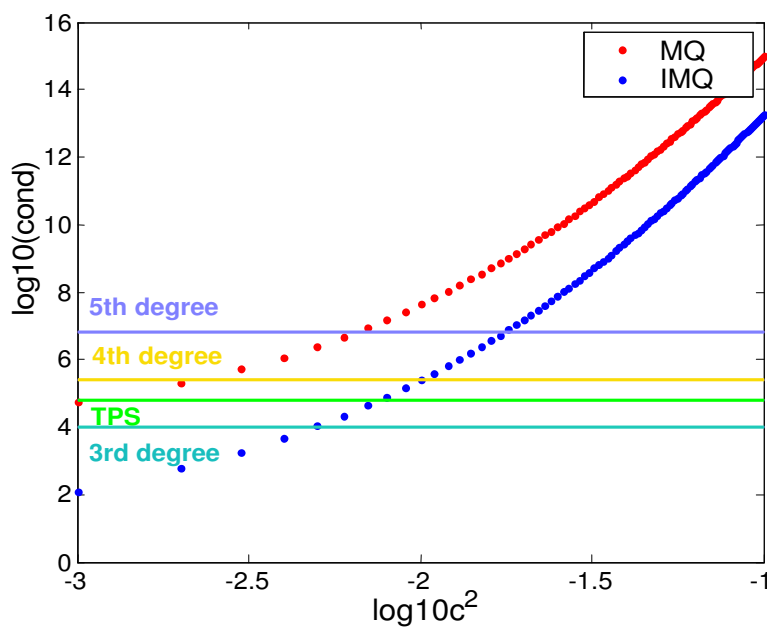


**Figure 3.4:** Condition number of the coefficient matrix as a function of the shape parameter for noise-free data given on a  $5^\circ \times 5^\circ$  grid.

### *Study case 2: Irregularly distributed data*

The second investigated case comprises noise-free irregularly distributed velocity data at 48 point locations from which a  $1^\circ \times 1^\circ$  surface is interpolated by means of the RBF interpolators including TPS, MQ, and IMQ functions. The data point locations correspond to real data sites with the majority of the sites located south of the 60 degree parallel. Only a few sites are found north. This makes the interpolation of the underlying vertical displacement surface particularly challenging. Larger errors could be expected in the areas where no data are available.

The performance of the RBF interpolators is compared in Table 3.2. The RMS error is computed by differencing the interpolated velocities on the  $1^\circ \times 1^\circ$  grid and the reference velocities on the same grid. The first important observation is that the TPS interpolator is less accurate than the MQ and IMQ interpolators. Significant reduction in the roughness parameter is observed, which means that the TPS interpolator gives a very smooth surface. As in Case 1, the MQ and IMQ interpolators perform equally well; the RMS error is 0.6 mm/yr if the optimal parameter value is reached. Since the coefficient matrices are computed with largely varying distances, which decreases the condition number, the shape of the base functions can be widely varied and the best interpolation results are obtained with  $c^2 = 0.16$  and  $c^2 = 0.23$  in unit distance for MQ and IMQ, respectively. Also, the area of overlap of the two interpolators increases (see Figure 3.5). This implies that, for a wide range of shapes, both MQ and IMQ provide a better than 1 mm/yr accuracy. The RMS error significantly increases as the parameter value goes beyond 0.5 (which corresponds to -0.3 in the log10 scale). The explanation is that the elements of the coefficient matrix become nearly equal when the shape parameter value starts to dominate the distances between the data points and as a result the condition number increases (see Figure 3.6).

**Table 3.2:** Comparison of the performance of the interpolators for interpolating noise-free irregularly distributed data

Method	RMS error, mm/yr	Roughness, $r_h$	Condition number
TPS	1.1	0.029	$6.2 \times 10^3$
MQ, $c^2 = 0.161 \sim -0.8 \log_{10}$	0.6	0.037	$3.3 \times 10^7$
MQ (Kansa's method)			
$c_{\min}^2 = 0.001 \sim -3 \log_{10}$	0.9	0.040	$4.0 \times 10^5$
$c_{\max}^2 = 0.200 \sim -0.7 \log_{10}$			
MQ (Foley-Carlson method)			
$c^2 = 0.003 \sim -2.5 \log_{10}$	0.9	0.036	$5.5 \times 10^3$
IMQ, $c^2 = 0.230 \sim -0.6 \log_{10}$	0.6	0.037	$9.2 \times 10^6$
3 <sup>rd</sup> degree polynomial	2.5	0.019	$1.1 \times 10^4$
4 <sup>th</sup> degree polynomial	2.1	0.012	$2.4 \times 10^5$
5 <sup>th</sup> degree polynomial	2.6	0.078	$7.1 \times 10^6$

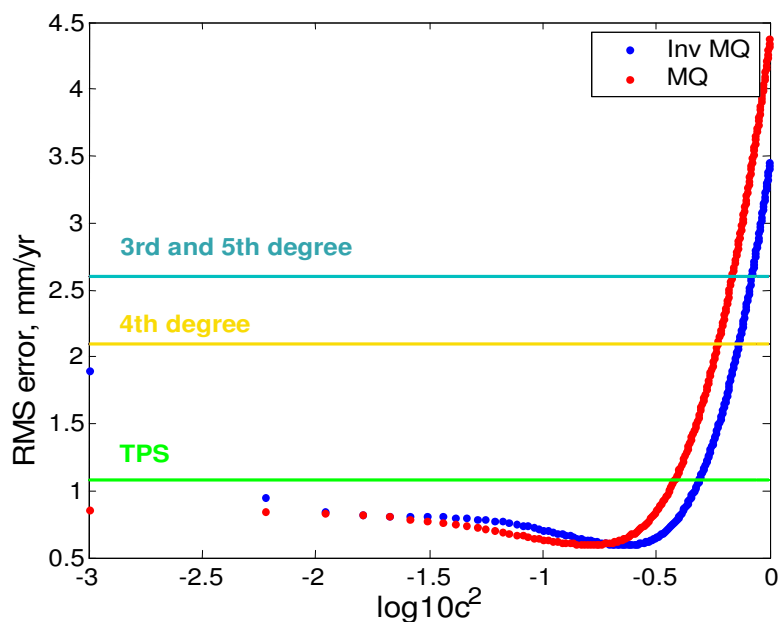


**Figure 3.5:** RMS error as a function of the shape parameter for noise-free irregularly distributed data.

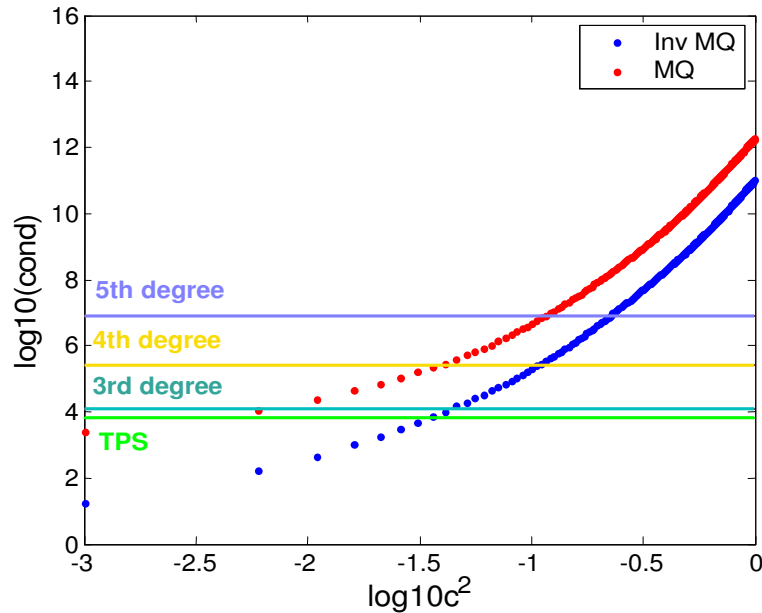


**Figure 3.6:** Condition number of the coefficient matrix as a function of the shape parameter for noise-free irregularly distributed data.

To assess the performance of the bi-variate polynomials, the RMS error and the condition number are shown in Figures 3.5 and 3.6, respectively, and in Table 3.2. The RMS error is far above the threshold of 1 mm/yr. The 5<sup>th</sup> degree polynomial again comprises an interesting case, in which the interpolated surface is over-parameterized. This illustrates the limited abilities of the bi-variate polynomial to adapt to the varying data density.

Another objective of the experiment is to investigate whether the variable value of the shape parameter for the multiquadric base function, according to Eq. (3.10), improves the interpolation accuracy. The maximum and minimum values for the shape parameter are varied to cover different subintervals from the parameter space. The best results are given in Table 3.2. Although the condition number decreases, the RMS error does not drop to the value obtained with the optimal  $c^2$ . The explanation could be that Kansa's approach works well with surfaces with significant variations in the gradient, while the vertical displacement surface in this case study has small gradients, and thus limits the use of the Kansa's approach in this case. Finally, the Foley-Carlson approach is tested. As seen from Table 3.2, the shape parameter is very small and does not lead to an improvement of the

interpolation accuracy (the RMS error is 0.9 mm/yr). The reason is that the underlying surface cannot be accurately represented by a quadratic surface.

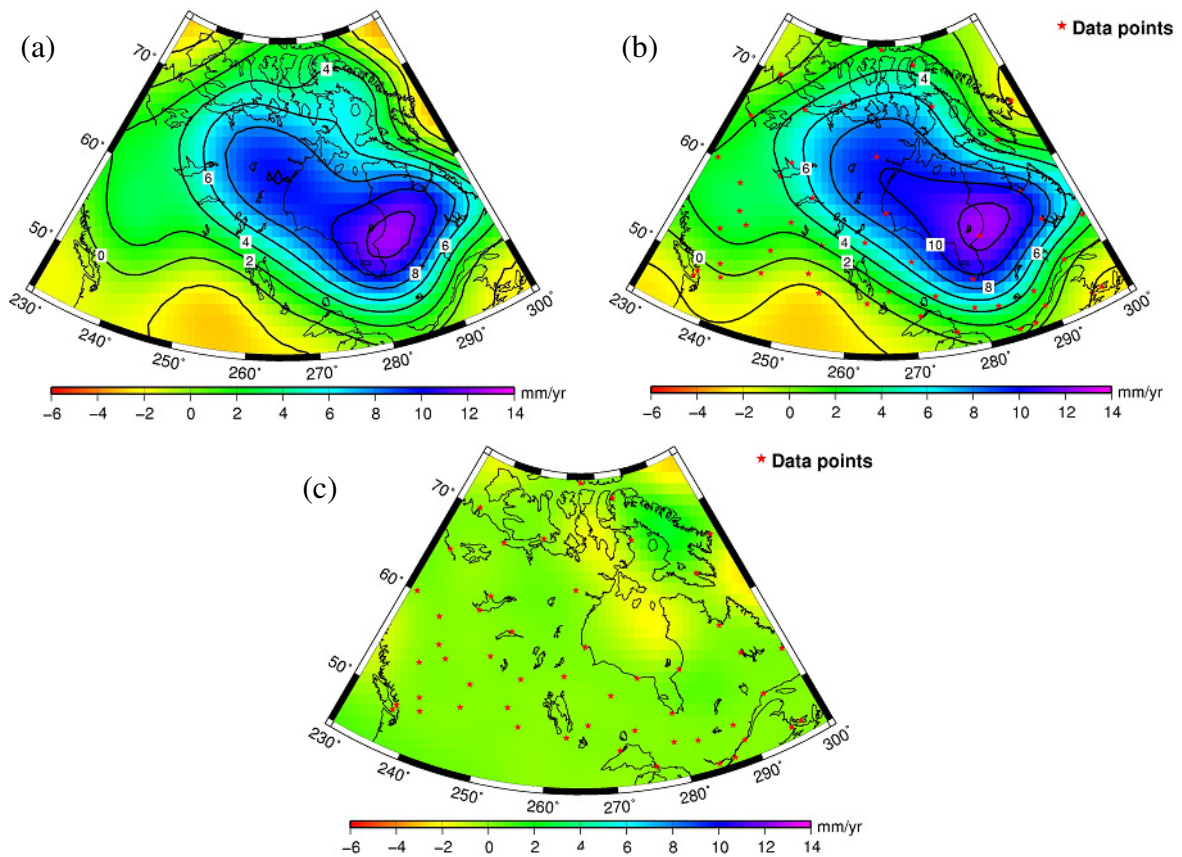


**Figure 3.7:** (a) Reference surface; (b) interpolated surface from noise-free irregularly distributed data with IMQ base functions and  $c^2 = 0.230$ ; and (c) differences between the interpolated and reference surfaces.

In Figure 3.7, the interpolated surface from the irregularly distributed data using the IMQ interpolator is compared with the reference surface. The differences vary spatially from -2 mm/yr to 2 mm/yr, and the largest errors are observed in the areas not constrained by the observations. In contrast, accurate interpolation is obtained in the areas with concentration of data points, including the hinge line. By placing the IMQ base functions at the data point locations, the surface gradient is accurately represented.

The results in this sub-section show that the MQ and IMQ base functions can provide very accurate interpolation of rates of vertical displacement from irregularly distributed observations if the shape of the base functions is adjusted accordingly. The experiments with vertical displacement rates obtained from postglacial rebound simulations with different viscosity profiles and/or ice de-glaciation histories lead to the same results and conclusions. More examples related to the implementation of the inverse multiquadrics in vertical crustal motion studies are given in Section 3.4.4.

### 3.4.2 Approximation of noise-free vertical displacement data

This case study offers an understanding of the role of the number and locations of the base functions on the accuracy of the approximated surface. For this purpose, different algorithms are applied: backward elimination and forward addition cross-validation (CV) algorithms with constant and adaptive shape parameters, and the modified Gram-Schmidt algorithm (GS). The number of the base functions in all of the cases is 24; see Figure 3.8.

In case (a), the forward addition CV algorithm with a constant shape parameter  $c^2 = 0.230$  leads to the largest RMS error of 1.2 mm/yr among all methods. This algorithm selects closely spaced knots, which worsens the condition number of the normal matrix because near equal matrix elements exist. If an informative knot (e.g., with a peak vertical displacement value) is disregarded by the algorithm, a large approximation error can be triggered in the vicinity of this location. Note the correlation between the magnitude of the approximation error over the north part of Hudson Bay and the knot with the maximum vertical displacement (circled in blue) on all plots.

In case (b), the forward addition CV algorithm with an adaptive shape parameter selects a different subset of knots. The order in which the knots are selected depends on the shape parameter value, with which the cross-validation algorithm is carried out. This algorithm locates the base functions in the areas with more significant changes of the surface gradient.

The knot subset determined by the modified GS algorithm in case (c) locates the base functions in the area with a very small gradient. Also, large errors (-3.5 mm/yr) along the

southwest edge of the studied region are observed. The RMS error, however, is as in case (b), i.e., 0.9 mm/yr. In addition, a small approximation error over Hudson Bay is observed.

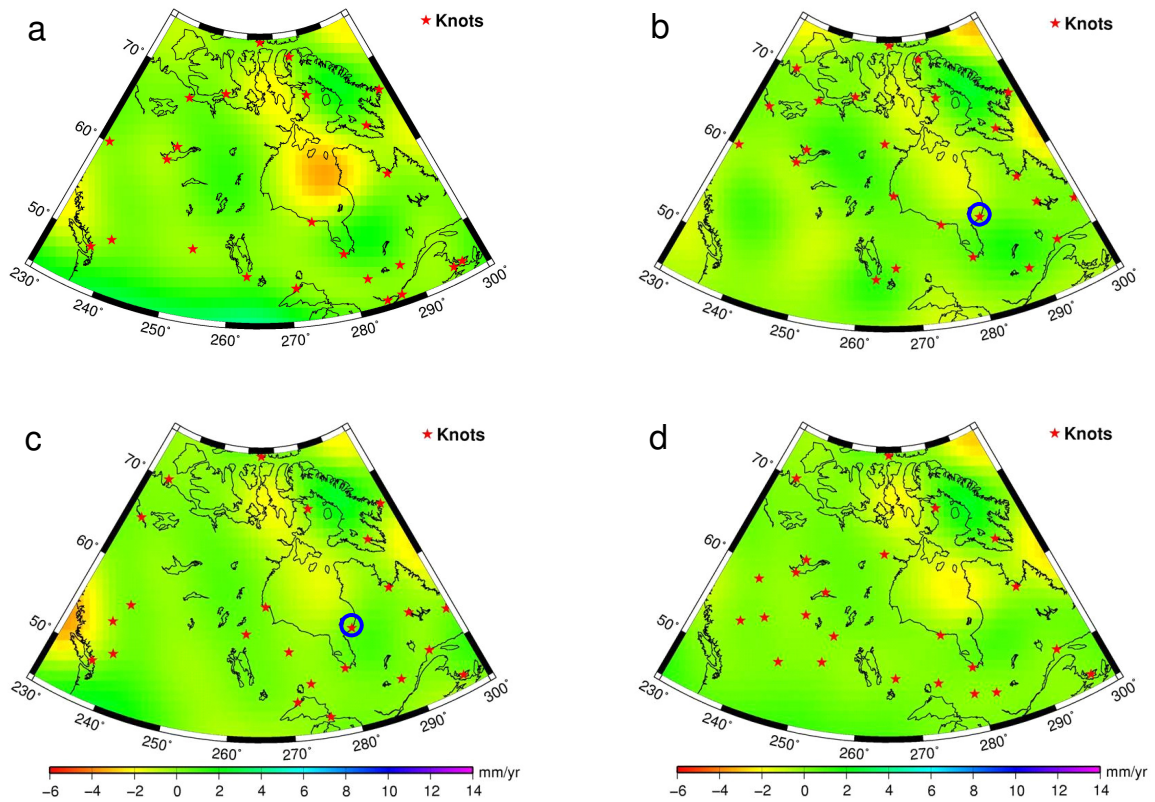


**Figure 3.8 :** Differences between the reference and approximated (with 24 base functions) surfaces: (a) forward CV with  $c^2 = 0.230$  and RMS error of 1.2 mm/yr, (b) forward CV with adaptive  $c^2$  and RMS error of 0.9 mm/yr; (c) modified GS with  $c^2 = 0.230$ , and RMS error of 0.9 mm/yr; (d) backward CV with adaptive  $c^2$  and RMS error of 0.8 mm/yr.

The last case (d) with a backward CV algorithm with an adaptive shape parameter distributes the base functions well over the territory and locates more base functions along the hinge line. This algorithm provides the least approximation error, i.e. 0.8 mm/yr, but removes the knot with the maximum vertical displacement value (at a very early stage of the elimination); consequently, the error in its vicinity increases in magnitude, though it is not as large as in the case (a).

From the results discussed above, it becomes clear that the forward algorithms depend on the value of the shape parameter with which the algorithms start and run. However, as shown in the interpolation case, a wide range of shape parameter values can provide acceptable results if the optimal shape parameter belongs to this range. Therefore, the optimal parameter value is important but not crucial for the performance of the IMQ approximator. The fact that the approximated surface is not known in reality as well as the presence of measurement noise forces the use of approximate shape parameter values.

Based on the results in this study case, it can be stated that the modified Gram-Schmidt algorithm can be as accurate as the algorithms based on the cross-validation technique. The Gram-Schmidt algorithm does not outperform the backward elimination algorithm; however, its main advantage, that is, controlling the balance between the accuracy of the approximation and the number of base functions through the threshold value, is used as an argument to utilize this method in the optimal combination of heterogeneous vertical displacement data in Chapter 4.

### 3.4.3 Approximation of noisy vertical displacement data

Gaussian noise with variances  $\sigma^2 = 0, 0.01, 0.25, \text{ and } 1.00 \text{ mm}^2/\text{yr}^2$  has been generated by the routines available in Matlab and added to the irregularly distributed noise-free vertical displacement data. Different threshold (tolerance) values are adopted as follows:  $\epsilon = 0.001, 0.01, \text{ and } 0.10$ . Each threshold defines the amount of the filtered data variance. For example, if the threshold is 0.001, then 0.1% of the data variance is filtered out. The forward GS selection algorithm is run with all different noise levels and threshold values 1000 times, and the average results are presented in the following.

The different cases are compared in terms of the size of the selected knot subset, the RMS error, and the condition number of the normal matrix. For  $\epsilon = 0.1$  and  $\sigma^2 = 0 \text{ mm}^2/\text{yr}^2$ , a large RMS error of 2.4 mm/yr, along with a small number of selected base functions (Figure 3.9), is observed. This accounts for under-fitting of the displacement surface. For the same threshold and  $\sigma^2 = 1.00 \text{ mm}^2/\text{yr}^2$ , the RMS error decreases to 1.8 mm/yr because part of the noise is filtered out. For smaller thresholds, the number of base functions

increases steadily with the increase in the noise variance because the larger the noise variance, the more base functions are required to fit the data. The approximation becomes very inaccurate since the approximator attempts to fit the noise; see the large RMS errors in Figure 3.10 and the condition numbers in Figure 3.11.

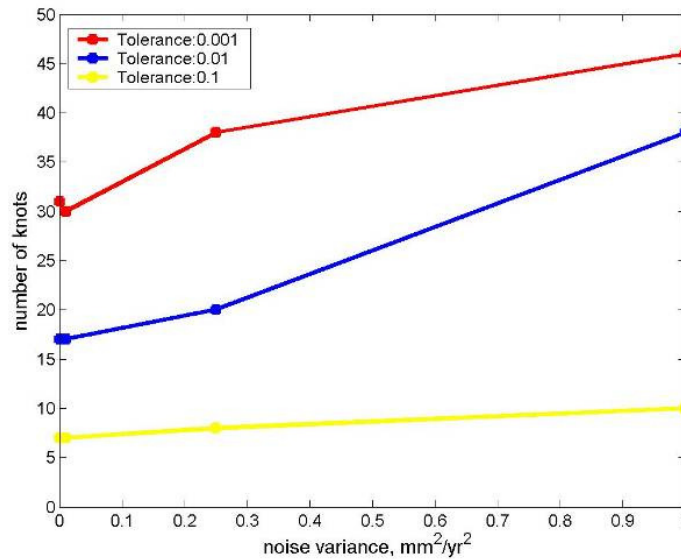


**Figure 3.9:** Number of base functions as a function of noise variance for different thresholds (tolerances).

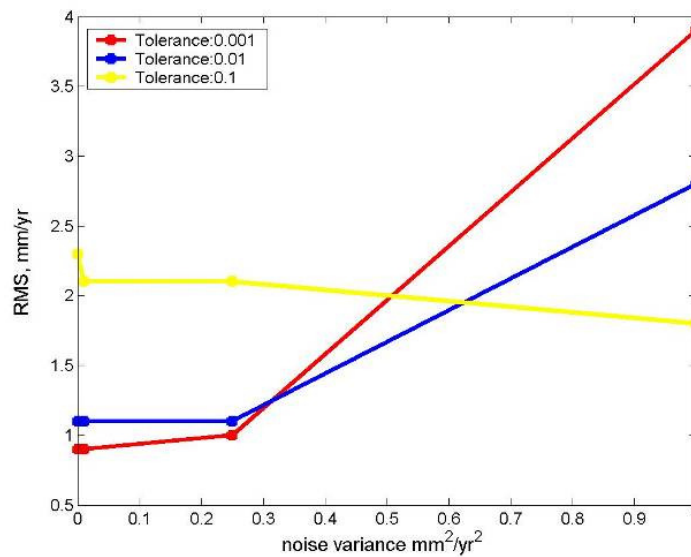


**Figure 3.10:** RMS error as a function of noise variance for different thresholds (tolerances).

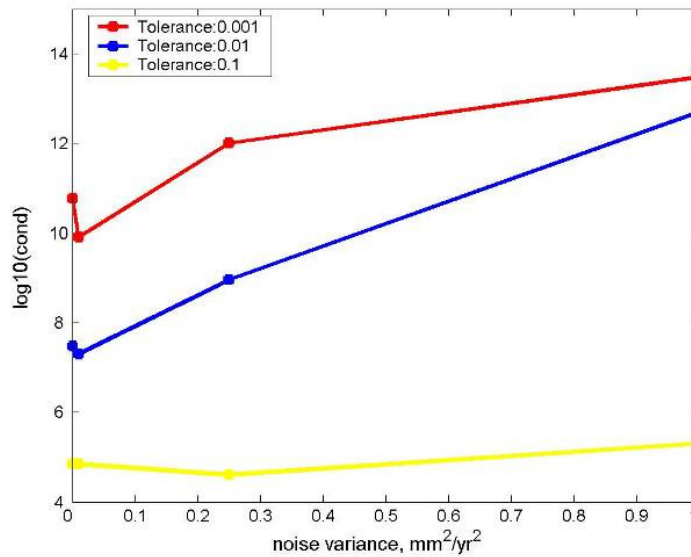


**Figure 3.11:** Condition number as a function of noise variance for different thresholds (tolerances).

In the case of noisy data ( $\sigma^2 = 1.00 \text{ mm}^2/\text{yr}^2$ ), it is observed that a wide range of parameters (from 0.01 to 1.00) provides reasonable approximation accuracy. A thorough search in the subinterval from 0.01 to 0.10 shows that the minimum RMS error of 1.4 mm/yr is estimated with  $c^2 = 0.06$  and 10 base functions (about 20% of the data point locations). Figure 3.12 represents the spatial variation of the differences between the approximated and reference surfaces. The largest errors of -2.5 mm/yr are observed in the northeast and southwest corners, where the IMQ approximator extrapolates the vertical displacement rates.

In summary, it is possible to reconstruct a smooth vertical displacement surface from noisy scattered data ( $\sigma^2 = 1.00 \text{ mm}^2/\text{yr}^2$ ) with only about 20% of the data point locations selected as base function knots, and the approximation error is 1.4 mm/yr. Although the results are obtained for a realistic noise level, the fact that the noise was treated as stationary can alter the conclusions drawn in this study. Nonetheless, it can be stated that an accurate approximation of smooth postglacial rebound vertical displacement surfaces from scattered data can be obtained with IMQ base functions with a shape parameter of approximately 0.1 of unit distance.

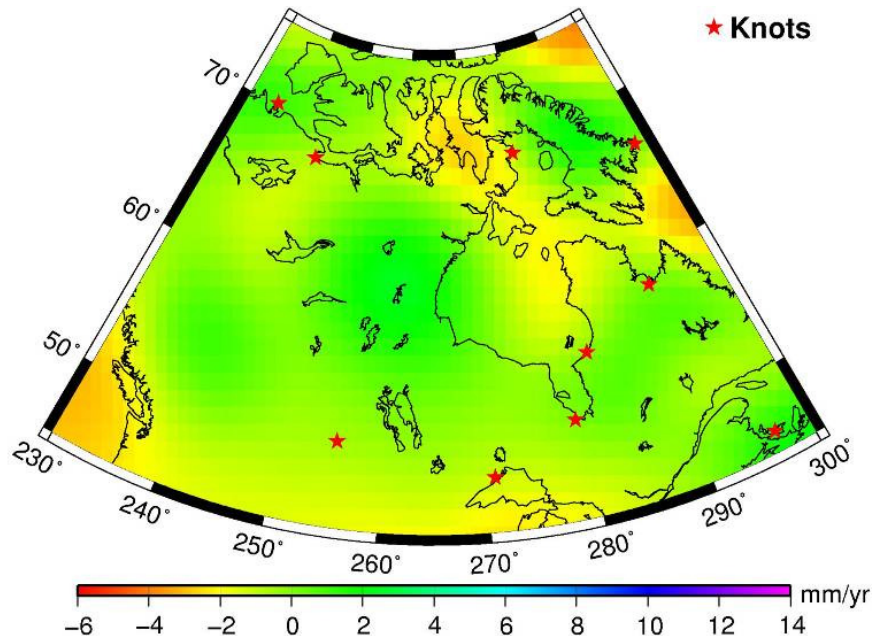


**Figure 3.12:** Differences between the approximated and reference surfaces by the modified GS selection algorithm ( $\sigma^2 = 1.00 \text{ mm}^2/\text{yr}^2$  and  $c^2 = 0.06$ ). The RMS error is 1.4 mm/yr.

#### 3.4.4 Applications of the inverse multiquadric approximator

The examples studied in this section illustrate the excellent fitting abilities of the IMQ approximator and the effectiveness of the Gram-Schmidt selection algorithm. Two opposite cases of vertical displacement surfaces, namely a smooth bowl-shaped surface and a discontinuous surface, are studied. The former is characteristic for land subsidence processes related to fluid extraction (e.g., Odijk, 2005). The latter is encountered in tectonically active areas, such as southeastern Canada, where the abundance of geological faulting is related to postglacial rebound processes (Wu and Hasegawa, 1996). In such cases, observed vertical crustal displacement shows abrupt changes across faulting lines.

##### *Smooth bowl-shaped surfaces*

The simulated surface in Figure 3.13a is approximated using 40 IMQ base functions ( $c^2 = 0.1$  and  $\varepsilon = 0.001$ ) selected by the GS algorithm (see Figure 3.15b) and the RMS error is 0.1 mm/yr. When Gaussian noise with a variance of  $1 \text{ mm}^2/\text{yr}^2$  (Figure 3.13c) is added, the

algorithm selects 23 base functions provided that  $\epsilon = 0.40$ , and the RMS error increases to 1 mm/yr; see Figure 3.13d.

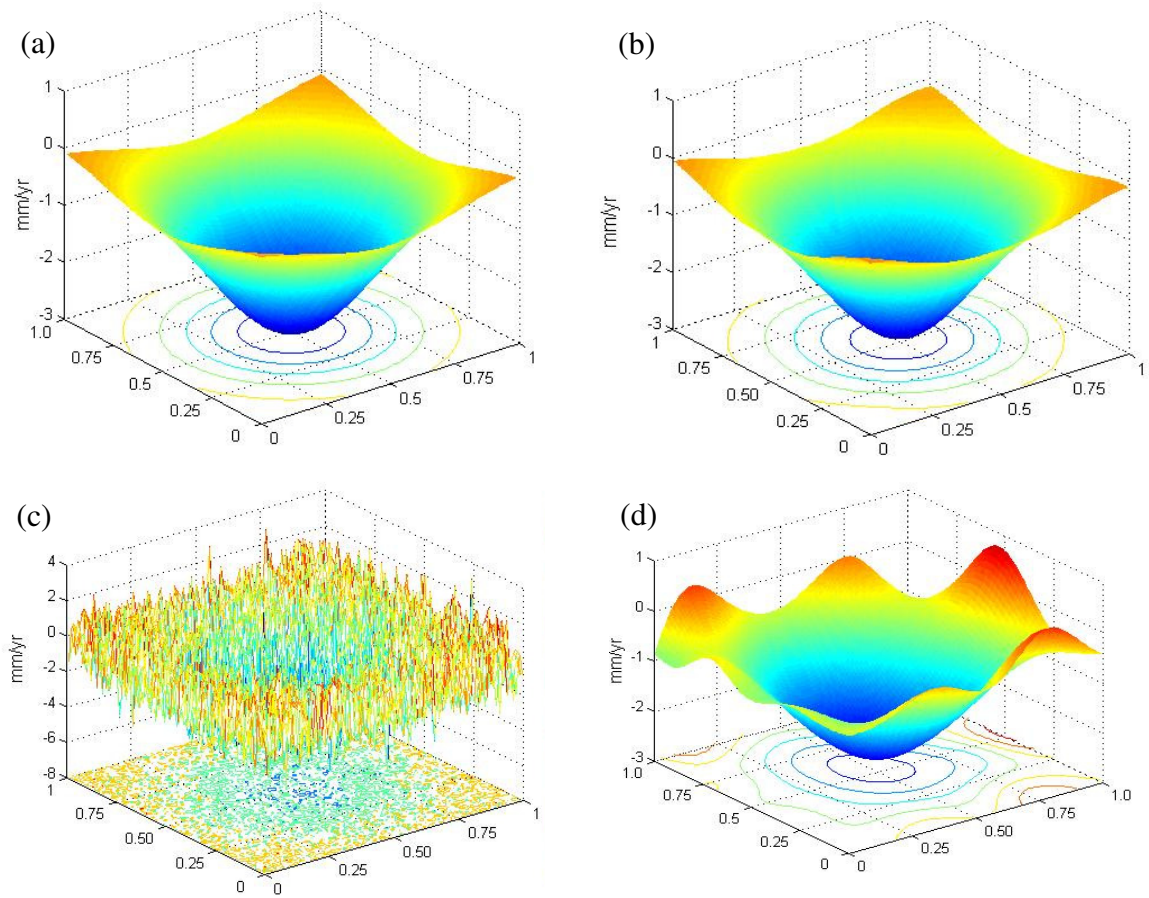


**Figure 3.13:** (a) Simulated bowl-like surface, (b) approximated surface, (c) simulated surface plus noise (note the different scale of the z-axis), and (d) smoothed surface.

### *Discontinuous surfaces*

Although there exist algorithms based on the RBF method that allow interpolation of scattered data across surface discontinuities (see, e.g., Arge and Floater (1994)), this example does not aim to argue in favour of such an approach. Instead, it illustrates the universal properties of the IMQ method for approximation of scattered data. The

approximated surface ( $c^2 = 0.01$ ) is shown in Figure 3.14a. Apparently, the base functions tend to group along the discontinuity of the underlying surface. In contrast with the smooth surface approximation in the first example, the modified GS algorithm does not succeed in filtering the noise present in the data (Figure 3.14b). In fact, the presence of noise requires a reduction of the number of the base functions and/or a larger shape parameter, which contradicts the need of many and more peaked base functions to properly represent discontinuities in the data (Figure 3.14c).

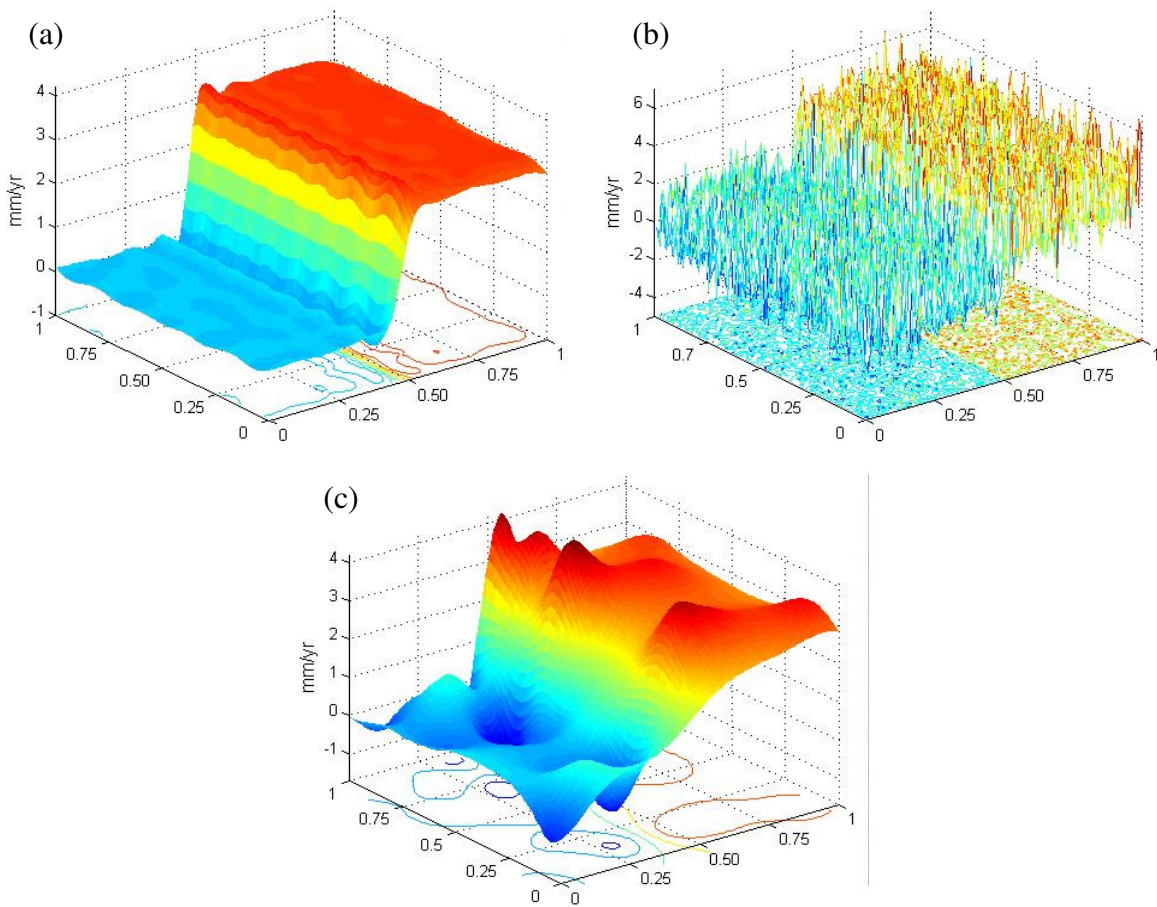


**Figure 3.14:** (a) Approximated surface – base functions tend to group along the discontinuity present in the data, (b) simulated surface plus noise (note the different scale of the z-axis), and (c) smoothed surface.

### 3.5 Relation between inverse multiquadric base functions and a mass flow model

In the preceding sections, the IMQ method has been studied from the perspective of the interpolation and approximation of scattered vertical displacement data; that is, only the mathematical aspects of the implementation have been addressed. The physical interpretation of the IMQ base functions stems from the harmonic theory of the potential. In particular, Eq. (3.4) can be rewritten as follows:

$$\Phi(\ell_j) = \frac{1}{\sqrt{(y^1 - y_j^1)^2 + (y^2 - y_j^2)^2 + (y^3 - y_j^3)^2}} = \frac{1}{\ell_j}. \quad (3.27)$$

Being the inverse distance between the base function and the running point,  $\Phi(\ell_j)$  is a harmonic function and is the kernel of the point mass method in the gravity field approximation (Barthelmes and Dietrich, 1991). The point mass method was used by Hardy (1977) for interpreting mass redistributions related to vertical crustal motion.

As explained in Chapter 2, an approximate relation between the rate of change of the absolute vertical displacement and the time derivatives of the geopotential coefficients can be used to compute the former. The fact that the postglacial rebound geoid change is mainly a result of mass anomalies associated with the deformation of the lithosphere can be used to link the vertical crustal displacement and the effect of the mass redistribution on the equipotential surface in the local case. The vertical crustal displacement,  $\delta h$ , is accompanied by a viscous flow of masses from below the lithosphere. Therefore, the change  $\delta h_i d\sigma_i$  of an infinitesimal mass volume located at a certain depth induces a change in the geoid height at point  $j$  as follows:

$$\delta N_j = \frac{G\rho_m}{g_a} \frac{\delta h_i d\sigma_i}{\ell_{ij}} = \frac{G\delta\mu_i}{g_a \ell_{ij}}, \quad (3.28)$$

where  $G$  is the gravitation constant,  $\rho_m$  is the mean density of the mantle ranging between  $3.00 - 3.50 \text{ g}\cdot\text{cm}^{-3}$  (Wahr *et al.*, 1995),  $g_a$  is the average gravity,  $d\sigma$  is the surface element, and  $\delta\mu = \rho_m \delta h d\sigma$  is the mass element. Eq. (3.28) was used by Sjöberg (1982) to model the geoid rate in Fennoscandia using levelled uplift. By means of the same equation,

the effect of the errors of the approximation of the scattered vertical displacement data (Figure 3.12) on the geoid is computed and presented in Figure 3.15. The depth of the mass element  $\delta\mu$  is assumed to be 120 km. The mismodelling of the rates of the vertical displacement would introduce in the rate of change of the geoid height an error of less than 0.1 mm/yr.

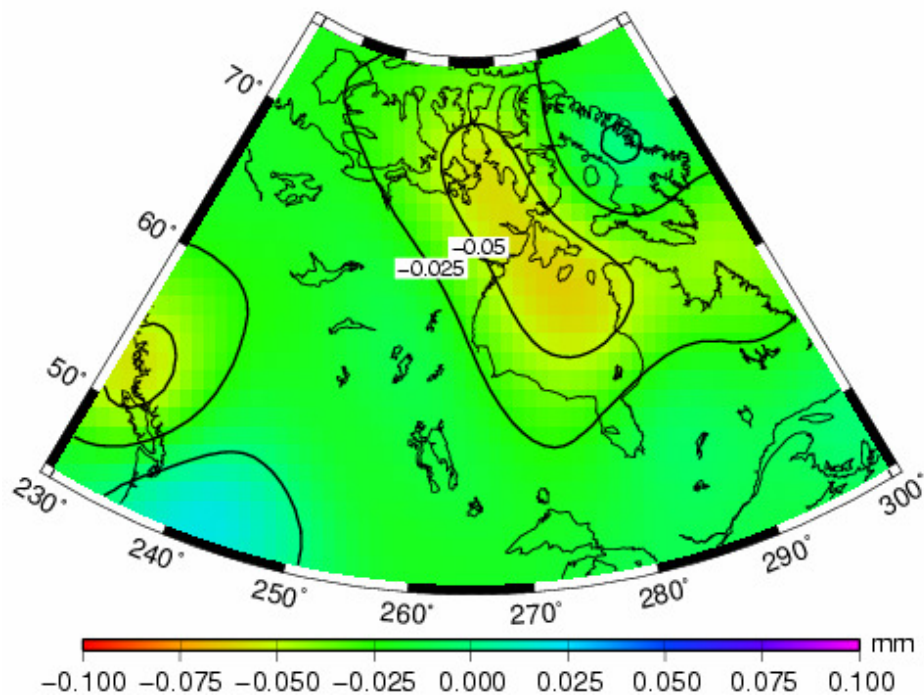


**Figure 3.15:** Effect of the approximation errors on the rate of change of geoid height, in mm/yr.

### 3.6 Summary

In this chapter, radial base functions have been studied in the context of the approximation of scattered vertical displacement data. By means of simulated postglacial rebound rates of vertical displacement, it has been shown that the IMQ and MQ methods can provide an accurate approximation of irregularly distributed observations if the base functions are

optimally scaled. This conclusion confirms the observations of Mautz *et al.* (2003). An empirical rule for scaling of the base functions has been developed and tested extensively.

Two classes of algorithms for determining the optimal number of the base functions have been implemented and tested including the backward elimination/forward addition of base functions based on the cross-validation technique and the modified Gram-Schmidt algorithm based on orthogonal least-squares. In spite of the simple logic of the cross-validation algorithms, they are computationally intensive (even for small-size problems) and, more importantly, the contribution of each base function to the output is not known. The modified Gram-Schmidt algorithm is computationally efficient, and its main advantage is that the output variance can be easily controlled by varying the threshold value. This makes the algorithm particularly useful for smoothing measurement errors in the vertical crustal displacement observations. Therefore, based on the results obtained in this chapter, the use of algorithms based on orthogonal least-squares for the purpose of approximating vertical displacement rates is recommended. The modified Gram-Schmidt algorithm will be employed in the optimal combination of heterogeneous data in Chapter 4.

It has been shown that the rates of change of the geoid height and the rates of the absolute vertical displacement can be linked by a physically meaningful relationship in terms of the inverse multiquadric base functions. This relationship is the basis for modelling the rates of the geoid height from terrestrial data in terms of GPS vertical velocities and rates of the terrestrial gravity in Chapters 4 and 5 of this thesis.

## **Chapter Four: Rates of change of geoid and heights obtained from terrestrial data**

The objective of this chapter is to develop, test, and validate a methodology for an optimal combination of heterogeneous data for prediction of rates of change of geoid and orthometric heights. This combination procedure uses least-squares collocation with parameters and allows for stepwise computations. The data include rates of change of the terrestrial gravity and GPS vertical velocities and comprise the minimum information required to estimate the mass redistribution component in the temporal variations of the gravity field (see Section 2.4.2 in Chapter 2). This requirement, however, does not limit the type of the data that can be inputted. Re-levelled segments of the primary vertical control network in Canada, tilts from tide gauges sea/water level recording, GRACE-observed rates of change of gravity and absolute displacement comprise other possible data input. In addition to the rates of change of the geoid and orthometric heights, rates of the terrestrial gravity and absolute vertical displacement can be estimated.

### **4.1 General least-squares collocation with parameters approach**

The following key steps of the procedure are described:

- Least-squares collocation with parameters solution and error estimation;
- Statistical testing including a test on the compatibility of the data with the mathematical model, data snooping for outlier detection, and variance component estimation;
- Validation of the predicted rates.

#### 4.1.1 Mathematical model

The observation equation in least-squares collocation with parameters is (Moritz, 1980)

$$\mathbf{l} = \mathbf{A}\mathbf{x} + \mathbf{s} + \mathbf{v}, \quad (4.1)$$

where  $\mathbf{l} = [l_1 \ l_2 \ \dots \ l_n]^T$  is a vector of observations,  $\mathbf{x} = [x_1 \ x_2 \ \dots \ x_k]^T$  is a vector of unknown parameters,  $\mathbf{A}$  is the  $(n \times k)$  coefficient matrix, and  $\mathbf{v} = [v_1 \ v_2 \ \dots \ v_n]^T$  is a vector of normally distributed errors (noise) with  $N(\mathbf{0}, \mathbf{C}_v)$  and  $\mathbf{C}_v = E\{\mathbf{v}\mathbf{v}^T\}$ .

The vector  $\mathbf{s} = [s_1 \ s_2 \ \dots \ s_n]^T$  contains signal components of the observations. In this research, signals are linear functionals of the rate of change of the potential and are represented as follows:

$$s_i = B\dot{W}_i, i = 1, 2, \dots, n, \quad (4.2)$$

where  $B$  is a linear operator. The functionals of the rate of change of the potential include rates of change of the terrestrial gravity and its mass component and rates of change of the ellipsoidal, geoid, and orthometric heights. Eq. (4.1) was originally used in the prediction of absolute vertical displacements from absolute gravity and levelling data in local tectonic areas (Heck, 1984). For Canada, the terrestrial gravity data and GPS vertical velocities comprise the terrestrial data that can be used for modelling the rates of the geoid and orthometric heights in the areas not covered by a vertical control network.

The vector  $\mathbf{s}$  is assumed normally distributed, i.e.,  $\mathbf{s} \sim N(\mathbf{0}, \mathbf{C}_s)$  with  $\mathbf{C}_s = M\{\mathbf{s}\mathbf{s}^T\}$ , where  $M$  is a homogeneous and isotropic averaging operator on the sphere (Moritz, 1980). The normal distribution of the local anomalous gravity field is justified by Wei (1987). According to Koch (1999), the observations  $l_i, i = 1, \dots, n$  are considered also normally distributed variables with  $N(\mathbf{A}\mathbf{x}, \mathbf{C}_l = \mathbf{C}_s + \mathbf{C}_v)$ .

Let the zero mean signal vector  $\bar{\mathbf{s}}$  contains the vector  $\mathbf{s}$  of the given signals and the vector  $\mathbf{s}_p$  of predicted signals at new locations, i.e.,  $\bar{\mathbf{s}} = [\mathbf{s}^T \ \mathbf{s}_p^T]^T$ . Then, the cross-covariance matrix of the predicted and given signals is defined as follows:

$$\mathbf{C}_{s_p s} = M\{\mathbf{s}_p \mathbf{s}^T\}. \quad (4.3)$$

The estimates of the vector of parameters  $\mathbf{x}$  and the signal vector  $\bar{\mathbf{s}}$  are obtained by minimizing the norm

$$\bar{\mathbf{s}}^T \mathbf{C}_{\bar{\mathbf{s}}} \bar{\mathbf{s}} + \mathbf{v}^T \mathbf{C}_v \mathbf{v} = \min \quad (4.4)$$

under the condition given by Eq. (4.1), where it is assumed that the signal and noise vectors are not correlated; that is,  $\mathbf{C}_{\bar{\mathbf{s}}v} = \mathbf{0}$ . The signal covariance matrix is given as

$$\mathbf{C}_{\bar{\mathbf{s}}} = \begin{bmatrix} \mathbf{C}_s & \mathbf{C}_{ss_p} \\ \mathbf{C}_{s_p s} & \mathbf{C}_{s_p} \end{bmatrix}. \quad (4.5)$$

The estimated vector of parameters is found by

$$\hat{\mathbf{x}} = (\mathbf{A}^T \mathbf{C}_l^{-1} \mathbf{A})^{-1} \mathbf{A}^T \mathbf{C}_l^{-1} \mathbf{l}. \quad (4.6)$$

The vector of predicted signals at the new locations is

$$\hat{\mathbf{s}}_p = \mathbf{C}_{s_p s} \mathbf{C}_l^{-1} (\mathbf{I} - \mathbf{A} \hat{\mathbf{x}}), \quad (4.7)$$

and the vector of estimated signals of the observations is

$$\hat{\mathbf{s}} = \mathbf{C}_s \mathbf{C}_l^{-1} (\mathbf{I} - \mathbf{A} \hat{\mathbf{x}}). \quad (4.8)$$

The estimated residuals are given by

$$\hat{\mathbf{v}} = \mathbf{C}_v \mathbf{C}_l^{-1} (\mathbf{I} - \mathbf{A} \hat{\mathbf{x}}). \quad (4.9)$$

The estimation errors are obtained from the covariance matrices

$$\mathbf{C}_{\hat{\mathbf{x}}} = (\mathbf{A}^T \mathbf{C}_l^{-1} \mathbf{A})^{-1}, \quad (4.10)$$

$$\mathbf{C}_{\hat{\mathbf{s}}_p} = \mathbf{C}_{s_p} - \mathbf{C}_{s_p s} \mathbf{C}_l^{-1} (\mathbf{I} - \mathbf{A} \mathbf{C}_{\hat{\mathbf{x}}} \mathbf{A}^T \mathbf{C}_l^{-1}) \mathbf{C}_{s_p s}^T, \quad (4.11)$$

$$\mathbf{C}_{\hat{\mathbf{x}} \hat{\mathbf{s}}_p} = -\mathbf{C}_{\hat{\mathbf{x}}} \mathbf{A}^T \mathbf{C}_l^{-1} \mathbf{C}_{s_p s}^T, \quad (4.12)$$

$$\mathbf{C}_{\hat{\mathbf{s}}} = \mathbf{C}_s - \mathbf{C}_s \mathbf{C}_l^{-1} (\mathbf{I} - \mathbf{A} \mathbf{C}_{\hat{\mathbf{x}}} \mathbf{A}^T \mathbf{C}_l^{-1}) \mathbf{C}_s^T, \quad (4.13)$$

and

$$\mathbf{C}_{\hat{\mathbf{v}}} = \mathbf{C}_v - \mathbf{C}_v \mathbf{C}_l^{-1} (\mathbf{I} - \mathbf{A} \mathbf{C}_{\hat{\mathbf{x}}} \mathbf{A}^T \mathbf{C}_l^{-1}) \mathbf{C}_v. \quad (4.14)$$

The covariance matrix of the predicted vector  $\hat{\mathbf{I}}_p = \mathbf{A}_p \hat{\mathbf{x}} + \hat{\mathbf{s}}_p$  is defined as

$$\mathbf{C}_{\hat{\mathbf{I}}_p} = \mathbf{A}_p \mathbf{C}_{\hat{\mathbf{x}}} \mathbf{A}_p^T + \mathbf{A}_p \mathbf{C}_{\hat{\mathbf{x}}\hat{\mathbf{s}}_p} + (\mathbf{A}_p \mathbf{C}_{\hat{\mathbf{x}}\hat{\mathbf{s}}_p})^T + \mathbf{C}_{\hat{\mathbf{s}}_p} \quad (4.15)$$

with the coefficient matrix  $\mathbf{A}_p$ .

#### 4.1.2 Statistical testing

The statistical testing related to the model of least-squares collocation with parameters involves the following tests:

1. Test on the compatibility of the data with the mathematical model

A test on the variance of unit weight (a *congruency test*) indicating the validity of the adopted model for the given data is performed. According to Dermanis and Rossikopoulos (1991), test failure indicates a problematic mathematical model without revealing the actual cause. The possible causes may include an incorrectly formulated mathematical model, incorrect signal and noise covariance matrices, or outliers present in the observations (Krakiwsky and Biacs, 1990).

The stochastic model used is

$$\begin{bmatrix} \mathbf{s} \\ \mathbf{v} \end{bmatrix} \sim N \left( \begin{bmatrix} \mathbf{0} \\ \mathbf{0} \end{bmatrix}, \sigma_o^2 \begin{bmatrix} \mathbf{Q}_s & \mathbf{0} \\ \mathbf{0} & \mathbf{Q}_v \end{bmatrix} \right), \quad (4.16)$$

where a common variance of unit weight  $\sigma_o^2$  is assumed.  $\mathbf{Q}_s$  and  $\mathbf{Q}_v$  are signal and error cofactor matrices, respectively. The estimate of  $\sigma_o^2$  is defined as follows:

$$\hat{\sigma}_o^2 = \frac{\Omega}{n-k} = \frac{\Omega}{f}, \quad (4.17)$$

where  $f$  stands for the degrees of freedom of the model. The quadratic form  $\Omega$  is defined as

$$\Omega = \hat{\mathbf{s}}^T \mathbf{C}_s^{-1} \hat{\mathbf{s}} + \hat{\mathbf{v}}^T \mathbf{C}_v^{-1} \mathbf{v} \quad (4.18)$$

and can be computed as follows (Wei, 1987):

$$\Omega = \mathbf{1}^T (\mathbf{C}_l^{-1} - \mathbf{C}_l^{-1} \mathbf{A} (\mathbf{A}^T \mathbf{C}_l^{-1} \mathbf{A})^{-1} \mathbf{A}^T \mathbf{C}_l^{-1}) \mathbf{1}. \quad (4.19)$$

The test on the variance of unit weight is defined (Vaníček and Krakiwsky, 1986; Dermanis and Rossikopoulos, 1991) as

$$\begin{aligned} H_o : \hat{\sigma}_o^2 &= \sigma_o^2 \\ H_a : \hat{\sigma}_o^2 &\neq \sigma_o^2 \end{aligned} \quad (4.20)$$

where  $\sigma_o^2 = 1$  is assumed, with a test statistic

$$\tilde{\chi}^2 = \frac{\Omega}{\sigma_o^2} = \frac{f \hat{\sigma}_o^2}{\sigma_o^2}. \quad (4.21)$$

The null hypothesis is accepted if

$$\chi_{1-\alpha/2}^2(f) \leq \tilde{\chi}^2 \leq \chi_{\alpha/2}^2(f), \quad (4.22)$$

where  $\alpha$  is the adopted level of significance.

## 2. Outlier detection

One of the possible reasons for the failure of the congruency test is the presence of erroneous observations (outliers). Testing for outliers is based on testing the null hypothesis

$$\begin{aligned} H_o : \nabla_i &= 0 \\ H_a : \nabla_i &\neq 0 \end{aligned} \quad (4.23)$$

where  $\nabla_i$  is the magnitude of the outlier present in the  $i^{th}$  observation. The Baarda's data-snooping method (Baarda, 1967; Teunissen, 2000) is used to test the individual residuals by means of the statistic

$$\tilde{N} = \frac{\hat{v}_i}{\sigma_{\hat{v}_i}} \sim N(0,1), \quad (4.24)$$

where  $\sigma_{\hat{v}_i} = \sqrt{\text{diag}(\mathbf{C}_{\hat{v}})_i}$ , if the scale of the error covariance matrix is known. An outlier is present in the  $i^{\text{th}}$  observation if

$$|\tilde{N}| > N_{1-\alpha/2}. \quad (4.25)$$

If the scale of the error covariance matrix is estimated, the statistic

$$\tilde{\tau} = \frac{\hat{v}_i}{\hat{\sigma}_{\hat{v}_i}} \sim \tau(f) \quad (4.26)$$

has a  $\tau$ -distribution and is computed with  $\hat{\sigma}_{\hat{v}_i} = \sqrt{\text{diag}(\hat{\mathbf{C}}_{\hat{v}})_i}$  (Vaníček and Krakiwsky, 1986). The null hypothesis is not accepted if

$$|\tilde{\tau}| > \tau_{1-\alpha/2}. \quad (4.27)$$

The  $\tau$ -distribution is related to the  $t$ -distribution by

$$\tau = \frac{\sqrt{f} t (f-1)}{\sqrt{f-1 + t^2 (f-1)}}. \quad (4.28)$$

### 3. Test on the model parameters

The statistical test on the model parameters allows one to leave out the insignificant components of the vector  $\hat{\mathbf{x}}$  and to increase the degrees of freedom of the model. For a definition of the test and a description of the appropriate statistics applied in the least-squares collocation method, Wei (1987) can be consulted. The developed procedure in this research does not incorporate the test on the model parameters. The modified Gram-Schmidt algorithm determines the location of the base functions (and their number) by ordering the regressors in terms of their contribution to the data variance (Section 3.3.2). Thus, the significance of each base function is assessed automatically.

### 4. Variance component estimation

When two or more heterogeneous groups of observations are included in the mathematical model in Eq.(4.1), variance component estimation is carried out. Proper weighting of the observations is required in order to estimate correctly the unknown parameters and to avoid

systematic distortions of results. The method applied in this thesis is the iterative BIQUE (Best Invariant Quadratic Unbiased Estimate); see, e.g., Koch (1999). Some examples for the implementation of this method include an analysis of terrestrial geodetic networks (Crocetto *et al.*, 2000), regularization of geopotential determined from gradiometric and satellite-to-satellite tracking data (Koch and Kusche, 2002), and optimal weighting of different groups of levelling data, GPS vertical velocities, and tide gauge data in the least-squares collocation modelling of the Fennoscandian uplift (Vestøl, 2006).

The vector of  $m$  heterogeneous and uncorrelated groups of observations is represented as  $\mathbf{l} = [\mathbf{l}_1^T \mathbf{l}_2^T \dots \mathbf{l}_m^T]^T$  with a vector of normally distributed errors,  $\mathbf{v} = [\mathbf{v}_1^T \mathbf{v}_2^T \dots \mathbf{v}_m^T]^T$ . In this thesis, the observations in each vector are assumed uncorrelated. Thus, the error covariance matrix,  $\mathbf{C}_v$ , has a block-diagonal structure as follows:

$$\mathbf{C}_v = \begin{bmatrix} \mathbf{C}_1 & \mathbf{0} & \dots & \mathbf{0} \\ \mathbf{0} & \mathbf{C}_2 & \dots & \mathbf{0} \\ \vdots & \vdots & \ddots & \vdots \\ \mathbf{0} & \mathbf{0} & \dots & \mathbf{C}_m \end{bmatrix} = \begin{bmatrix} \sigma_1^2 \mathbf{Q}_1 & \mathbf{0} & \dots & \mathbf{0} \\ \mathbf{0} & \sigma_2^2 \mathbf{Q}_2 & \dots & \mathbf{0} \\ \vdots & \vdots & \ddots & \vdots \\ \mathbf{0} & \mathbf{0} & \dots & \sigma_m^2 \mathbf{Q}_m \end{bmatrix} \quad (4.29)$$

with diagonal covariance matrices  $\mathbf{C}_i, i = 1, \dots, m$  and variance components  $\sigma_i^2, i = 1, \dots, m$ .

The variance components are collected in the vector  $\boldsymbol{\theta} = [\sigma_1^2, \sigma_2^2, \dots, \sigma_m^2]^T$ , which is estimated by solving the system (see, e.g., Crocetto *et al.*, 2000)

$$\mathbf{S}\hat{\boldsymbol{\theta}} = \mathbf{q}. \quad (4.30)$$

The matrix  $\mathbf{S}$  is defined as follows:

$$\mathbf{S} = [\text{tr}(\mathbf{V}\mathbf{Q}_i\mathbf{V}\mathbf{Q}_j)], \quad i, j = 1, \dots, m, \quad (4.31)$$

where  $\text{tr}(\cdot)$  is the trace operator, and  $\mathbf{Q}_i$  is a positive definite cofactor matrix for the  $i^{\text{th}}$  group of observations. Because  $\mathbf{S}$  may not be of full rank, it has a pseudo inverse  $\mathbf{S}^+$ .

The symmetric matrix  $\mathbf{V}$  is defined as follows:

$$\mathbf{V} = \mathbf{P}(\mathbf{I} - \mathbf{A}(\mathbf{A}^T \mathbf{P} \mathbf{A})^{-1} \mathbf{A}^T \mathbf{P}), \quad (4.32)$$

where  $\mathbf{A}$  is a coefficient matrix and  $\mathbf{P}$  is a block-diagonal matrix

$$\mathbf{P} = \begin{bmatrix} \mathbf{Q}_1^{-1} & \mathbf{0} & \cdots & \mathbf{0} \\ \mathbf{0} & \mathbf{Q}_2^{-1} & \cdots & \mathbf{0} \\ \vdots & \vdots & \ddots & \vdots \\ \mathbf{0} & \mathbf{0} & \cdots & \mathbf{Q}_m^{-1} \end{bmatrix} = \left( \sum_{i=1}^m \mathbf{Q}_i \right)^{-1}. \quad (4.33)$$

The vector  $\mathbf{q}$  contains the quadratic forms

$$\mathbf{q} = [\hat{\mathbf{v}}_i^T \mathbf{P} \mathbf{Q}_i \mathbf{P} \hat{\mathbf{v}}_i], i = 1, \dots, m, \quad (4.34)$$

where  $\hat{\mathbf{v}}_i, i = 1, \dots, m$  are estimated vectors of residuals.

The vector of the unknown variance components is estimated iteratively using the re-scaled cofactor matrices. For example, at the  $\tilde{r}^{th}$  iteration, the cofactor matrices are computed as

$$\mathbf{Q}_i^{(\tilde{r})} = \hat{\theta}_i^{(\tilde{r})} \dots \hat{\theta}_i^{(0)} \mathbf{Q}_i, i = 1, \dots, m, \quad (4.35)$$

and the updated  $\mathbf{P}$  matrix used in the next iteration is

$$\mathbf{P}^{(\tilde{r})} = \left( \sum_{i=1}^m \mathbf{Q}_i^{(\tilde{r})} \right)^{-1}. \quad (4.36)$$

The criterion for termination of the iterations is  $\hat{\boldsymbol{\theta}}^{(r)} \rightarrow [1, \dots, 1]^T$ . The estimated variance components are computed as follows:

$$\hat{\theta}_i = \prod_{\tilde{r}=1}^r \hat{\theta}_i^{(\tilde{r})}, i = 1, \dots, m. \quad (4.37)$$

## 4.2 Optimal combination of heterogeneous terrestrial data

The observation vector is defined as  $\mathbf{l} = [\dot{\mathbf{g}}^T \dot{\mathbf{h}}^T]^T$ , where  $\dot{\mathbf{g}} = [\dot{g}_1 \ \dot{g}_2 \ \dots \ \dot{g}_{n_1}]^T$  and

$\dot{\mathbf{h}} = [\dot{h}_1 \ \dot{h}_2 \ \dots \ \dot{h}_{n_2}]^T$  are the vectors of the rates of the terrestrial gravity (given at  $n_1$  point

locations) and the rates of the ellipsoidal height, i.e., the GPS vertical velocities, at  $n_2$  point locations. The data covariance matrix is the fully-populated matrix

$$\mathbf{C}_l = \begin{bmatrix} \mathbf{C}_{\dot{g}} + (\mathbf{C}_v)_{\dot{g}} & \mathbf{C}_{\dot{g}h} \\ \mathbf{C}_{\dot{h}g} & \mathbf{C}_{\dot{h}} + (\mathbf{C}_v)_{\dot{h}} \end{bmatrix}, \quad (4.38)$$

where  $\mathbf{C}_{\dot{g}}$  and  $\mathbf{C}_{\dot{h}}$  are the signal auto-covariance matrices of the rates of change of the terrestrial gravity and ellipsoidal height, respectively; the matrix  $\mathbf{C}_{\dot{g}h} = \mathbf{C}_{\dot{h}g}^T$  contains the signal cross-covariances; and  $(\mathbf{C}_v)_{\dot{g}}$  and  $(\mathbf{C}_v)_{\dot{h}}$  are the error covariance matrices. The vector of the predicted functionals at  $p$  point locations,  $\mathbf{s}_p = [\mathbf{g}_p^T \mathbf{H}_p^T \dot{\mathbf{N}}_p^T \mathbf{h}_p^T]^T$ , includes the rates of change of the terrestrial gravity,  $\mathbf{g}_p = [\dot{g}_1 \dot{g}_2 \dots \dot{g}_p]^T$ , orthometric height,  $\mathbf{H}_p = [\dot{H}_1 \dot{H}_2 \dots \dot{H}_p]^T$ , geoid height,  $\dot{\mathbf{N}}_p = [\dot{N}_1 \dot{N}_2 \dots \dot{N}_p]^T$ , and ellipsoidal height,  $\mathbf{h}_p = [\dot{h}_1 \dot{h}_2 \dots \dot{h}_p]^T$ .

The covariance matrix of the predicted functionals and signal components is defined as follows:

$$\mathbf{C}_{s_p s_{n_1+n_2}} = \begin{bmatrix} \mathbf{C}_{\dot{g}_p s_{n_1+n_2}} \\ \mathbf{C}_{\dot{H}_p s_{n_1+n_2}} \\ \mathbf{C}_{\dot{N}_p s_{n_1+n_2}} \\ \mathbf{C}_{\dot{h}_p s_{n_1+n_2}} \end{bmatrix}, \quad (4.39)$$

where

$$\mathbf{C}_{\dot{g}_p s_{n_1+n_2}} = \begin{bmatrix} \mathbf{C}_{\dot{g}_p \dot{g}_{n_1}} \\ \mathbf{C}_{\dot{g}_p \dot{h}_{n_2}} \end{bmatrix}, \quad \mathbf{C}_{\dot{H}_p s_{n_1+n_2}} = \begin{bmatrix} \mathbf{C}_{\dot{H}_p \dot{g}_{n_1}} \\ \mathbf{C}_{\dot{H}_p \dot{h}_{n_2}} \end{bmatrix}, \quad \mathbf{C}_{\dot{N}_p s_{n_1+n_2}} = \begin{bmatrix} \mathbf{C}_{\dot{N}_p \dot{g}_{n_1}} \\ \mathbf{C}_{\dot{N}_p \dot{h}_{n_2}} \end{bmatrix}, \quad \text{and} \quad \mathbf{C}_{\dot{h}_p s_{n_1+n_2}} = \begin{bmatrix} \mathbf{C}_{\dot{h}_p \dot{g}_{n_1}} \\ \mathbf{C}_{\dot{h}_p \dot{h}_{n_2}} \end{bmatrix}.$$

#### 4.2.1 Modelling the trend component

The trend of the surface is modelled using the inverse multiquadric base functions defined by Eq.(3.4). Because the inverse multiquadric is a strictly positive definite function, no polynomial term needs to be added in Eq.(4.1); see Section 3.3. To scale the base functions, a shape parameter of 0.1 of unit distance (the data are scaled to a unit cube) can be used a priori and subsequently improved in the least-squares collocation solution.

The coefficient matrix  $\mathbf{A}$  is structured as

$$\mathbf{A} = \begin{bmatrix} \mathbf{A}_{\dot{g}} \\ \mathbf{A}_{\dot{h}} \end{bmatrix}, \quad (4.40)$$

where

$$\mathbf{A}_{\dot{g}} = \frac{\dot{g}}{h} \mathbf{A}_h = \frac{\dot{g}}{h} [\Phi_{ij}], \quad i = 1, \dots, n_1, \quad j = 1, \dots, k \quad (4.41)$$

is the  $(n_1 \times k)$  coefficient matrix of the rates of change of the terrestrial gravity and

$$\mathbf{A}_{\dot{h}} = [\Phi_{ij}], \quad i = 1, \dots, n_2, \quad j = 1, \dots, k \quad (4.42)$$

is the  $(n_2 \times k)$  coefficient matrix of the rates of change of the ellipsoidal height. The base functions  $\Phi_{ij}$  are computed by means of Eq.(3.4). The coefficient matrix for the rates of change of the orthometric height,  $\mathbf{A}_{\dot{H}}$ , can be obtained from  $\mathbf{A}_{\dot{g}}$  and  $\mathbf{A}_{\dot{h}}$  as follows:

$$\mathbf{A}_{\dot{H}} = \frac{\dot{H}}{\dot{g}} \mathbf{A}_{\dot{g}} = \frac{\dot{H} / \dot{g}}{h / \dot{g}} \mathbf{A}_h. \quad (4.43)$$

When the rate of change of the geoid height is predicted, the coefficient matrix is computed by means of Eq.(3.27).

#### 4.2.2 Modelling the signal component

If the displacement of the fundamental benchmark in Eq.(2.37) is assumed zero, the rate of change of the potential is computed as (see Eq.(2.38)):

$$\dot{W} = St(\dot{g} + \frac{2g_a}{R}\dot{H}), \quad St(\cdot) = \frac{R}{4\pi} \iint_{\sigma} (\cdot) S(\psi) d\sigma. \quad (4.44)$$

$\dot{W}$  is a sum of two components as follows:

$$\dot{W} = \dot{W}_1 + \dot{W}_2 = St(\dot{g}) + \frac{2g_a}{R} St(\dot{H}). \quad (4.45)$$

$\dot{g}$  and  $\dot{H}$  are linear functionals of the rate of change of the geopotential. With the inverse Stokes operator  $St^{-1}(\cdot) = -\frac{\partial(\cdot)}{\partial r} - \frac{2(\cdot)}{R}$ , they are represented as (Heck, 1984)

$$\dot{g} = St^{-1}(\dot{W}_1) = L_1 \dot{W}_1 \quad (4.46)$$

and

$$\dot{H} = \frac{R}{2g_a} St^{-1}(\dot{W}_2) = L_2 \dot{W}_2. \quad (4.47)$$

The covariances between the rates of the two components of the potential,  $\dot{W}_i, i=1,2$ , at points P and Q on the sphere with a radius  $R$  are defined as

$$C_{ij}(P,Q) = C_{ij}(\dot{W}(P), \dot{W}(Q)) = \text{cov}\{\dot{W}_i(P), \dot{W}_j(Q)\}, \quad i, j = 1, 2 \quad (4.48)$$

and are propagated as follows (Moritz, 1980):

$$\text{cov}\{L_i^P \dot{W}_i(P), L_j^Q \dot{W}_j(Q)\} = L_i^P L_j^Q \text{cov}\{\dot{W}_i(P), \dot{W}_j(Q)\} = L_i^P L_j^Q C_{ij}(P,Q), \quad i, j = 1, 2. \quad (4.49)$$

In gravity field approximation, various local covariance function models exist that are homogeneous, isotropic, and symmetric (with respect to the points P and Q) analytical functions (see, e.g., Jordan 1972; Moritz, 1980 and Meier, 1981). However, only functions that allow a harmonic expansion of the potential in the outer space can be used to approximate the covariance function of the components of the potential and its functionals as well as their temporal variations. According to Reilly (1979), such a function is the Gaussian model

$$C(P,Q) = C^1 = \frac{D\tau^2}{2} e^{-\rho^2/2\tau^2}, \quad (4.50)$$

where  $\rho$  denotes the planar distance between the points P and Q,  $D\tau^2/2$  stands for the variance, and  $\tau$  is a parameter related to the correlation length of the Gaussian model. For points not on a plane, the model in Eq. (4.50) is generalized to (*ibid.*)

$$C(P,Q) = C^1 = \frac{D\tau^4}{2} \int_{\phi=0}^{\infty} \phi e^{-\phi(z_p+z_q)} e^{-\phi^2\rho^2/2} J_o(\phi\rho) d\phi, \quad (4.51)$$

from which the covariance function of the vertical derivative of the rate of change of the potential is found as follows:

$$C\left(\frac{\partial\dot{W}}{\partial z}, \frac{\partial\dot{W}}{\partial z}\right) = \frac{\partial}{\partial z_p} \frac{\partial}{\partial z_q} C(\dot{W}, \dot{W}) = \frac{D\tau^4}{2} \int_{\phi=0}^{\infty} \phi^3 e^{-\phi(z_p+z_q)} e^{-\phi^2\rho^2/2} J_o(\phi\rho) d\phi. \quad (4.52)$$

In Eqs. (4.51) and (4.52),  $J_o(\phi\rho)$  is the zero order Bessel function (e.g., Korn and Korn, 1968). If  $z_p = z_q = 0$ , Eq. (4.52) reduces to

$$C\left(\frac{\partial\dot{W}}{\partial z}, \frac{\partial\dot{W}}{\partial z}\right) = C^3 = D \left(1 - \frac{\rho^2}{2\tau^2}\right) e^{-\rho^2/2\tau^2}. \quad (4.53)$$

The covariance function  $C(\partial\dot{W}/\partial z, \dot{W})$  is computed by

$$C\left(\frac{\partial\dot{W}}{\partial z}, \dot{W}\right) = -C^2 = D \frac{\tau}{2} \sqrt{\frac{\pi}{2}} e^{-\rho^2/2\tau^2} {}_1F_1\left(-\frac{1}{2}, 1; \frac{\rho^2}{2\tau^2}\right), \quad (4.54)$$

where  ${}_1F_1(-1/2, 1; \rho^2/2\tau^2)$  is the confluent hypergeometric function of the first kind (Abad and Sesma, 1995).

Using Eqs. (4.50), (4.53), and (4.54), the auto- and cross-covariance matrices of the rates of the terrestrial gravity, geoid, orthometric, and ellipsoidal heights are computed as shown by Heck (1984). The derivations are given in Appendix A, and the final expressions for the covariance functions are presented in the following.

$$\text{cov}(\dot{N}(P), \dot{N}(Q)) = \frac{1}{g_a^2} (C_{11}^1 + C_{12}^1 + C_{21}^1 + C_{22}^1) \quad (4.55)$$

$$\text{cov}(\dot{g}(P), \dot{g}(Q)) = C_{11}^3 - \frac{4}{R} C_{11}^2 + \frac{4}{R^2} C_{11}^1 \quad (4.56)$$

$$\text{cov}(\dot{H}(P), \dot{H}(Q)) = \frac{R^2}{4g_a^2} C_{22}^3 - \frac{R}{g_a^2} C_{22}^2 + \frac{1}{g_a^2} C_{22}^1 \quad (4.57)$$

$$\text{cov}(\dot{h}(P), \dot{h}(Q)) = \frac{1}{g_a^2} \frac{R^2}{4} C_{22}^3 + \frac{1}{g_a^2} \frac{R}{2} (C_{12}^2 + C_{21}^2) + \frac{1}{g_a^2} C_{11}^1 \quad (4.58)$$

$$\text{cov}(\dot{N}(P), \dot{g}(Q)) = \text{cov}(\dot{g}(P), \dot{N}(Q)) = \frac{1}{g_a} (C_{11}^2 + C_{21}^2) - \frac{2}{g_a R} (C_{11}^1 + C_{21}^1) \quad (4.59)$$

$$\text{cov}(\dot{N}(P), \dot{H}(Q)) = \text{cov}(\dot{H}(P), \dot{N}(Q)) = \frac{R}{2g_a^2} (C_{12}^2 + C_{22}^2) - \frac{1}{g_a^2} (C_{12}^1 + C_{22}^1) \quad (4.60)$$

$$\text{cov}(\dot{g}(P), \dot{H}(Q)) = \text{cov}(\dot{H}(P), \dot{g}(Q)) = \frac{R}{2g_a} C_{12}^3 - \frac{2}{g_a} C_{12}^2 + \frac{2}{g_a R} C_{12}^1 \quad (4.61)$$

$$\text{cov}(\dot{g}(P), \dot{h}(Q)) = \text{cov}(\dot{h}(P), \dot{g}(Q)) = \frac{1}{g_a} (C_{11}^2 - C_{12}^2 - \frac{2}{R} C_{11}^1 + \frac{R}{2} C_{12}^3) \quad (4.62)$$

$$\text{cov}(\dot{N}(P), \dot{h}(Q)) = \text{cov}(\dot{h}(P), \dot{N}(Q)) = \frac{1}{g_a^2} (C_{11}^1 + C_{12}^1 + \frac{R}{2} C_{12}^2 + \frac{R}{2} C_{22}^2) \quad (4.63)$$

$$\text{cov}(\dot{H}(P), \dot{h}(Q)) = \text{cov}(\dot{h}(P), \dot{H}(Q)) = \frac{1}{g_a^2} (\frac{R^2}{4} C_{22}^3 + \frac{R}{2} C_{21}^2 - \frac{R}{2} C_{22}^2 - C_{21}^1) \quad (4.64)$$

### 4.2.3 Description of the computational algorithm

The computational algorithm, outlined by Rangelova *et al.* (2006a), is presented schematically by the flowchart in Figure 4.1. The input consists of rates of the terrestrial gravity and ellipsoidal height and the gravity-to-height ratio estimated from these data. The modified Gram-Schmidt algorithm is applied to determine the optimal number and locations of the base functions. To compute the signal auto- and cross-covariance matrices, first, the parameters of the Gaussian model,  $D_{ij}$  and  $\tau_{ij}$ ,  $i, j = 1, 2$ , are estimated by a least-squares fit to the empirical covariances of the rates of change of the potential components defined by Eq. (4.45).

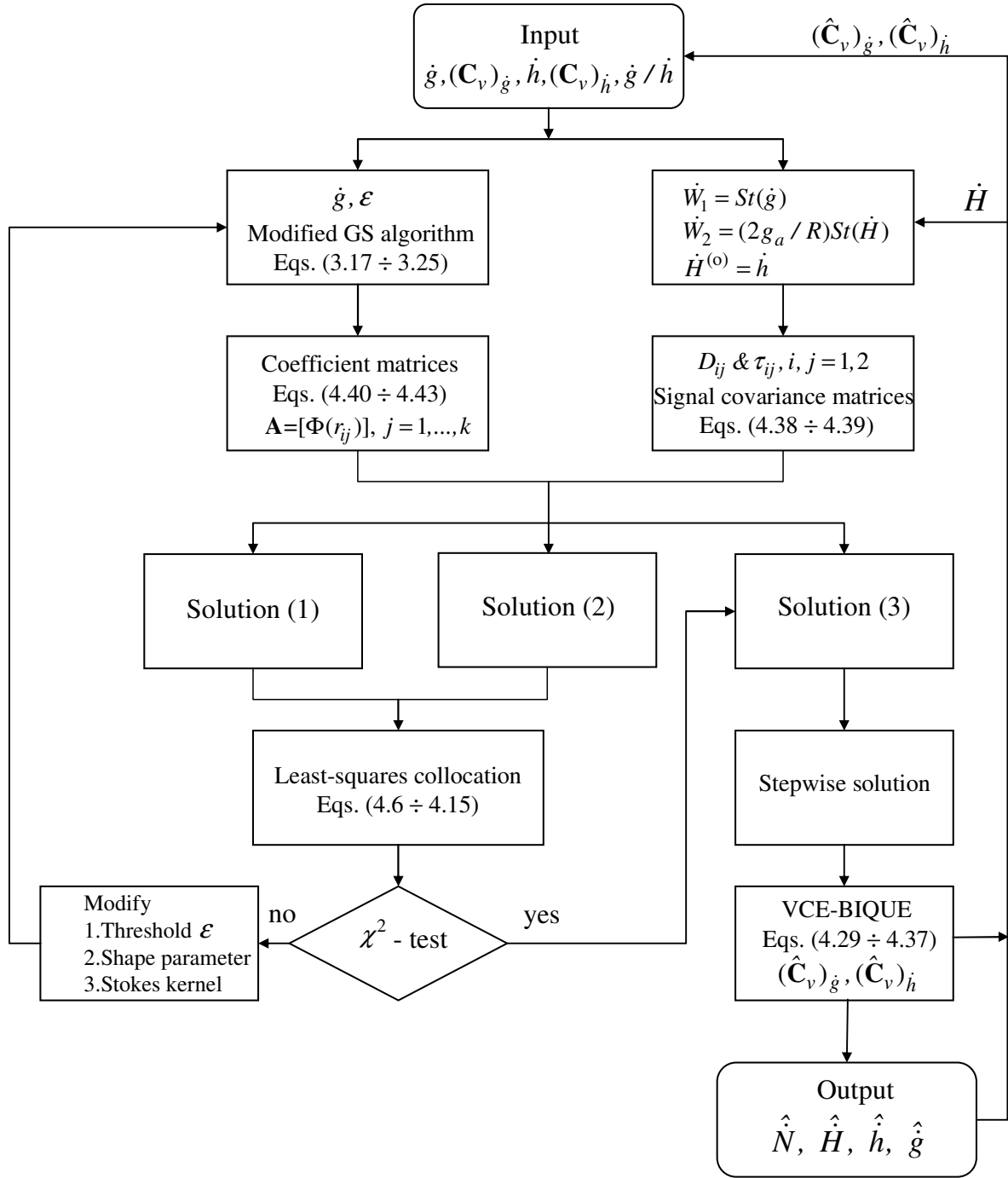


**Figure 4.1:** Flowchart of the computational procedure.

For this purpose, the rates of the terrestrial gravity and the GPS velocities are integrated using a spheroidal Stokes kernel of degree  $L$  (see, e.g., Vaníček and Featherstone, 1998)

$$S^L(\psi) = S(\psi) - \sum_{l=2}^L \frac{2l+1}{l-1} P_l(\cos \psi) = \sum_{l=L+1}^{\infty} \frac{2l+1}{l-1} P_l(\cos \psi), \quad (4.65)$$

where  $P_l(\cos \psi)$  are the Legendre polynomials. The first  $L$  spherical harmonic degrees, assumed to represent the spectrum of the postglacial rebound signal, are filtered out. The degrees higher than  $L$  are assumed to represent isotropic geopotential changes  $\dot{W}_1$  and  $\dot{W}_2$  with covariance functions computed by the Gaussian model in Eq.(4.50).  $\dot{W}_1$  and  $\dot{W}_2$  can contain a residual postglacial rebound signal, a local tectonic signal, and local gravity field changes with an anthropogenic origin.

The computational algorithm is iterative with the number of iterations being two. The Stokes integral should be evaluated with the rates of the orthometric height, which are substituted with the GPS velocities at the first iteration. This is allowed because the rate of change of the orthometric height comprises approximately 90% of the rate of change of the ellipsoidal height. In the second iteration, the Stokes integral is evaluated using the predicted rates of the orthometric height and the computational algorithm is repeated.

In principle, three different least-squares collocation solutions can be obtained using the following data:

1. terrestrial gravity rates and gravity-to-height ratio,
2. GPS velocities and gravity-to-height ratio, and
3. terrestrial gravity rates and GPS velocities.

The first two options allow one type of data to be used with a gravity-to-height ratio computed from geophysical models or estimated from previous studies in the region or a different region with similar geodynamics. The flowchart in Figure 4.1 includes three solutions that compare to the three listed options as follows. **Solution (1)** is a realization of option (1) with the gravity-to-height ratio estimated from the terrestrial gravity rates and GPS vertical velocities. The  $\dot{g}/\dot{h}$  value is used to compute both the trend surface and the

signal covariance matrices. As shown in Section 2.4.7, the estimated  $\dot{g}/\dot{h}$  is close to the theoretical value for postglacial rebound and to the empirical values obtained in the recent studies for North America. Thus, the predicted rates of change of the geoid and orthometric heights will be interpreted entirely in terms of postglacial rebound. **Solution (2)** is a modification of options (1) and (3). The trend surface is computed using the terrestrial gravity rates and the  $\dot{g}/\dot{h}$  value, but the signal covariance matrices in Eqs. (4.55)–(4.64) are computed with both terrestrial gravity and GPS data. This allows one to alleviate the stringent assumption related to postglacial rebound in Solution (1), and to account for the existence of local processes. **Solution (3)** is a realization of option (3) in a stepwise manner (Moritz, 1980, pp. 144 ÷ 156). In fact, the trend component estimated in Solution (2) is improved by adding the GPS vertical velocities. The signal covariance matrices are again computed with both types of data.

Different models can be obtained by varying the threshold value  $\varepsilon$  in the modified Gram-Schmidt algorithm, the shape parameter of the inverse multiquadric base functions, and the degree  $L$  of the spheroidal kernel. This is a nonlinear problem which is solved by fixing the shape parameter and varying the threshold value and the degree  $L$ . The scale of the multiquadric base functions has been resolved in Chapter 2. The degree of the spheroidal kernel is varied between degrees 10 and 20, which account for 92% and 98% of the total power of the GIA geoid rate signal. The mathematical models in Solutions (1) and (2) are tested by the congruency test described in Section 4.1.2. If the null hypothesis is accepted, the threshold value and the degree of the spheroidal kernel are used to obtain Solution (3). The failure of the congruency test is an indication for an inadequate model, which can be improved by changing either one of the above parameters. Although the procedure allows for changing the scale of the inverse multiquadrics, the a priori value of 0.1 in unit distance remains constant throughout all computations.

If two types of data (terrestrial gravity rates and GPS velocities) are combined as in Solution (3), the scale factors of the error covariance matrices are determined by variance component estimation described in Section 4.1.2. The rescaled covariance matrices are used in the second iteration of the computational procedure as shown in Figure 4.1. It should be

noted that the signal auto- and cross-covariance matrices in all three solutions are assumed to be properly scaled. According to Dermanis and Rossikopoulos (1991), the scale of the signal covariance matrices should be determined together with the scale of the error covariance matrices in a variance component estimation procedure. The estimated vector of variance components can also include the parameters  $D_{ij}$  and  $\tau_{ij}$ ,  $i, j = 1, 2$  of the Gaussian covariance kernels. This rigorous statistical procedure can be applied if a four-dimensional (three spatial coordinates and time) integrated network is realized. However, if the signal component in Eq. (4.1) represents mass redistribution accompanying the vertical crustal displacement, the variance component estimation can be applied only to models that treat the gravity signals as deterministic parameters (*ibid.*, 1991).

#### 4.2.4 Validation of predicted rates

Hypothesis testing in stepwise least-squares collocation can be used to validate the predicted rates of change using independent data. According to Wei (1987), the observation vector  $\mathbf{I}^t$  can be considered as a general linear hypothesis

$$\begin{aligned} H_o : \mathbf{I}^t &= \mathbf{A}^t \mathbf{x} + \mathbf{s}^t + \mathbf{v}^t \\ H_a : \mathbf{I}^t &\neq \mathbf{A}^t \mathbf{x} + \mathbf{s}^t + \mathbf{v}^t \end{aligned} \quad (4.66)$$

by means of which the compatibility of the predicted signal  $\mathbf{s}^t$  with the observation vector  $\mathbf{I}^t$  can be tested. The test statistic is defined as

$$\tilde{F} = \frac{\Omega^t / f^t}{\Omega / f} \sim F(f^t, f), \quad (4.67)$$

where the quadratic form  $\Omega^t$  is computed with the error covariance matrix

$$\mathbf{C}_1^t = \mathbf{A}^t \mathbf{C}_{\hat{\mathbf{x}}} (\mathbf{A}^t)^T + \mathbf{A}^t \mathbf{C}_{\hat{\mathbf{x}}\hat{\mathbf{s}}^t} + (\mathbf{A}^t \mathbf{C}_{\hat{\mathbf{x}}\hat{\mathbf{s}}^t})^T + \mathbf{C}_{\hat{\mathbf{s}}^t} + \mathbf{C}_{\mathbf{v}^t} \quad (4.68)$$

of the estimates  $\hat{\mathbf{I}}^t$  as follows:

$$\Omega^t = (\mathbf{I}^t - \hat{\mathbf{I}}^t)^T \mathbf{C}_1^t (\mathbf{I}^t - \hat{\mathbf{I}}^t). \quad (4.69)$$

The quadratic form  $\Omega$  has been defined in Eqs. (4.18) and (4.19). The null hypothesis is accepted if  $\tilde{F} < F_\alpha(f^t, f)$ , where  $f^t$  is the number of observations  $\mathbf{I}^t$ . When a single observation is tested, the test statistic defined by Eq. (4.67) reduces to

$$\tilde{t} = \frac{(l_i^t - \hat{l}_i^t) / \sqrt{N_{ii}^t}}{\sqrt{\Omega / f}} \sim t_\alpha(f). \quad (4.70)$$

The null hypothesis is accepted if  $\tilde{t} < t_\alpha(f)$ .

### 4.3 Models of the rates of change of the terrestrial gravity, geoid, and heights

This section presents the estimated rates of the terrestrial gravity and height components using the data from the two basic networks in Canada; that is, the Canadian Gravity Standardization Network (CGSN) and the Canadian Base Network (CBN) both described in Chapter 2. CGSN and CBN have different network topologies, number of sites, and time spans of the measurements. Nevertheless, the rates from the two networks are in general agreement and also agree with postglacial rebound model predictions (see Pagiatakis and Salib, 2003; Henton *et al.*, 2006).

#### 4.3.1 Description of the terrestrial gravity and GPS velocity data

The CGSN and CBN data are interpolated by means of the inverse multiquadric base functions with a shape parameter of 0.1 of unit distance (Figures 4.2 a and b). Despite the very weak constraints on the vertical displacement surface provided by the CBN data in the northern areas, the smooth interpolation ensured by the inverse multiquadrics leads to some similarities in the patterns in Figures 4.2 a and b.

The largest uplift for both data sets is observed on the east coast of Hudson Bay. The estimated terrestrial gravity rate of  $-2.35 \mu\text{Gal/yr}$  corresponds to an uplift of  $13.1 \text{ mm/yr}$  when a gravity-to-height ratio of  $-0.18 \mu\text{Gal/mm}$  is used. GPS observes an uplift of  $12.5 \text{ mm/yr}$  that transforms into a negative rate of terrestrial gravity of  $-2.25 \mu\text{Gal/yr}$ . Although the terrestrial gravity decreases at a higher rate compared to that observed by the GPS

measurements, the data agree generally well with the postglacial model predictions based on the ICE-3G and ICE-4G models (see Pagiatakis and Salib, 2003; Henton *et al.*, 2006). The lack of observations west of Hudson Bay does not allow for constraining the model predictions and the Keewatin dome of ice present in the ICE-5G model. The terrestrial gravity decrease and the crustal uplift in the Yellowknife area, believed to account for the Keewatin signal, do not agree well. Larger vertical displacement rates than that observed by GPS are required to match the observed decrease in the terrestrial gravity. An important difference between the gravity and GPS data is the line of zero motion, which for the gravity sites follows the large Canadian lakes west and northwest of the Hudson Bay region but for the GPS stations lies south to the lakes. In eastern Canada, the GPS hinge line is also south of the gravity hinge line. The Great Lakes region is not included in the modelling because the gravity sites do not sample that region.

Characteristic for the gravity rates is the subsidence corridor starting west of the Great Lakes area, continuing northwest of Hudson Bay and to the north including the Mackenzie River Delta. In the latter, subsidence from natural gas extraction is superimposed on the postglacial rebound signal, but geodetic measurements are taken under the conditions of active permafrost. This area is not sampled by the CBN stations. Another difference between the rates of the terrestrial gravity and GPS velocities is the strong decrease in the terrestrial gravity in the western prairies, whose origin is unclear (Pagiatakis and Salib, 2003). One possible reason could be the mass decrease following the extraction of oil in this area. However, rapid subsidence which usually accompanies fluid extraction (see Section 2.4.7) is not confirmed by the very small (close to zero) GPS velocities. Both terrestrial gravity and GPS data account for crustal uplift in the northern Cascadia subduction zone.

Table 4.1 summarizes the standard deviations of the gravity and GPS data obtained from the error covariance matrices of the least-squares adjustment of CGSN and CBN. The mean standard deviation of the gravity rates, i.e.,  $0.43 \mu\text{Gal/yr}$ , corresponds to the mean standard deviation of the GPS velocities, i.e.,  $2.4 \text{ mm/yr}$ , computed with  $\dot{g}/\dot{h} = -0.18 \mu\text{Gal/mm}$ . This accounts for equivalent average accuracy of both data sets.

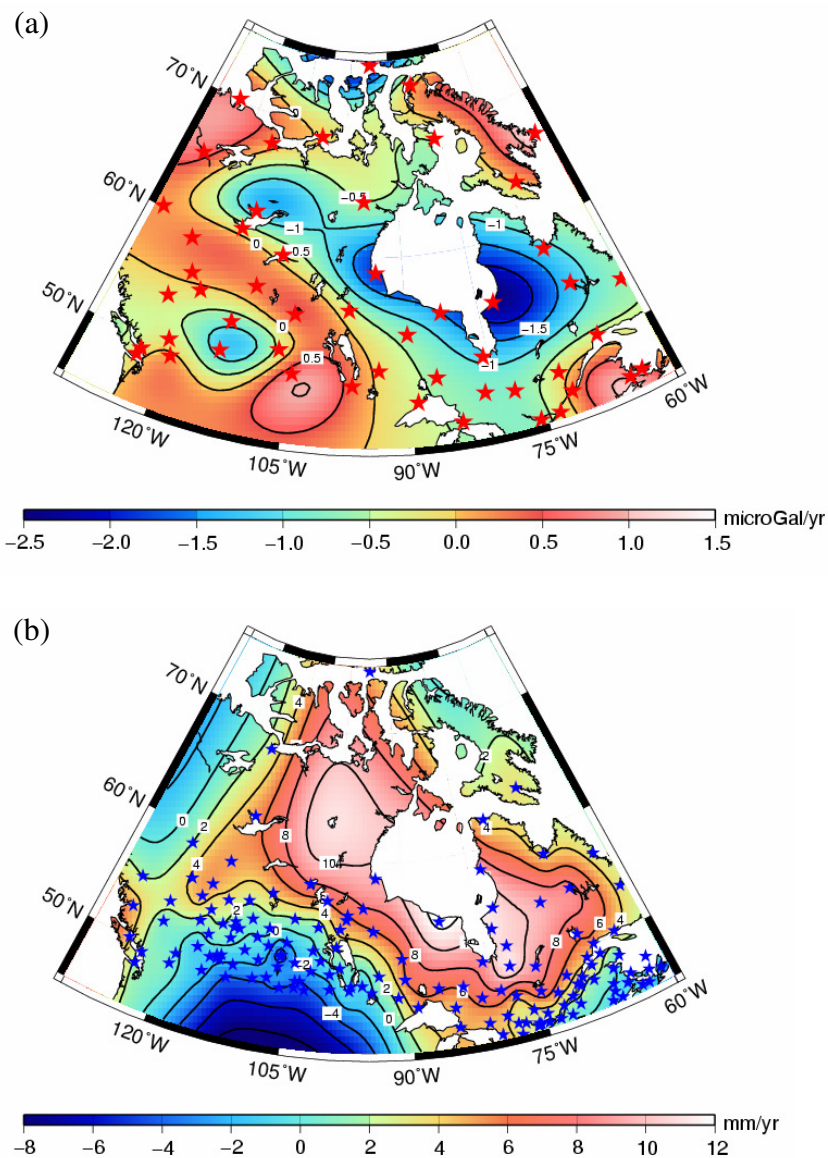


**Figure 4.2:** (a) Rates of the terrestrial gravity (the CGSN sites are plotted in red) and (b) GPS velocities (the CBN stations are plotted in blue).

**Table 4.1:** Standard deviations of the terrestrial gravity rates and GPS velocities

Observations	Min	Max	Mean
$\sigma_{\dot{g}}$ , $\mu\text{Gal/yr}$	0.06	0.90	0.43
$\sigma_{\dot{h}}$ , $\text{mm/yr}$	0.1	5.0	2.4

### 4.3.2 Signal auto- and cross- covariance functions

Table 4.2 contains the parameters of the covariance functions of  $\dot{W}_i, i=1,2$  obtained by integration with a spheroidal kernel of degree  $L = 15$ . For the purpose of computing the empirical covariances, the integrated GPS velocities are interpolated at the gravity sites. As seen from Table 4.2, the rates of the ellipsoidal height lead to a larger variance  $D_{22}\tau_{22}^2/2$  and correlation length  $\xi_{22}$  of the covariance kernel  $C_{22}(P,Q)$  compared to  $C_{11}(P,Q)$ , which accounts for the gravity data only. The larger correlation length suggests that GPS data may sample crustal deformation processes with larger spatial wavelengths than the gravity data.

In general, the signal auto- and cross-covariance functions given by Eqs. (4.55)–(4.64) consist of terms that account for the effect of the vertical crustal displacement and the mass redistribution. The contribution of the different terms is illustrated by means of the cross-covariance function of the rates of the ellipsoidal and orthometric heights defined by Eq. (4.64) and plotted in Figure 4.3. The cross-covariance function is dominated by the term  $R^2C_{22}^3/(4g_a^2)$ , where  $C_{22}^3$  is the covariance function of the vertical derivative of  $\dot{W}_2$  defined by Eq. (4.53). Consequently, the main contribution comes from the vertical displacement of the crust. This is counteracted by the terms  $-RC_{22}^2/g_a^2$ ,  $R[C_{12}^2 + C_{21}^2]/(2g_a^2)$ , and  $C_{11}^1/g_a^2$ . The last term accounts for the small contribution of the mass redistribution, i.e., the contribution of the change in the geoid height.

Figure 4.4 shows all of the covariance functions used in the combined procedure.

**Table 4.2:** Parameters of the covariance kernels defined by Eq. (4.50)

$C_{ij}(P,Q), i,j=1,2$	$D_{ij}, \mu\text{Gal}^2/\text{yr}^2$	$\tau_{ij} \times 10^2, \text{km}$	$D_{ij}\tau_{ij}^2/2, \mu\text{Gal}^2\text{mm}^2/\text{yr}^2$	$\xi_{ij}, \text{km}$
$C_{11}(P,Q)$	0.2069	4.072	1.715	232.3
$C_{12}(P,Q)$	-0.1174	5.144	-1.553	408.4
$C_{21}(P,Q)$	-0.1174	5.144	-1.553	408.4
$C_{22}(P,Q)$	0.3032	4.774	3.455	379.1

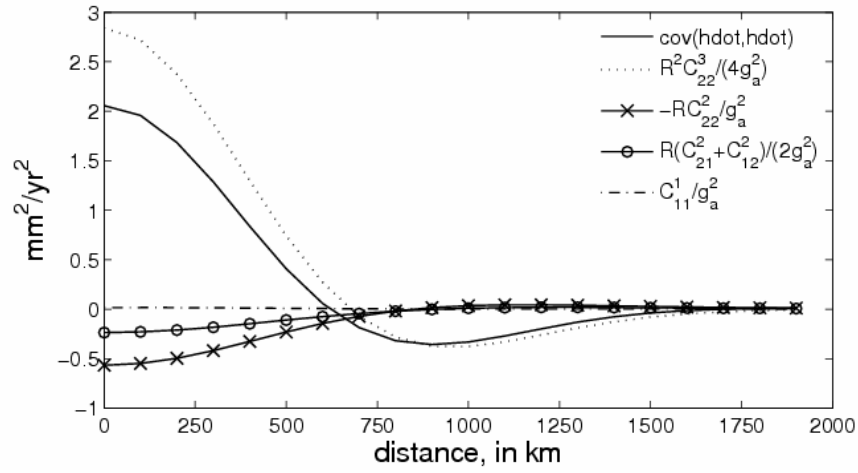


Figure 4.3: Signal cross-covariance function of  $\dot{h}$  and  $\dot{H}$ .

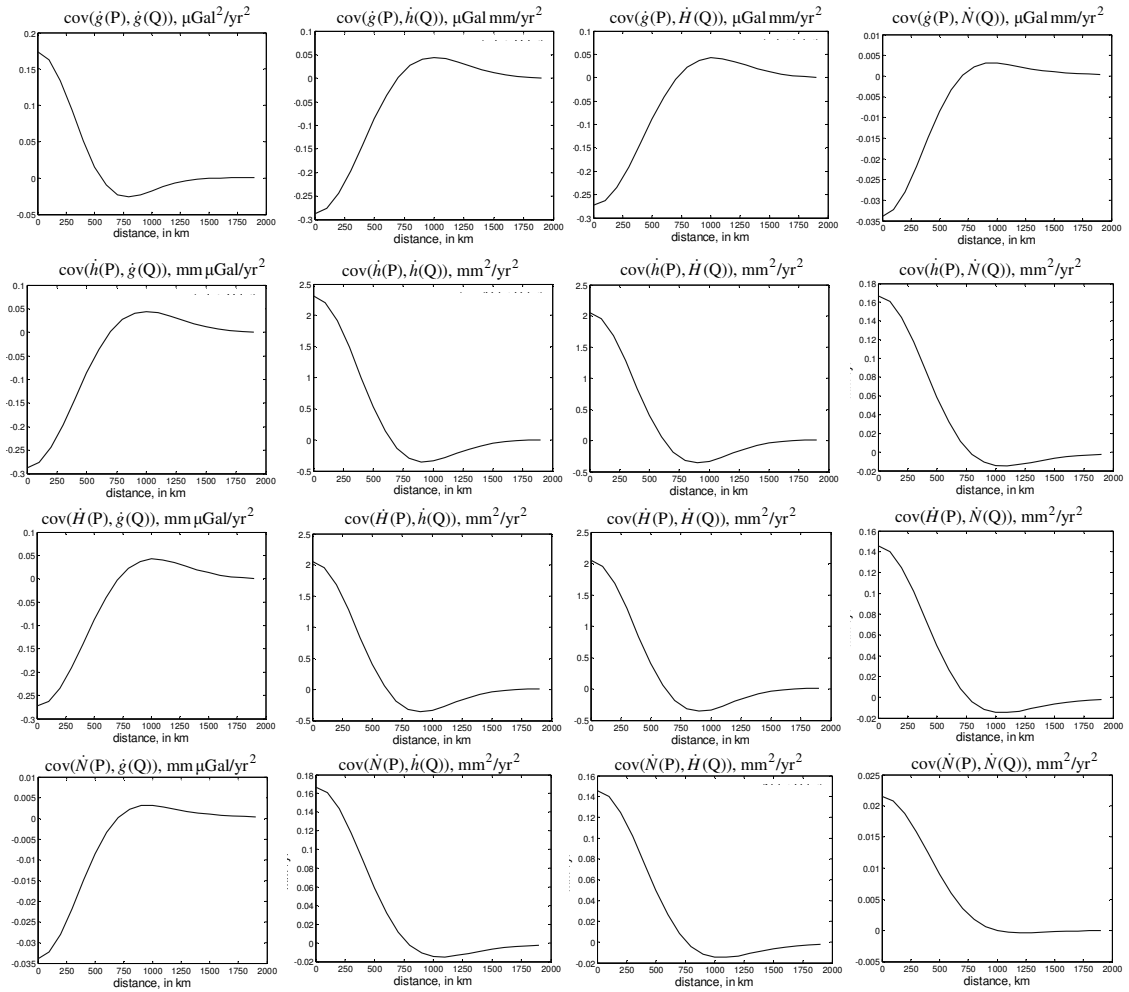


Figure 4.4: Signal auto- and cross-covariance functions.

### 4.3.3 A priori threshold value for selecting optimal locations of base functions

An a priori value of the threshold for the modified Gram-Schmidt algorithm, which is applied to determine the number and locations of the base function for modelling the trend component of the predicted rates, is required. To determine this a priori threshold, a test gravity network including fourteen sites from CGSN is constructed using the original gravity ties to simulate the measured gravity differences between the sites. The measurements are simulated for 25 epochs from 1980 to 2004.

The observation equation for a gravity difference reads:

$$\Delta g_{ij} = -(g_i^0 - \dot{g}_i(t_{ij} - t_0)) + (g_j^0 - \dot{g}_j(t_{ij} - t_0)) + v_{ij}, \quad (4.71)$$

where the absolute gravity value  $g^0$  and the rate  $\dot{g}$  at the gravity sites  $i$  and  $j$  are unknown parameters,  $t_{ij}$  is the epoch of the measured gravity difference between the sites  $i$  and  $j$ , and  $t_0$  is the reference epoch of 2000.0;  $v_{ij}$  comprises Gaussian noise. The drift and scale factors of the instruments are assumed to be known.

The gravity rates over Canada result from a superposition of many factors. In general, the signal from postglacial rebound can be superimposed by a local signal of a tectonic or anthropogenic origin. Thus, the smooth postglacial rebound pattern can be corrupted by local vertical crustal displacements. The simulated sparse gravimetric network cannot provide sufficient spatial sampling of the local processes, but the characteristic wavelengths of the postglacial rebound signal can be modelled.

It is assumed that a vector of the rates of the terrestrial gravity is represented by the sum

$$\dot{\mathbf{g}} = \dot{\mathbf{g}}^{\text{PGR}} + \dot{\mathbf{g}}^{\text{local}}, \quad (4.72)$$

where  $\dot{\mathbf{g}}^{\text{local}}$  is a vector of independent variables uniformly distributed

$$f_{G_1 \dots G_n}(\dot{g}_1^{\text{local}}, \dots, \dot{g}_n^{\text{local}}) = \begin{cases} \frac{1}{\prod_i^n (b_i - a_i)}, & (\dot{g}_1^{\text{local}}, \dots, \dot{g}_n^{\text{local}}) \in D \\ 0, & \text{otherwise} \end{cases}, \quad (4.73)$$

where  $D = \{(\dot{g}_1^{\text{local}}, \dots, \dot{g}_n^{\text{local}}) : a_i \leq \dot{g}_i^{\text{local}} \leq b_i, i = 1, \dots, n\}$ . The vector  $\dot{\mathbf{g}}^{\text{local}}$  could represent the effect of a variety of factors, such as tectonic coseismic displacements, anthropogenic subsidence due to gas and oil extraction, erosion, and subsidence due to melting of the permafrost. The temporal behaviour of the instabilities of the gravity sites can be modelled by a random-walk process in which the instabilities are allowed to increase with time but are assumed uncorrelated in space (e.g., Odijk, 2005). In this simulation, the gravity sites are assumed stable.

The unknown absolute gravity values and their rates are estimated by means of least-squares adjustment with a minimal constraint of the absolute gravity and its rate at the Churchill site. A set of five postglacial rebound models, selected among the models described in Section 2.2, are used to obtain the vector  $\dot{\mathbf{g}}^{\text{PGR}}$ . The vector  $\dot{\mathbf{g}}^{\text{local}}$  is computed using a Monte Carlo simulation of  $10^8$  runs with uniformly distributed random velocities with  $a = -0.5 \mu\text{Gal}$  and  $b = 0.5 \mu\text{Gal}$  and Gaussian noise with  $\sigma_v^2 = 10 \mu\text{Gal}$ . The average of the data variance of the adjusted rates from all runs is used to compute the ratio of the data variances in Table 4.3. The postglacial rebound models could explain from 70 to 86 percent of the data variance of the simulated and adjusted gravity rates. Further investigation of the effect of the threshold value on the modelled trend surface is given in the following section.

**Table 4.3:** Variance ratio computed for the PGR models by the Monte Carlo simulation

Variance ratio	Model 1	Model 2	Model 3	Model 4	Model 5
$\text{Var}(\dot{g}^{\text{PGR}}) / \text{Var}(\dot{g})$	0.70	0.80	0.83	0.85	0.86

#### 4.3.4 Effect of the threshold value on the trend surface

In the following, the effect of the varying threshold value (or the number of base functions) on the trend component of the modelled surfaces is studied. In Chapter 3, the threshold value has been used to filter out stationary noise from a simulated vertical displacement surface. It has been shown that a threshold value of 0.1 of unit distance ensures the accurate

approximation of the displacement surface. Based on the simulations in the previous section, it could be expected that the threshold values can be varied from 0.15 (for  $\text{Var}(\dot{g}^{\text{PGR}})/\text{Var}(\dot{g}) = 0.85$ ) to 0.3 (for  $\text{Var}(\dot{g}^{\text{PGR}})/\text{Var}(\dot{g}) = 0.70$ ). Therefore, it is instructive to provide an assessment of the quality of the approximated velocity surface for these threshold values. This analysis also facilitates understanding of the interaction between the trend, signal and noise components in the model of least-squares collocation with parameters defined by Eq.(4.1). For this purpose, two criteria will be employed: namely, the adjusted coefficient of determination (see, e.g., Fotopoulos, 2003) and the condition number of the normal matrix. The latter indicates instabilities in the model. The former indicates the goodness-of-fit of the model and has the form

$$R_{\alpha}^2 = 1 - \frac{\left[ \sum_{i=1}^n (\hat{v}'_i)^2 / (n-k) \right]}{\left[ \sum_{i=1}^n (l_i - \bar{l})^2 / (n-1) \right]}, \quad (4.74)$$

where  $\hat{v}'$  is obtained by means of

$$\hat{v}' = \hat{v} + \hat{s} = \mathbf{I} - \mathbf{A}\hat{\mathbf{x}}. \quad (4.75)$$

Theoretically, the adjusted coefficient of determination takes on values between zero and one, i.e.,  $0 \leq R_{\alpha}^2 \leq 1$ , thus indicating a poor or excellent fit as the value of  $R_{\alpha}^2$  approaches the two limits.

The adjusted coefficient of determination and the condition number are plotted in Figures 4.5a and b against the threshold value and for different degrees of the spheroidal kernel. For the extremely large threshold values of 0.35 and 0.4, the trend component of the velocity surface will be under-fitted. This is indicated by the smaller values of the adjusted coefficient of determination observed in Figure 4.5a. In the case of a larger signal variance obtained by integration with a ten-degree spheroidal kernel (see Section 4.2.3), the estimated signal component accounts entirely for the residual velocities, thus leaving small residuals estimated by Eq.(4.9). For a twenty-degree spheroidal kernel, small signals and large biased residuals are estimated when using large threshold values. A negative adjusted coefficient of determination is observed in Figure 4.5a, which could be due to the under-fitting of the surface. In the other extreme case, i.e., small threshold values, the trend

velocity surface is over-fitted which is indicated by the large condition number of the normal matrix in Figure 4.5b. As in the first case, it is observed that the variance of the estimated residuals increases with the decrease of the variance of the estimated signal component. The coefficient of determination improves, but also effects of numerical instabilities in the predicted rates are observed. For the fifteen-degree kernel, the adjusted coefficient of determination increases steadily over the analyzed range of threshold values. For thresholds smaller than 0.25, i.e., a variance ratio larger than 0.75, the model with a fifteen-degree kernel outperforms the models for the other two cases.

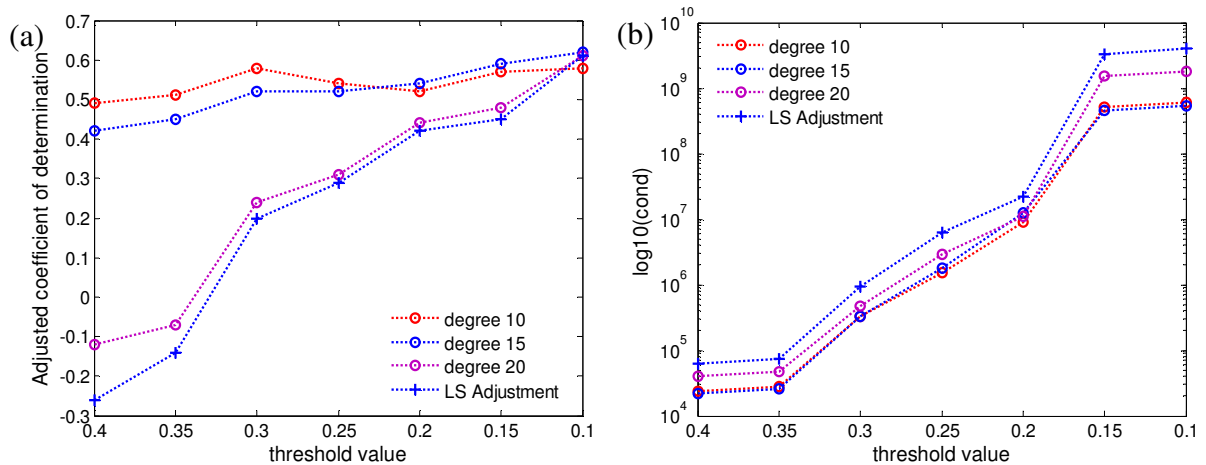


**Figure 4.5:** (a) Adjusted coefficient of determination and (b) condition number of the normal matrix as a function of the threshold value.

Figures 4.5a and b also include the adjusted coefficient of determination and the condition number when the signal component is disregarded thus adopting the functional modelling approach and applying least-squares adjustment. As observed, the least-squares adjustment model is characterised by a smaller coefficient of determination and a larger condition number compared to the least-squares collocation models. Clearly, the addition of the signal component improves the condition number approximately by one order of magnitude. Thus, the inclusion of the signal component has a regularization role in the least-squares collocation model, which results in reduced numerical instabilities.

As in the least-squares collocation case, a negative adjusted coefficient of determination is observed for the larger threshold values in the least-squares adjustment case. The same effect has been observed by Fotopoulos (2003) in least-squares fitting of low degree polynomial surfaces to height misclosures computed by means of Eq. (2.10). In both cases, the negative  $R_{\alpha}^2$ -values indicate severe under-fitting, which can be improved by either increasing the number of the estimated parameters or including a signal component in the observations.

#### **4.3.5 Empirical models of the rates of the terrestrial gravity, geoid, and heights**

In this section, results of the least-squares collocation modelling of the rates of the terrestrial gravity and the height components (the ellipsoidal, orthometric, and geoid heights) are presented and discussed. The solutions presented in the following are obtained with a spheroidal kernel of degree 15 and 13 inverse multiquadric base functions. No modification of the a priori threshold value of 0.3 in the modified Gram-Schmidt selection algorithm is applied. The standard deviations of the predicted rates are computed with the re-scaled error covariance matrices after variance component estimation has been applied. The discussion starts with the rates of the ellipsoidal height followed by the rates of the terrestrial gravity. This allows for assessing the performance of the adopted approach and clearly demonstrates the improvement of the accuracy of the predicted rates when more data are available in the areas above the degree 60 parallel.

##### ***Rates of change of the ellipsoidal height (rates of the absolute vertical displacement)***

Figure 4.6 shows the computed rates, the predicted signals, and the standard errors for the three solutions. **Solution (1)** recovers the pattern of the rate of the terrestrial gravity and predicts a postglacial uplift maximum of  $13.1 \pm 1.1$  mm/yr located on the east coast of Hudson Bay. It should be noted that the rates of the ellipsoidal height from Solution (1) are interpreted entirely in terms of postglacial rebound. Obviously, the predicted signals (with maximum and minimum values of 2.5 and -2.5 mm/yr in Figure 4.6b) are correlated with the gravity site locations. This correlation is reduced in **Solution (2)** as a result of using the

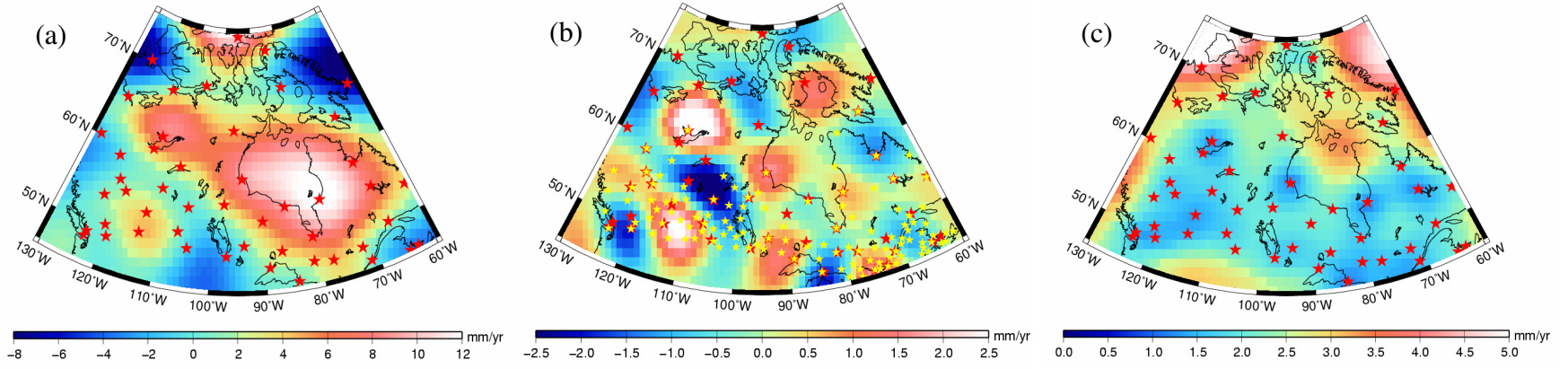
signal covariance information obtained from the GPS velocities. The predicted uplift in the Yellowknife area and western prairies is also decreased. The latter effect is more pronounced in **Solution (3)**, in which the local uplift in the western prairies diminishes. As discussed in Section 4.3.1 of Chapter 2, the strong gravity decrease translated to uplift in Solution (1) is of unknown origin. The CBN GPS vertical velocities do not support this uplift. In fact, very small (close to zero) vertical displacements are observed in this area. This strongly suggests that the value of  $-0.18 \mu\text{Gal}/\text{mm}$  for the gravity-to-height ratio is not valid for the western prairies, which is mitigated by the addition of the GPS velocities in Solution (3).

The maximum rate predicted on the east coast of Hudson Bay decreases to  $11.2 \pm 0.8$  mm/yr in Solution (3). Clearly, the combined solution with the terrestrial gravity rates and the GPS vertical velocities restores the vertical velocity pattern in the areas where more CBN stations are available and retains the terrestrial gravity data pattern in the areas above degree 60 latitude. It also shows a less pronounced single dome pattern observed for Solution (1) that is partly a result of the insufficient density of the gravity data compared to the CBN data. The standard error for the computed rates in Solution (1) ranges from 1.0 mm/yr for the gravity site locations to the maximum of 6.1 mm/yr for the northwest corner, where no data points are available and the ellipsoidal heights are extrapolated (Table 4.4). The average standard deviation of 2.6 mm/yr corresponds to the average standard deviation of the GPS velocity data. When both data sets are combined in Solution (3), the average accuracy improves to 1.8 mm/yr and the maximum error decreases to 4.8 mm/yr. Also, a significant decrease exists in the standard deviation of the rates in the northern areas of Hudson Bay (Figure 4.6c) due to the addition of the GPS data.

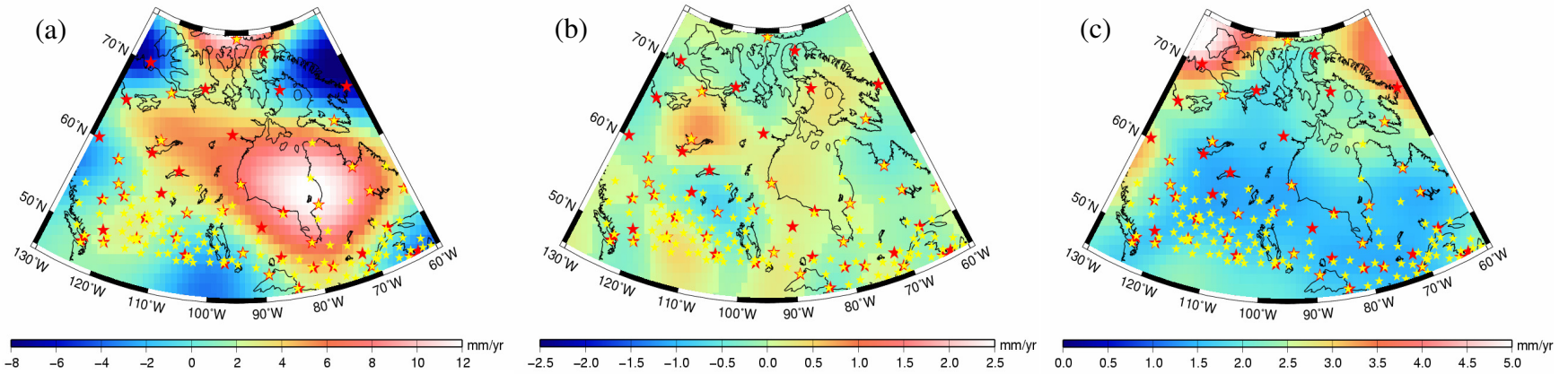
**Table 4.4:** Standard deviations of the predicted rates of the ellipsoidal height, in mm/yr

Solution	Min	Max	Mean
(1)	1.0	6.1	2.6
(2)	1.4	5.4	2.2
(3)	0.7	4.8	1.8

Solution (1)



Solution (2)



## Solution (3)

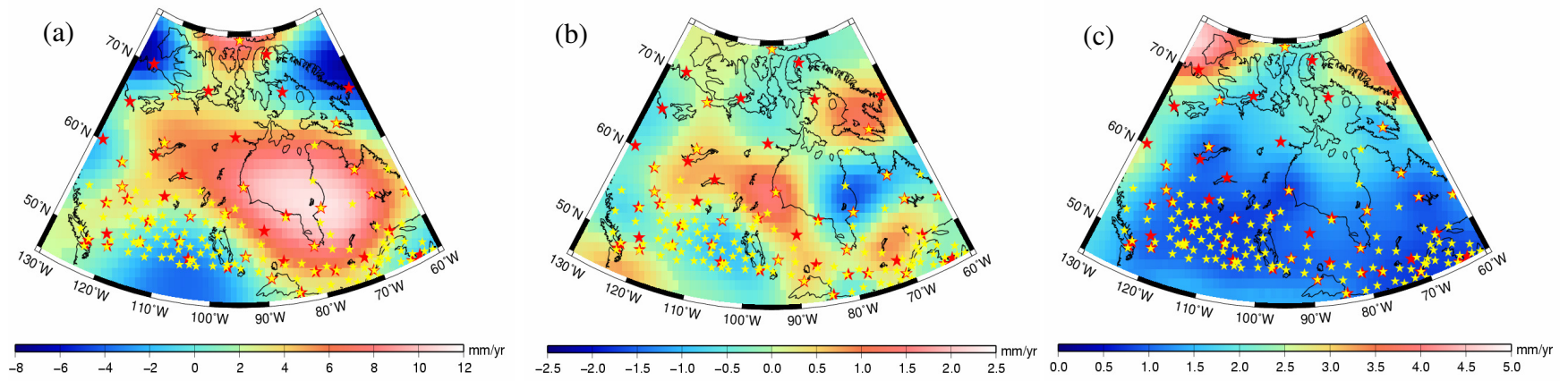


**Figure 4.6:** Predicted rates of change of ellipsoidal height for the three solutions: (a) total rate, (b) predicted signal, and (c) accuracy of prediction. Red and yellow stars denote the CGSN sites and CBN stations, respectively.

### *Rates of change of terrestrial gravity*

Two empirical models can be obtained for the rates of the terrestrial gravity (Figure 4.7). **Solution (1)** involves the use of the gravity data only, and the computed gravity rates should restore the data if no filtering of the noise is performed. The minimum terrestrial gravity rate of  $-2.36 \pm 0.07$   $\mu\text{Gal}/\text{yr}$  is located on the east coast of Hudson Bay, and the maximum rate of  $1.70 \pm 1.09$   $\mu\text{Gal}/\text{yr}$  is observed for the Arctic areas, where rates are extrapolated. The average error of the predicted rates is 0.43  $\mu\text{Gal}/\text{yr}$  (see Table 4.5) and matches the average error of the terrestrial gravity rates data. **Solution (3)** shows that the addition of GPS data can change the terrestrial gravity rates by as much as  $\pm 0.5$   $\mu\text{Gal}/\text{yr}$ . However, the prediction accuracy improves to 0.38  $\mu\text{Gal}/\text{yr}$  on average. For the absolute gravity sites “collocated” with CBN stations, the error decreases to 0.04  $\mu\text{Gal}/\text{yr}$ .

**Table 4.5:** Standard deviations of the predicted rates of the terrestrial gravity, in  $\mu\text{Gal}/\text{yr}$

Solution	Min	Max	Mean
(1)	0.07	1.09	0.43
(3)	0.04	0.90	0.38

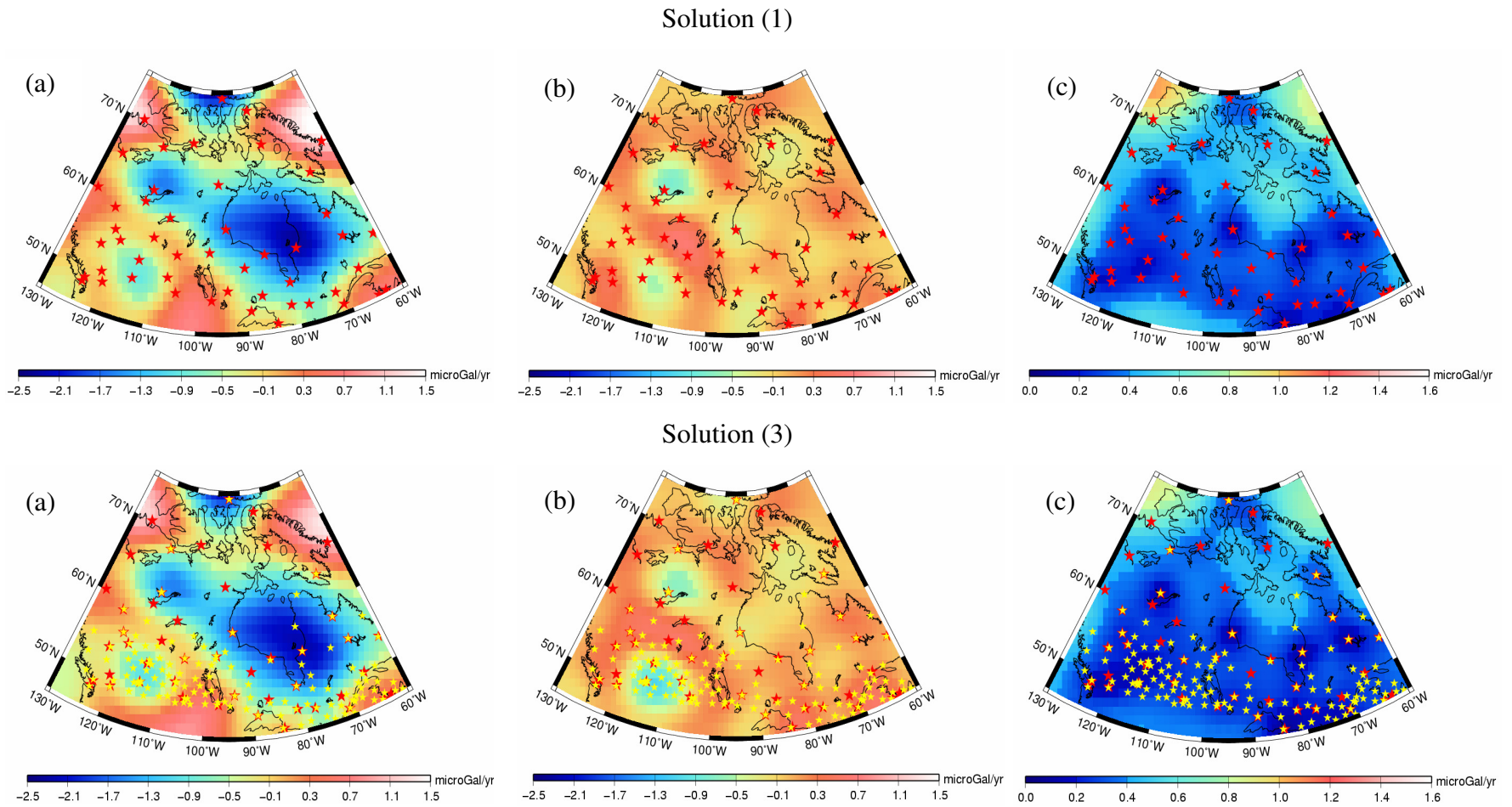


**Figure 4.7:** Rates of change of the terrestrial gravity from the three solutions: (a) total rate, (b) predicted signal, and (c) accuracy of prediction. Red and yellow stars denote the CGSN sites and CBN stations, respectively.

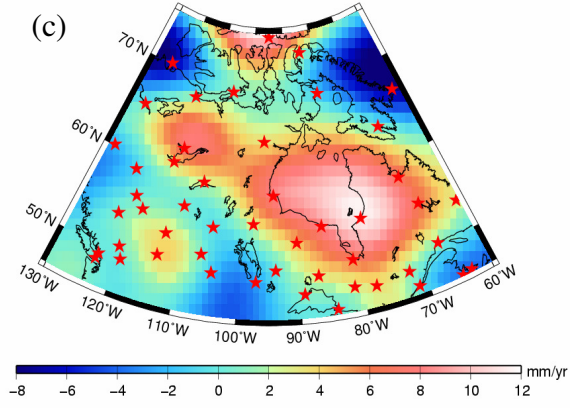
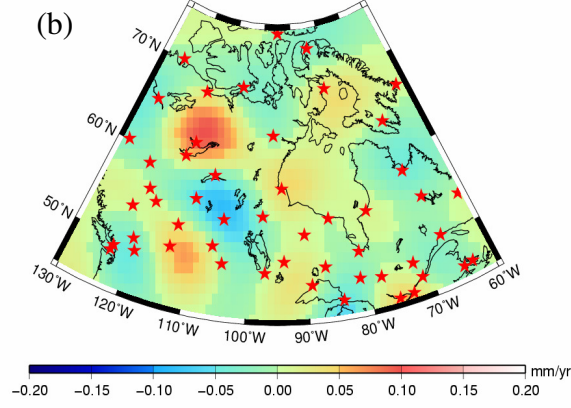
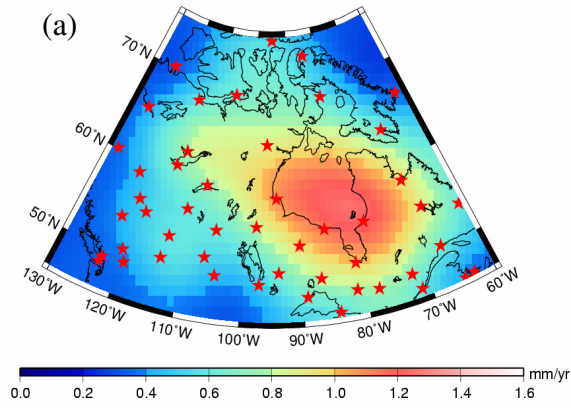
### ***Rates of change of the geoid and orthometric height***

Predicted rates of the geoid height by means of the procedure outlined in Figure 4.1 are positive across Canada and have a peak value located on the east coast of Hudson Bay (Figure 4.8a). The gravity data in **Solution (1)** predicts a peak rate of 1.2 mm/yr, but the use of the stochastic signal information from the GPS velocities leads to a decrease by 0.1-0.2 mm/yr in **Solution (2)**; see also Figure 4.9. **Solution (3)** systematically shows larger rates compared to Solution (2). The prediction accuracy is at the level of 0.1-0.2 mm/yr (Table 4.6), which corresponds to the accuracy of 1.0-2.0 mm/yr for the predicted rates of the ellipsoidal height.

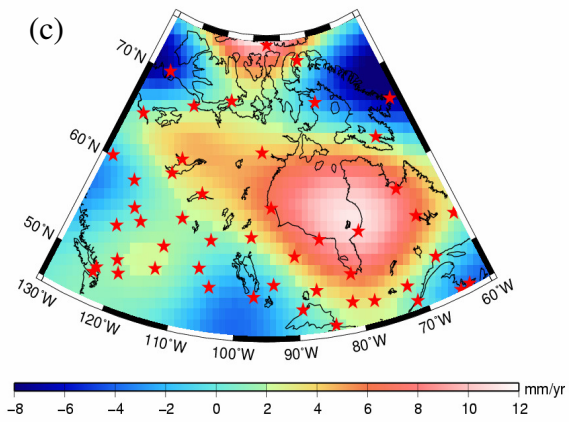
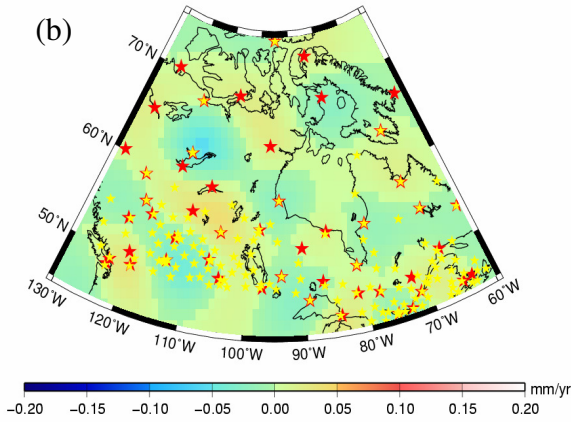
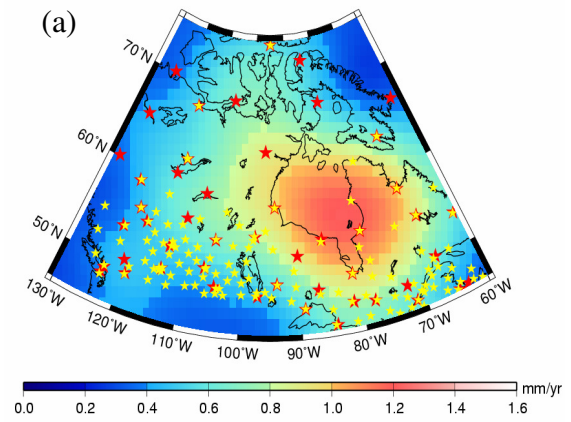
Figure 4.8c depicts the rates of change of the orthometric height. The LSC-predicted rates repeat the pattern of the rates of the ellipsoidal height, but the amplitude decreases by an amount that accounts for the rates of the geoid height.

The geoid rates do not solely account for postglacial rebound. However, because the local processes can have a much smaller contribution to the rate of the geoid height, a comparison with the PGR simulation outputs can serve as validation of the predicted rates. As shown in Figure 4.9, in the Hudson Bay region, the predicted geoid rates agree relatively well with the model rates based on the ICE-4G de-glaciation history and a viscosity profile with an upper mantle viscosity of  $0.4 \times 10^{21}$  Pa·s and a lower mantle viscosity of  $2 - 4 \times 10^{21}$  Pa·s (close to the VM2 values). In the areas north of the degree 65 parallel, where few gravity sites and GPS stations are available, the LSC-predicted rates are lower than the model-based rates. The geoid rates obtained with a higher lower mantle viscosity of  $20 \times 10^{21}$  Pa·s are far higher than the rates predicted by the least-squares collocation approach. Because of the insufficient data coverage west and north of Hudson Bay, the predicted rates of change of the geoid height provide very weak constraints on the postglacial rebound models in these areas.

Solution (1)



Solution (2)



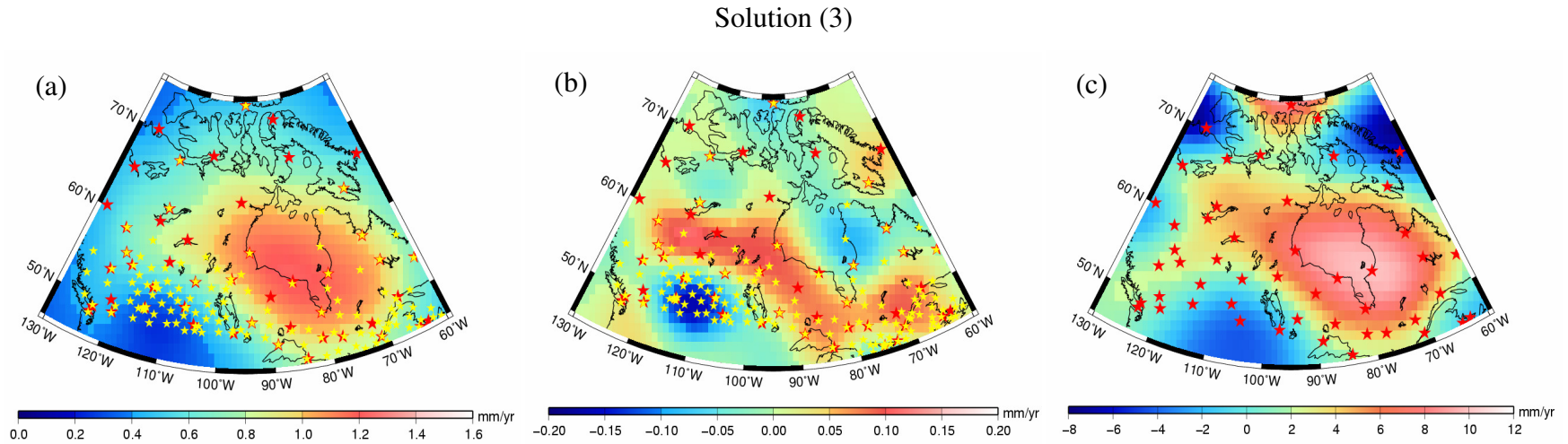


**Figure 4.8:** (a) Predicted total rates of change of the geoid height (b) predicted signal of the rate of geoid height, and (c) predicted rate of the orthometric height. Red and yellow stars denote the CGSN sites and CBN stations, respectively.

**Table 4.6:** Standard deviations of the predicted rates of the geoid height, in mm/yr

Solution	Min	Max	Mean
(1)	0.08	0.12	0.10
(2)	0.14	0.16	0.15
(3)	0.08	0.11	0.10

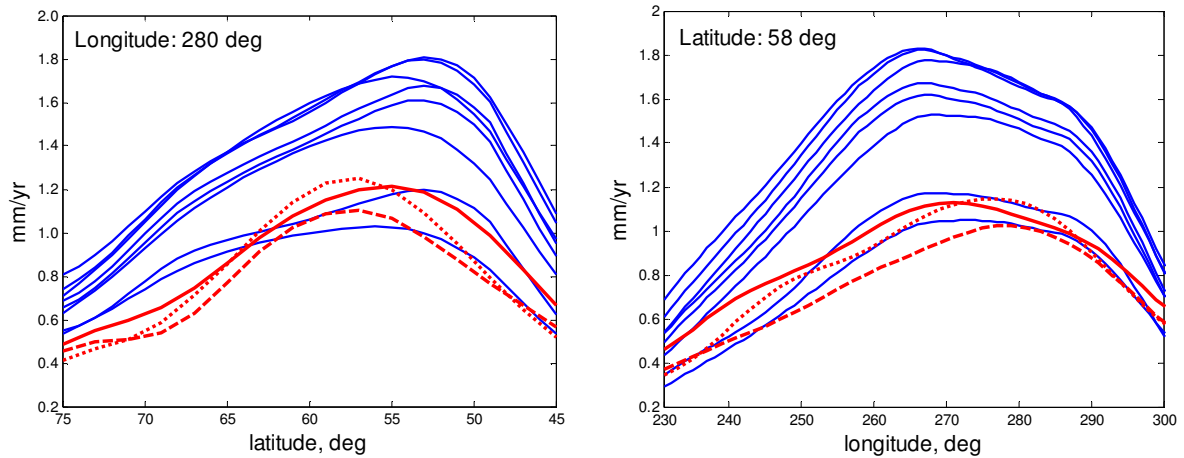


**Figure 4.9:** Comparison of the geoid rates along north-south and west-east profiles: outputs from the PGR model simulations are plotted in blue, Solution (1) is plotted in dotted red line, Solution (2) is plotted in dashed red line, and Solution (3) is in solid red line.

#### 4.3.6 Validation of predicted rates of change of terrestrial gravity and ellipsoidal height

The predicted rates of change of the terrestrial gravity and ellipsoidal height are validated by means of a comparison with data provided by the North American mid-continent tilt project (see Section 2.4.2). The rates and their  $1\sigma$  error bars are plotted in Figure 4.10. As seen from Figure 4.10a, the LSC-predicted terrestrial gravity rates are systematically higher than the mid-continent tilt project rates. Systematic differences are observed also for the GPS velocities in Figure 4.10b. The rates of the ellipsoidal height predicted in Solutions (2) and (3) (except for CHUR) are smaller than the validation GPS velocities. One possible reason could be a bias present in the CGSN gravity rates due to, for example, systematic errors in the instruments with which absolute gravity and gravity differences were measured. This is supported by the fact that the rates of the terrestrial gravity and ellipsoidal height in Solution (3) predicted with the addition of the GPS data are closer to the validation rates.

Using the  $F$ -statistic in Eq.(4.67), the compatibility of the predicted signal with the validation data is tested with a null hypothesis postulated in Eq.(4.66). This is done separately for the terrestrial gravity rates and GPS velocities at significance level  $\alpha = 0.05$ . The null hypothesis is not accepted for both rates of the terrestrial gravity and the ellipsoidal height in Solution (3). This fact requires closer examination of the predicted rates tested individually by means of the  $t$ -statistic given by Eq.(4.70). For two of the gravity sites, namely CHUR and PINA/DUBO, the LSC-predicted rate of terrestrial gravity are not compatible with the mid-continent tilt project rates. While for CHUR the alternative hypothesis  $H_a$  cannot be firmly accepted ( $\tilde{t} = 1.74 > t_{0.05}(186) = 1.65$ ), for the PINA/DUBO site,  $H_a$  is strongly accepted ( $\tilde{t} = 3.59 > 1.65$ ). This is also valid for the predicted rate of the ellipsoidal height at the DUBO station with  $\tilde{t} = 2.33 > 1.65$ . Moreover, a change in the sign of the predicted rate at this station is observed.

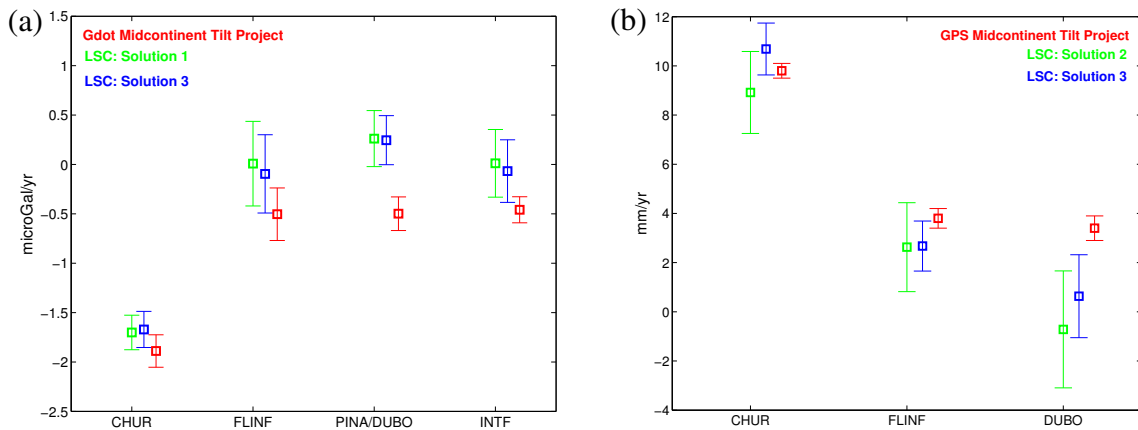


**Figure 4.10:** Predicted rates of change of (a) the terrestrial gravity and (b) the ellipsoidal height (absolute vertical displacement) compared with the Mid-continent tilt project data.

The validation of the predicted rates with the independent data has shown that the least-squares collocation with parameters approach has been successfully implemented to predict the rates of change of the terrestrial gravity at FLINF and INTF sites and the rates of change of the ellipsoidal height (absolute vertical displacement) at CHUR and FLINF

stations. It is expected that with the addition of vertical velocities obtained from GPS measurements with a longer time span and improved accuracy, the agreement of the predicted rates and the Mid-continent tilt project data will improve. Additional validation is required for the rates of the geoid and orthometric heights.

#### **4.4 Summary**

In this chapter, a methodology based on the least-squares collocation with parameters approach for predicting rates of change of the terrestrial gravity and ellipsoidal, geoid, and orthometric heights has been developed and presented. Least-squares collocation allows heterogeneous data input; thus, different types of terrestrial data can be combined in the optimal estimation procedure. This is particularly important for Canada, where the available observations are complementary to each other. It has been demonstrated that the GPS velocities improve the rates predicted solely from the gravity data. Although the re-levelling data in Canada are scattered in space and time and thus of low quality, it could be expected that the re-levelled segments of the primary vertical control network would improve the results in the southern areas of Canada by increasing the data density of the CBN GPS stations.

The developed computational procedure in this chapter uses inverse multiquadric base functions for modelling the spatial trend of the predicted rates. By extensive testing with simulated vertical displacement rates in Chapter 3, it has been shown that the inverse multiquadrics provide accurate approximation from irregularly distributed data if the base functions are appropriately scaled. The empirical rule for a priori scaling of the base functions established in Chapter 3 has been tested with real data. Modifications of the shape of the multiquadrics do not introduce significant changes in the modelled spatial trend provided that the shape parameter varies within 0.05 and 0.2 of unit distance.

Another parameter that has been tested at length in this chapter is the threshold value in the modified Gram-Schmidt algorithm, through which the number and locations of the base functions are determined. The threshold values have been obtained by means of Monte Carlo simulations using model-based data. Although these values are valid only for the

empirical models developed in this research, the methodology is general and can be applied in other similar problems.

The results of the least-squares collocation procedure have been validated with postglacial rebound model-based rates and independent data from the Mid-continent tilt project data. It has been shown that the empirically predicted geoid rates are in agreement (within 0.1-0.2 mm/yr in the areas with peak signal) with the model-based rates obtained with the ICE-4G de-glaciation history and a viscosity profile that is an approximation of the VM2 model. Also, it has been shown that the predicted rates of change of the terrestrial gravity and the absolute vertical displacement agree within the prediction accuracy with the data from the Mid-continent profile at most of the gravity and GPS sites. An important observation for the validation of the proposed methodology is the fact that the addition of the GPS velocities improves the agreement with the validation data sets. It can be expected that the methodology developed in this chapter will provide better predictions with the longer time span of the GPS measurements.

Although a general agreement exists between the empirical and the model-based geoid rates, it should be noted that the empirical models can be subject to erroneous data. This problem can be significant if the data sets are sparse and the vertical displacement surface is weakly constrained. As a consequence, the amplitude and slope of the predicted rates can deviate in the different empirical models. Of particular interest is the hinge line, which is an important constraint in the postglacial rebound modelling. More studies on this subject are included in Chapter 6, where the problem with outliers present in the data sets is dealt with by means of robust least-squares procedures.

Finally, it should be emphasized that the combined procedure allows for stepwise computations, which makes possible the improvement of the predicted rates by correcting them for new data when available.

## Chapter Five: GRACE-observed rates of change of the geoid height and absolute vertical displacement

In this chapter, the GRACE-observed rates of the geoid height and absolute vertical displacement are modelled. For this purpose, the principal component (empirical orthogonal functions) analysis is studied extensively. The estimated rates are validated by the traditional least-squares fitting to the time series of the spherical harmonic (SH) coefficients by means of Eq. (2.33), and the advantages of using principal components are emphasized. Moreover, the effects of the GRACE measurement errors, different filtering techniques, and the uncertainties in the hydrology corrections on the estimated GRACE rates are quantified. It will be shown that the trend-like hydrology signal (over the analyzed four years) introduces the largest uncertainty in the estimated rates. Of particular interest is the optimal combination of the GRACE and Earth surface data including terrestrial gravity rates and GPS vertical velocities. The proposed method is the least-squares collocation approach.

Forty-four CSR RL-01 gravity field solutions (Bettadpur, 2004) that span four complete years (from April/May 2002 to March 2006) are used to estimate the GRACE-observed rates of change of the geoid height and the rates of the absolute vertical displacement. The GRACE  $C_{20}$  spherical harmonic coefficient is replaced with the SLR-determined values as in Chen *et al.* (2005b). The ocean pole tide correction is applied according to the IERS conventions (IERS 2003), and no correction is applied for the S2 tide.

### 5.1 Error propagation

Errors of the SH coefficients can be propagated into the errors of the change in the geoid height  $C_{\delta N}$  as follows (Becker, 2004):

$$\mathbf{C}_{\delta N} = \bar{\mathbf{A}}^T \mathbf{C} \bar{\mathbf{A}}, \quad (5.1)$$

where

$\mathbf{C} = \begin{bmatrix} \mathbf{C}_C & \mathbf{C}_{CS} \\ \mathbf{C}_{SC} & \mathbf{C}_S \end{bmatrix}$  is the error covariance matrix of the residual (with respect to the long

term mean) SH coefficients and

$$\bar{\mathbf{A}} = \begin{bmatrix} W_{lm} \bar{P}_{lm}(\sin \varphi) \cos m\lambda \\ W_{lm} \bar{P}_{lm}(\sin \varphi) \sin m\lambda \end{bmatrix}. \quad (5.2)$$

The values  $W_{lm}$  are the weighting coefficients of the smoothing filter applied. Generally, the weighting coefficients can depend both on the spatial wavelength (degree  $l$ ) and the orientation (order  $m$ ). Eq.(5.1) can be further simplified if  $\mathbf{C}_{CS} = \mathbf{C}_{SC} = \mathbf{0}$  and  $\sigma_{C_{lmq}} = \sigma_{S_{lmq}} = 0, l \neq p$  and  $m \neq q$ . With these assumptions, the standard deviation of the change of the geoid height at the location  $(\varphi, \lambda)$  is computed as follows:

$$\sigma_{\delta N}(\varphi, \lambda) = R \left[ \sum_{l=2}^{l_{\max}} \sum_{m=0}^l \bar{P}_{lm}^2(\sin \varphi) \{ W_{lm}^2 \cos^2(m\lambda) (\sigma_{C_{lm}})^2 + W_{lm}^2 \sin^2(m\lambda) (\sigma_{S_{lm}})^2 \} \right]^{\frac{1}{2}}. \quad (5.3)$$

The error for a particular spherical degree is represented by the error degree amplitude, i.e., the square-root error degree variance, (Wahr *et al.*, 1998):

$$(\sigma_{\delta N})_l = R \sqrt{\sum_{m=0}^l (\sigma_{C_{lm}}^2 + \sigma_{S_{lm}}^2)}, \quad (5.4)$$

where  $\sigma_{C_{lm}}$  and  $\sigma_{S_{lm}}$  are the standard deviations of the fully normalized SH coefficients.

## 5.2 Methodology of post-processing of GRACE data and error analysis

The GRACE monthly gravity solutions exhibit increased errors in high frequencies that obscure the derivation of geophysical signals. Truncating the gravity spectrum at a lower degree is not desirable because part of the geophysical signal remains in the truncated SH coefficients apart from the leakage effect introduced in the spatial field. Numerous filters have been designed to mitigate the effect of the errors starting with the simplest isotropic Gaussian kernel (Wahr *et al.*, 1998), Wiener-Kolmogorov filter (Sasgen *et al.*, 2007), optimal filters minimizing leakage effects, GRACE error, or both (Swenson and Wahr, 2002; Becker, 2004; Seo *et al.*, 2006), and non-isotropic kernels (Han *et al.*, 2005b). Furthermore, sophisticated filters based on varying signal-to-noise ratios for SH coefficients of different degrees and orders (Chen *et al.*, 2006c) as well as filters based on regularization of the SH coefficients are developed (Kusche, 2007). The latter uses a non-isotropic smoothing kernel that is position-dependent. Because the filter uses the full GRACE error covariance matrix, the errors related to the orbital characteristics and the data processing strategies, which appear in the monthly geoid change spatial maps as stripes with north-south orientation, are also accounted for. In contrast with the stochastic-based filtering methods, Swenson and Wahr (2006) follow a more empirical approach in designing an efficient non-isotropic filter, which deals with the correlated errors. This filter is based on fitting one-dimensional spline polynomials to the SH series of the same order as a function of spherical degree and removing the trend through which the SH coefficients in the series are correlated; see also Chambers (2006a). Because the GRACE errors are not accounted for, subsequent smoothing with a Gaussian filter is applied. In the post-processing of the GRACE monthly gravity fields for the purpose of estimating the rate of change of the geoid height in this study, a hybrid approach is followed. It includes a de-correlation filter followed by either isotropic smoothing or stochastic-based smoothing.

### 5.2.1 De-correlation filter

In this thesis, a filter based on a wavelet decomposition of the series of the even and odd coefficients is constructed. The first level of approximation represents the trend in the

series. The residuals are not correlated and are used to synthesize back the geoid changes for each month. After applying the filter, a significantly smaller correlation of the monthly geoid changes in high latitudes, where previously glaciated areas are located, is observed. The filter is less efficient in the polar and equatorial areas.

As shown by Swenson and Wahr (2006), the de-correlation filter can remove real geophysical variability together with correlated errors. Figure 5.1a depicts the effect of the de-correlation on simulated GIA geoid rates. As evident from the figure, the filter alters the peak (by approximately 0.05 mm/yr) and the pattern of the geoid rate in Laurentide. The introduced error depends on the amplitude of the PGR signal but does not exceed 0.1 mm/yr. It should be noted, however, that in reality the effect of the de-correlation of the SH coefficients on the geoid rate could be smaller. Moreover, the isotropic smoothing applied afterwards decreases the effect of the de-correlation as shown in Figure 5.1b. Because most of the power of the Laurentide postglacial rebound signal is below spherical degree 10 with a peak of the spectrum at degree 5, the coefficients below degree 10 should not be de-correlated to avoid possible distortions in the geoid rate pattern.

Assessment of the errors of the SH coefficients after applying the de-correlation filter can be based on the residuals estimated by fitting and removing a trend and periodic variability from the time series of the coefficients as shown in Section 2.5.1 of Chapter 2. The residuals are assumed to sample the true GRACE errors (Wahr *et al.*, 2006). However, it is imperative to point out that the residuals can contain inter-annual and non-periodic geophysical signals, and, in this case, they are overestimated. The error degree amplitudes of the change of the geoid height is computed by means of Eq.(5.4) using the RMS values of the residuals of the SH coefficients (Figure 5.2). It is compared with the calibrated error degree amplitudes. The latter exceeds significantly the RMS of the residuals for degrees below 5, while for the rest of the spectrum the RMS spectrum and the calibrated errors spectrum are close. Exceptions are the higher RMS values for degrees 15 and 30 explained by deficiencies in the GRACE background models propagated into the monthly geoid solutions (Gunter *et al.*, 2006). The figure makes it evident that the power of the RMS values decreases significantly after de-correlating the SH coefficients.

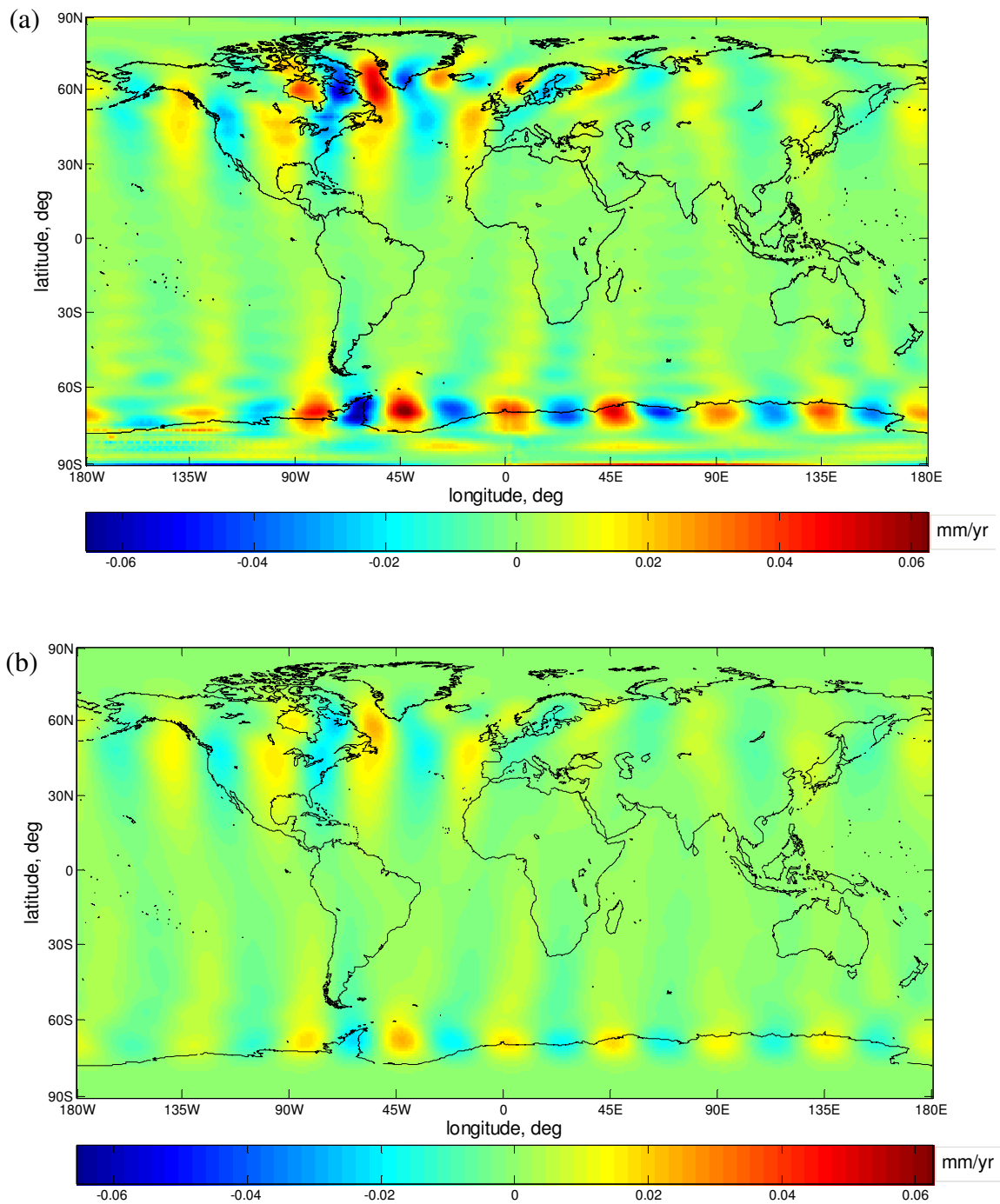


**Figure 5.1:** Distortions in the rate of change of the geoid height: (a) after a de-correlation filter is applied and (b) smoothed with a Gaussian filter.

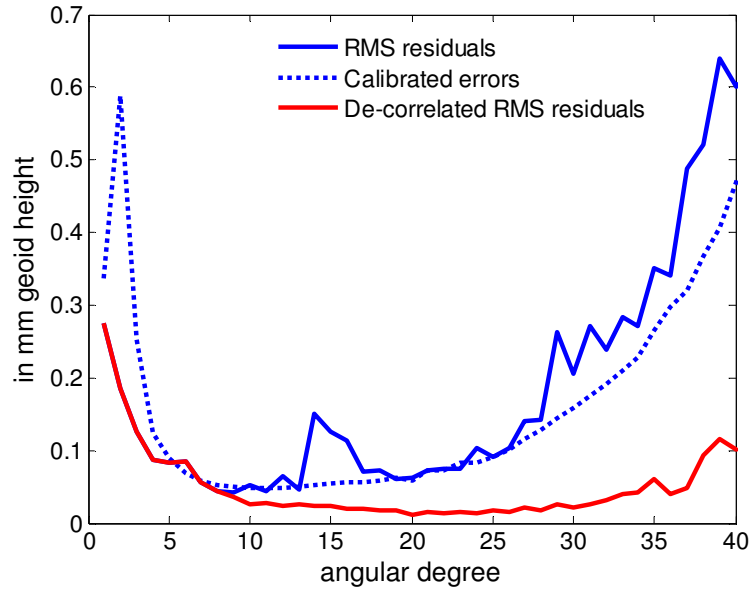


**Figure 5.2:** Error degree amplitudes in mm of the geoid height.

### 5.2.2 Smoothing filters

The isotropic Gaussian filter, which is introduced in the gravity field approximation by Jekeli (1981) and adopted for time-variable gravity field by Wahr *et al.* (1998), is characterized by the ease of implementation and interpretation of the filter's parameter. However, the Gaussian filter is not an optimal filter in the sense that it does not minimize any error. In addition, the choice of the parameter of the filter is somehow arbitrary and is usually governed by the specific problem analyzed. For the purpose of estimating the rate of change of the geoid height, the isotropic Gaussian filter is tested and compared with a stochastic-based filter.

#### *Isotropic filtering*

An isotropic averaging filter on the sphere is defined by means of the function

$$W(\psi) = \sum_{l=0}^{\infty} \frac{2l+1}{2} W_l P_l(\cos \psi) \quad (5.5)$$

that depends only on the spherical distance  $\psi$  between the points  $(\theta_1, \lambda_1)$  and  $(\theta_2, \lambda_2)$  computed by means of  $\cos \psi = \cos \theta_1 \cos \theta_2 + \sin \theta_1 \sin \theta_2 \cos(\lambda_1 - \lambda_2)$ .

The spectrum of the function  $W(\psi)$ , which consists of the weighting coefficients  $W_l$ , is defined by the one dimensional Legendre transform (Jekeli, 1981)

$$W_l = \int_0^\pi W(\psi) P_l(\cos \psi) \sin \psi d\psi. \quad (5.6)$$

In Eqs. (5.5) and (5.6),  $P_l(\cos \psi)$  are the Legendre polynomials.

The isotropic Gaussian filter is constructed by means of the averaging function

$$W(\psi) = \frac{b}{2\pi} \frac{\exp[-b(1 - \cos \psi)]}{1 - e^{-2b}} \quad (5.7)$$

with a parameter  $b = \frac{\ln(2)}{[1 - \cos(r/R)]}$ , where the averaging radius  $r = R\psi$  is the distance at

which  $W(r) = W(\psi = 0)/2$ . It is also called a half-width of the filter. The coefficients  $W_l$  are computed by means of recursive relations (see, e.g. Wahr *et al.*, 1998). Alternatively,  $W_l$  can be computed by numerical integration using Eq. (5.6).

Multiplication of the SH coefficients with the degree-dependent weighting coefficients corresponds to a convolution of the isotropic function in Eq. (5.5) with the monthly maps of changes in the geoid height. As a result, a decrease in the amplitude of the geophysical signals of interest is observed. Usually, the GRACE-observed amplitudes can be rescaled to match the model-based signal. The approach followed in this study is to smooth the simulated postglacial rebound signal with the same filter.

The decrease in amplitude of simulated geoid rates for a different half-width of the Gaussian filter is depicted in Figure 5.3. Gaussian noise with a variance obtained from the residual RMS values (after de-correlation has been applied) in Section 5.2.1 has been added to the SH coefficients of a simulated GIA geoid trend using the ICE-4G model and a four-layer approximation of the VM2 model. Next, the SH coefficients are multiplied by the coefficients of a Gaussian filter with a half-width of 400, 600, 750 and 1000 km. The

smoothed GIA geoid rates are obtained by means of Eq. (2.32), and differences with the original rates are computed. For the Laurentide signal, the maximum difference in amplitude increases from 0.15 mm/yr for  $r = 400$  km to 0.65 mm/yr for  $r = 1000$  km. This demonstrates that even for smaller values of  $r$ , the geoid rates can be significantly smoothed. This effect compares with the differences of the GIA model predictions with different viscosity profiles (Figure 2.3 in Chapter 2). The same smoothing effect is computed for the GRACE-observed geoid rates (Table 5.1). A difference of 0.2 mm/yr for the peak geoid rates obtained with the different half-widths exists. This shows that the level of smoothing is an important factor to consider in inferences of the mantle viscosity from an inversion of the GRACE-observed geoid and gravity rates.

**Table 5.1:** Effect of the radius of the Gaussian filter on the geoid rate\*

Half-width $r$ , in km	400	600	750	1000
Geoid rate, in mm/yr	1.8	1.6	1.4	1.2

\*The hydrology signal is not removed from the GRACE-observed geoid height change.

Based on the quality of the RL-01 gravity field solutions, a Gaussian filter with a half-width of 400 km is used to obtain the GRACE-observed rates of change of the geoid height. Frequencies higher than degree 20, which account for only 2% of the power of the GIA geoid change, are down-weighted significantly. For a half-width of 400 km, the combined leakage effect of the Greenland and Alaska signals over Hudson Bay is -0.2 mm/yr at most.

### ***Stochastic-based filtering***

According to Chen *et al.* (2006c), the weighting coefficient (of degree  $l$  and order  $m$ ) of the stochastic-based filter is defined as follows:

$$W_{lm} = \frac{\text{var}(K_{lm}, K_{lm})}{\text{var}(K_{lm}, K_{lm}) + \sigma_{K_{lm}}^2}, \quad (5.8)$$

where  $K_{lm} = \{C_{lm}, S_{lm}\}$ ;  $\sigma_{K_{lm}}^2$  is the error variance for the coefficient  $K_{lm}$ .

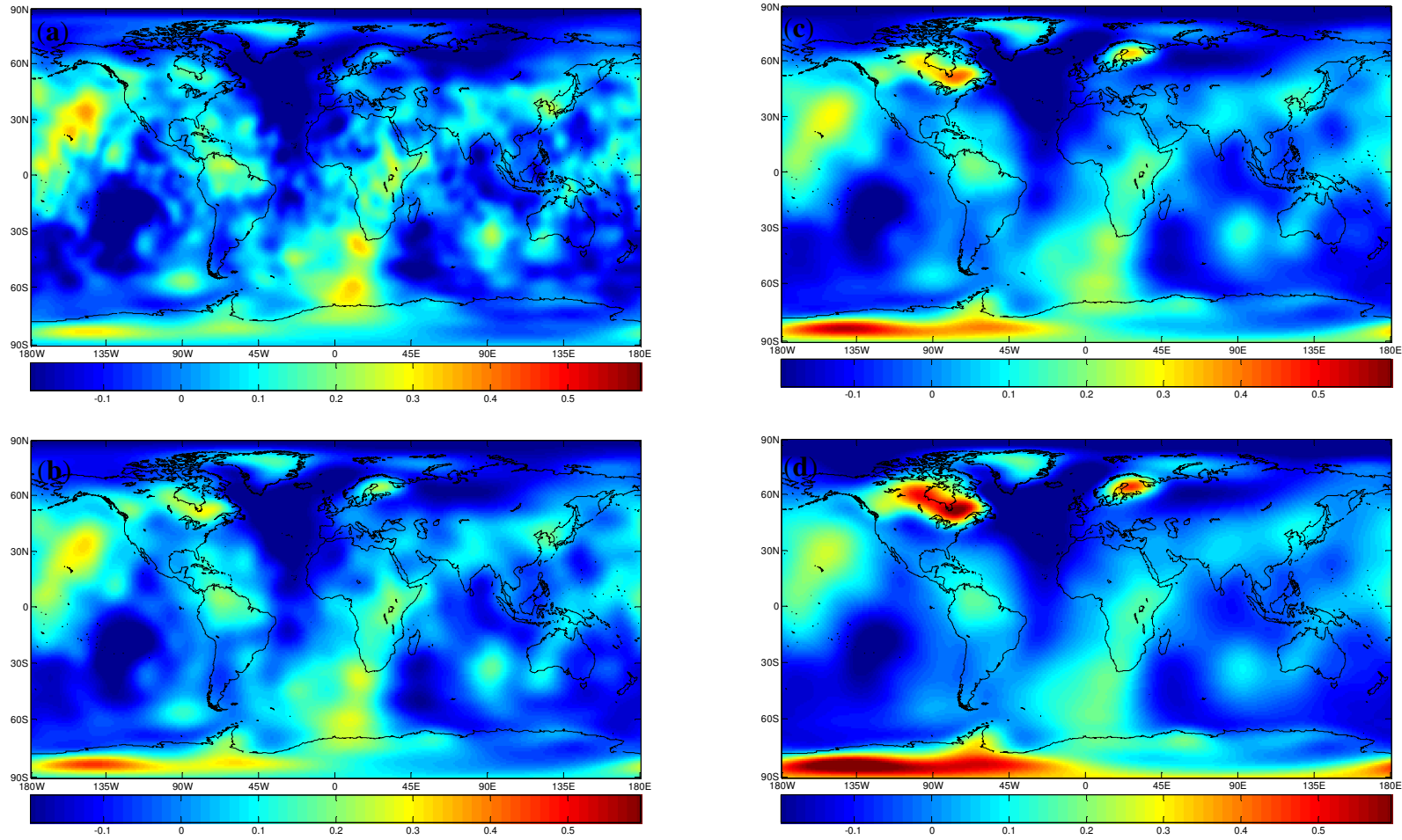


**Figure 5.3:** Effect of the Gaussian smoothing on the simulated GIA geoid rate. A filter with half-width  $r$  of (a) 400 km, (b) 600 km, (c) 750 km, and (d) 1000 km is used. Differences are plotted in mm/yr.

An equivalent form of Eq. (5.8) is

$$W_{lm} = \frac{1}{1 + \sigma_{K_{lm}}^2 / \text{var}(K_{lm}, K_{lm})}. \quad (5.9)$$

If  $\sigma_{K_{lm}}^2 \ll \text{var}(K_{lm}, K_{lm})$ , the weighting coefficient  $W_{lm} \rightarrow 1$ . If  $\sigma_{K_{lm}}^2 \gg \text{var}(K_{lm}, K_{lm})$ , then  $W_{lm} \rightarrow 0$ . Thus, the filter adapts to the varying noise in the SH coefficients and suppresses the coefficients with larger errors. If the signal and error degree variances, i.e.,

$s_l^2 = \sum_{m=0}^l (\bar{C}_{lm}^2 + \bar{S}_{lm}^2)$  and  $\sigma_l^2 = \sum_{m=0}^l (\sigma_{C_{lm}}^2 + \sigma_{S_{lm}}^2)$ , are substituted in Eq. (5.8), the filter is

$$W_l = \frac{s_l^2}{s_l^2 + \sigma_l^2}, \quad (5.10)$$

which is the isotropic Wiener-Kolmogorov filter (Rummel, 1996).

The stochastic-based filter is tested with the same simulated geoid rates and noise as the Gaussian filter. The signal variances are the squared SH coefficients of the simulated GIA geoid rate while the error variances are the squared residual RMS values from Section 5.2.1. The differences of the reference (Figure 5.4a) and smoothed geoid rates depict a maximum value of 0.2 mm/yr in Laurentide (Figure 5.4b). This value compares with the result obtained with a Gaussian filter with a half-width of 400 km. It should be noted, however, that the stochastic smoothing is able to filter out much more noise from the simulated geoid rates. This result is expected since the stochastic filter is based on the optimal least-squares criterion.

Figure 5.5 displays the standard deviation of the GRACE-observed geoid rate obtained by error propagation according to Eq.(5.3). Evident from Figure 5.5a, is the good performance of the de-correlation filter for 30 - 80 degree in latitude, where the formal error of the estimated geoid rate is 0.2 - 0.3 mm/yr. In a small polar spherical cap and in the equatorial areas, the error reaches 0.6 - 0.7 mm/yr. After smoothing with a 400 km Gaussian filter, the formal error of the rate of change of the geoid height decreases to 0.14 - 0.18 mm/yr (Figure 5.5b).

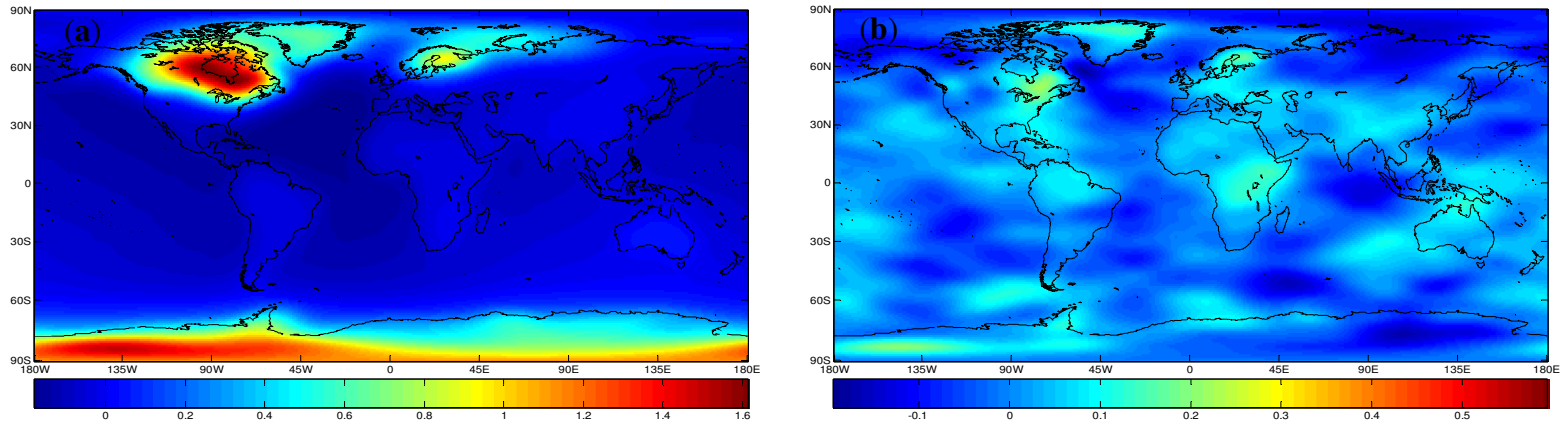


**Figure 5.4:** Effect of the stochastic-based smoothing on the GIA-induced geoid rates: (a) reference geoid rates; (b) differences between the reference and filtered rates.

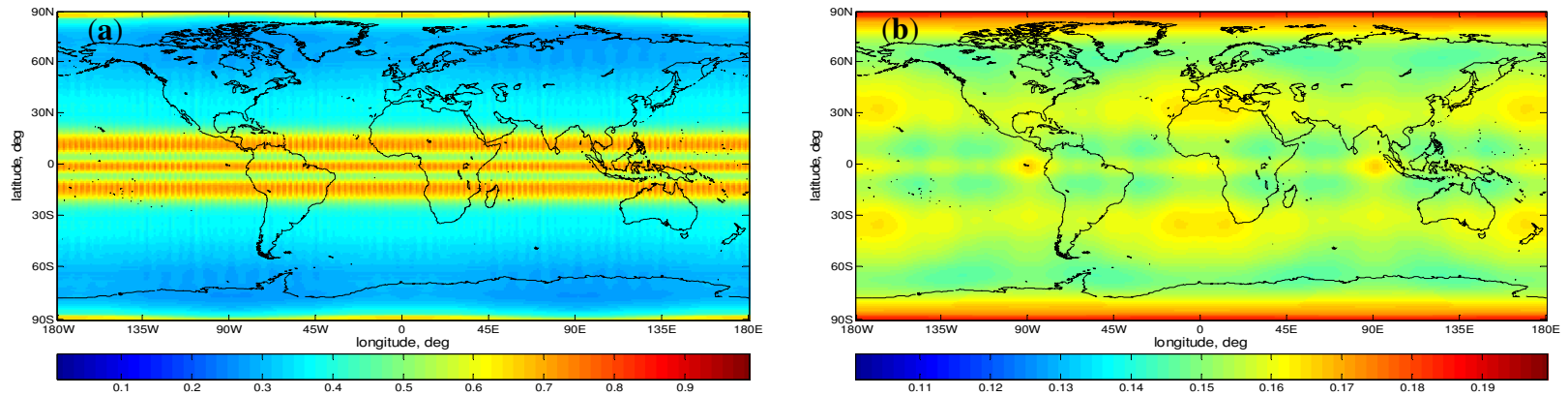


**Figure 5.5:** Formal errors of the geoid rates from least-squares fitting to the four-year time series of GRACE SH coefficients smoothed with: (a) a de-correlation filter and (b) a de-correlation filter and Gaussian filter with  $r = 400$  km.

### 5.2.3 Uncertainties in the secular geoid rate from the continental hydrology correction

In order to obtain the GIA-induced rates of change of the geoid height, the continental hydrology signal should be removed from the GRACE-observed geoid changes. This is achieved by correcting the GRACE SH coefficients with the SH coefficients obtained from a harmonic analysis of water mass anomalies from global hydrology models. It should be noted that uncertainties in the hydrology models will project into the GIA signal.

Generally, the continental water storage models provide gridded water equivalent outputs of predicted soil moisture, groundwater, rootzone, and snow water equivalent data. The input can consist of satellite, ground-based, and merged observations of precipitation and outputs from atmosphere data assimilation systems as well as other parameters, such as vegetation, soils, and elevation. According to Gottschalck *et al.* (2005), precipitation is the critical forcing factor for the model simulations and the accuracy of the precipitation input governs the simulation outputs.

One of the most accurate global hydrology models is the Global Land Data Assimilation System (GLDAS); see Rodell *et al.* (2004). The GLDAS model provides soil moisture in four layers, snow water equivalent, and canopy water storage. The model output used in this thesis is based on the Noah land surface model (Chen *et al.*, 1996) and is averaged from the original 3-hourly data.

In order to transform the water equivalent data in terms of geopotential, first the mass anomalies are computed by subtracting the mean for the time period of the GRACE data. The transformation procedure consists of the following steps:

1. Performing spherical harmonic analysis of the mass anomalies; de-correlation and Gaussian filters are applied. The degree one coefficients have been ignored because GRACE gravity field models do not include degree one spherical harmonics.
2. Multiplying each spherical harmonic coefficient of the surface mass anomalies with a degree-dependent factor using the relationship between a thin layer of equivalent water thickness and the geoid height (Wahr *et al.*, 1998):

$$\begin{Bmatrix} \delta C_{lm} \\ \delta S_{lm} \end{Bmatrix} = \frac{3\rho_W}{R\rho_a} \frac{1+k_l}{2l+1} \begin{Bmatrix} \delta \hat{C}_{lm} \\ \delta \hat{S}_{lm} \end{Bmatrix}, \quad (5.11)$$

where  $\delta \hat{C}_{lm}$ ,  $\delta \hat{S}_{lm}$  are the SH coefficients for the surface load,  $\rho_W$  is the water density of  $1000 \text{ kg}\cdot\text{m}^{-3}$ ,  $\rho_a$  is the average density of the Earth, i.e.,  $5517 \text{ kg}\cdot\text{m}^{-3}$ , and  $k_l$  is the elastic Love number of degree  $l$ .

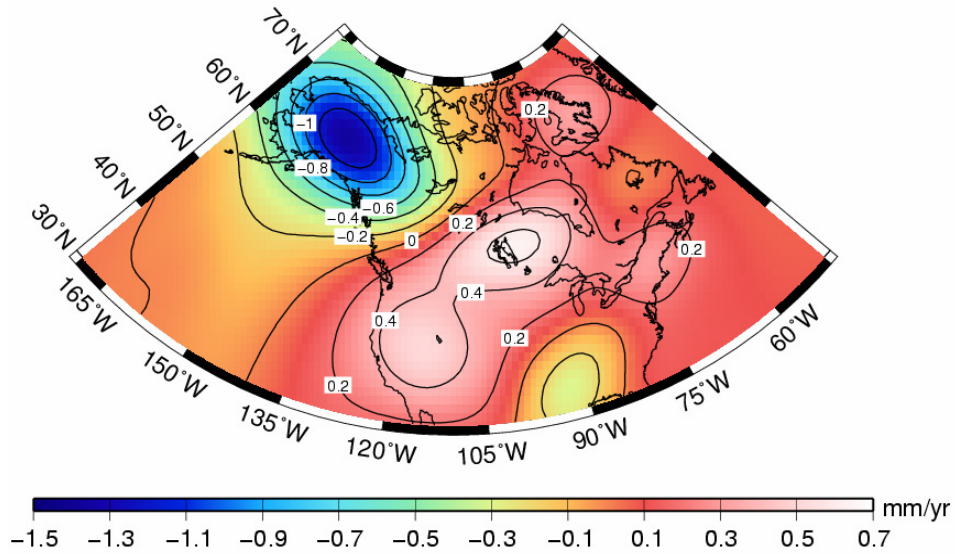


**Figure 5.6:** Pattern of the water mass increase that interferes with postglacial rebound signal. Least-squares fitting to the time series of the SH coefficients of the GLDAS model is applied.

### 3. Correcting GRACE SH coefficients for hydrology signal.

The continental hydrology models contribute to the error of the GRACE-observed geoid rate through uncertainties in the pattern and amplitude of the trend-like water mass changes. The GLDAS pattern in Figure 5.6 depicts a geoid rate of  $0.1 - 0.6 \text{ mm/yr}$  (over the analyzed four-year period) across most of North America and negative rates in non-glaciated areas of Alaska. It is not clear if this trend-like variability represents real hydrology signals, a deficiency of the model, or aliased higher frequency signals as a result of the time

averaging of the original 3-hourly data. Clearly, the peak of 0.6 mm/yr located southwest of Hudson Bay will interact with the postglacial rebound signal and will determine the location of the secular geoid rate peak.

One limitation of the global hydrology models is that the model errors remain unknown. For the purpose of the studies of the secular geoid rate, the error introduced by the hydrology correction can be assumed to be equal to the modelled signal. Thus, 0.6 mm/yr can be considered to be a pessimistic estimate of the uncertainty of the GRACE-observed postglacial rebound geoid rate as a result of the applied hydrology correction. This value is relevant for the time interval of the GRACE time series used in this research, and it will change for a different time interval. The trend-like water mass changes over the analyzed time period is less likely to affect the secular geoid rate with the increase of the time span of the GRACE mission. The effect of disregarding the contribution of the degree one coefficients in the hydrology model is not studied and is subject to future research.

Figure 5.7 depicts the GRACE-observed geoid rate obtained with (a) a Gaussian filter with  $r = 400$  km and (b) stochastic-based smoothing. The GIA-induced geoid rates after correcting the SH coefficients for hydrology and smoothing with the Gaussian filter and the stochastic-based filter are given in Figures 5.7c and d, respectively. Approximately the same amplitude of the geoid rate is observed in both figures. The use of the weighting coefficient for each degree and order, however, enhances the east-west features in the geoid rate pattern. These include possible distortions due to errors in the GLDAS model. Therefore, the Gaussian filter is preferred in this thesis. Table 5.2 summarizes the uncertainties in the rate of change of the geoid height estimated in this study from a four-year GRACE time series. The GRACE error contributes 20% to the total error estimate of the GIA geoid rate; see also Chen *et al.* (2006b). It should be noted that the time span of the GRACE time series also introduces uncertainties in the estimated geoid rate. For example, the differences of the geoid rate in the Hudson Bay region estimated from a three- and four-year time series is approximately 0.2 - 0.3 mm/yr, which is still above the formal error estimate from the least-squares fitting of the trend.

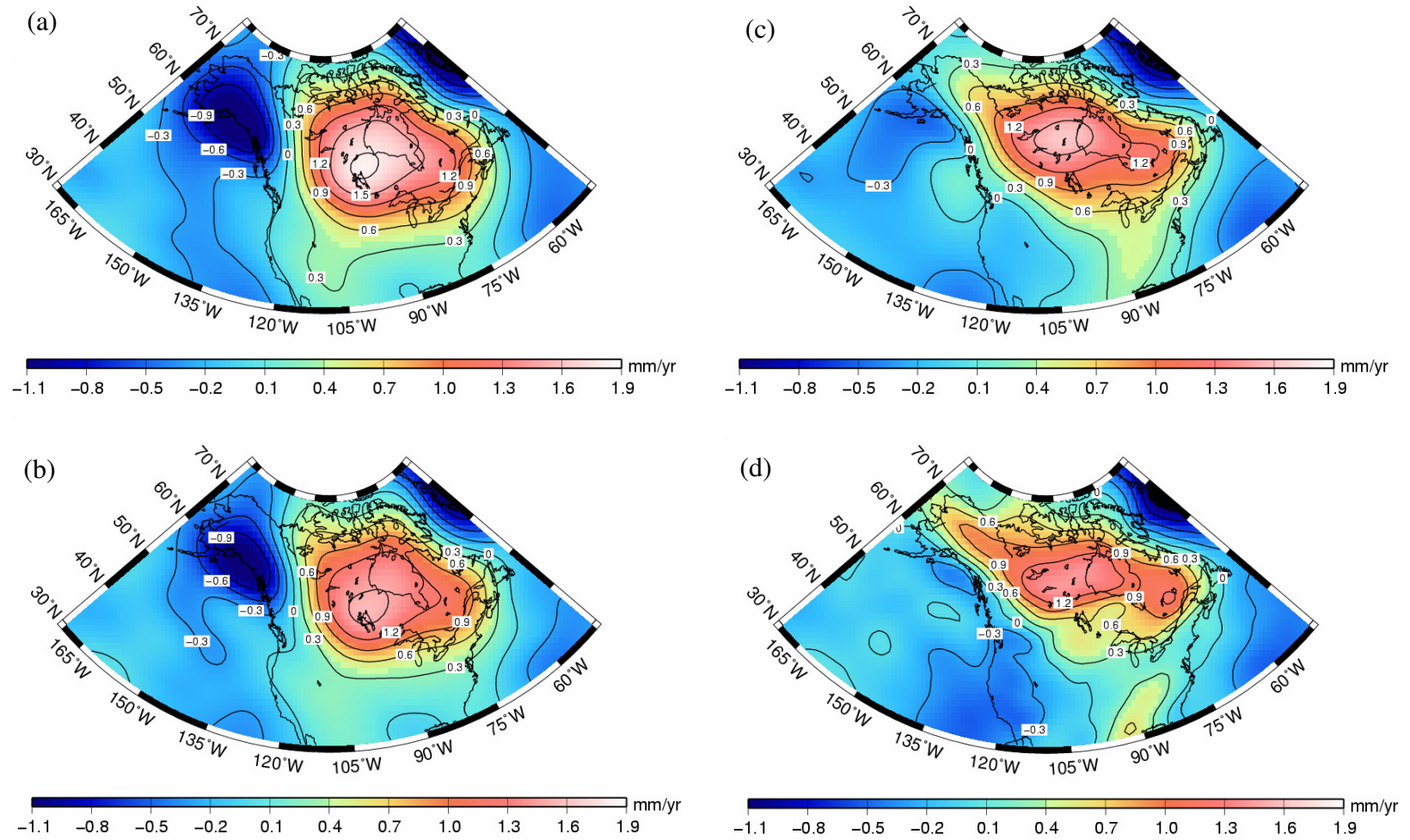


**Figure 5.7** GRACE-observed rates of change of the geoid height obtained with (a) a Gaussian filter with  $r = 400$  km, (b) stochastic smoothing, (c) and (d) the same, but a correction for the hydrology signal is applied.

**Table 5.2:** Uncertainties in the GRACE-observed postglacial rebound geoid rate

Source	Error, mm/yr
GRACE measurement errors	0.1 - 0.2 (Figure 5.5)
Decrease in amplitude due to smoothing of errors	0.2 (Figure 5.3, Figure 5.4, and Table 5.1)
Hydrology correction	0.6 (Figure 5.6)
Total	0.6 - 0.7

### 5.3 PC/EOF analysis of GRACE-observed geoid changes

Principal component (PC) analysis is based on the idea that variations of correlated variables (data) can be described by uncorrelated variables (principal components) obtained by means of a linear transformation of the data. The principal components are found from the solution of the eigenvalue-eigenvector problem for a positive definite matrix that contains data variances and covariances (Jolliffe, 2002).

In oceanographic and meteorological studies, PC analysis is known as empirical orthogonal function (EOF) analysis that is applied for modelling spatio-temporal variability of a single scalar field. This method provides EOF spatial loading patterns and their temporal variations given by the principal component time series. In addition to the periodic variability of the scalar field, the PC/EOF analysis has been applied for modelling inter-annual changes and long-term trends, for example, in sea level (Nerem *et al.*, 1997 and Woolf *et al.*, 2003), upper air-circulation fields (Shin and Deng, 2000), global sea surface temperature (Robertson and Mechoso, 1998), and in coupled patterns of sea surface temperature and radar satellite altimetry sea surface heights (Leuliette and Wahr, 1999). In relation to the GRACE-observed mass variations, the PC/EOF analysis has been applied by Wiehl *et al.* (2005) and Viron *et al.* (2006). In the first work, the low frequency sea water mass variability in the Baltic Sea is studied with relation to possible masking of the PGR geoid signal. The second study deals with global climate signals extracted from the

GRACE-observed mass changes. The PC/EOF analysis has been implemented also for studying the main signals of the seasonal steric sea level variations by Chambers (2006b).

In this thesis, the PC/EOF analysis is applied to the time series of the GRACE-observed changes in the geoid height to extract a trend, periodic, and non-periodic variations. A comparison with the traditional approach of least-squares fitting as well as the advantages and disadvantages of the proposed PC/EOF approach are given in Section 5.3.5.

### 5.3.1 Mathematical background

In the spatio-temporal analysis of a single scalar field, data are organized in a  $(n \times p)$  matrix  $\mathbf{D} = [d_{ij}]$ ,  $i = 1, \dots, n$ ,  $j = 1, \dots, p$ , where  $n$  is the number of observations and  $p$  is the number of variables. In the analysis of GRACE time series, the variables are the grid values of the analysed gravity field functional (a grid of resolution  $1^\circ \times 1^\circ$  can be taken) and the observations are the monthly values. The data covariance matrix is defined as

$$\mathbf{S} = \frac{1}{n-1} \mathbf{D}^T \mathbf{D} \quad (5.12)$$

with zero mean observations, i.e.,  $E\{d_j\} = 0$ ,  $j = 1, 2, \dots, p$ . This is fulfilled by the GRACE time series computed with respect to the long-term mean; see Section 2.5.1.

The data matrix  $\mathbf{D}$  is decomposed by singular value decomposition (SVD) as follows (see, e.g., Jolliffe, 2002):

$$\mathbf{D} = \mathbf{U} \mathbf{L} \mathbf{V}^T, \quad (5.13)$$

where  $\mathbf{U}$  and  $\mathbf{V}$  are  $(n \times n)$  and  $(p \times p)$  orthonormal matrices such that  $\mathbf{U}^T \mathbf{U} = \mathbf{I}$  and  $\mathbf{V}^T \mathbf{V} = \mathbf{I}$ .  $\mathbf{V}$  contains the eigenvectors of the matrix  $\mathbf{D}^T \mathbf{D}$  and provides the EOF patterns.  $\mathbf{L}$  is a diagonal matrix of rank  $r \leq \min(n, p)$  with a diagonal  $L_{ij} = \delta_{ij} \sqrt{\lambda_i}$ ,  $i = 1, \dots, r$ , where  $\lambda_i, i = 1, \dots, r$  are the eigenvalues of the covariance matrix  $\mathbf{S}$ . The squared diagonal elements of the matrix  $\mathbf{L}$  are the variances explained by each principal component. The eigenvalues

are ordered in decreasing significance, i.e., with respect to the fraction of the data variance explained.

The principal component time series are obtained from the column vectors of the following matrix  $\mathbf{T}$  of rank  $r$ :

$$\mathbf{T} = \mathbf{UL}. \quad (5.14)$$

The SVD method for computing the EOF loading patterns and their principal component time series has a number of advantages. In addition to its ease of implementation, the SVD method provides the means for a graphical representation and interpretation of the results of the PC/EOF analysis. Thus, the EOF patterns represent the amplitudes of the modes of the spatio-temporal variability of the analyzed scalar field, while the PC time series represent the weights of these amplitudes at the different time epochs. In addition, the SVD method is related to the principal component regression, in which the data matrix is approximated by the first  $m$  principal components.

According to Jolliffe (2002), the matrix

$${}_m\hat{\mathbf{D}} = {}_m(\mathbf{ULV}^T) \quad (5.15)$$

computed with the first  $m$  principal components minimizes the Euclidian norm

$$\|\mathbf{D} - {}_m\hat{\mathbf{D}}\|_2 \quad (5.16)$$

over all  $(n \times p)$  matrices  ${}_m\mathbf{D}$  of rank  $m$ . The equivalent form of Eq. (5.15) is

$$\sum_{i=1}^n \sum_{j=1}^p (d_{ij} - {}_m\hat{d}_{ij})^2 = \min. \quad (5.17)$$

*A note on missing data.* The PC/EOF method requires data that are continuous in space and time. In general, missing data can include observations of one or more variables for one or more epochs. If a GRACE time series is analyzed, the missing data will include the observations for all variables (grid values) at one or more epochs. In such a case, the data gaps can be filled by least-squares predicted observations using the estimated amplitudes and phases of the annual and semi-annual signals and possibly a trend. Alternatively, the

missing observations can be filled with zeros. In both cases, the data covariance matrix has a rank deficiency that equals the number of the missing epochs. The significant eigenvalues of the data covariance matrix can differ by approximately 1% if the missing data comprise 10% of the size of the data matrix.

### 5.3.2 Selecting a subset of principal components

The number of principal components retained is often based on a subjective decision and experience rather than on an objective criterion. Often, simple but efficient rules of thumb are preferred. Generally, there exist three groups of methods for selecting the significant principal components. The first group includes methods based on the amount of the data variance explained. The usually applied *ad hoc* rule of thumb is to retain enough principal components so that at least 70% of the variance of the analyzed data set is explained. This selection criterion is based on the cumulative percent variance computed as

$$CPV(m) = 100 \left[ \frac{\sum_{i=1}^m \lambda_i}{\sum_{i=1}^n \lambda_i} \right] \% , \quad (5.18)$$

where  $m$  is the number of the principal components retained (Valle *et al.*, 1999).

A powerful testing method is North's rule of thumb. According to North *et al.* (1982), the 95% confidence error of the estimated eigenvalues is computed by the approximate relationship

$$\Delta\lambda \approx \lambda \sqrt{2/f} , \quad (5.19)$$

where  $f$  denotes the degrees of freedom, i.e., the number of the independent observations. To compute the degrees of freedom, the autocorrelation of the data should be known. The rule of thumb states that if the error of the eigenvalue is larger than or comparable with the difference between two adjacent eigenvalues then it is unlikely that these eigenvalues represent separate modes. Another simple and efficient method is an inspection of the leveraging point of the eigenvalue spectrum that marks the transition from the more rapid decline of the signal modes to the more gradually decreasing spectrum of the noise components.

The second group includes the time history methods that test the principal component time series for being random samples of a white noise process. One such method is the Kolmogorov-Smirnov (KS2) rule given by Preisendorfer (1988). If the postulated null hypothesis (the principal component represents white noise) is not accepted at the chosen significance level, the principal component is accepted to represent a signal mode.

The third group includes space-map methods that are based on the examination of the EOF patterns that should resemble some predefined signal mode patterns. Though heuristic, the space-map method is an effective approach in the PC/EOF analysis of the GRACE signal over the continents for identifying the main signal modes. For example, in North America, the main modes of variability are expected to account for continental water mass changes and the interior Earth mass redistribution due to postglacial rebound.

The eigenspectrum of the data covariance matrix of the GRACE-observed geoid changes in North America contains signal modes explaining the continental water mass variability and the postglacial rebound mass redistribution, and very likely errors in the de-aliasing models of atmospheric variability, tides and ocean signal, leakage of the ocean signal over the continent, and residual correlated errors (not removed by the de-correlation filter). The residual correlated errors are additionally smoothed by the isotropic filter applied and may appear as signals. Because of the complexity of the GRACE errors, in this thesis, it is found that the *ad hoc* rule of thumb complemented with the space-map methods is the most efficient technique for selecting the number of the retained principal components.

### **5.3.3 Rotation of principal components**

PC/EOF analysis decomposes the data matrix in orthogonal modes, which do not necessarily correspond to physical modes; see, e.g., Benzi *et al.* (1997). Because of the orthogonal constraints imposed on the loading patterns, some undesirable effects may exist. The most important effect is the dependence of the patterns on the size and shape of the area, which is the so-called “data domain dependence”. In this case, the interpretation of the extracted modes as geophysical signals is meaningless. According to Richman (1985), rotation of principal components allows for detecting the unwanted effects. Essentially, the purpose of rotation is to find a new basis in the  $m$ -dimensional space, in which the rotated

modes are linear combinations of the original modes. One of the commonly applied algorithms is the *varimax rotation* of either the EOF patterns or principal component time series (see, e.g., Preisendorfer, 1988). The varimax rotation of the latter maximizes the variance of the squared covariances between each rotated principal component and each of the original principal component time series. Maximizing the variance leads to few large loading patterns and many close to zero patterns. Hence, the rotation helps to discriminate among the modes and facilitates their interpretation. Because the rotated EOF (REOF) patterns are not orthogonally constrained, they are less dependent on the data domain (Horel, 1981). Moreover, for simple signals, the varimax rotated principal components are independent of the data domain (*ibid.*). A matrix form code for the iterative algorithm for varimax rotation of the principal component time series is given by Björnsonn and Venegas (1997) as follows:

$$\begin{aligned}
& \tilde{\mathbf{V}} = {}_m\mathbf{D}^T {}_m\mathbf{T} \\
& \text{limit} = 1 \\
& \text{while } \text{limit} > 1.10^{-7} \\
& \quad \mathbf{Z} = {}_m\mathbf{D} \left[ \tilde{\mathbf{V}}^3 - \tilde{\mathbf{V}} \text{diag}(\text{mean}(\tilde{\mathbf{V}}^2)) \right] \\
& \quad [\mathbf{W}, \mathbf{K}] = \text{eig}(\mathbf{Z}^T \mathbf{Z}) \\
& \quad {}_m\tilde{\mathbf{T}} = \mathbf{Z} \mathbf{W} \mathbf{K}^{-1/2} \mathbf{W}^T \\
& \quad \tilde{\mathbf{V}} = {}_m\mathbf{D}^T {}_m\tilde{\mathbf{T}} \\
& \quad \text{limit} = \max({}_m\tilde{\mathbf{T}} - {}_m\mathbf{T}) \\
& \text{end}
\end{aligned} \tag{5.20}$$

where the matrix  ${}_m\mathbf{T}$  contains  $m$  principal component time series. The new rotated principal component time series are given in  ${}_m\tilde{\mathbf{T}}$ , and the new EOF patterns are given in the column vectors of  $\tilde{\mathbf{V}}$ .

For the sake of visualization, the principal component time series are normalized by their maximum values. Therefore, the EOF patterns are multiplied by the respective normalization factor to obtain the spatial amplitudes of the extracted signal modes.

### 5.3.4 GRACE-observed geoid changes in North America

The selected region for this study spans 30°N to 75°N and 170°W to 50°W and covers most of North America. The study area is characterized by complex spatio-temporal mass changes including ice/snow and liquid water variations, postglacial rebound, and melting of the Canadian ice cap and Alaska glaciers. The polar areas of Canada are excluded because of uncertainties in the estimates of the melt rates of the polar ice caps, but the Alaska glaciers are retained. The study area also includes the Canadian and US Cordillera and the Québec-Labrador region, both of which exhibit a large amplitude annual signal predicted by the continental water storage models.

Essentially, two cases that use the PC/EOF analysis can be outlined. First, the GRACE-observed water mass variations can be analyzed and compared with hydrology model outputs. For this purpose, the GRACE time series should be corrected for the postglacial rebound signal. Second, the GRACE-observed geoid change signal can be analyzed in terms of the Earth interior mass redistribution associated with postglacial rebound. In this case, the hydrology signal should be removed from the GRACE time series before the PC/EOF analysis. In both cases, it should be ensured that

- the extracted modes of variability are not subject to distortions as a result from the imposed orthogonality constraints;
- the significant modes represent geophysical phenomena validated by means of a comparison with geophysical models.

The capabilities of the PC/EOF analysis for extracting water mass variations in North America have been studied by Rangelova *et al.* (2007a). In this thesis, the total GRACE-observed change in the geoid height (Case 1), including postglacial rebound and hydrology, is analyzed. This allows, without contaminating the GRACE signal with errors in the hydrology model correction, for studying the effect of rotation of principal components and mitigating the possible distortion in the analyzed signal due to the imposed orthogonality constraints. Subsequently, the GRACE-observed change in the geoid height corrected for hydrology is analyzed in Case 2.

***Case 1- total GRACE-observed change in the geoid height***

Figure 5.8a shows the first twelve principal components ordered in percentage of the total data variance explained. Based on an inspection of the eigenspectrum, it can be expected that the first four principal components represent signal modes, which is confirmed with 95% confidence by the KS2 selection rule. The first and second principal components explaining approximately 80% of the data variance (see Table 5.3) are clearly distinguishable in the spectrum. The third and fourth principal components account for approximately 12% of the data variance. Only the first four principal components are rotated. Experiments in this study have shown that the rotated principal components are insensitive to the dimension of the space in which the rotation is performed. This has been verified by rotating a different number of the principal components.

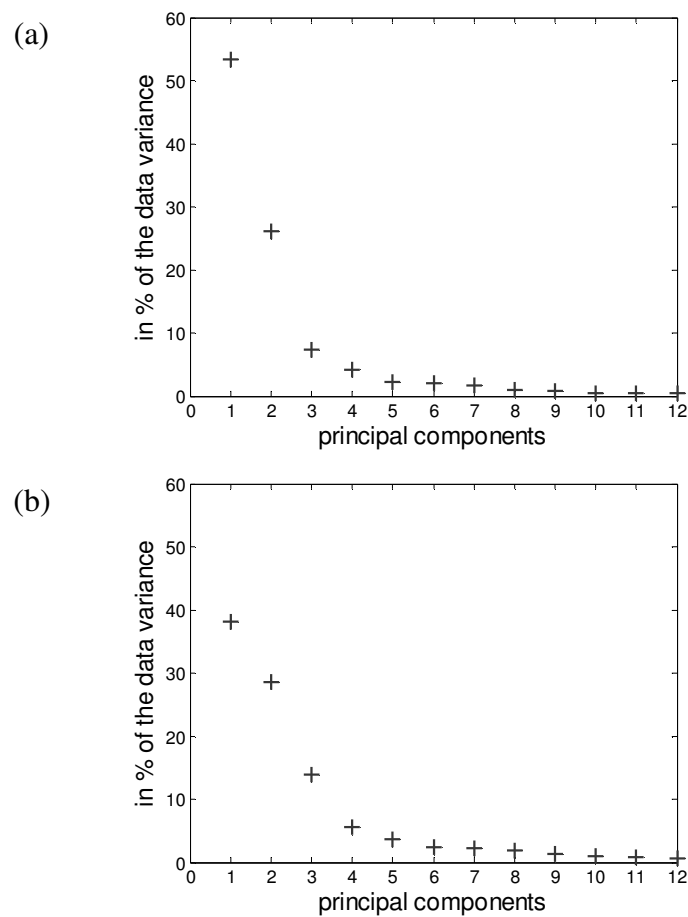


**Figure 5.8:** Principal components for (a) Case 1 and (b) Case 2.

**Table 5.3:** Data variance (in percentage) explained by the principal components

Case study	1 PC	2 PC	3 PC	4 PC
Case 1	53.5	26.0	7.2	4.3
Case 2	38.5	28.7	13.9	5.6

The first mode represents the annual cycle of the snow mass changes in the Cordillera and the Québec-Labrador regions (Figure 5.9). The first principal component time series in Figure 5.10 accounts for a maximum (positive change) in April and a minimum (negative change) in September/October. This time evolution is clearly visible from the fall of 2003 until the spring of 2006. Because the first mode has a positive EOF pattern over the analyzed region, according to Horel (1981), the second mode could then be bi-polar (one negative and one positive loading over the data domain) with a zero line passing close to the maximum of the first mode. This, in fact, is observed for the second EOF pattern. The varimax rotation of the principal components should be able to eliminate this effect if it was a result of the imposed orthogonality on the eigenvectors. The first rotated EOF (REOF) in Figure 5.9 contains the pattern originally seen in the second EOF, which rejects possible distortions of the signal mode. In fact, the patterns observed in the second EOF are associated with geophysical signals. The negative EOF values and the positive slope of the second principal component time series in Figure 5.10 account for negative geoid changes in southeastern Alaska due to glaciers melting (see Tamisiea *et al.*, 2005 and Chen *et al.*, 2006a). The positive pattern southwest of Hudson Bay accounts for positive geoid changes as a result of a water mass increase in the prairie region observed also in the water storage models. The third and fourth modes have small amplitudes and do not account for significant geoid changes, neither do they change upon rotation. The examination of their principal component time series does not reveal structured signals.

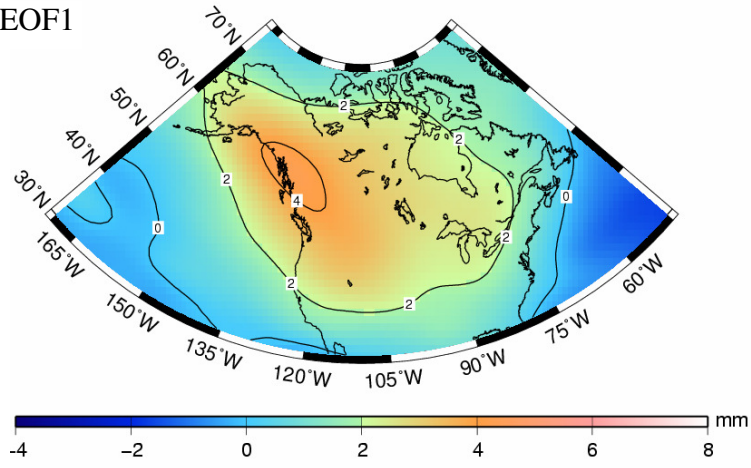
### ***Case 2- GRACE-observed change in geoid height corrected for hydrology***

One disadvantage of the PC/EOF analysis consists in the fact that if a periodic signal and a trend have a common geographical footprint, then the method cannot separate them. The principal component time series will show both signals. An example is the principal component time series in Figure 5.10 of a negative trend with a superimposed annual cycle. This is also observed for the secular GIA geoid rate superimposed by the annual snow variations in the Québec-Labrador region and by the long-term hydrology geoid changes southwest of Hudson Bay; see the second REOF in Figure 5.9. Therefore, additional information is necessary to separate the geophysical signals. The GLDAS hydrology model is used to correct the GRACE SH coefficients.

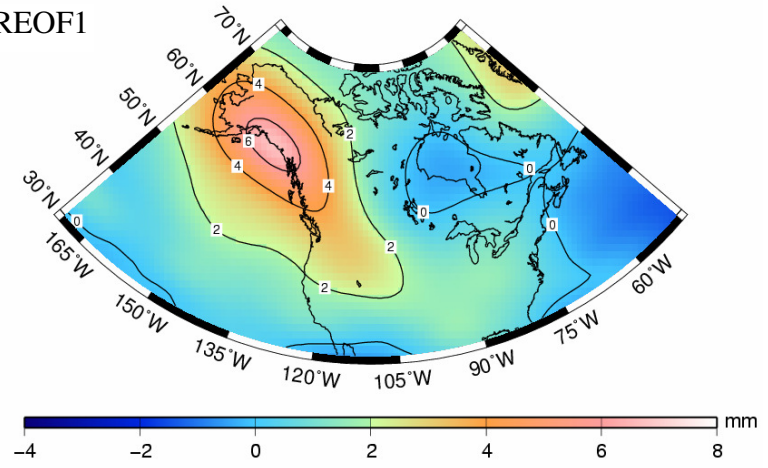
The first principal component time series shows annual periodic variations with a broad late spring-early summer maximum and a sharp fall minimum (Figure 5.10). This signal could be associated with a hydrology signal observed by GRACE but not accounted for in the GLDAS model (Figure 5.11). The second EOF and the principal component time series show a geoid rise west of Hudson Bay and in the Québec region. According to Table 5.3, the removal of the hydrology signal decreases significantly the amount of the variance explained by the first mode, while the amount of the variance associated with the second mode increases. This suggests that the two modes may not be separated and, in fact, represent one signal. This is supported by the first REOF which represents positive geoid changes in the Hudson Bay region that resembles well the pattern of the postglacial rebound signal but still exhibits annual variations.

The role of the rotation in the PC/EOF analysis should not be overestimated since this is one of the infinitely many solutions that can be obtained from the original principal components. Thus, it is always possible that a better method exists. For example, the oblique methods of rotation could also provide acceptable results in the studied case. In addition, there is no guarantee that a physically meaningful explanation can be attached to the rotated principal components. Therefore, validation with geophysical models must rule any decision whether the principal components represent real signals.

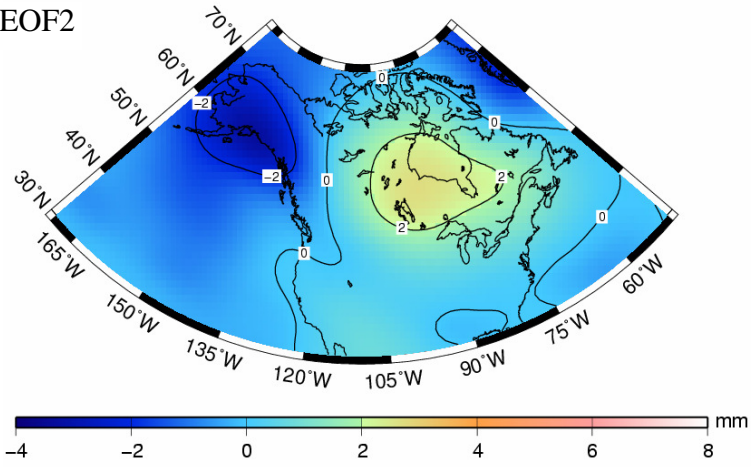
EOF1



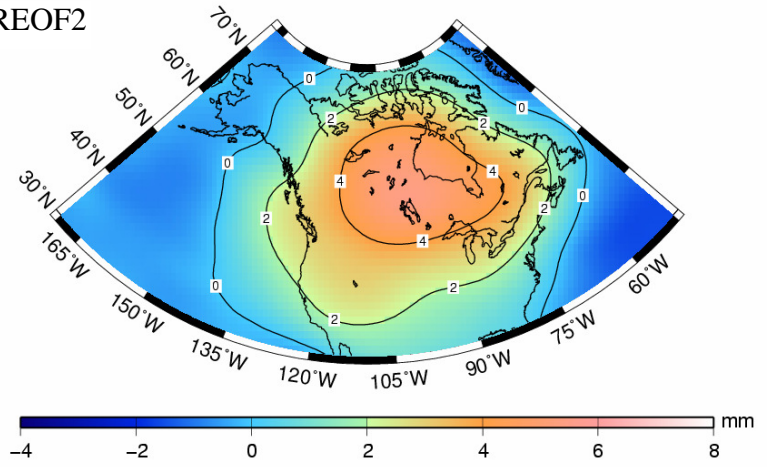
REOF1



EOF2



REOF2



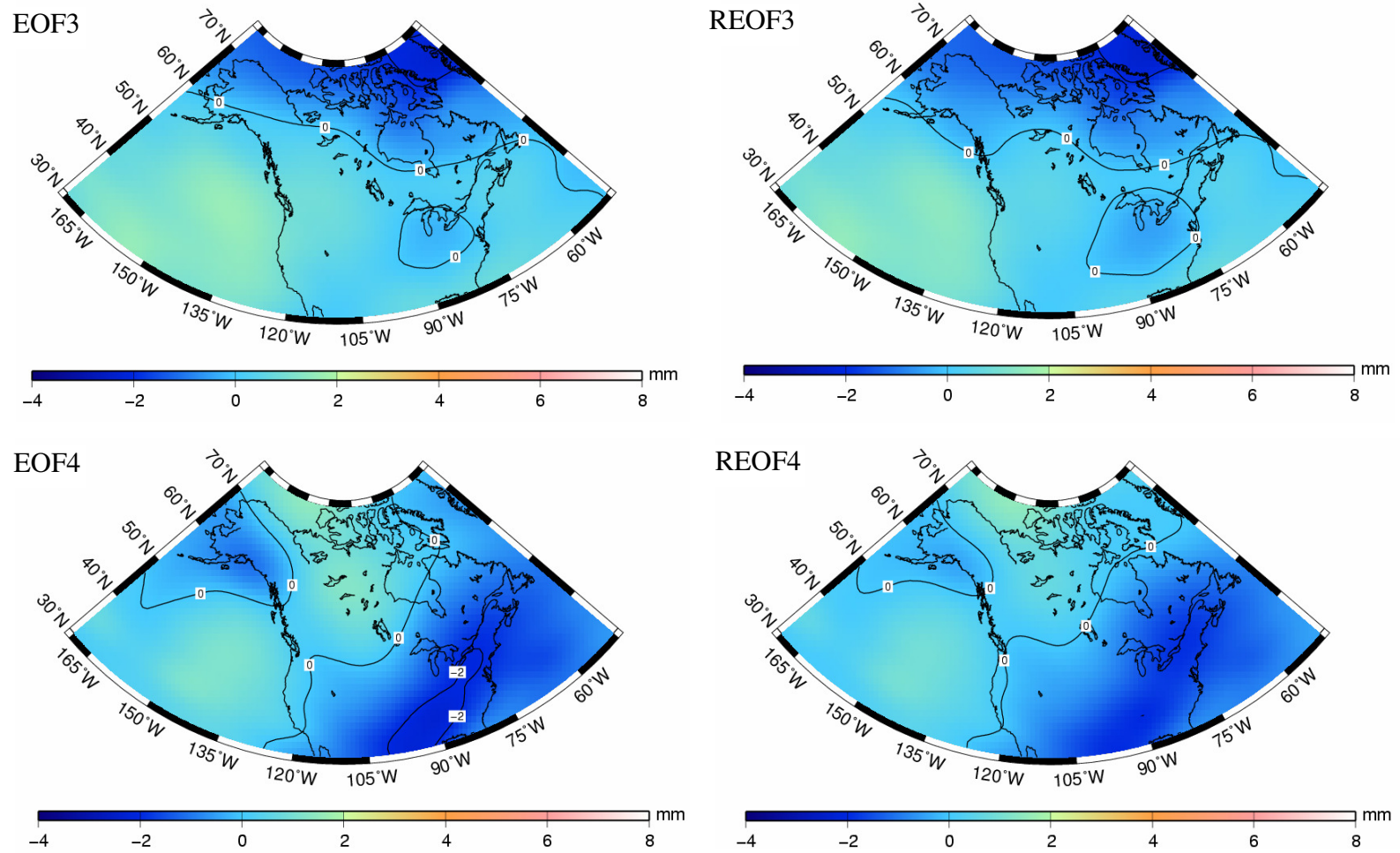


**Figure 5.9:** EOF and REOF loading patterns for Case 1.

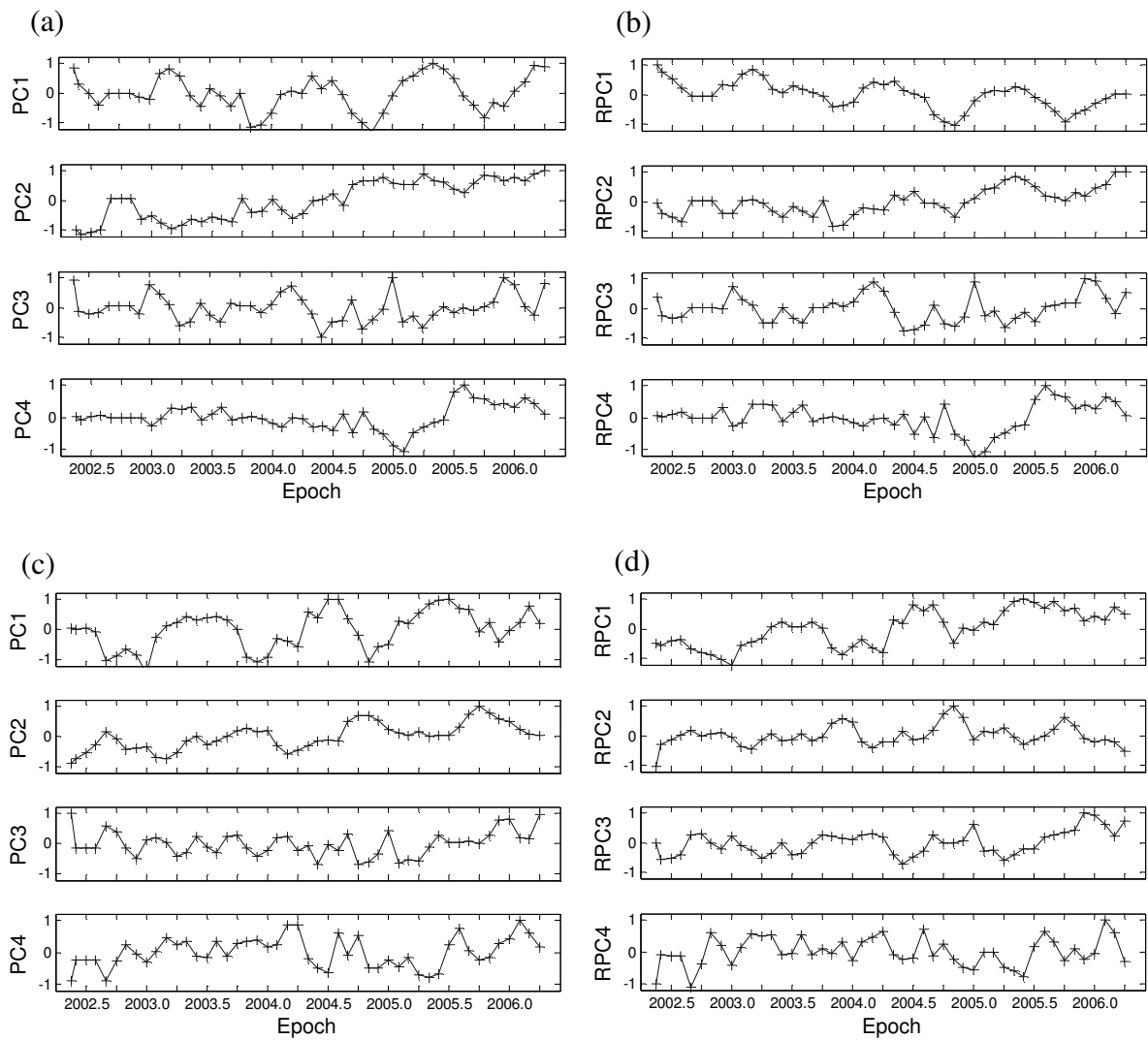
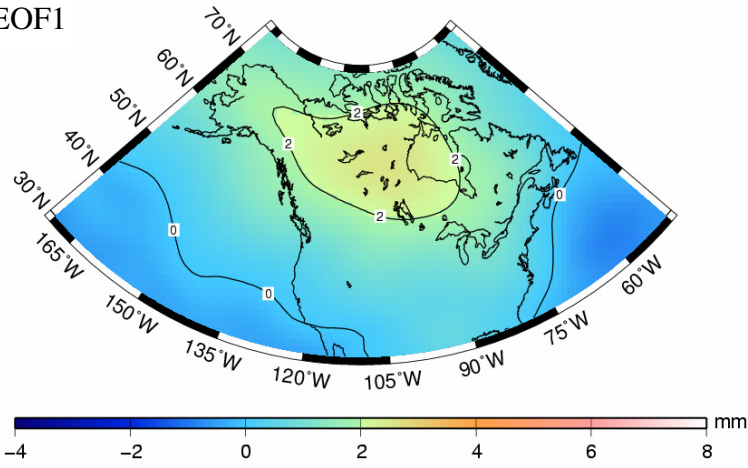
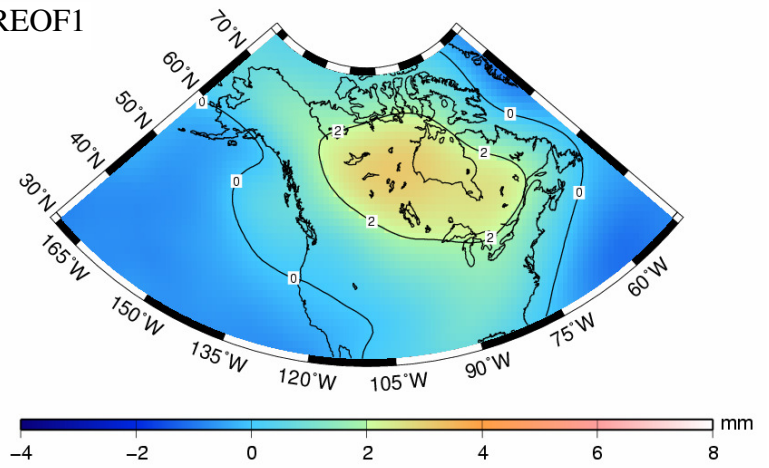


**Figure 5.10:** PC and rotated PC time series for Case 1 (a and b) and Case 2 (c and d).

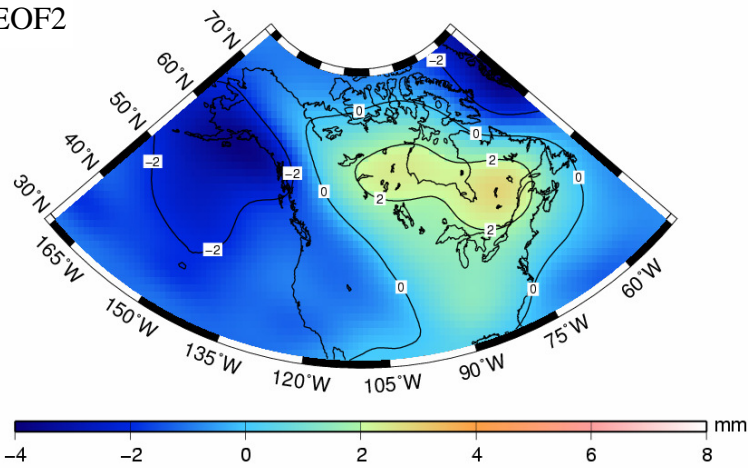
EOF1



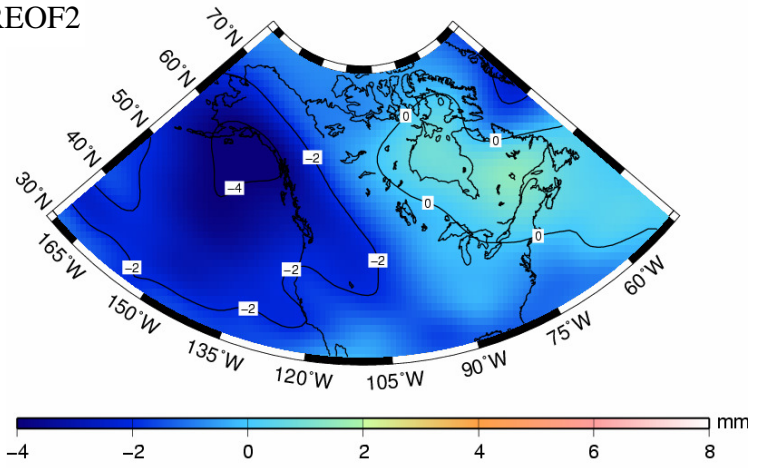
REOF1



EOF2



REOF2



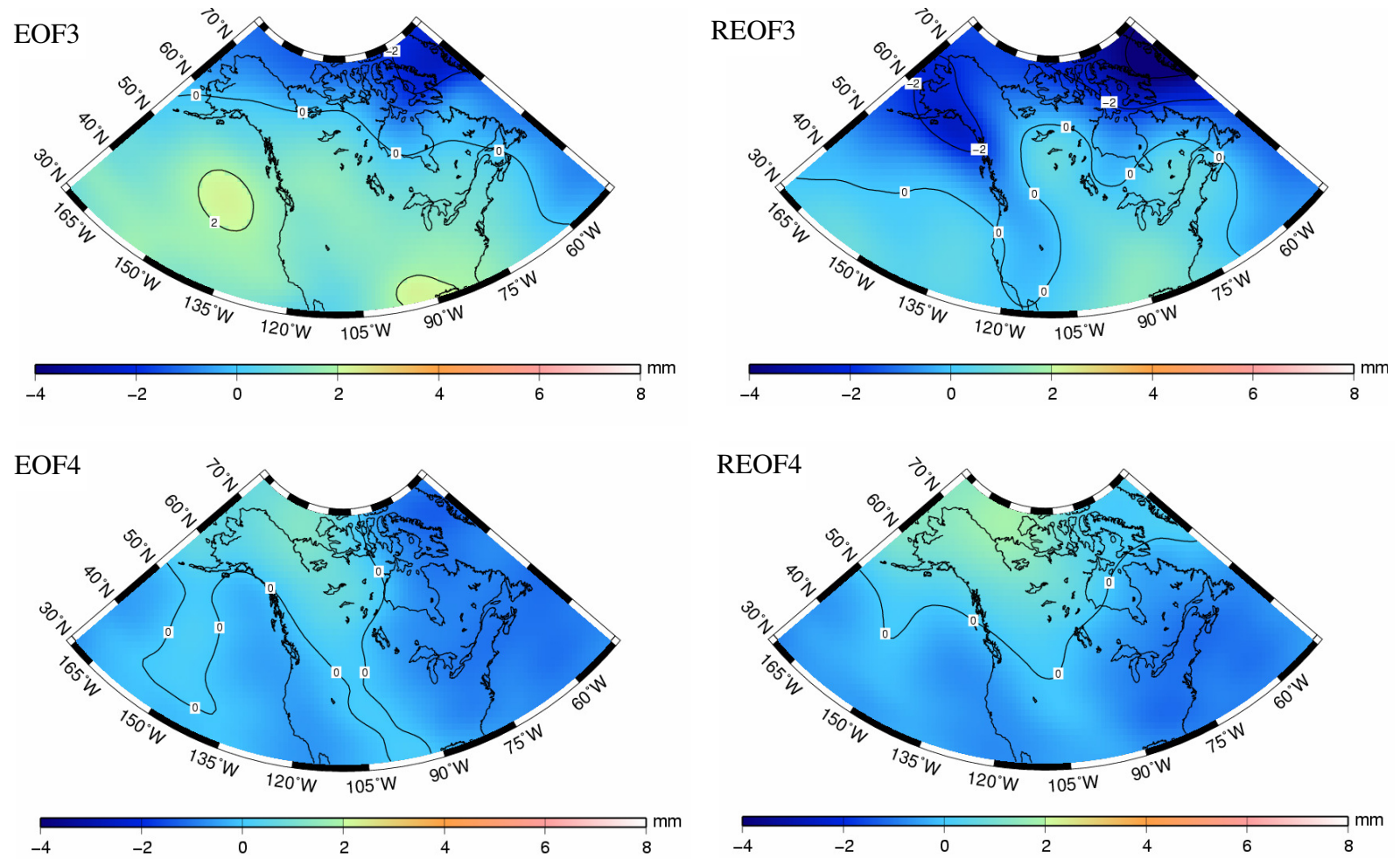


**Figure 5.11:** EOF and REOF loading patterns for Case 2.

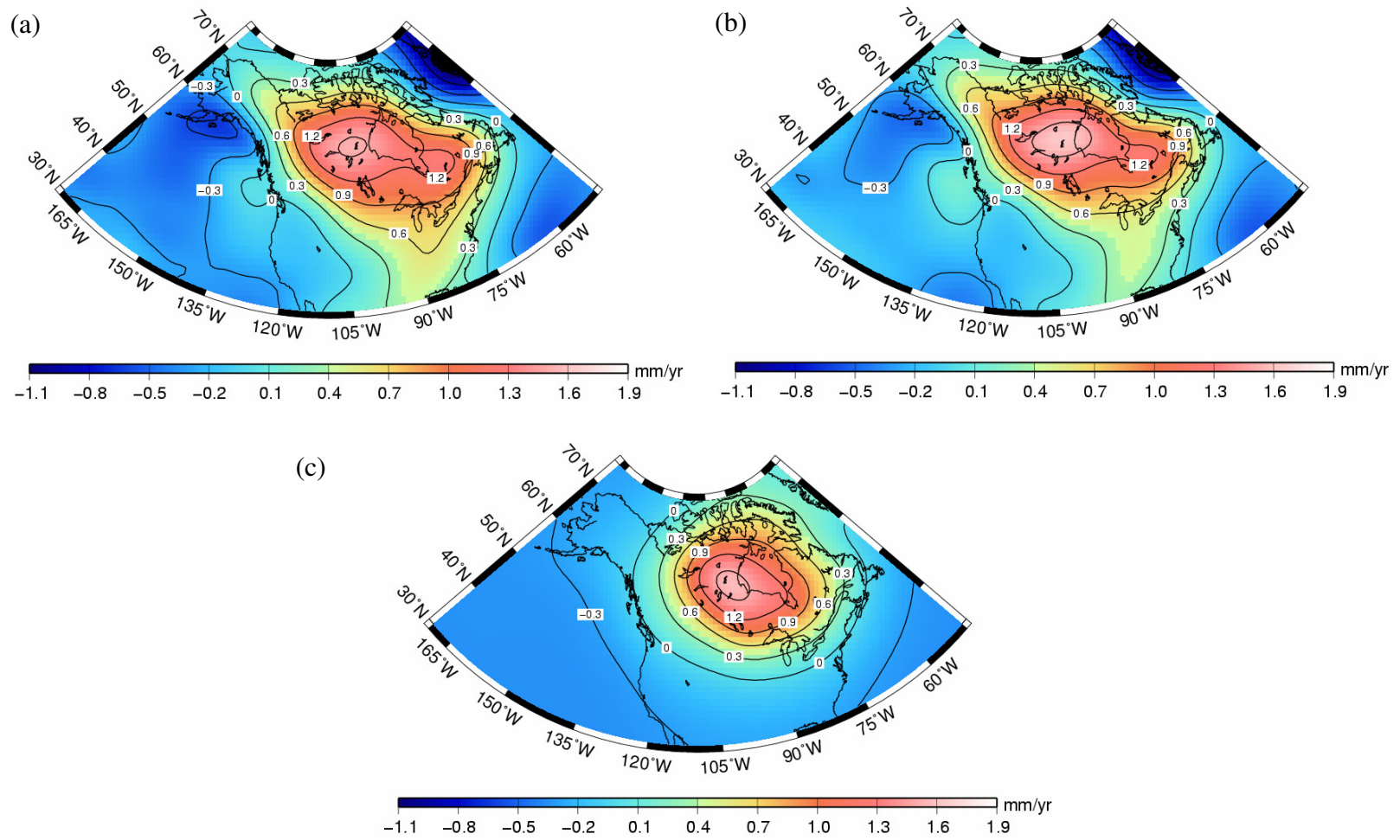
### 5.3.5 Validation of the PC/EOF geoid rate and summary

Figure 5.12a depicts the geoid rate derived from the first three rotated principal components by weighting the EOF patterns with the trend component estimated by means of a least-squares fit to the principal component time series. The PC/EOF geoid rate is compared with the rate estimated by least-squares fitting of the time series of the SH coefficients (Figure 5.12b). Small differences that result from the filtered principal components are observed. The PC/EOF geoid rate is compared with the GIA-induced geoid rate predicted by the ICE-5G (VM2) model of Peltier (2004) of spherical degree and order 70 and smoothed with a Gaussian filter of 400 km half-width (Figure 5.12c). Evident from the comparison is the similar geoid rate peak located west of Hudson Bay. The differences in the geoid rate pattern are possibly due to a long-term hydrology variability not removed by the GLDAS correction, the spatial leakage of the Greenland and Alaska ice melting, and propagated GRACE measurement and data processing errors in the observed geoid trend.

In this section, by means of the two studied cases, it has been shown that the PC/EOF analysis is an efficient method for modelling the temporal geoid variations on a continental scale. For the purpose of future applications, the main advantages and shortcomings of the method are summarized in the context of estimating the GRACE-observed geoid rates.

#### *Advantages*

- A non-parametric method, whose base functions are data-dependent and adapt to the particular data set.
- It allows for assessing the effect of the inter-annual and long-term geoid variability on the estimated trend.
- By appropriate rotation of the base functions and data variance redistribution, it could be possible to separate two spatial trends (with different geographical footprint) in different principal components. This opens possibilities for studying leakage of different signals over the continental land masses.



**Figure 5.12:** Rate of change of the geoid height derived from (a) the first three principal components in Case 2, (b) a least-squares fit of the GRACE SH time series, and (c) the smoothed ICE-5G (VM2) model.

### *Disadvantages*

- Distortions in the extracted spatial patterns due to the imposed orthogonality of the base functions are possible.
- The method does not allow error propagation.
- Requires continuous data both in space and time.

## **5.4 Optimal combination of GRACE, terrestrial gravity, and GPS data**

In the context of the velocity surface approximation, the optimal combination of GRACE-observed rates of the absolute vertical displacement, terrestrial gravity rates, and GPS vertical velocities requires appropriate base functions. Rangelova and Sideris (2006b) have suggested combining the GRACE-observed geoid rates and the geoid rates estimated from the Earth's surface data in a spherical cap using spherical cap harmonic functions and least-squares adjustment. One limitation of the proposed approach is the low degree of the base functions used to approximate the surface. Because of the small radius of the spherical cap, higher degree harmonics are unstable, which leads to ill-conditioned matrices in the least-squares adjustment. Another limitation stems from the fact that the terrestrial gravity rates and GPS velocities do not cover the entire spherical cap, causing loss of orthogonality of the base functions. To avoid these shortcomings, a least-squares collocation approach for combining GRACE and Earth surface data is studied in the following section.

### **5.4.1 Mathematical model**

The mathematical model is given by Eq.(4.1). Here, the observation vector

$\mathbf{I} = [\mathbf{I}_{\text{GRACE}}^T \mathbf{I}_{\text{AG}}^T \mathbf{I}_{\text{GPS}}^T]^T$  includes the GRACE-observed rates of the absolute vertical displacement,  $\mathbf{I}_{\text{GRACE}} = [\dot{h}_1 \ \dot{h}_2 \ \dots \ \dot{h}_n]^T$ ; the rates of change of the terrestrial gravity,  $\mathbf{I}_{\text{AG}} = [\dot{g}_1 \ \dot{g}_2 \ \dots \ \dot{g}_{n_2}]^T$ ; and the GPS vertical velocities,  $\mathbf{I}_{\text{GPS}} = [\dot{h}_1 \ \dot{h}_2 \ \dots \ \dot{h}_{n_3}]^T$ .

The  $(n \times k)$  coefficient matrix  $\mathbf{A}$ , where  $n = n_1 + n_2 + n_3$  and  $k$  is the number of the base functions, is defined as

$$\mathbf{A} = \begin{bmatrix} \mathbf{1} & \mathbf{0} & \mathbf{A}_{\text{GRACE}} \\ \mathbf{0} & \begin{bmatrix} \dot{\mathbf{g}} \\ \mathbf{h} \end{bmatrix} & \mathbf{A}_{\text{AG}} \\ \mathbf{0} & \mathbf{0} & \mathbf{A}_{\text{GPS}} \end{bmatrix}. \quad (5.21)$$

The vector  $\mathbf{x} = [x_1 \ x_2 \ \cdots \ x_k]^T$  contains two bias terms of the GRACE and terrestrial gravity data with respect to the GPS velocities and the unknown weights of the base functions. The error covariance matrix is defined as

$$\mathbf{C}_v = \begin{bmatrix} \mathbf{C}_{v_{\text{GRACE}}} & \mathbf{0} & \mathbf{0} \\ \mathbf{0} & \mathbf{C}_{v_{\text{AG}}} & \mathbf{0} \\ \mathbf{0} & \mathbf{0} & \mathbf{C}_{v_{\text{GPS}}} \end{bmatrix} = \begin{bmatrix} (\sigma^2 \mathbf{P}^{-1})_{\text{GRACE}} & \mathbf{0} & \mathbf{0} \\ \mathbf{0} & (\sigma^2 \mathbf{P}^{-1})_{\text{AG}} & \mathbf{0} \\ \mathbf{0} & \mathbf{0} & (\sigma^2 \mathbf{P}^{-1})_{\text{GPS}} \end{bmatrix}. \quad (5.22)$$

Similar to Section 4.2 in Chapter 4, the data covariance matrix  $\mathbf{C}_l$  is defined as

$$\mathbf{C}_l = \begin{bmatrix} \mathbf{C}_{v_{\text{GRACE}}} & \mathbf{0} & \mathbf{0} \\ \mathbf{0} & \mathbf{C}_{\dot{g}} + \mathbf{C}_{v_{\text{AG}}} & \mathbf{C}_{\dot{g}h} \\ \mathbf{0} & \mathbf{C}_{h\dot{g}} & \mathbf{C}_h + \mathbf{C}_{v_{\text{GPS}}} \end{bmatrix}, \quad (5.23)$$

where  $\mathbf{C}_{\dot{g}}$  and  $\mathbf{C}_h$  are the signal auto-covariance matrices of the terrestrial gravity rates and GPS velocities, respectively, and  $\mathbf{C}_{\dot{g}h} = (\mathbf{C}_{h\dot{g}})^T$  is their cross-covariance matrix. It is assumed that the GRACE-observed rates do not contain a signal component. The covariance matrices of the predicted rates and the signal components of the terrestrial gravity and GPS observations are given by Eq. (4.39) and are not repeated here.

#### 5.4.2 Combined models for rates of the vertical displacement and the geoid height

Upon solving the minimization problem given by Eq.(4.4), the rates of the vertical displacement, terrestrial gravity, and the geoid height are predicted. The GRACE-observed rates of the vertical displacement are computed by means of Eq.(2.34). The error covariance matrices are taken to be diagonal; for the GRACE-observed rates of the vertical displacement, a standard deviation  $\sigma_{\text{GRACE}} = 1.4 \text{ mm/yr}$  is assumed. This implies that if the error of the GRACE-observed vertical displacement is 1 mm/yr, the covariance matrix is scaled by  $\sigma_{\text{GRACE}}^2 = 2.0$ . The scale factors of the error covariance matrices of the terrestrial gravity rates and GPS velocities are unknown. Therefore,  $\sigma_{\text{AG}}^2 = 1.0$  and  $\sigma_{\text{GPS}}^2 = 1.0$  are assumed. Variance component estimation (VCE) using the BIQUE technique (Section 4.2.1) is applied to resolve the relative weighting among the three data types (Figure 5.13). Because the estimated variance components depend on outliers in the data, the procedure includes Baarda's data-snooping outlier detection (Section 4.2.1). The outliers are removed before estimating the variance components and scaling the error covariance matrices. Different strategies to deal with outliers are studied extensively in Chapter 6 of this thesis.

The estimated rates of the terrestrial gravity and GPS velocities (Figure 5.14) at the data point locations allow to assess the capabilities of the least-squares collocation approach for combining the longer wavelength GRACE data (Figure 5.15a) with the local gravity and GPS data. Clearly, the trend component does not describe correctly the rates at the majority of the gravity sites and GPS stations. One logical question is whether the pure functional approach can provide satisfactory approximation by increasing the number of the base functions. As shown in Chapter 3, the approximation of the smooth postglacial rebound surface requires (inverse) multiquadrics with a large shape parameter, which increases the condition number of the normal matrix. This imposes restrictions on the number of the base functions used. Decreasing the shape parameter (and the condition number at the same time) leads to over-fitting the noise in the gravity and GPS data. As in Chapter 4, in this section, it is found that the "multistage" approximation provided by the least-squares collocation approach is more accurate than the functional approach.

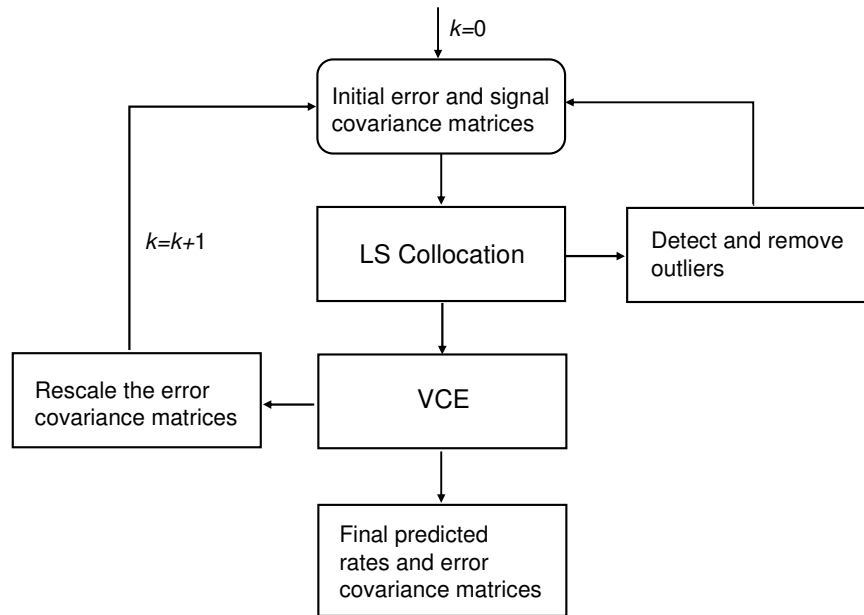


**Figure 5.13:** An iterative estimation procedure including VCE and outlier detection.

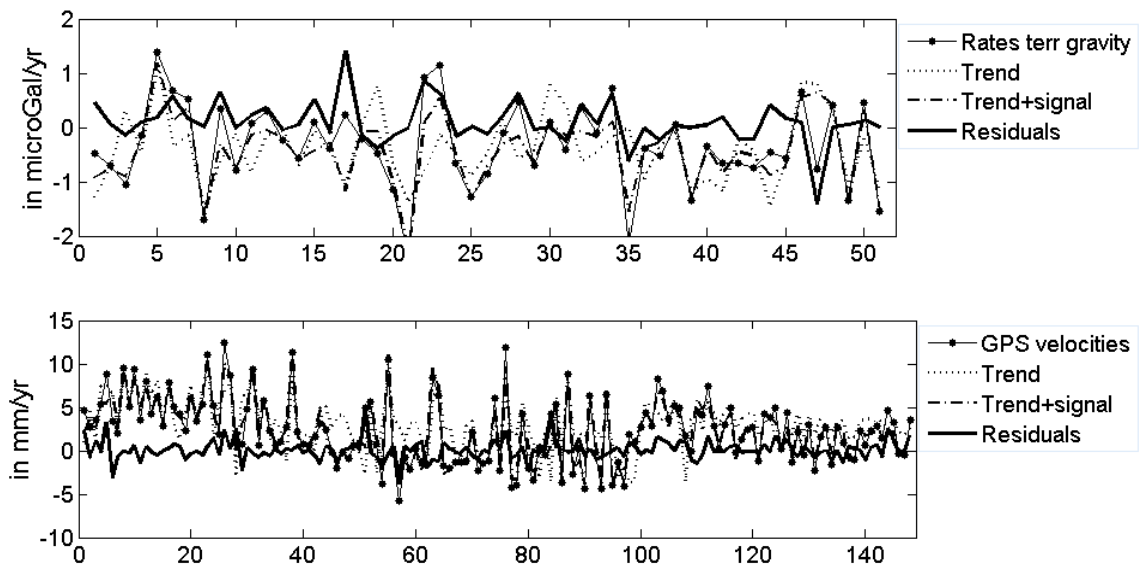


**Figure 5.14:** Estimated rates of the terrestrial gravity and GPS velocities.

Figure 5.15c shows the trend in the vertical displacement rates, which is dominated by the GRACE data. By adding the predicted signal, which varies between  $-0.6$  and  $0.6$  mm/yr, the total rates of the vertical displacement are predicted (Figure 5.15e). The maximum predicted rate of  $12.2 \pm 0.5$  mm/yr is located on the southeast coast of Hudson Bay as in the model in Figure 4.6. Both models have a similar pattern for the southern areas of Canada. Rates from the combined model, however, do not show the pattern in the northern areas inherited from the terrestrial gravity rates in the model in Figure 4.6. The formal accuracy of the predicted vertical displacement rates is given in Table 5.4. As seen from the comparison with the formal errors in Table 4.4, the accuracy of prediction improves significantly with the addition of the GRACE data.

The signal component in the combined model contains mainly unmodelled rates but may contain also correlated measurement and data processing errors in the terrestrial gravity and GPS velocities. Although it is assumed that the latter contribution is smaller than the unmodelled geophysical signal, it is likely that such correlated errors contribute to the signal covariance functions, and therefore can be wrongly interpreted as a real vertical displacement signal. At the same time, these errors can be significantly underestimated if diagonal error covariance matrices are used. Therefore, caution is advised if the predicted signal is interpreted in terms of geophysical or other processes related to vertical crustal displacement and/or mass redistribution.

Figures 5.15b, d, and f display the GRACE-observed rate of change of the geoid height, the trend component, and the total geoid rate. The modelled trend closely resembles the pattern of the GRACE-observed rates with an exception of the peak west of Hudson Bay. The maximum predicted rate is  $1.5 \pm 0.04$  mm/yr over Hudson Bay.

**Table 5.4:** Accuracy of predicted rates of vertical displacement and geoid height, mm/yr

Rate	Min	Max	Mean
$\dot{h}$	0.3	0.4	0.6
$\dot{N}$	0.03	0.04	0.06

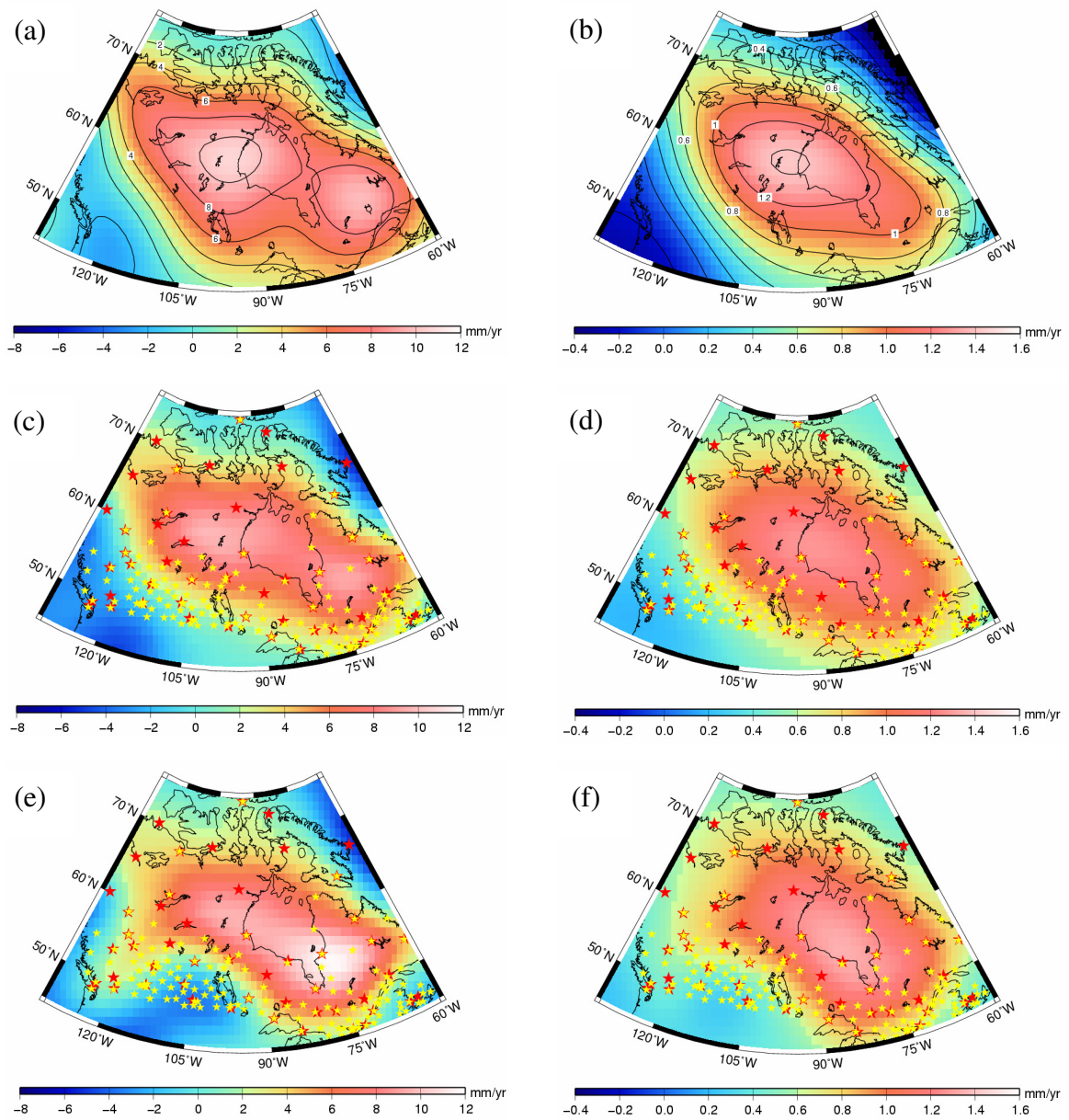


**Figure 5.15:** Predicted rates of the vertical displacement and the rate of change of the geoid height for Canada: (a) and (b) GRACE-observed rates, (c) and (d) modelled trend component, and (e) and (f) the trend plus the signal components. The gravity sites and GPS stations are plotted with red and yellow stars, respectively.

Table 5.5 includes estimated variance components after two iterations. At the first iteration, three outliers in the terrestrial gravity rates are detected. At the second iteration, outliers are found at six GPS stations. As seen from the estimated variance components, all three error covariance matrices need to be down-scaled after removing the outliers. As a consequence, the mean standard deviations (the last column in Table 5.5) also decrease. Referring to the discussion above, the residuals are likely to be underestimated if the signal covariance matrices absorb correlated measurement and data processing errors as a result of the isotropic spatial averaging used to compute the empirical covariance functions. In this case, the estimated variance factors would provide optimistic error covariance matrices. This problem can be overcome only if full error covariance matrices are available together with estimating covariance factors as well as signal variances. Such a rigorous approach would require collocated GPS and gravity data, which, at present, are not available.

**Table 5.5:** Estimated variance factors and a posteriori standard deviations, in mm/yr

Data set	$\hat{\sigma}^2$	Min	Max	Mean
GRACE	0.25	0.5	0.5	0.5
AG (in $\mu\text{Gal}/\text{yr}$ )	0.64	0.05	0.72	0.33
GPS	0.50	0.04	5.3	1.7

## 5.5 Summary

In this chapter, the GRACE-observed rates of the geoid height and the absolute vertical displacement have been modelled. For this purpose, the PC/EOF analysis and the traditional least-squares (LS) fitting have been used. By means of two studied cases (Figure 5.9, Figure 5.10, and Figure 5.11), the capabilities of the PC/EOF analysis of extracting the GRACE-observed rates are definitely demonstrated. The results of the two methods are compared in Figure 5.12 and Figure 5.16. Evidently, the differences in the geoid rates do not exceed 0.2 mm/yr along the north-south profile. Much smaller differences are observed along the west-east profile.

Perhaps the most interesting outcomes of the studies performed in this chapter are the combined empirical models of the rates of the geoid height and the absolute vertical displacement (Section 5.4 and Figure 5.15). It has been shown that the least-squares collocation approach can be applied to combine the GRACE and terrestrial data. The combined model is compared with the GRACE-observed rates of change of the geoid height and the smoothed ICE-5G (VM2) model in Figure 5.16. An interesting observation is the significant deviation of the combined geoid rates from the ICE-5G (VM2) model and the GRACE-observed rates west of Hudson Bay. The combined solution in that area is dominated by few terrestrial gravity rates and GPS velocities that are more accurate than the GRACE-observed rates. In fact, the terrestrial gravity and GPS data do not indicate the large geoid rise signal predicted by the ICE-5G (VM2) model. This demonstrates the importance of the availability of well distributed terrestrial data for validating the secular rates of change of the geoid height.

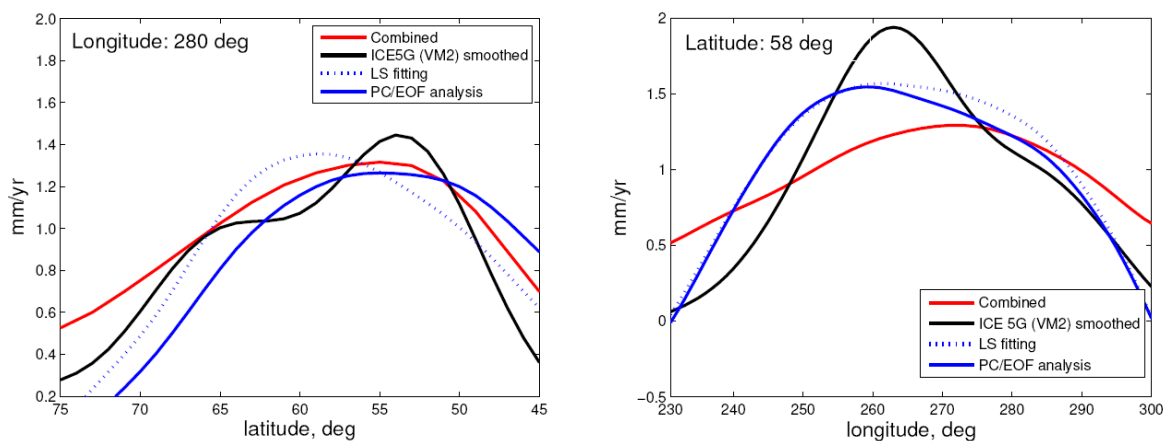


**Figure 5.16:** Comparison of the geoid rates computed by least-squares (LS) fitting and PC/EOF analysis of the GRACE-observed geoid changes and a combination of terrestrial and GRACE data along north-south and west-east profiles. The smoothed with a Gaussian filter (400 km) ICE-5G (VM2) model is also given.

By means of applying iterated outlier detection (Baarda's data snooping method) and variance component estimation (BIQUE method) in the combined solution, it has been shown that the estimated variance factors of the error covariance matrices of the terrestrial gravity and GPS data decrease after removing the erroneous observations. In Chapter 6, the problem with outliers in combining heterogeneous data will be dealt using a robust least-squares adjustment procedure.

## Chapter Six: Practical aspects of modelling rates of vertical displacement and geoid height

As the measurements from geodetic observations become more accurate, they are implemented to not only empirically derive velocity surfaces (e.g., Sella *et al.*, 2007) but also to infer mantle viscosity (e.g., Park *et al.*, 2002). Accurate empirical models for vertical crustal displacement are of particular interest in the Great Lakes region, where the line of zero motion (hinge line) is an important constraint for postglacial rebound modelling (Tushingham, 1992; Mainville and Craymer, 2005). With the abundance of geodetic observations in this region, the gradient of the velocity surface (tilting) can be described relatively well; however, the hinge line can deviate from one data set to another due to datum inconsistencies, different time span and accuracy of measurements, different spatial resolution and presence of erroneous data (outliers), as well as the underlying mathematical model. Outliers can also have a large influence on estimated relative errors of the data sets. Reliably estimated error bounds of the empirical rates of crustal displacement are required to define the uncertainty with which the mantle viscosity profile can be inferred in the inversion of the empirical rates (e.g., Paulson *et al.*, 2007).

The objectives of the study in this chapter involve

- studying the influence of outliers on the hinge line and gradient of the vertical velocity surface;
- studying the capabilities of different approaches to handle outliers including the conventional methods for outlier detection, such as the data snooping technique, and robust methods, such as the iterative re-weighting least-squares approach.

## 6.1 Problem statement

Different approaches to deal with outliers have been outlined by Kern *et al.* (2005). The most intuitive way is to remove the outliers from the data set at the expense of losing information about the approximated surface. This can be an important consequence if the data points are very irregularly distributed and large areas have minimal data constraints. Alternatively, the outliers can be kept, but their influence can be reduced. This latter approach appears to be more suitable in North America because, as discussed in Chapter 2, crustal displacement is not well constrained in the Hudson Bay region, where the largest PGR signal is observed. Therefore, the iterative re-weighting least-squares (IRLS) approach is implemented and investigated in this study.

In order to properly treat the erroneous data in the empirical models for the vertical displacement rates, an iterative procedure is designed which consists of the following:

- identifying and removing the outliers by data snooping or minimizing their effect by means of IRLS.
- estimating the relative errors of the data sets using variance component estimation (VCE).

Usually, an outlier is defined as an observation that is inconsistent with the rest of the observations due to a grossly falsified measurement (Koch, 1999). Outliers can be classified as (i) additive outliers that appear to be erroneous values isolated from the other values, (ii) innovative outliers that have an effect on the neighbouring values through existing correlations and local patterns, and (iii) bulk of outliers that appear as a group of erroneous values (e.g., Kern *et al.*, 2005). In this study, a classification more relevant to crustal deformation studies is adopted. According to Hekimoğlu (1997), outliers can be classified as random scattered, random adjacent and jointly influential outliers. Random outliers occur accidentally. It is believed that random outliers are normally distributed, but their distribution is different from the distribution of the random errors. In this study, the geometrical distribution of the random outliers in the data domain determines if they are scattered or adjacent. Jointly influential outliers appear as a group of observations affected by an unknown disturbing source. For example, jointly influential outliers could be a few

data points in a GPS network displaced along the vertical due to a measurement fault or a post-processing error. In agreement with Hekimoğlu (1997), it is assumed that the jointly influential outliers have a uniform distribution.

Also, outliers can be classified with respect to their magnitude. Small outliers have a magnitude within  $3\sigma$  and  $6\sigma$ , where  $\sigma$  is the standard deviation of observations, while large outliers have a magnitude between  $6\sigma$  and  $9\sigma$ . Large outliers in a data set likely explain a large portion of data variation. As a consequence, the modified Gram-Schmidt (GS) algorithm (see Chapter 3) would place a base function at that point locations. Therefore, large outliers must be removed from the data set or significantly down-weighted relatively to the good observations.

The problem with outliers is tightly related to the type of base functions employed for approximation of the underlying surface. Inverse multiquadric base functions used extensively in this thesis possess certain robustness with respect to erroneous data. By decreasing the shape parameter of the base functions, the effect of outliers can be localized and vice versa. The larger shape parameter, required for approximation of a smoother vertical displacement surface, allows for spreading the effect of the outliers. In the well constrained areas, this effect can be partly compensated by averaging more data; however, as it will be shown later, the effect of outliers could be significant in the areas with lack of data constraints. Moreover, because the larger shape parameter increases the condition number of coefficient and normal matrices in least-squares adjustment, numerical instabilities can occur. As a consequence, in the weakly constrained areas, the underlying mathematical surface may oscillate resulting in increased possibility that the observations in those areas appear to be erroneous.

Two study cases are investigated: (i) least-squares approximation of vertical displacement rates from a single data set and (ii) an optimal least-squares combination of different data sets. The first case includes simulated outliers and allows for assessing effectiveness of each of the investigated approaches. The output of the second case is a combined model of the rates of vertical displacement in the Great Lakes region based on the most recent GRACE, GPS, and joint tide gauge and satellite altimetry data.

## 6.2 Combined least-squares adjustment model

In this section, the combined least-squares adjustment model given by Rangelova *et al.* (2007b) is presented. The model for a single data set follows directly from the equations below by deleting the matrices related to the second and third data sets.

The observation vector  $\mathbf{l}$  of dimension  $(n \times 1)$ , where  $n = n_1 + n_2 + n_3$ , is expressed as follows:

$$\mathbf{l} = [\mathbf{l}_{\text{GRACE}}^T \ \mathbf{l}_{\text{GPS}}^T \ \mathbf{l}_{\text{TGA}}^T]^T \quad (6.1)$$

with

$$\mathbf{l}_{\text{GRACE}} = [\dot{h}_1 \ \dot{h}_2 \ \dots \ \dot{h}_{n_1}]^T, \quad (n_1 \times 1), \quad (6.2)$$

$$\mathbf{l}_{\text{GPS}} = [\dot{h}_1 \ \dot{h}_2 \ \dots \ \dot{h}_{n_2}]^T, \quad (n_2 \times 1), \quad (6.3)$$

$$\mathbf{l}_{\text{TGA}} = [\dot{h}_1 \ \dot{h}_2 \ \dots \ \dot{h}_{n_3}]^T, \quad (n_3 \times 1). \quad (6.4)$$

The error covariance matrix is the block-diagonal matrix

$$\mathbf{C}_l = \begin{bmatrix} (\sigma^2 \mathbf{P}^{-1})_{\text{GRACE}} & \mathbf{0} & \mathbf{0} \\ \mathbf{0} & (\sigma^2 \mathbf{P}^{-1})_{\text{GPS}} & \mathbf{0} \\ \mathbf{0} & \mathbf{0} & (\sigma^2 \mathbf{P}^{-1})_{\text{TGA}} \end{bmatrix}. \quad (6.5)$$

Observations in each data set are assumed to be not correlated.

The coefficient matrix is defined as

$$\mathbf{A} = \begin{bmatrix} \mathbf{A}_0 & \mathbf{0} & \mathbf{A}_{\text{GRACE}} \\ \mathbf{0} & \mathbf{0} & \mathbf{A}_{\text{GPS}} \\ \mathbf{0} & \mathbf{1} & \mathbf{A}_{\text{TGA}} \end{bmatrix}, \quad (6.6)$$

where the matrix  $\mathbf{A}_0$  consists of the row-vectors  $(\mathbf{a}_0)_i = [1 \ \varphi_i - \bar{\varphi} \ \lambda_i - \bar{\lambda}]$ ,  $i = 1, \dots, n_1$ , with  $\bar{\varphi}$  and  $\bar{\lambda}$  denoting the mean latitude and longitude for the region. Through parameterization of a plane, the bias and tilt (with respect to the GPS data) of the GRACE-

observed rates of vertical displacement are modelled. The TGA data are assumed to be biased with respect to the GPS velocities.

The coefficient matrices  $\mathbf{A}_{\text{GRACE}} (n_1 \times k)$ ,  $\mathbf{A}_{\text{GPS}} (n_2 \times k)$ , and  $\mathbf{A}_{\text{TGA}} (n_3 \times k)$  are computed by Eq. (4.42) with  $k$  inverse multiquadric base functions.

The velocity of a new point  $p$  is computed as

$$\dot{h}_p = \mathbf{a}_p \hat{\mathbf{x}}' = \sum_{j=1}^k \Phi_{pj} \hat{x}_j, \quad (6.7)$$

where  $\hat{\mathbf{x}}'$  is a sub-vector of the vector of estimated parameters  $\hat{\mathbf{x}}$  and includes the estimates  $\hat{x}_j, j=1, \dots, k$  of the weights of the inverse multiquadric base functions. The first four elements of  $\hat{\mathbf{x}}$  are the estimated bias and the north-south and east-west tilts for the GRACE data and the TGA data bias.

According to Rousseeuw and Leroy (1987), an IRLS solution for the vector of parameters  $\mathbf{x}$  is given by the equation

$$\hat{\mathbf{x}} = (\mathbf{A}^T \mathbf{W} \mathbf{A})^{-1} \mathbf{A}^T \mathbf{W} \mathbf{I}. \quad (6.8)$$

where the weight matrix  $\mathbf{W}$  is diagonal and depends on the estimated residuals  $\hat{v}$ . Therefore,  $\mathbf{W}$  is computed iteratively. If diagonal error covariance matrices for the GRACE, GPS, and TGA data are given, the so-called equivalent weight matrix  $\bar{\mathbf{W}}$  (see e.g., Hekimoğlu and Berber, 2003) is computed as in Eq. (6.9) and used in Eq. (6.8).

$$\bar{\mathbf{W}} = \mathbf{W} \mathbf{C}_l^{-1} = \begin{bmatrix} \frac{w_1(v_1)}{\sigma_1^2} & \dots & 0 & \dots & 0 \\ \vdots & \ddots & 0 & \vdots & \vdots \\ 0 & \dots & \frac{w_i(v_i)}{\sigma_i^2} & \dots & 0 \\ \vdots & \vdots & \vdots & \ddots & \vdots \\ 0 & \dots & 0 & \dots & \frac{w_n(v_n)}{\sigma_n^2} \end{bmatrix}. \quad (6.9)$$

The vector of residuals  $\hat{\mathbf{v}}$  in the IRLS algorithm is expressed as follows:

$$\hat{\mathbf{v}} = (\mathbf{I} - \mathbf{A}(\mathbf{A}^T \bar{\mathbf{W}} \mathbf{A})^{-1} \mathbf{A}^T \bar{\mathbf{W}}) \mathbf{l}. \quad (6.10)$$

To ensure scale invariance, standardized residuals are computed from the estimated residuals (Eq. (4.9)) as (Vaníček and Krakiwsky, 1986):

$$\hat{v}_i = \frac{\hat{v}_i}{s_i}, i = 1, \dots, n. \quad (6.11)$$

If the variance factors  $\sigma_{\text{GRACE}}^2$ ,  $\sigma_{\text{GPS}}^2$ , and  $\sigma_{\text{TGA}}^2$  are known, the scale estimator  $s_i$  is computed as follows:

$$s_i = \sigma_{\hat{v}_i} = \sqrt{\text{diag}(\mathbf{C}_{\hat{v}})_i}. \quad (6.12a)$$

with  $\mathbf{C}_{\hat{v}} = \mathbf{W}^{-1} \mathbf{C}_l - \mathbf{A}(\mathbf{A}^T \mathbf{W} \mathbf{C}_l^{-1} \mathbf{A})^{-1} \mathbf{A}^T$ . Otherwise, if the variance factors are estimated, the scale estimator is

$$s_i = \hat{\sigma}_{\hat{v}_i} = \sqrt{\text{diag}(\hat{\mathbf{C}}_{\hat{v}})_i}. \quad (6.12b)$$

with  $\hat{\mathbf{C}}_{\hat{v}} = \mathbf{W}^{-1} \hat{\mathbf{C}}_l - \mathbf{A}(\mathbf{A}^T \mathbf{W} \hat{\mathbf{C}}_l^{-1} \mathbf{A})^{-1} \mathbf{A}^T$ .

According to Rousseeuw and Croux (1993), the median absolute deviation (MAD) of the residuals about the median is a more robust scale estimator than the standard deviation in Eqs. (6.12a) and (6.12b). The MAD estimator is computed as follows:

$$s = \text{med}\{|\hat{\mathbf{v}} - \text{med}\{\hat{\mathbf{v}}\}|\}. \quad (6.13)$$

The weights for each data point,  $w_i, i = 1, \dots, n$ , are computed as:

$$w_i = \frac{\Psi(\hat{v}_i)}{\hat{v}_i}, \quad (6.14)$$

where  $\Psi$  is the influence function. The Fair influence function defined in Eq. (6.15) below is implemented because the function increases monotonically and provides convergence to the global minimum of IRLS (e.g., Basu and Paliwal, 1989).

$$\Psi(\hat{v}_i) = \frac{\hat{v}_i}{1 + |\hat{v}_i|/F}, \quad (6.15)$$

where a value of 1.4 is chosen for  $F$ , but it can be varied to tune the weights.

Different estimators are obtained by combining the scale estimators given by Eqs. (6.12a,b) and (6.13) with the Fair influence function. For example, the Fair-MAD estimator uses the Fair influence function with the MAD scale estimator, and the Fair-sigma estimator combines the influence function with the scale estimators given by Eqs. (6.12a) and (6.12b).

A flowchart that summarizes the IRLS adjustment algorithm is given in Figure 6.1. The algorithm starts with the estimated parameters  $\hat{\mathbf{x}}$  and standard deviations of the residuals  $\sigma_{\hat{v}}$  (assuming known variance factor) from the ordinary least-squares adjustment with  $\bar{\mathbf{W}} = \mathbf{C}_l^{-1}$  and terminates at the  $m^{\text{th}}$  iteration when  $|\hat{\mathbf{x}}^{(m)} - \hat{\mathbf{x}}^{(m-1)}| < \varepsilon$  with  $\varepsilon = 10^{-4}$ .

### 6.3 Approximation of a single velocity data set

This case study includes approximation of a single data set of rates of vertical displacement given on a grid with resolution  $2^\circ \times 2^\circ$  (Figure 6.2a). The base functions (with a shape parameter of 0.5 in unit distance) are also chosen on a grid to homogeneously cover the entire region, but the grid resolution is decided upon the condition number of the coefficient matrix (see Chapter 3). For all observations, a standard deviation  $\sigma = 1.0$  mm/yr is assumed. Outliers are simulated according to the definitions in Section 6.1 as follows:

random scattered (Figure 6.2b) and adjacent (Figure 6.2c) outliers with magnitudes of  $3\sigma$  (small outliers) and  $6\sigma$  (large outliers) are added to the observed velocities at two data points. The randomness of the outliers is defined by their opposite signs.

jointly influential outliers (Figure 6.2d), uniformly distributed between 0.5 and 2 mm/yr, are added to five point velocities.

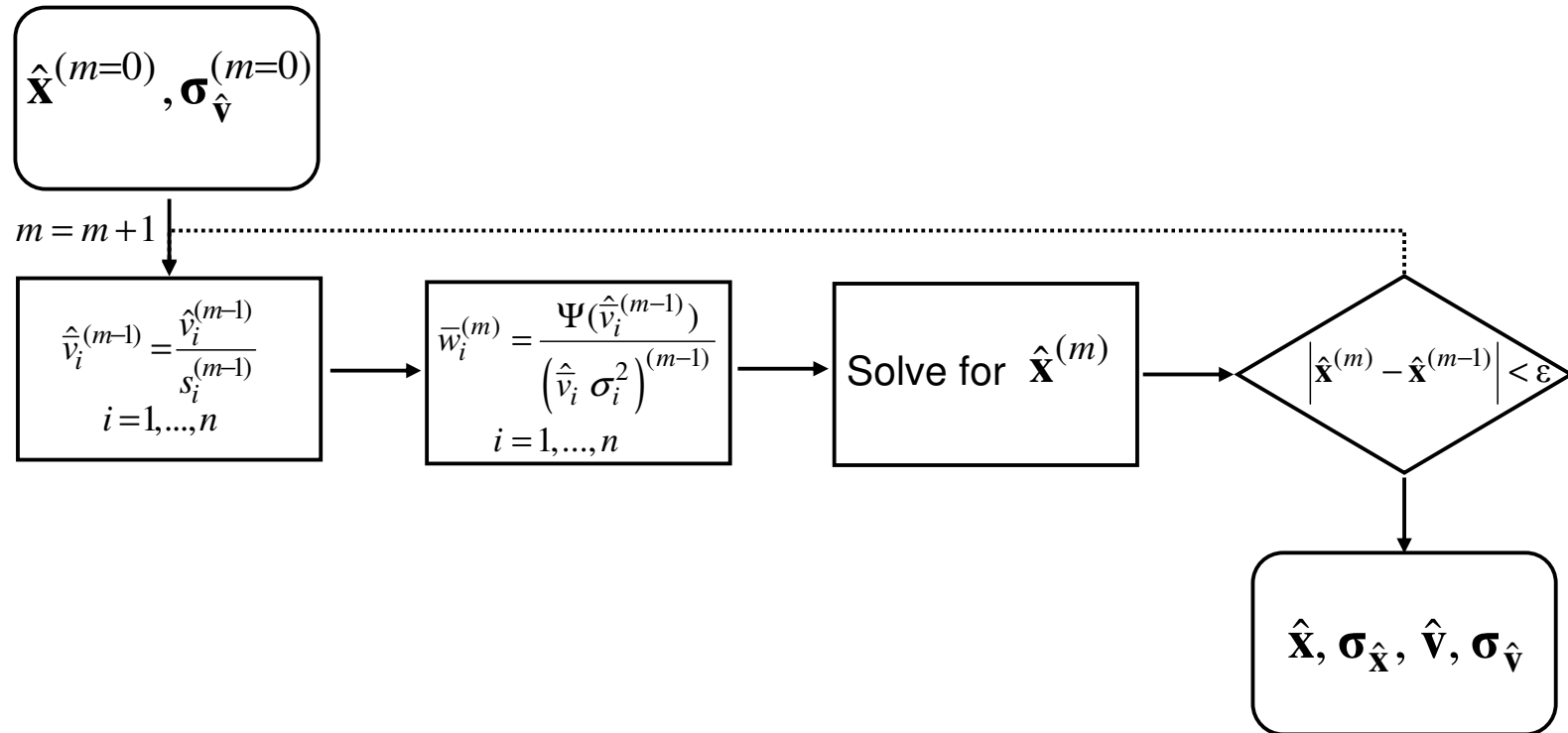


**Figure 6.1:** Iterative re-weighting least-squares (IRLS) adjustment.

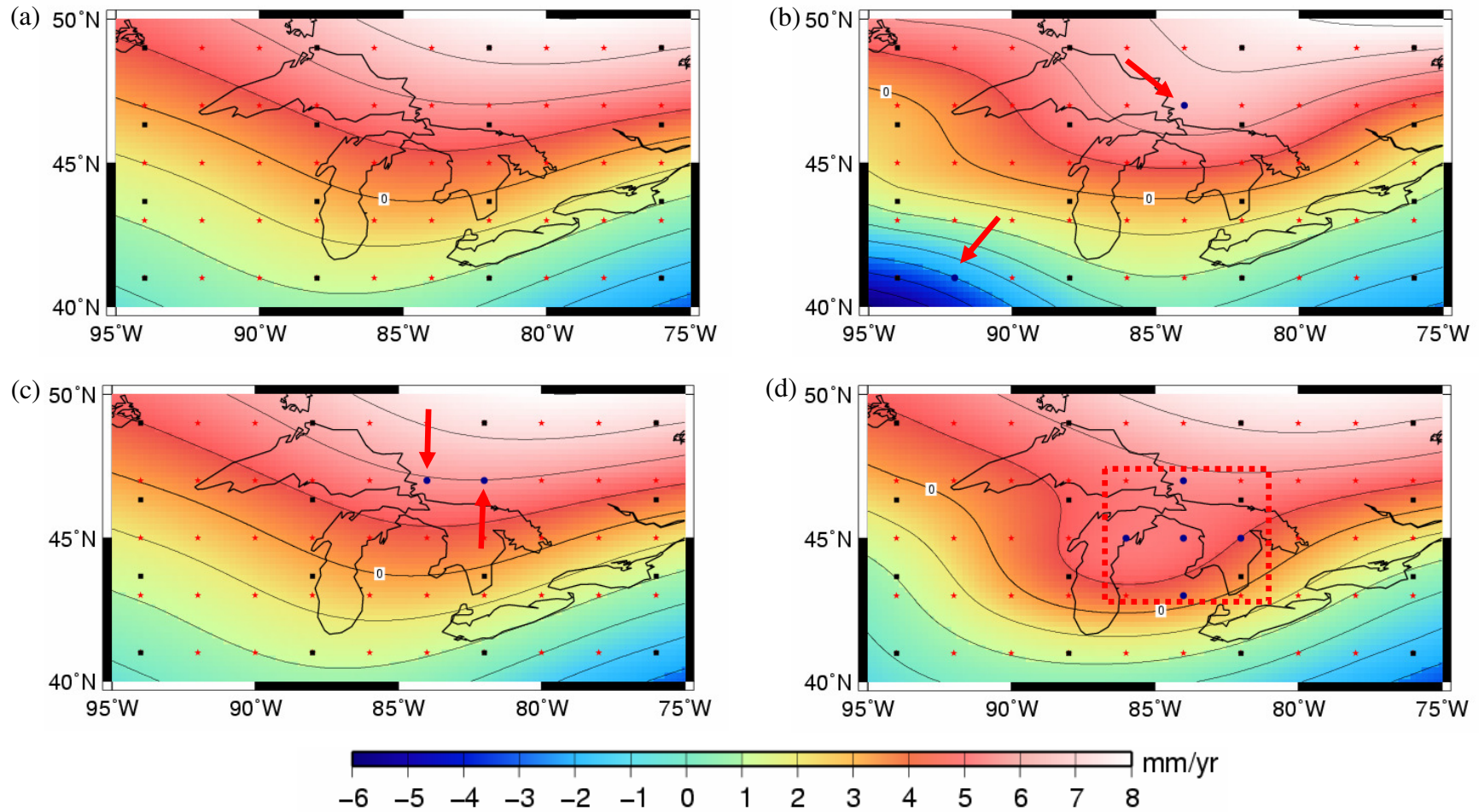


**Figure 6.2:** (a) Test surface sampled by means of 50 point velocity observations (red stars) and 12 base functions (black squares), (b) approximated surface with two random scattered outliers, (c) approximated surface with two random adjacent outliers, and (d) approximated surface with five jointly influential outliers.

Quantitative and qualitative assessment of the effect of the outliers on the approximated vertical displacement rates is given in Table 6.1. On the one hand, because the base functions have good localising properties, the maximum effect is observed in the proximity of the outliers. On the other hand, because the base functions are global, the effect of the large outliers can spread out. From Figure 6.2d and Table 6.1, it is evident that the largest effect on the hinge line is observed if the data set contains jointly influential outliers.

Outliers can have large influence on the approximated surface in the weakly constrained areas. Figures 6.3a and b show the effect of a large single outlier and joint influence outliers, respectively, on the velocity surface if the observations do not cover homogeneously the entire area but contain a data gap. For this purpose, two of the data points in the northwest corner are deleted. The largest effect of approximately 0.5 and 0.9 mm/yr depending on the type of outliers is observed in the proximity of the deleted observations. These values also include the small difference of 0.1 mm/yr between the approximated surface with all of the observations and with the data gap. The presence of a single erroneous observation in such peripheral areas can skew the vertical displacement surface significantly.

**Table 6.1:** Effect of outliers on the approximated surface

Type of outliers	Maximum effect, in mm/yr	Effect on the hinge line and gradient
small single	0.6	very small
large single	1.2	large, skews the hinge line
small scattered	< 1	can cancel out
large scattered	> 1	can skew the hinge line
small adjacent	< 0.5	cancels out
large adjacent	< 1	skews the hinge line
jointly influential	1.2	large, skews the hinge line

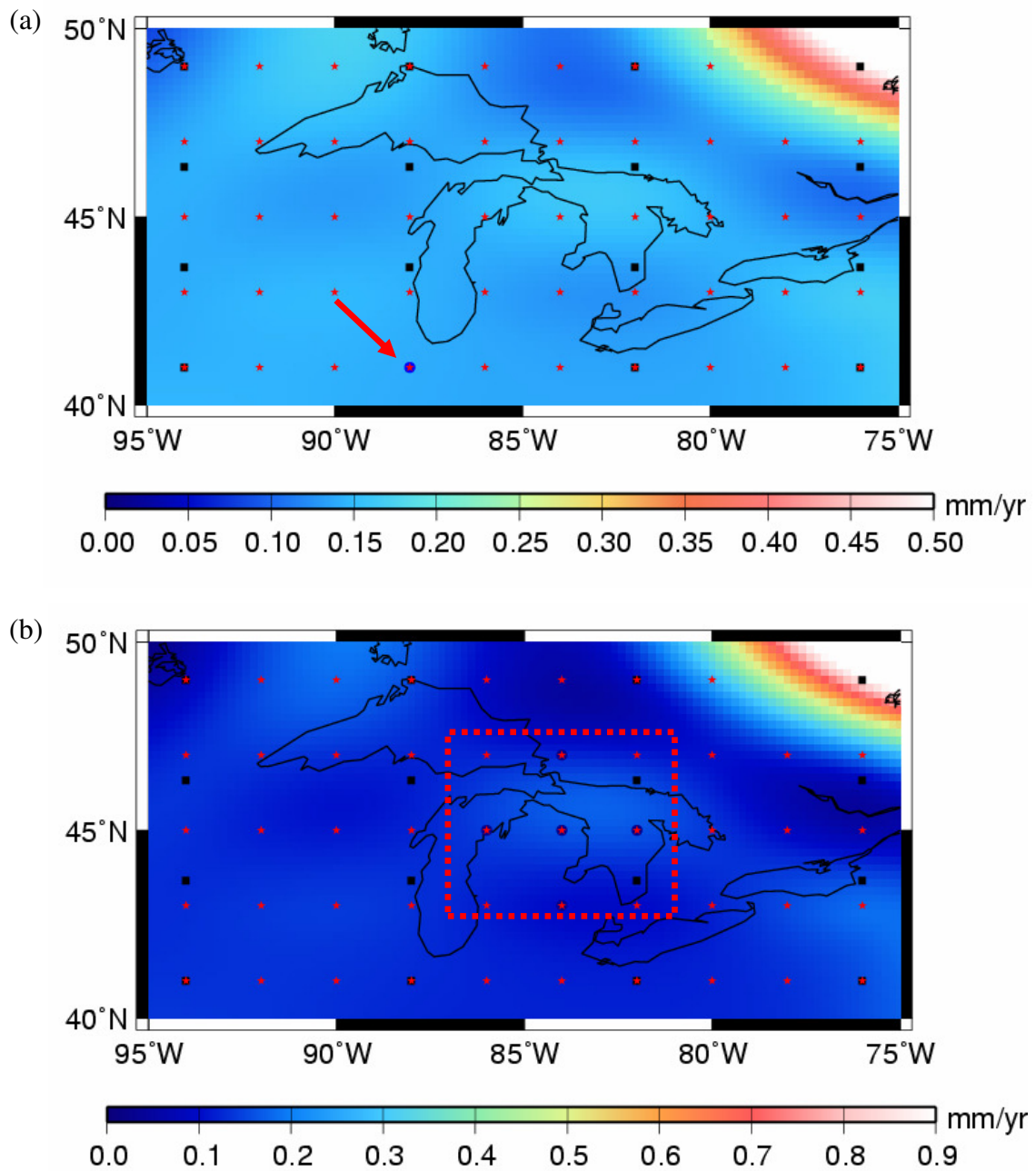


**Figure 6.3:** Effect of (a) a single random and (b) jointly influential outliers on the approximated velocity surface with a data gap.

Baarda's data snooping with the  $\tau$ -statistic given by Eq.(4.26) is applied iteratively at a significance level  $\alpha=0.05$  deleting the outlier with the largest statistic according to Eq.(4.27). Data snooping does not detect the simulated small scattered outliers; however, it succeeds in detecting the large random outliers. Swamping effects (good data are tested to be outliers) are observed in the area with lack of data constraints. Another interesting observation is related to the test of the small adjacent outliers. At the first step of the procedure, data snooping detects the two simulated adjacent outliers; however, at the second step, the second outlier is tested to be a good observation after the first outlier is removed. As a result, a large distortion of the vertical displacement surface is observed. In addition, data snooping fails in detecting the simulated jointly influential outliers and a single outlier in the weakly constrained areas.

In contrast with the conventional statistical testing, the robust Fair-MAD estimator detects and down-weights all simulated outliers. The assigned weights for the case with random scattered and joint influential outliers are given in Figures 6.4a and b, respectively. However, the estimator down-weights significantly even the good observations adjacent to the outliers. Therefore, by increasing the tuning constant  $F$  from 1.4 to 6.0, the weights of the good observations are increased to match the weights assigned by the Fair-sigma estimator in Figures 6.4c and d while keeping the weights for the erroneous observations below 0.1. In contrast with the Fair-MAD estimator, the Fair-sigma estimator does not down-weight significantly the outliers relatively to the good observations. This is observed for all of the cases. Thus, the approximated surface is still influenced by the outliers.

To summarize, the conventional data snooping technique can be applied to detect and remove large random scattered and adjacent outliers but is not appropriate for small and jointly influential outliers. Also, the use of the Fair-sigma estimator for the case of the small random and joint influential outliers is not recommended. In contrast, the Fair-MAD estimator is able to treat properly all kinds of outliers investigated in this study.

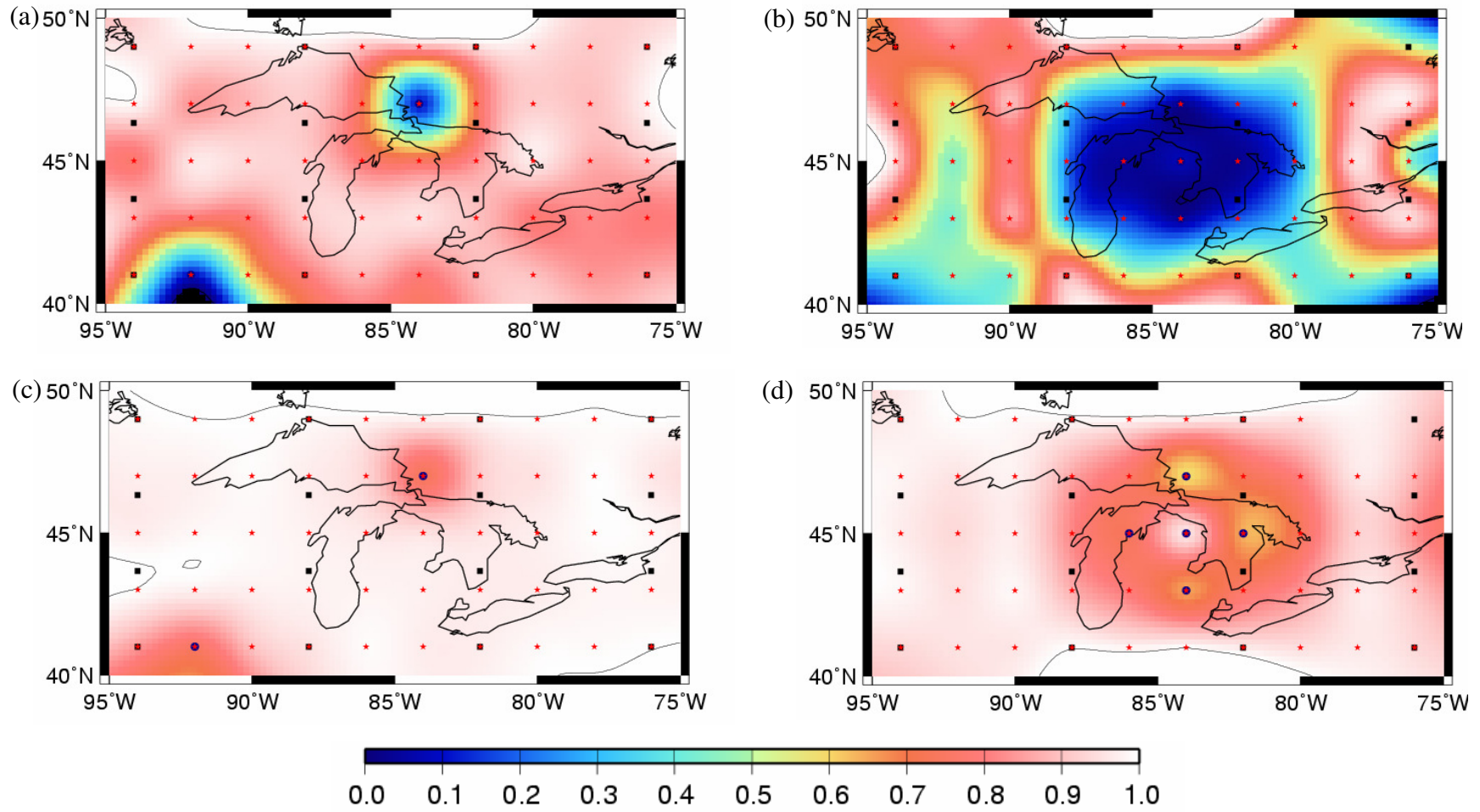


**Figure 6.4:** Weights of the observations for the cases of random scattered outliers and jointly influential outliers computed by the Fair-MAD estimator, (a) and (b), and by the Fair-sigma estimator, (c) and (d).

#### 6.4 Combined model for vertical displacement rates

The GRACE-observed rates of vertical displacement are given in Figure 6.5a. For the purpose of this study, they are interpolated at the GPS stations. Evident is the northeast-southwest surface slope resembling the pattern of the postglacial rebound signal obtained with the ICE-4G de-glaciation history and a four-layer approximation of the VM2 viscosity model (Figure 6.5b and Chapter 2). A positive bias with respect to the GPS vertical velocities in Figure 6.5c (Sella *et al.*, 2007) is also observed. Generally, the interpolated GPS velocities show a larger slope, which sharply decreases from 7-8 mm/yr northeast to the hinge line veering off through the lakes. Also, evident is the correlation of the interpolated velocities with the locations of the GPS stations in the lake areas. Figure 6.5d depicts the rate of vertical displacement obtained from combined tide gauge and satellite altimetry water surface heights (TGA) according to Kuo (2006). The TGA data repeat the general pattern of the GPS velocities, but the hinge line is located south of the GPS hinge line. It should be noted that the local vertical displacements (if any) could have been largely filtered out in the optimal combination of the tide gauges and altimetry data.

The different data sets are derived from different time spans of measurements and have different datums. It is reasonable to assume that the latter results in a long wavelength signal that can be parameterized as a bias or a plane in the combined least-squares adjustment model. In addition, GRACE-observed rates of vertical displacement would be subject to leakage of geophysical signals from outside the area of interest. Any errors in the hydrology correction would also contribute to the inconsistencies between the GRACE-observed rates and the GPS and TGA rates. The data sets also differ in terms of the a priori accuracy with which they are provided. The error covariance matrices are available in a diagonal form; thus, the correlation between the rates within each data set is assumed to be negligible. Table 6.2 includes the a priori accuracy of the three data sets. The formal errors of the GRACE and TGA data are significantly smaller than the formal errors of the GPS velocities. Therefore, the error covariance matrices of the TGA and GRACE-observed rates of vertical displacement are re-scaled by factors of 7.0 and 2.0, respectively.

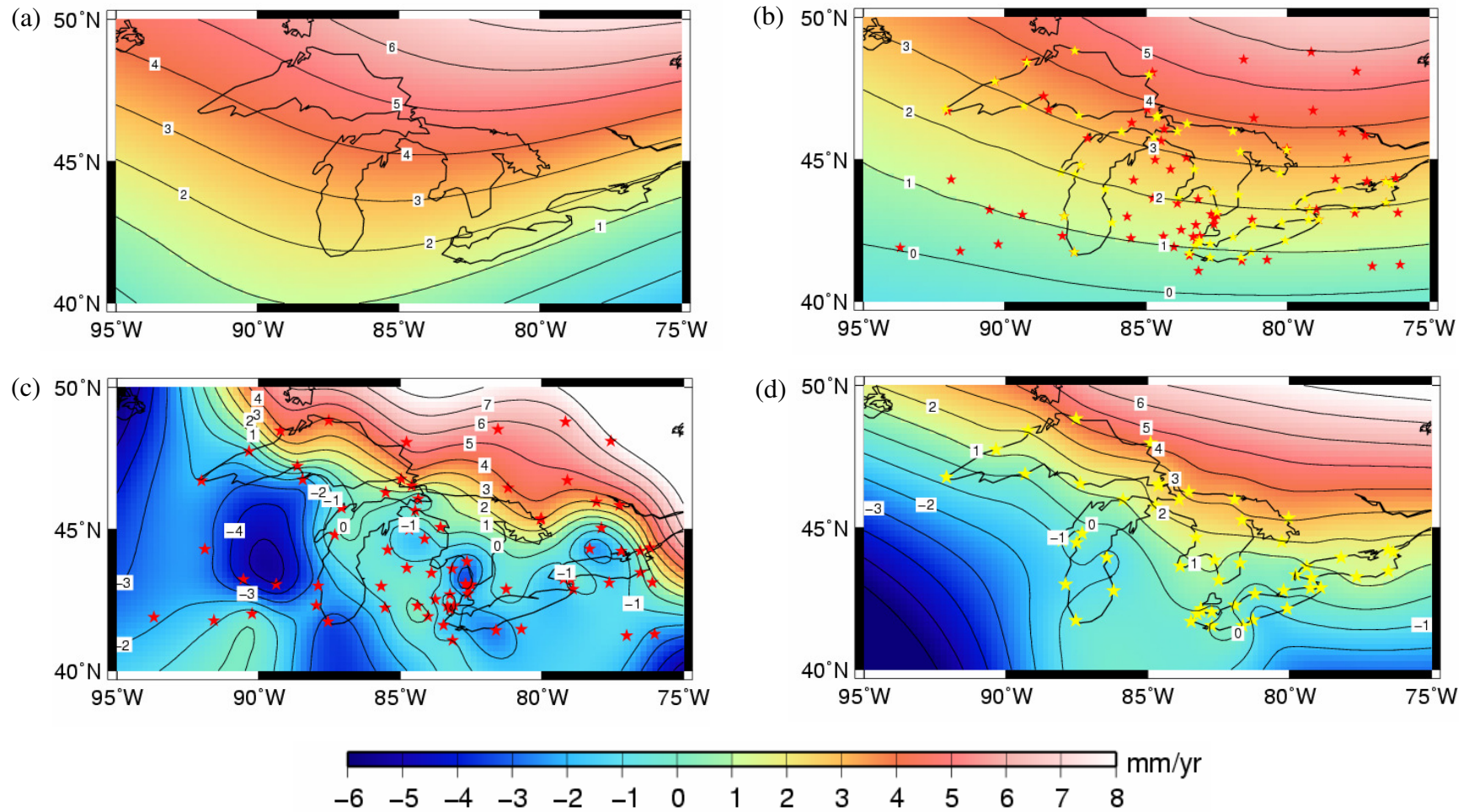


**Figure 6.5:** Rates of vertical displacement from (a): GRACE, (b) PGR model with a four-layer approximation of the VM2 model and the ICE-4G de-glaciation history, (c) GPS measurements (red stars), and (d) an optimal combination of water tide gauge records and TOPEX/Poseidon altimetry water surface heights (yellow stars).

**Table 6.2:** Statistics of the a priori (not scaled) standard deviations

Data set	Number of points	Min, mm/yr	Max, mm/yr	Mean, mm/yr
GRACE	71	1.4	1.4	1.4
GPS	71	0.5	5.3	2.0
TGA	51	0.1	0.3	0.2

Four combined models of the rates of vertical displacement are obtained. Figure 6.6 represents the least-squares adjustment model without taking care of outliers. Figure 6.7 shows the approximated surface by least-squares adjustment with data snooping. The combined models obtained by means of IRLS adjustment and different estimators are given in Figure 6.8 (the Fair-sigma estimator) and Figure 6.9 (the Fair-MAD estimator). The approximated surface is very well constrained in the lakes area, where all of the models have almost the same surface gradient and a hinge line that deviates slightly. The largest differences among the models are observed in the peripheral areas.

It should be noted that the outlier detection and the VCE are interrelated and are applied in an iterative procedure as explained in Section 6.1. However, for the sake of clarity, the following discussion presents outlier detection and VCE for this case study separately.

#### 6.4.1 Outlier detection

Baarda's data snooping given by Eqs.(4.24) and (4.25) is applied at significance level  $\alpha = 0.05$ . Outliers are removed sequentially as the data point value with the largest test statistic is removed at each step. After all of the outliers are removed, VCE is applied to obtain new scales for the error covariance matrices. The data snooping procedure is repeated using the rescaled matrices in the new least-squares adjustment. Four iterations are necessary to obtain "clean" data sets of GPS and TGA observations; see Table B.1. It should be noted that the outliers in the combined case are examined together. This is necessary because swamping and masking effects are observed between the GPS and TGA data as shown in the table. Nine outliers are detected and removed from the GPS velocities (Table B.2). Evident from Figure 6.7 is that the data snooping procedure removes mostly

GPS data points from the periphery of the region. As a result, significant differences of the approximated surface are observed southwest from the lakes. Another nine TGA data points are tested to be outliers and removed (Table B.3).

#### 6.4.2 Variance component estimation and a posteriori accuracy

The variance factors of the error covariance matrices are estimated using the BIQUE method described in detail in Section 4.1.2 of Chapter 4. Table 6.3 provides statistics of the variance factors and standard deviations of the observations estimated in the four least-squares adjustment models. In the least-squares adjustment case without outlier detection, the error covariance matrices for the GRACE-observed vertical displacement rates and GPS vertical velocities should be re-scaled by 0.06 and 0.9, respectively. In contrast, the estimated variance factor of 10.0 for the TGA error covariance matrix justifies that the a priori accuracy of the data set is too optimistic. If data snooping is applied, the variance factors for the GPS and TGA error covariance matrices drop to 0.41 and 4.61, respectively. The large differences in the estimated variance factors show that outliers in the two data sets have a significant influence on the estimated scales of the error covariance matrices.

Because the equivalent weight matrix  $\bar{\mathbf{W}}$  replaces the data weight matrix  $\mathbf{P}$  in the IRLS adjustment, the estimated variance components are the scale factors for the cofactor matrices  $\mathbf{Q}^{(m)} = (\bar{\mathbf{W}}^{(m)})^{-1} = (\mathbf{W}^{(m)}\mathbf{P}^{(m)})^{-1}$  with  $\mathbf{P}^{(m)} = \bar{\mathbf{W}}^{(m-1)}$ . Variance factors of one (Table 6.3) are obtained at the fifth iteration of the procedure.

More insight into the a posteriori accuracy of the data sets can be obtained by examining the statistic of the a posteriori standard deviations in Table 6.3. The comparison with the a priori accuracy in Table 6.2 reveals that the error of the GRACE-observed rates of vertical displacement, on average, decreases from 1.4 to 0.2 - 0.4 mm/yr. The mean standard deviation for the GPS vertical velocities decreases from 2.0 to 1.3 mm/yr, while the standard deviation of the TG/Alt rates increases from 0.2 to 1.1 mm/yr on average. The least-squares adjustment with data snooping tends to provide significantly smaller a posteriori errors compared to the IRLS adjustment. The IRLS adjustment with the Fair-MAD estimator provides the largest maximum errors among all methods.

The a priori and a posteriori standard deviations for all GPS and TGA observations are compared in Figures 6.6, 6.7, 6.8, and 6.9 and Tables B.2 and B.3. A decrease in the a posteriori GPS errors is evident, but also a significant reduction of the largest errors is observed. The a posteriori errors of the TGA rates have an apparent geographical pattern with maximum values of 0.8 – 1.1 mm/yr estimated for Lake Michigan.

**Table 6.3:** Estimated variance factors and a posteriori standard deviations in mm/yr

Data set	$\hat{\sigma}^2$	Min	Max	Mean
Least-squares adjustment				
GRACE	0.06	0.2	0.2	0.2
GPS	0.90	0.5	5.0	1.9
TGA	10.0	0.3	1.0	0.6
Least-squares adjustment with data snooping				
GRACE	0.04	0.2	0.2	0.2
GPS	0.41	0.5	3.4	1.3
TGA	4.61	0.2	0.6	0.4
IRLS adjustment with Fair-sigma estimator				
GRACE	0.88	0.3	0.4	0.7
GPS	1.03	0.5	4.1	1.7
TGA	1.07	0.2	0.8	0.4
IRLS adjustment with Fair-MAD estimator				
GRACE	0.95	0.2	0.4	0.3
GPS	1.01	0.3	6.4	1.8
TGA	1.03	0.2	1.1	0.5

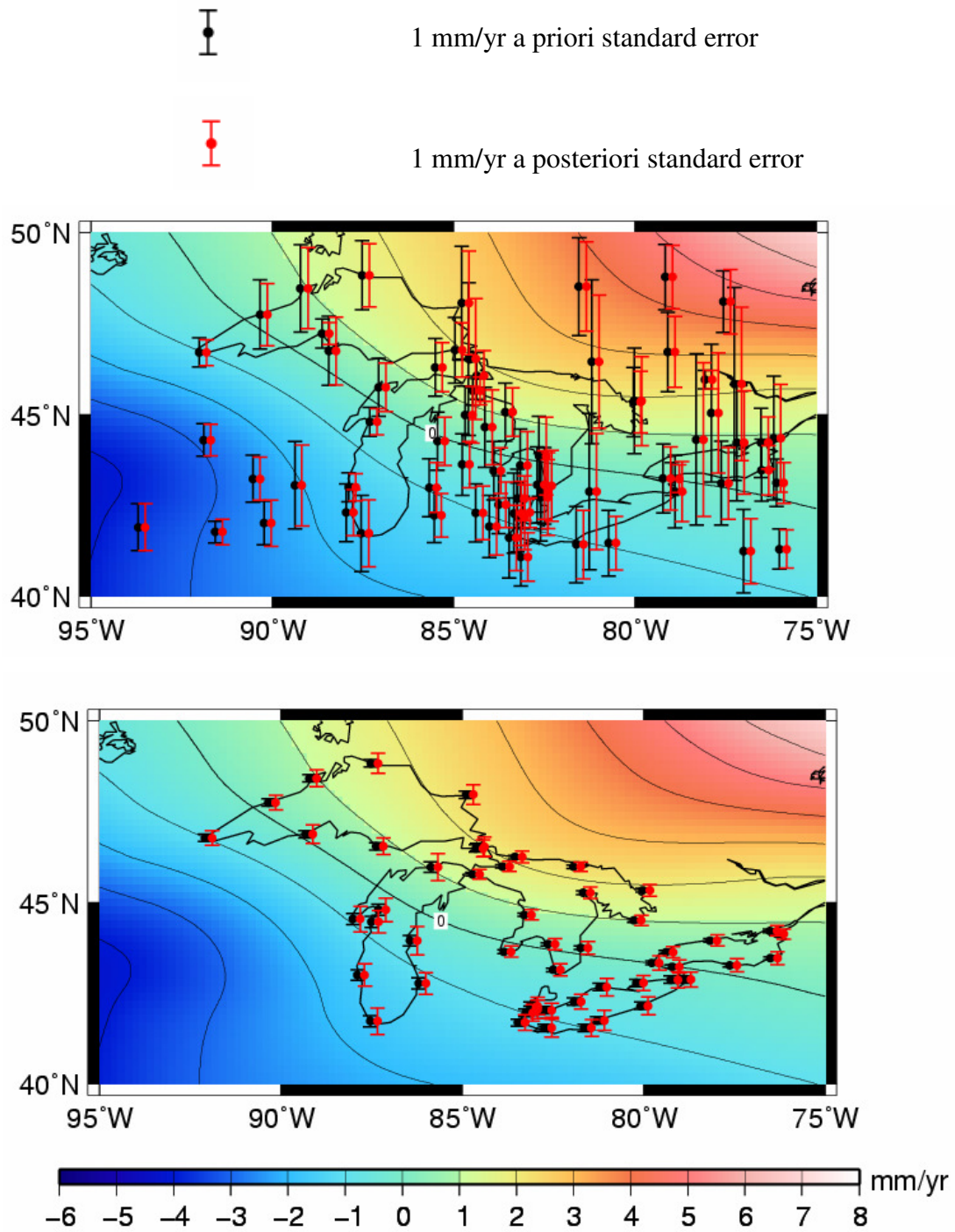


**Figure 6.6:** Combined model using least-squares adjustment (no outliers removed). A priori (black) and a posteriori (red) standard deviations of the GPS vertical velocities and TGA vertical displacement rates are given in the upper and lower plots, respectively.

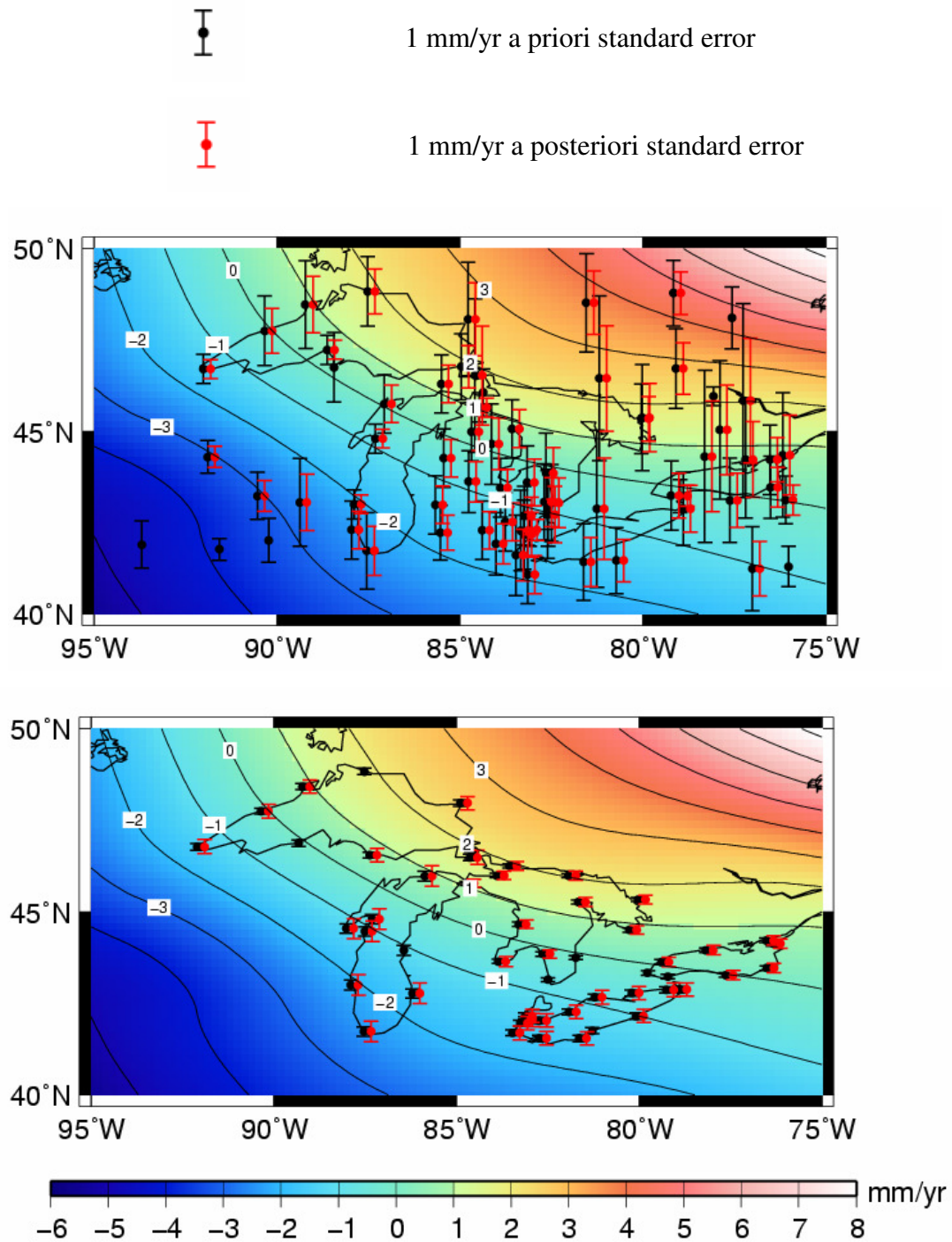


**Figure 6.7:** Combined model using least-squares adjustment with Baarda's data snooping. A priori (black) and a posteriori (red) standard deviations of the GPS vertical velocities and TGA vertical displacement rates are given in the upper and lower plots, respectively.

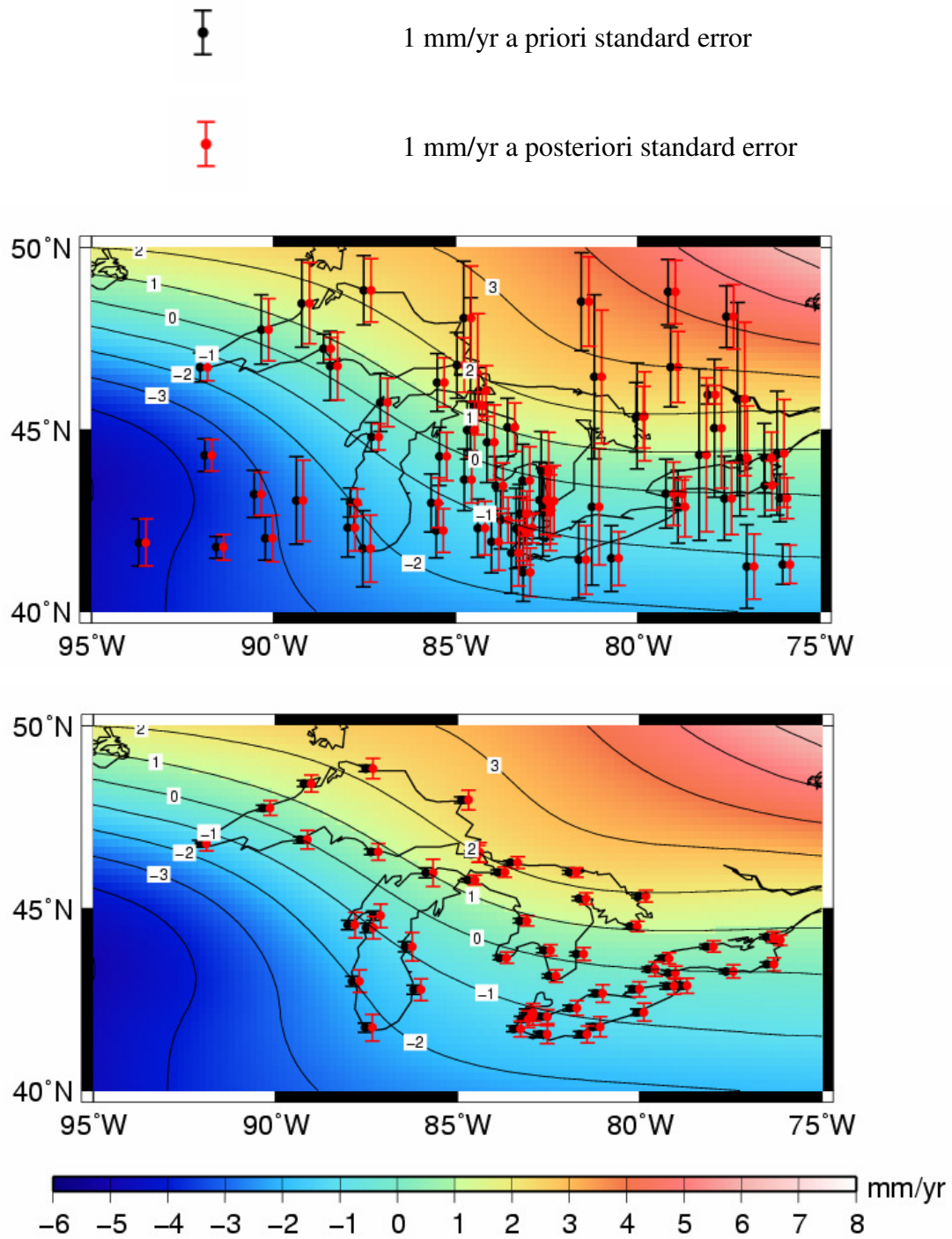


**Figure 6.8:** Combined model using IRLS adjustment with the Fair-sigma estimator. A priori (black) and a posteriori (red) standard deviations of the GPS vertical velocities and TGA vertical displacement rates are given in the upper and lower plots, respectively.

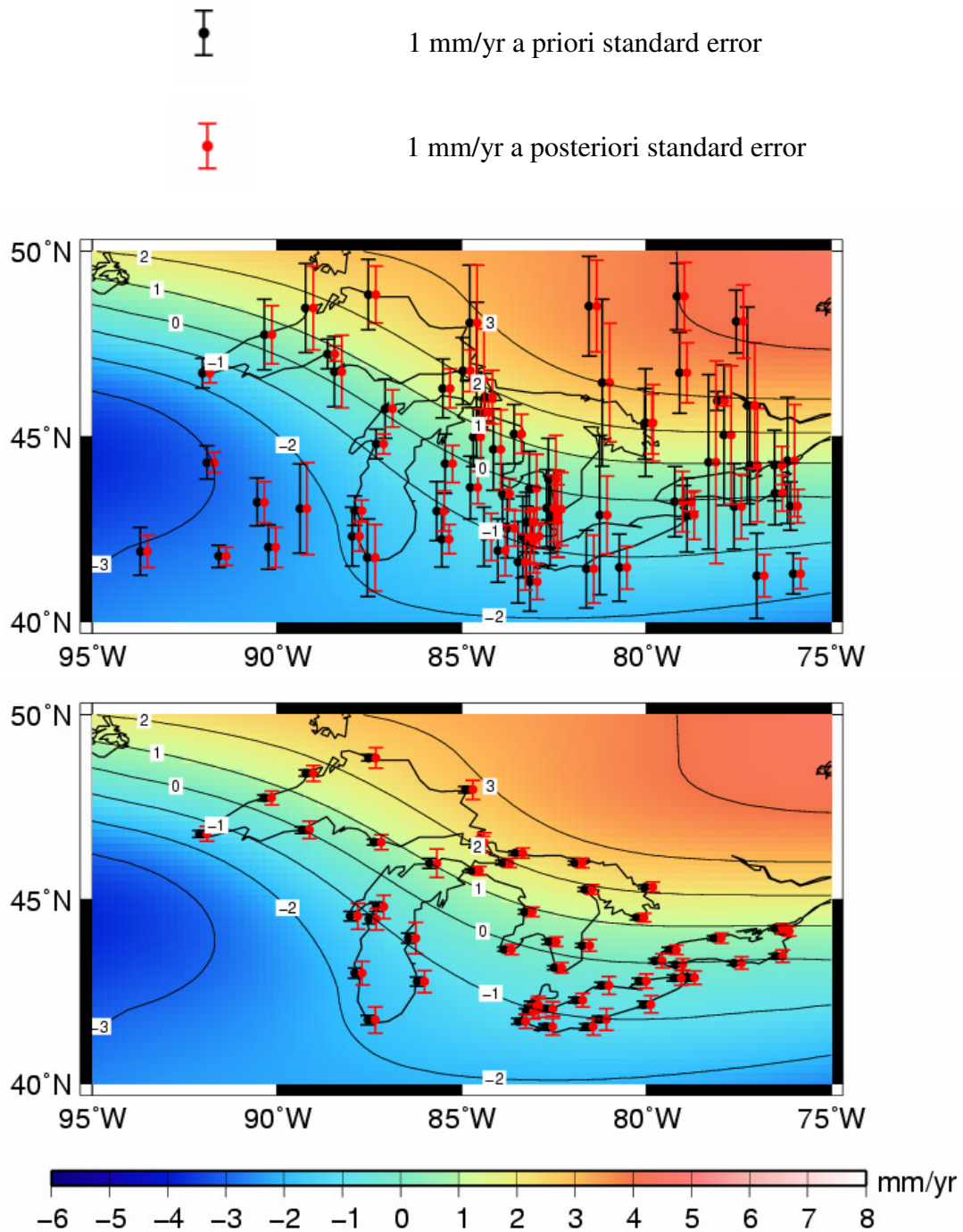


**Figure 6.9:** Combined model using IRLS adjustment with the Fair-MAD estimator. A priori (black) and a posteriori (red) standard deviations of the GPS vertical velocities and TGA vertical displacement rates are given in the upper and lower plots, respectively.

## 6.5 Summary

As demonstrated in this chapter, the outlier detection is an important issue when inverse multiquadrics are used in the mathematical model because the robustness of the base functions decreases with the increase in the shape parameter. This results in spreading the effect of the outliers in the areas weakly constrained by the data. In those areas, even good observations may appear to be erroneous. Therefore, based on the results of this study, it is recommended that robust least-squares procedures, such as the one designed in this chapter, be applied when optimally combining different displacement data sets. Since the procedure is not a priori based on the use of inverse multiquadrics, it can be applied with other types of base functions.

It has been demonstrated that different data sets of vertical displacement rates (GRACE, GPS, and joint tide gauges and altimetry data in the studied example) can be optimally combined using the iterative re-weighting least-squares adjustment approach. By significantly down-weighting the erroneous observations, their effect on the approximated surface is minimized. The estimated scales of the error variance matrices are free from the effect of the outliers. Thus, more reliable empirical constraints for postglacial rebound modelling are provided.

## Chapter Seven: Implementing the dynamic geoid model as a vertical datum

The objective of this chapter is to provide a feasibility study on incorporating the temporal changes in the geoid height into the vertical datum in Canada. For this purpose, the most accurate GPS ellipsoidal heights from CBN, orthometric heights from the most recent minimally constraint adjustment of the primary vertical control network, and the most recent geoid model for Canada are used.

The chapter begins with a definition of the dynamic geoid, followed by a discussion of the propagated effect of geodynamics in Canada in the geoid model computed by means of the traditional *remove-compute-restore* procedure. Finally, an analysis on the effect of the temporal changes in the geoid height on the contemporary vertical datum in Canada is presented and discussed.

### 7.1 Definition of the dynamic geoid

The geoid height can be represented as a function of the location  $(\varphi, \lambda)$  and time epoch  $t$  as

$$N(\varphi, \lambda, t) = N^{\text{stat}}(\varphi, \lambda) + \dot{N}(\varphi, \lambda)t + \tilde{N}(\varphi, \lambda, t). \quad (7.1)$$

$N^{\text{stat}}(\varphi, \lambda)$  is the static geoid that also can be the mean geoid over a sufficiently long period of time so that all periodic variations average out.  $\dot{N}(\varphi, \lambda)$  is the estimated trend (rate of change) of the geoid height from the empirical models developed in Chapters 4 and 5. The last term in Eq. (7.1), i.e.,  $\tilde{N}(\varphi, \lambda, t)$ , could represent semi-annual, annual, inter-annual, non-periodic, and episodic changes in the geoid height over the time period of

interest. As shown in Chapter 5, the main periodic signal in the geoid height in North America is the annual cycle of snow mass accumulation and melting. Other temporal variations of interest are the trend-like hydrology changes over the analyzed time period, which might be a part of a long-period signal that could average out with the increase of the time span of the GRACE mission.

The geoid model used in the GNSS/levelling can be computed using the *remove-compute-restore* technique. The simple Helmert condensation method (Sideris, 1994a; 1994b), which will be described in the following, allows one to easily propagate the temporal effects into the computed geoid height.

The geoid height is computed as follows:

$$N = N^{\text{GM}} + N^{\Delta g} + N^I, \quad (7.2)$$

where

$$N(\varphi, \lambda)^{\text{GM}} = R \sum_{l=2}^{l_{\max}} \sum_{m=0}^l \bar{P}_{lm}(\sin \varphi) [\bar{C}_{lm} \cos(m\lambda) + \bar{S}_{lm} \sin(m\lambda)] \quad (7.3)$$

is the contribution of a global geopotential model of maximum degree  $l_{\max}$ ,  $\bar{P}_{lm}$  are the fully normalized Legendre functions,  $\bar{C}_{lm}$  and  $\bar{S}_{lm}$  are the fully normalized coefficients of the anomalous potential,  $R$  is the mean radius of the Earth, and  $\varphi$  and  $\lambda$  are the latitude and longitude of the computation point. The contribution of the gravity anomalies is computed as follows:

$$N^{\Delta g} = \frac{R}{4\pi\gamma_{\sigma}} \iint (\Delta g^{\text{F}} - \Delta g^{\text{GM}}) S(\psi) d\sigma, \quad (7.4)$$

where the integration is performed locally over the part of the sphere with a size determined by the shortest wavelength present in the geopotential model;  $\Delta g^{\text{GM}}$  is the contribution of the geopotential model; and  $\Delta g^{\text{F}}$  is the Faye gravity anomaly

$$\Delta g^{\text{F}} = \Delta g - \frac{\partial \gamma}{\partial h} H + c^{\text{T}}, \quad (7.5)$$

where  $\Delta g$  is the Free-air gravity anomaly computed at the topographic surface,  $\partial\gamma/\partial h$  is the normal gravity gradient,  $H$  is the orthometric height, and  $S(\psi)$  is the Stokes kernel;  $c^T$  is the terrain correction computed by the equation

$$c^T = \frac{G\rho R^2}{2} \iint_{\sigma} \frac{(H_P - h_Q)^2}{l_{PQ}^3} d\sigma_Q, \quad (7.6)$$

where P and Q are points at the Earth's surface (Heiskanen and Moritz, 1967).

The last term in Eq. (7.2) is the indirect effect on the geoid due to the condensation of the topography on the geoid, which, to the first order approximation, is computed as

$$N^I = -\frac{\pi G\rho}{\gamma} H^2. \quad (7.7)$$

Table 7.1 summarizes the maximum values of the rates of change of each term used in the remove-compute restore procedure. It is assumed that the gravity and levelling measurements are corrected for the inconsistencies of the measurement epochs. The rate of change of the geoid height is simply obtained by differentiating each term in Eq. (7.2) with respect to time as follows:

$$\dot{N} = \dot{N}^{\text{GM}} + \dot{N}^{\Delta g} + \dot{N}^I. \quad (7.8)$$

The term  $\dot{N}^{\text{GM}}$  can be thought of as the estimated (in Chapter 5) GRACE-observed rates of change of the geoid height. The term  $\dot{N}^{\Delta g}$  is the time derivative of Eq. (7.4), i.e.,

$$\dot{N}^{\Delta g} = \frac{R}{4\pi\gamma} \iint_{\sigma} (\Delta\dot{g}^{\text{F}} - \Delta\dot{g}^{\text{GM}}) S(\psi) d\sigma, \quad (7.9)$$

$$\Delta\dot{g}^{\text{F}} = \dot{g} - \frac{\partial\gamma}{\partial h} \dot{H} + \dot{c}^T, \quad (7.10)$$

and  $\Delta\dot{g}^{\text{GM}}$  is the GRACE-observed rate of change of gravity. Eq. (7.9) shows that the rate of change of the free-air gravity correction compensates for the effect of the vertical crustal displacement in the rate of the terrestrial gravity. Thus, the rate of change of the Faye

anomaly can be written as  $\Delta\dot{g}^F = \delta\dot{g} + \dot{c}^T$ , where  $\delta\dot{g}$  is the contribution of the redistributed masses and  $\dot{c}^T$  is the time derivative of the terrain correction. The latter has a negligibly small value of  $2 \times 10^{-4} \mu\text{Gal/yr}$ . The former is observed by GRACE with a peak value of  $1.5 \mu\text{Gal/yr}$  for the Hudson Bay region, and is equal to the  $\Delta\dot{g}^{\text{GM}}$  term; therefore,  $\dot{N}^{\Delta g}$  can be assumed zero. The rate of the indirect effect term  $\dot{N}^I$  in Eq. (7.8) is  $1 \times 10^{-4} \text{ mm/yr}$  at most.

From the discussion above, it is clear that the geoid rate can be represented by the GRACE-observed rate. The contribution of local mass redistributions can be modeled by the least-squares collocation approach as in Chapters 4 and 5. Thus, the dynamic geoid is given by

$$N(\varphi, \lambda, t) = N^{\text{stat}}(\varphi, \lambda) + \dot{N}(\varphi, \lambda)t. \quad (7.11a)$$

For the purpose of a dynamic geoid-based vertical datum, this equation can be rewritten as follows:

$$N(\varphi, \lambda, t) = N(\varphi, \lambda, t_0) + \dot{N}(\varphi, \lambda)(t - t_0), \quad (7.11b)$$

where  $N(\varphi, \lambda, t_0)$  is the geoid model for the reference epoch  $t_0$ .

**Table 7.1:** Temporal effects in the geoid model

Term	Value
Rate of change of the geoid height, Eqs. (7.1) and (7.8)	1.5 mm/yr
Free-air gravity correction in Eq. (7.5)*	3 $\mu\text{Gal/yr}$
Faye gravity anomaly, Eq. (7.5)	1.5 $\mu\text{Gal/yr}$
Terrain correction, Eq. (7.6)	$2 \times 10^{-4} \mu\text{Gal/yr}$
Indirect effect on the geoid, Eq. (7.7)	$1 \times 10^{-4} \text{ mm/yr}$

\*  $\dot{H} = 10 \text{ mm/yr}$  is assumed.

In view of the vertical datum modernization in Canada, the secular rate in the geoid height is the sole temporal effect of interest. However, the secular changes in gravity and heights propagate into the geoid height through all terms in the *remove-compute-restore* procedure. The most significant of these effects originates from the inconsistencies of the measurement epochs of the terrestrial gravity used to create the Canadian Gravity Anomaly Data Base (CGADB). Ali (2006) quantified this effect and showed that the geoid changes are negative over eastern Canada and the Hudson Bay region with a peak of -0.13 m and positive over western Canada with a peak of 0.14 m centered in Yukon (Ali, 2006, Figure 5.4). It should be noted that the computed change in the geoid height includes both the effect of the mass redistribution and the vertical crustal displacement on the terrestrial gravity values. The geoid changes are of long to medium wavelength and resemble the map of the rates of change of the terrestrial gravity (Figure 4.2a in this thesis).

The postglacial rebound signal is present also in the global gravity anomaly, i.e., the  $\Delta g^{\text{GM}}$  term. In the pre-CHAMP and GRACE geopotential models, e.g., EGM96 (Lemoine *et al.*, 1998), postglacial rebound possibly affects the long wavelength spectrum of the geopotential through the different epochs of the satellite arcs used in recovering the geopotential from satellite tracking data. Through homogenization (both in space and time) of the global gravity field by observations from GRACE and the future GOCE satellite mission, the global geoid models will be free from the described effects. For example, the recent Canadian geoid model CGG05 (Huang *et al.*, 2006) is based on the GRACE GGM02C geopotential model, and, therefore, it can be assumed that wavelengths up to degree 90 are free from the postglacial rebound effect. However, corrections in the gravity anomaly data base for Canada are still necessary because the medium and short-wavelength gravity anomalies can contain biases and systematic distortions from the inconsistencies of the gravity measurement epochs.

## **7.2 Role of the dynamic geoid in the vertical datum problem**

According to Véronneau *et al.* (2006), the new geoid-based datum for Canada will be constrained to a “framework” of fundamental points that includes the most accurate GPS

stations linked to the existing primary vertical control network. At those fundamental points, by differencing the measured ellipsoidal height and the geoid height from the contemporary regional geoid model, the orthometric height (referenced to the geoid-based vertical datum) will be computed. This approach is an implementation of option 2 for vertical datum realization explained in Section 2.1.1 of Chapter 2. In this scenario, the re-adjusted primary vertical control network links the geoid-based and levelling-based vertical datum. In addition to providing a connection to the local mean sea level, the levelling-based vertical datum assists the validation of recent global and regional geoid models as well as the studies of levelled vertical crustal displacement. Because the latter is present in the levelled height differences, the vertical control network is subject to systematic effects that need to be taken into account if validation of the contemporary accurate geoid models is undertaken. Conversely, the geoid-based vertical datum will not contain these systematic effects, but the vertical reference surface will change with time.

In the approach adopted in this research, the dynamic geoid is treated in the context of the combined adjustment of the ellipsoidal, orthometric, and geoid heights. This approach provides a means for studying the effect of the dynamic component of the geoid height and weighting this effect against the errors of the three height components. Therefore, this study should be accepted as a feasibility study with results indicating the importance of integrating the temporal component in the vertical datum. In addition, the effect of the levelled crustal displacement on the vertical datum is assessed.

### **7.2.1 Combined adjustment of ellipsoidal, geoid, and orthometric heights**

The basic observation equation for a combined adjustment of ellipsoidal, orthometric, and geoid heights is given by Eq. (2.10) in Chapter 2, Section 2.1. From the discussion in this section, it follows that the height misclosure consists of a systematic component and three noise components attributed to the three height types. The former can be represented by a smooth *parametric* surface that absorbs all distortions, long wavelength geoid errors, and datum inconsistencies among the ellipsoidal, orthometric, and geoid heights (Schwarz *et al.*, 1987). In the areas with a maximum rebound signal, the parametric surface will also

absorb the distortions caused by the different epochs of the levelling measurements in the different parts of the vertical control network and the temporal changes of the geoid height.

The parametric surface allows the orthometric height to be obtained by differencing the GPS-determined ellipsoidal height and the geoid height at new points for establishing a vertical control in the territory of interest. The combined least-squares adjustment model for the height misclosure  $l_P$  at the GPS-on-benchmark point P,

$$l_P = h_P - N_P - H_P, \quad (7.12)$$

is defined as follows. Let  $\mathbf{l} = [l_1 \ l_2 \ \dots \ l_n]^T$  be a vector of height misclosures (observations) at  $n$  benchmarks of the vertical control network,  $\mathbf{x} = [x_1 \ x_2 \ \dots \ x_k]^T$  is a vector of  $k$  unknown parameters;  $\mathbf{A}$  is the coefficient matrix with vector rows  $\mathbf{a}_i = [a_1 \ a_2 \ \dots \ a_k]$ ,  $i = 1, \dots, n$  and of full column rank, i.e.,  $\text{rank } \mathbf{A} = k$ ; and  $\mathbf{v} = [v_1 \ v_2 \ \dots \ v_n]^T$  is a vector of zero-mean residuals, i.e.,  $E\{\mathbf{v}\} = 0$ .

The observation equation of the combined least-squares adjustment model is

$$\mathbf{l} = \mathbf{A}\mathbf{x} + \mathbf{v}, \text{ with } E\{\mathbf{v}\mathbf{v}^T\} = \mathbf{C}_v. \quad (7.13)$$

The covariance matrix  $\mathbf{C}_v$  is defined as

$$\mathbf{C}_v = \mathbf{C}_h + \mathbf{C}_H + \mathbf{C}_N, \quad (7.14)$$

where  $\mathbf{C}_h$ ,  $\mathbf{C}_H$ , and  $\mathbf{C}_N$  are the error covariance matrices for the ellipsoidal, orthometric, and geoid heights, respectively.

The systematic component  $\mathbf{A}\mathbf{x}$  can be parameterized using low degree bi-variate polynomials or other simple mathematical surfaces. As found in previous studies, the classic four-parameter model given by Heiskanen and Moritz (1967) provides the best representation of the systematic errors among the GPS, orthometric, and geoid heights in Canada (Fotopoulos, 2003). The systematic component at the GNSS/levelling point  $(\varphi_i, \lambda_i)$  is represented as

$$\mathbf{a}_i^T \mathbf{x} = x_1 + x_2 \cos \varphi_i \cos \lambda_i + x_3 \cos \varphi_i \sin \lambda_i + x_4 \sin \varphi_i . \quad (7.15)$$

The standard deviation of the parametric surface computed at point  $i$  is

$$\hat{\sigma}_i^a = \sqrt{\mathbf{a}_i^T \mathbf{C}_{\hat{\mathbf{x}}} \mathbf{a}_i} , \quad (7.16)$$

where the covariance matrix of the estimated parameters  $\mathbf{C}_{\hat{\mathbf{x}}}$  is computed as

$$\mathbf{C}_{\hat{\mathbf{x}}} = (\mathbf{A}^T \mathbf{C}_v^{-1} \mathbf{A})^{-1} . \quad (7.17)$$

Two cases for the error covariance matrix  $\mathbf{C}_v$  can be considered in the combined adjustment. In the first case, correlations between the observations in each height component can be disregarded; thus, diagonal error covariance matrices  $\mathbf{C}_h, \mathbf{C}_H,$  and  $\mathbf{C}_N$  are assumed. In the second case, the correlations are taken into account through the fully-populated error covariance matrices. As shown by Fotopoulos (2003) in a case study for Canada, “overly-optimistic” (with small variance factors) covariance matrices are estimated when the first case is chosen. This effect has been observed for the ellipsoidal heights which are highly correlated. Conversely, it has been found that if the fully-populated covariance matrices are included in the adjustment model, then more realistic error estimates are obtained.

### 7.2.2 Effect of geodynamics on the parametric surface

In this section, the effect of the dynamic geoid and orthometric heights on the parametric surface is studied. For this purpose, it is assumed that a levelling-based vertical datum is established at epoch  $t_0$ . For the same epoch, a geoid model  $N(\varphi, \lambda, t_0)$  is computed. At epoch  $t$ , the orthometric height is computed as

$$H(\varphi, \lambda, t) = h(\varphi, \lambda, t) - N(\varphi, \lambda, t_0) - (\mathbf{a}^T \hat{\mathbf{x}})_t , \quad (7.18)$$

where the parametric surface component  $(\mathbf{a}^T \hat{\mathbf{x}})_t$  should include the effect of the temporal change in the geoid height,  $\delta N = (t - t_0) \dot{N}$ , and the change in the orthometric height,  $\delta H = (t - t_0) \dot{H}$ , for the time interval  $(t - t_0)$  for all GPS-on-benchmark points in the area

of interest. Ideally, it is assumed that the “fundamental point” of the vertical datum is not subject to vertical crustal motion, nor does the equipotential surface through the fundamental point change with time. If the temporal effects were corrected for, the parametric surface would account for all “static” discrepancies among the ellipsoidal, orthometric, and geoid heights discussed in Section 2.1 of Chapter 2. Therefore, the following representation for the parametric surface is assumed:

$$(\mathbf{a}^T \hat{\mathbf{x}})_t = (\mathbf{a}^T \hat{\mathbf{x}})_o + \delta N + \delta H . \quad (7.19)$$

In order to quantify the effect of the dynamic geoid and orthometric heights on the parametric surface, a set of 430 of the most accurate GPS-on-benchmark points in Canada is used. The ellipsoidal heights were determined from the campaign GPS surveys after 1994. The orthometric heights were computed from the geopotential numbers obtained from the minimally constrained least-squares adjustment of the levelling measurements after 1981. The geoid heights are computed from the CGG05 model based on the GGM02C GRACE geoid model. This set of GPS-on-benchmark points has been used in the latest calibration of the errors of the CGG05 geoid model (Huang *et al.*, 2006). For all points, the height misclosures have been made available together with the fully-populated cofactor matrices and the scale factors for the ellipsoidal, orthometric, and geoid heights (Fotopoulos, 2007, personal communication). The data set is divided into three regions (Figure 7.1): namely, **region A** (206 points), **region B** (76 points), and **region C** (148 points). Region A is characterized by densely distributed points along the levelling lines, but large areas are not covered by data. Region B is relatively homogeneously covered, but the data points are sparsely distributed. Region C has a mixed type of data coverage.

Table 2.1 contains statistics of the standard deviations of the three data sets. Clearly, the accuracy of the orthometric heights degrades from region A to region C as a result of increasing the systematic errors in the vertical control network. The errors of the ellipsoidal heights range from a sub-centimetre level to two decimetres with mean values of 37 and 47 mm. The average error of the geoid height increases from 28 mm for region B (flat terrain) to 53 mm for region C (rocky terrain).

The rates of change of the geoid and orthometric heights are interpolated at the GPS-on-benchmarks points using the empirical models developed in Section 5.4.2 of Chapter 5. As seen in Figure 7.1, the GPS-on-benchmarks points do not cover the areas around Hudson Bay, where the maximum changes in the geoid and orthometric heights are observed. The parametric surfaces for the three regions are shown in Figure 7.2. A significant east-west slope is observed in all three of them. This slope is attributed mainly to the systematic errors present in the levelling data and accumulated over the levelling lines between the east and west coasts. Figure 7.2 also shows the total effect of the dynamic components  $\delta N$  and  $\delta H$  on the parametric surface for each region and for a ten-year time period. The effect of the  $\delta N$  component comprises approximately 10% of the total effect. Thus, if the maximum change in the parametric surface is 100 mm, 10 mm are due to the change in the geoid height.

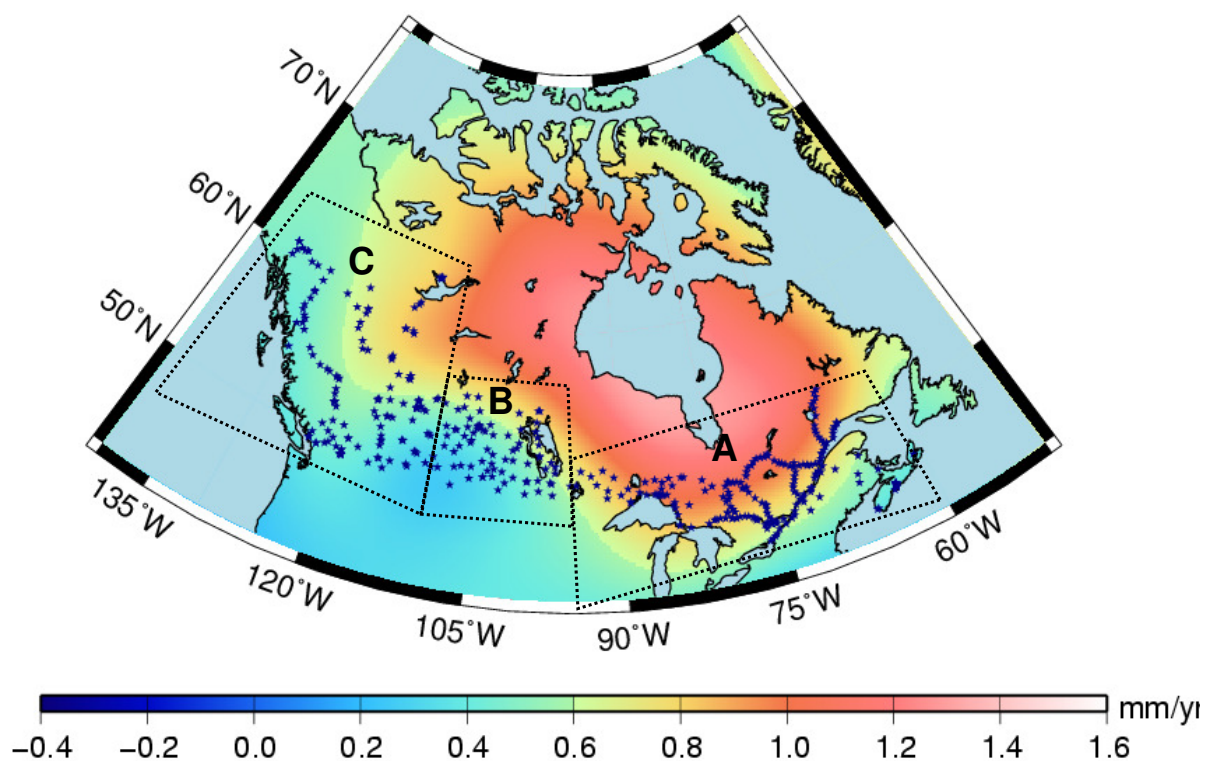


**Figure 7.1:** GPS on first order levelling benchmarks for the three regions and modelled rates of change of the geoid height.

**Table 7.2:** Statistics of the errors of the ellipsoidal, geoid, and orthometric heights, in mm

$\sigma$	Region A			Region B			Region C		
	Min	Mean	Max	Min	Mean	Max	Min	Mean	Max
h	6	37	162	9	37	80	5	47	230
H	31	83	142	143	158	169	161	181	208
N	28	34	59	25	28	32	22	53	169

The effect of the dynamic component of the geoid and orthometric heights on the parametric surface will be compared with the errors of the ellipsoidal, geoid, and orthometric heights for each of the three regions. For this purpose, the following relative variables are defined:

$$\max \left( \frac{(\delta N)_i}{\hat{\sigma}_i^a} \right) \quad (7.20a)$$

and

$$\max \left( \frac{(\delta N + \delta H)_i}{\hat{\sigma}_i^a} \right) \quad (7.20b)$$

are the maximum ratios of the temporal effect and the estimated error of the parametric surface and have a meaning of a signal-to-noise ratio. Values larger than 1.0 (above the noise level) indicate that the dynamic effect should be accounted for.

$$\max \left( \frac{\bar{\sigma}_\vartheta}{\hat{\sigma}_i^a} \right), \vartheta = h, H, N \quad (7.21)$$

is the maximum ratio of the average standard deviation  $\bar{\sigma}_\vartheta$  for each of the three height components and the estimated error of the parametric surface.

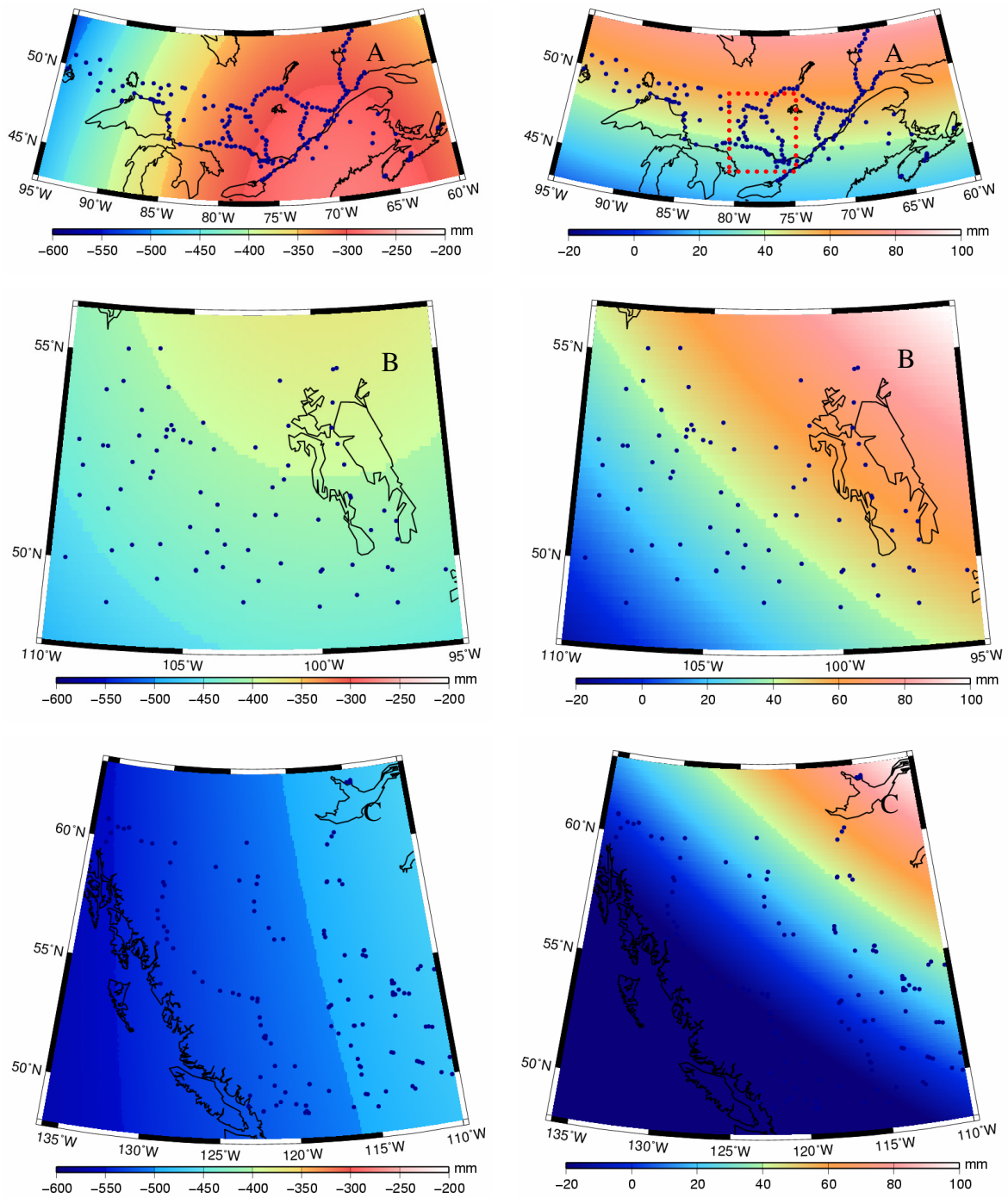


**Figure 7.2:** Left: parametric surfaces for the three regions; right: total dynamic effect on the parametric surfaces.

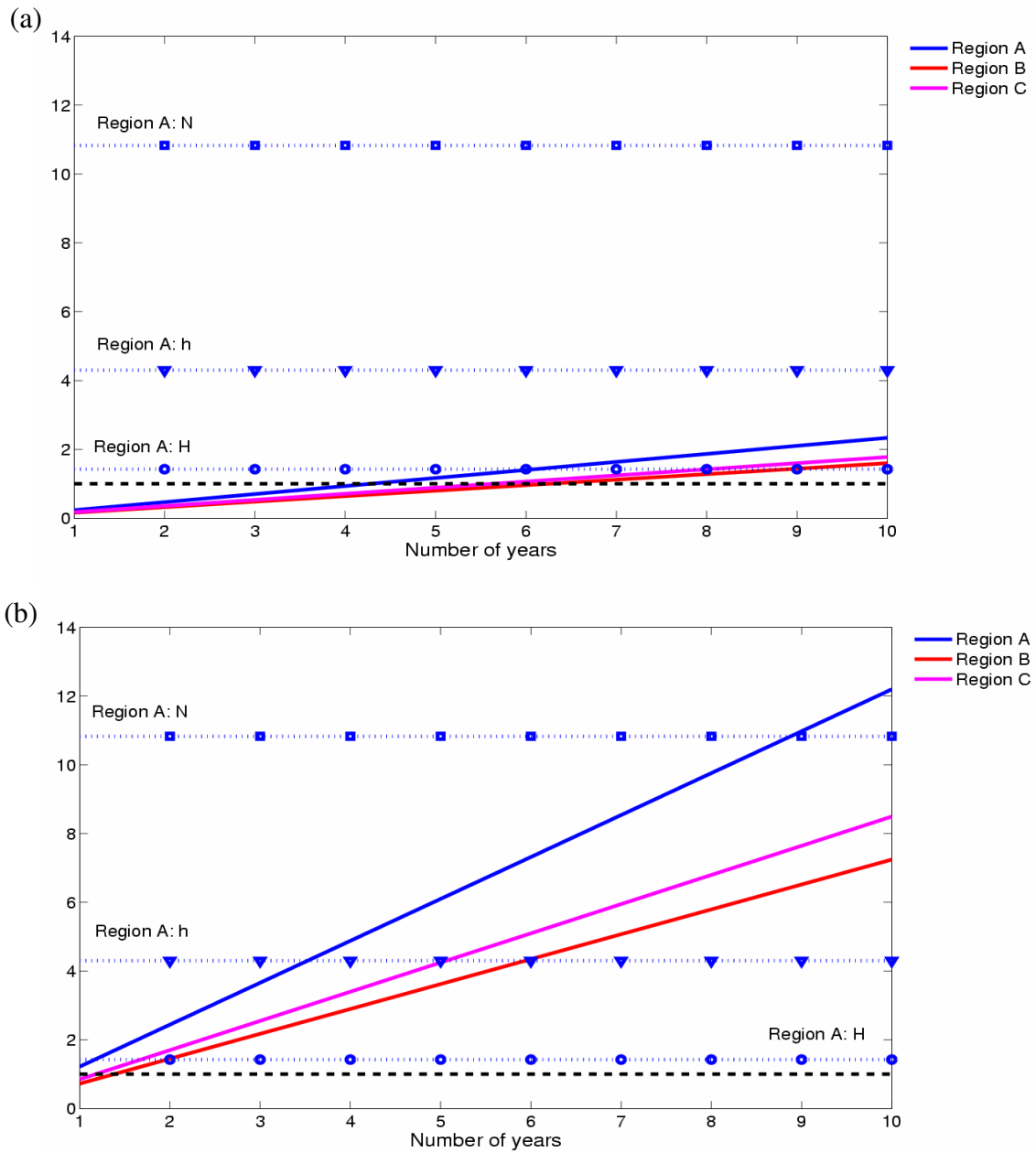


**Figure 7.3:** Effect of dynamic components and relative errors from diagonal error covariance matrices: (a) change in geoid height and (b) change in geoid and orthometric heights. The vertical axis shows relative variables.

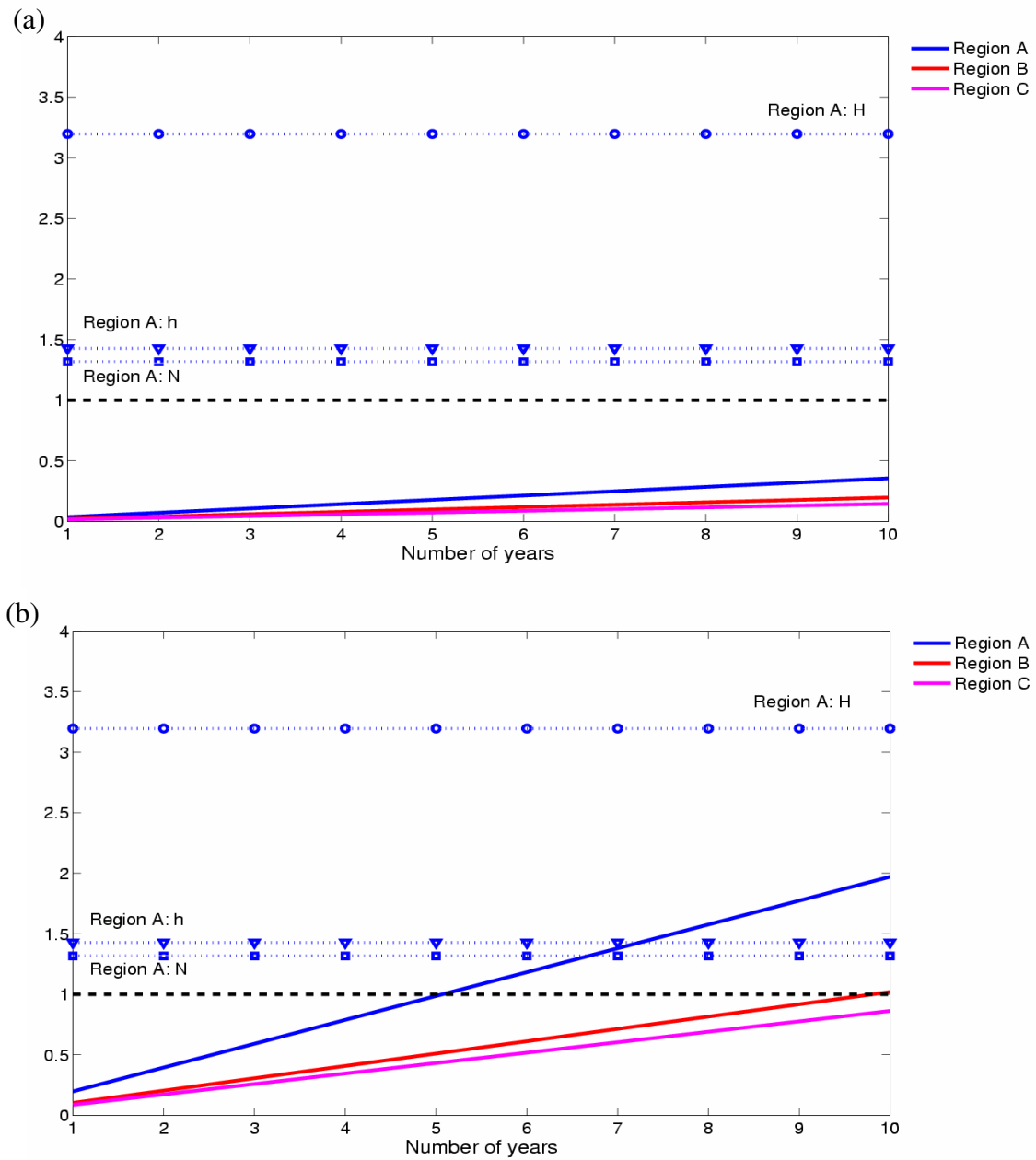


**Figure 7.4:** Effect of the dynamic components and relative errors from fully-populated error covariance matrices: (a) change in geoid height and (b) change in geoid and orthometric heights. The vertical axis shows relative variables.

### 7.2.3 Analysis of results

First, the combined least-squares adjustment of the ellipsoidal, orthometric, and geoid heights is performed with the diagonal error covariance matrices. The effect of the temporal changes in the geoid height (Figure 7.3a) and in the geoid and orthometric heights (Figure 7.3b) are computed by means of Eqs. (7.20a) and (7.20b) and plotted as a linear increase for a ten-year time interval. Evidently, the change in the geoid height becomes significant (above the signal-to-noise ratio of 1.0) after 4 years for region A and after 6 years for regions B and C. As shown in Figure 7.2 and Table 7.2, Region A is characterized by densely distributed GPS-on-benchmarks points and more accurate orthometric heights, and, as a consequence, the parametric surface is determined more accurately. However, the effect of the dynamic geoid component is far below the mean error of the geoid heights, computed by means of Eq. (7.21). When both the temporal changes in the geoid and orthometric heights are taken into account, the total dynamic effect far exceeds the signal-to-noise ratio after the first year; however, it needs to be accounted for after the ninth year when the mean error of the geoid heights is exceeded.

As pointed out in Subsection 7.2.1, the ellipsoidal and orthometric heights could have rather optimistic errors if the errors are obtained from calibrated diagonal error covariance matrices. If this is the case, the parametric surface may be unrealistically accurate and, as a result, the computed dynamic effect may be overestimated. Another consequence from the up-weighting of the ellipsoidal and orthometric heights is that the geoid errors may appear unrealistically large. Thus, the lower accuracy of the geoid heights appears to be the limiting factor for incorporating the dynamic component of the geoid and orthometric heights into the vertical datum.

If the fully-populated error covariance matrices are used in the combined adjustment of the ellipsoidal, orthometric, and geoid heights, an increase is observed for the errors of the parametric surfaces for the three regions. As a result, much smaller ratios are computed by means of Eqs. (7.20a) and (7.20b); see Figures 7.4a and b. For all of the regions, the contribution of the dynamic geoid component is far below the estimated errors of the parametric surfaces. The total dynamic component becomes significant after 5 years for

region A and after 10 years for region B. However, the dynamic effect is much less than the mean error of the orthometric heights, which is the least accurate among the three height components; see Table 7.2. For comparison, the mean errors of the ellipsoidal and geoid heights are approximately equal for all of the regions.

Based on the results obtained in this study using the most recent and accurate height data available in Canada, some important conclusions can be drawn. First, the contemporary accuracy of the three height components precludes the incorporation of a dynamic geoid and orthometric heights in the vertical datum of Canada. Second, the assessment of the contribution of the dynamic components clearly depends on the proper relative weighting of the ellipsoidal, orthometric, and geoid heights. As evident from the discussion above, the accuracy of the orthometric heights appears to be a limiting factor for incorporating the dynamic geoid in the vertical datum. This issue is investigated further by means of a simulated study.

For the test area denoted by a red square in Figure 7.2, the significance of the temporal changes in the geoid and orthometric heights for a 10-year time interval is assessed for different mean variances of the ellipsoidal, orthometric, and geoid heights. From the GPS-on-benchmarks points in the area, a subset of points with a mean distance of 80 - 100 km, at which the ellipsoidal heights are not correlated, is chosen. These GPS-on-benchmarks points provide a datum for GNSS/levelling in the test area, through which the orthometric heights can be obtained with respect to the mean sea level in Rimouski. The mean variances are used to scale the three cofactor matrices of the data.

In Figure 7.5, the maximum ratio of the temporal effect of the geoid height and the estimated error of the parametric surface is plotted for different mean standard deviations of the three height components. Ellipsoidal heights should be known with accuracy of at least 10 mm in order to incorporate the dynamic geoid height in the vertical datum. The maximum errors of the geoid and orthometric heights are 11 and 12 mm, respectively. At present, the orthometric heights, computed from the latest adjustment of the primary vertical control network of Canada, have an order of magnitude lower accuracy. It is accepted that the orthometric heights are accurate at decimetre level with respect to the

equipotential surface through the fundamental datum point in Rimouski (Véronneau, 2006; see Table 7.2). The main difficulty for improving the accuracy of the orthometric heights is the accumulation of systematic errors along the levelling lines of magnitude of 0.1 mm/km as well as undetected erroneous observations (*ibid.*). The computational accuracy of the geoid height can be improved further until it reaches the expected 1-cm level of after-GOCE geoid models (Chapter 1). Provided that the errors of the three height components reach 10 - 15 mm, the geoid heights should be corrected for the dynamic effect every 10 years (Figure 7.6), and the levelled vertical crustal motion should be accounted for every 2 years.

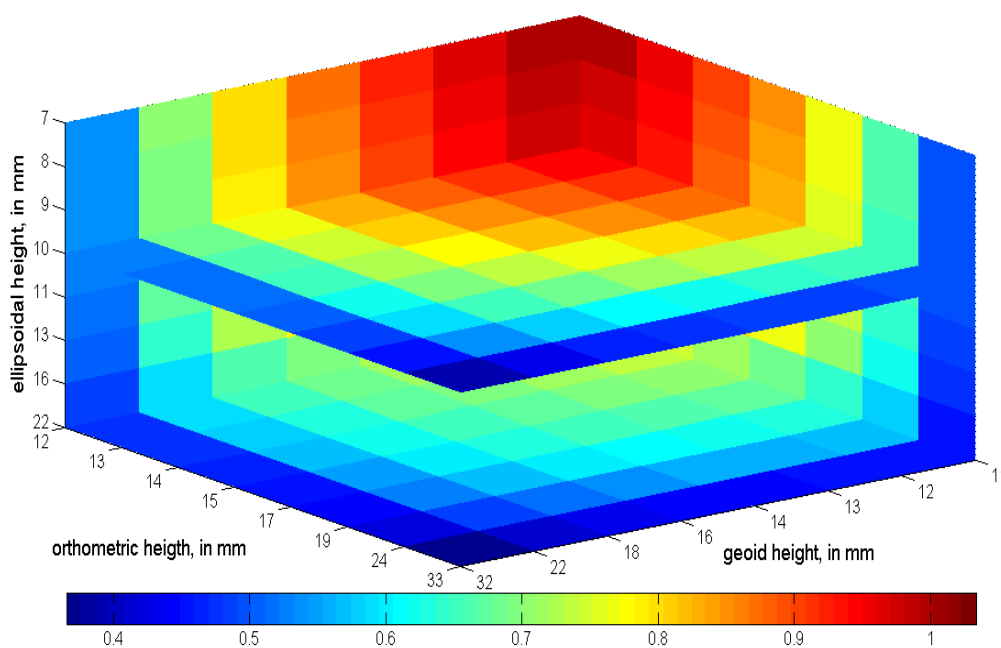


**Figure 7.5:** Effect of the temporal change in the geoid height for a 10-year time period as a function of the mean standard deviation of the three height data components.

### 7.3 Summary

The dynamic geoid has been considered as a vertical datum for orthometric heights in the context of the combined adjustment of ellipsoidal, orthometric, and geoid heights in Canada. Using the most recent and accurate height data at GPS-on-benchmark points, the

effect of incorporating the dynamic vertical reference surface for orthometric heights has been assessed. It has been shown that the present-day accuracy of the three height components precludes the implementation of the dynamic vertical datum, and the accuracy of the orthometric heights appears to be the limiting factor. By means of a simulated example, it has been shown that the dynamic vertical datum requires accuracy of 10 - 15 mm for the three height components. If this level of accuracy is reached, the vertical reference surface needs to be corrected for the secular geodynamic effect after 8 - 10 years elapsed from the reference epoch. For comparison, vertical crustal motion causes significant systematic discrepancies among the ellipsoidal, orthometric, and geoid heights over a two-year time interval.

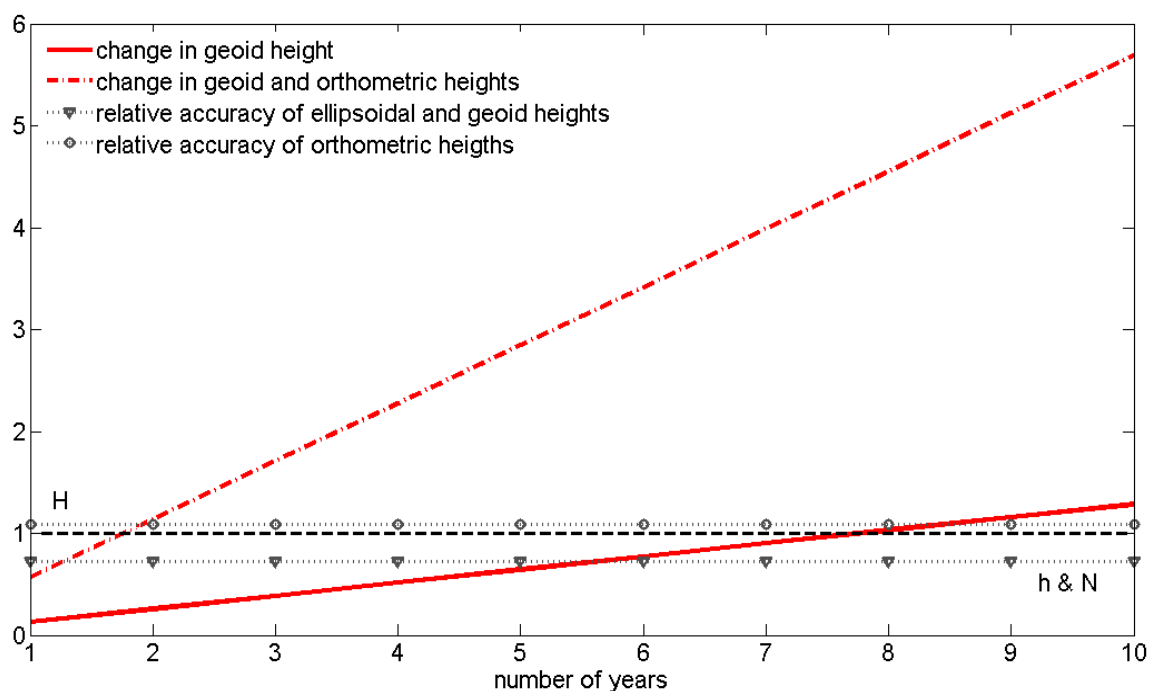


**Figure 7.6:** Effect of the temporal changes in the geoid and orthometric heights over 10 years. Vertical axis shows relative variables.

## Chapter Eight: Concluding Remarks

In this chapter, the major conclusions and outlook for future research that can be drawn from the results in this thesis are outlined. The main objective was to develop a methodology for optimally combining the available geodetic data to model the temporal variations of the geoid and orthometric heights in Canada. These models can contribute to the definition and realization of a dynamic geoid-based vertical datum for Canada, but they also comprise independent constraints for postglacial rebound modelling. An excellent example is the study in the Great Lakes area (Chapter 6), in which GRACE data were combined with GPS vertical velocities and joint tide gauge/altimetry data.

### 8.1 Conclusions

The proposed methodology is based on the general least-squares collocation approach for predicting rates of change of the geoid and orthometric heights. It combines the functional approach for modelling a velocity surface by means of analytical functions and the stochastic approach for modelling the residual velocity signal by means of covariance functions. The methodology is efficient with respect to the available terrestrial data in Canada. In particular, it accounts for the sparse and very irregular distribution of the terrestrial gravity and GPS data over the Canadian landmasses. However, this does not preclude the application of the developed methodology and the designed procedures in other regions with a similar geodynamic signal, such as Fennoscandia.

The main advantage of the least-squares collocation with parameters approach, from which this research benefited, is the ability to handle heterogeneous data input and output. Essentially, all kinds of data that account for vertical crustal displacement and/or the Earth's interior mass redistribution (terrestrial gravity rates, GPS vertical velocities, re-

levelling data, combined tide gauge/altimetry data, GPS-observed rates of change of the geoid height, and estimates of gravity-to-height ratio) can be inputted in the computational procedures and can be predicted as well. Several important issues related to the optimal combination of heterogeneous data were resolved: the choice of the base functions and their optimal location and scaling, modelling the stochastic signal component, outlier detection, and proper weighting of error covariance matrices of the different data types using variance component estimation.

With regard to the developed methodology, a list of the main achievements and conclusions follows:

- A critical review of the available data in North America, and Canada, in particular, was undertaken in Chapter 2. A general framework (not limited to postglacial rebound) for combining heterogeneous data for empirical modelling of the rates of change of the geoid and heights was developed (Figure 2.7). The input data and the desired output can change accordingly to the nature of the process causing the temporal variations and the availability of the data for the areas of interest.
- An extensive study of the application of the radial base functions for approximating vertical displacement rates was undertaken. The results of these simulation studies showed that the (inverse) multiquadrics base functions provide excellent approximation for irregularly distributed data if the base functions are scaled appropriately. An empirical rule for scaling the base functions was determined and tested. By means of several examples, it was shown that the inverse multiquadric functions could model a wide range of vertical displacement surfaces in addition to postglacial rebound signal.
- Algorithms for selecting the optimal location of the base functions were constructed using the statistical cross-validation and (Gram-Schmidt) orthogonal least-squares techniques. An implementation of these two methods for parametric surface modelling in the GNSS/levelling can be found in (Fotopoulos, 2003). The main difference, however, consists in the fact that the

modified Gram-Schmidt algorithm implemented in this thesis orders the base functions in terms of their significance to the approximated vertical displacement surface. Therefore, there is no need of applying statistical testing to assess the significance of each base function. This approach could be implemented even in the case of approximating vertical displacement rates by polynomial surfaces.

- The predicted rates of change of the geoid height from the combined terrestrial gravity rates and GPS vertical velocities agree within 0.1-0.2 mm/yr in the areas with a peak signal with the postglacial rebound model predictions using an approximation of the VM2 model and the ICE-4G de-glaciation history.
- It was shown that the predicted rates of change of the terrestrial gravity and the absolute vertical displacement agree within the prediction accuracy with the data from the Mid-continent profile at most of the sites. It was observed that the addition of the GPS velocities improves the agreement with the validation data sets. Therefore, it can be expected that the methodology developed in this research is capable of improving the predicted rates with a longer time span of GPS measurements.
- The proposed methodology was successfully applied for the first time (according to the author's knowledge) to combine terrestrial data with GRACE-observed vertical displacement rates. The homogeneous GRACE data coverage compensates for the rather irregular distribution of the terrestrial data, while the effect of the large scale uncertainties in the former can be corrected for by the use of the precise terrestrial observations.
- The capabilities of the PC/EOF analysis to extract the geoid rate from the time series of GRACE-observed geoid changes in North America were investigated. It was found that the PC/EOF analysis provides identical results with the traditional least-squares fitting of time series. However, the main advantage of applying the PC/EOF analysis is that it allows for assessing the effect of the inter-annual and long-term geoid variability on the estimated trend.

- In order to provide reliable constraints for GIA models in terms of a line of zero motion, tilting, and a peak signal that are free from the influence of erroneous observations, a robust method for combined least-squares adjustment was presented. This method includes variance component estimation in order to ensure reliably estimated error bounds of the empirical rates of crustal displacement required for inverse GIA modelling.
- For the purpose of definition of a dynamic geoid-based vertical datum, the effect of temporal variations of the terrestrial gravity, orthometric, and geoid heights was assessed using the remove-compute-restore procedure and Helmert condensation method. For vertical datum modernization only the rate of change of the geoid height obtained by the methodology and procedures developed in this study is found to be sufficient.
- The current accuracy of the GPS-determined ellipsoidal, orthometric, and geoid heights does not allow incorporation of the geodynamic effect in the levelling-based vertical datum. One limiting factor is the orthometric height component, which exhibits large systematic errors across the vertical control network. It has been shown that the dynamic vertical datum requires accuracy of 10-15 mm for the three height components that, at present, is not achieved.

## 8.2 Outlook for future research

A list of recommendations for future research is presented in the following:

- The methodology developed in this research could be tested with other types of data in areas with similar deformation characteristics. Ultimately, another suitable test region is Fennoscandia, where the historic re-levelling data, tide gauge recording, and collocated absolute gravimetry and GPS sites can provide further validation of the proposed methodology. Another area of interest is southeastern Alaska with dominating viscoelastic crustal deformation (Larsen *et al.*, 2004).

- The proposed methodology allows for combining the geodynamic model predictions of postglacial rebound rates with the empirical approach in a rigorous dynamic-based procedure. In such a hybrid approach, the spatial trend of the geoid and vertical displacement rates could be predicted by postglacial rebound simulations, while the empirical modelling could focus on the stochastic component accounting for local vertical displacement and mass redistribution processes or correlated measurement errors. First results from applying a dynamic Kalman filtering and assimilation of GPS velocities have been demonstrated by Blewitt *et al.* (2005).
- A non-linear optimization least-squares procedure can be developed to determine both the shape and location of the multiquadric base functions. This could be combined with iterative outlier detection and variance component estimation.
- A better gravity-to-height ratio needs to be determined and incorporated in the combined procedure provided that a network of collocated terrestrial gravity sites and permanent GPS stations is realized across Canada and long records of measurements are available. Such integral networks exist in Fennoscandia and in the eastern areas of Canada. This will open the possibility for studying the lateral variations of the gravity-to-height ratio.
- The combined least-squares collocation procedure could be modified to predict rates of horizontal crustal displacements in addition to the vertical component of the crustal deformation. An example for predicting shear strain rates in tectonically active areas from GPS velocities using least-squares collocation is found in the work of Li *et al.* (1999).
- Different methods for rotation of principal components in the PC/EOF analysis of time series of GRACE-observed geoid change can be investigated. In particular, the oblique rotation might be more suitable than the orthogonal varimax rotation because neither the spatial patterns, nor the principal component time series of geoid changes are expected to be orthogonal.

Moreover, by appropriate rotation of base functions and data variance redistribution, it could be possible to separate two spatial trends (with a different geographical footprint) in different principal components. Thus, the PC/EOF analysis can be helpful in studying spatial leakage of different signals over the continental landmasses of North America.

### **8.3 Recommendations for establishing a geoid-based, dynamic vertical datum for Canada**

Given that a geoid-based datum will be established in Canada by the end of the decade, several practical considerations and recommendations are outlined in the following.

#### **8.3.1 A dynamic geoid model**

- For the purpose of modernizing the vertical datum in Canada, the dynamic geoid consists of a static geoid model computed for one *reference epoch* and a model for the rates of change of the geoid height provided that a slow deformation of the Earth and its gravity field is assumed.
- The reference epoch can be the epoch of 2010. The geoid height for any other epoch is computed by correcting the static geoid height with the change for the time interval elapsed from the reference epoch to the required epoch.
- A model for the rates of change of the geoid height can be obtained by means of the methods used in this research and summarized in Figure 8.1. However, it is recommended that GRACE data are combined with terrestrial data using the method of least-squares collocation with parameters. The available terrestrial data provide constraints for the GRACE-observed rates of deformation in southern areas of Canada.
- The gravity-to-height ratio used in the combined procedure of the GRACE and terrestrial data should be computed from measurements at collocated absolute gravity sites and GPS stations well distributed across Canada. To provide better

data constraints for the GRACE-observed deformation field and glacial isostatic adjustment modelling, collocated sites west and north of Hudson Bay are required.

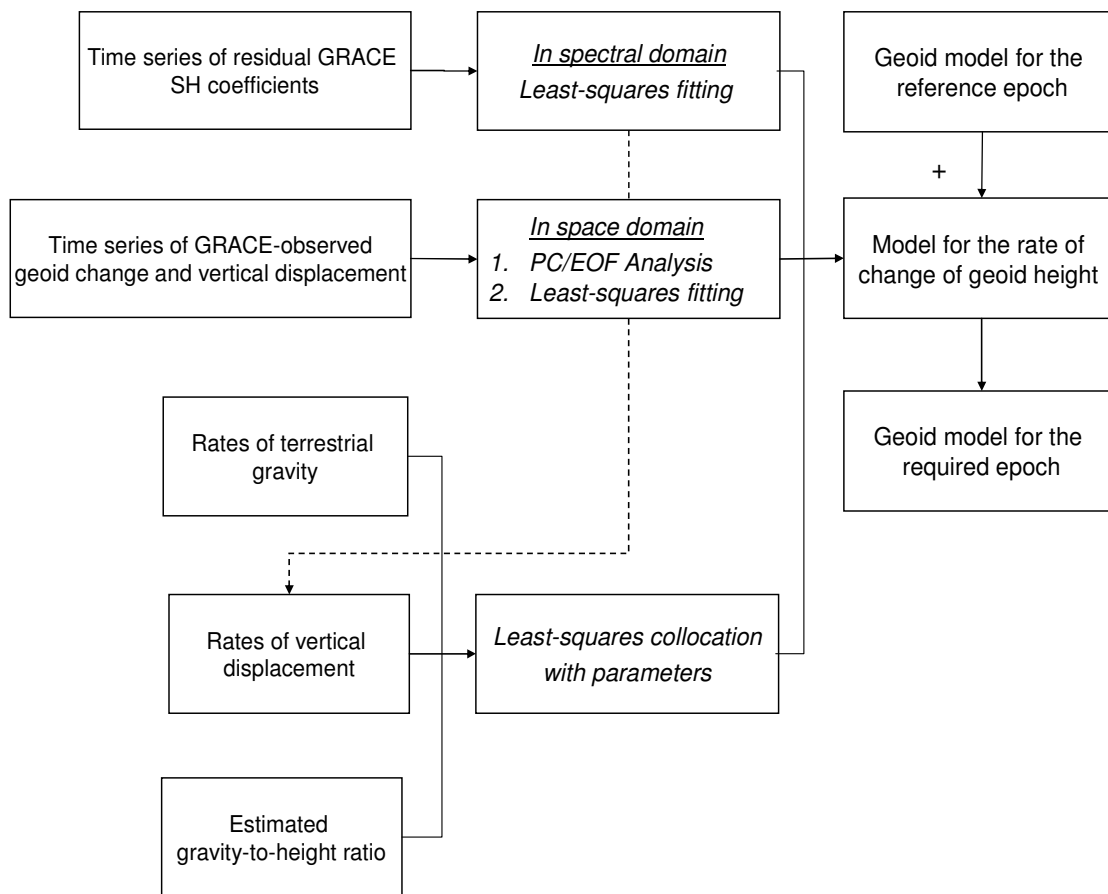


**Figure 8.1:** A general scheme for computing a dynamic geoid model.

### 8.3.2 A dynamic vertical datum

In view of the required one centimetre accuracy of the three height components (Chapter 7), a dynamic vertical datum based on the dynamic geoid can be established as follows (see also Figure 8.2):

1. The vertical reference surface is defined by the static geoid model computed for the reference epoch.
2. Calibrated errors of the geoid model are computed by means of combined adjustment of ellipsoidal, orthometric, and geoid heights of the GPS-on-benchmarks points in Canada (Fotopoulos, 2005). The geoid heights should be computed from the geoid model for the reference epoch, and the ellipsoidal and orthometric heights should be corrected for the vertical crustal displacement and referenced to the epoch of the geoid model. For a recent study on the rectification of the epoch of GPS-derived ellipsoidal heights in Canada, Fotopoulos *et al.* (2007) can be consulted. To obtain temporally homogeneous height data, consistent models of the rates of change of the geoid, orthometric, and ellipsoidal heights, as the models developed in this research, should be used.
3. A criterion for “stability” of the vertical reference surface can be introduced in terms of the mean calibrated error of the static geoid model. The vertical reference surface can be assumed “stable” if the temporal changes in the geoid height for the time elapsed from the reference epoch remain below the mean calibrated geoid error. The vertical reference surface should be corrected for the temporal changes in the geoid height if the stability requirement is not longer fulfilled.
4. A new reference surface should be defined when errors of the modelled rates of change of the geoid height become comparable with the magnitude of the rates. For example, if the models developed in this research are used, and the model error obtained from the validation with glacial isostatic model outputs is 0.1 – 0.2 mm/yr, 10 to 15 years can be considered as a limit for the existence of the established dynamic datum. Also, a new reference surface should be defined if a more accurate geoid model is available.

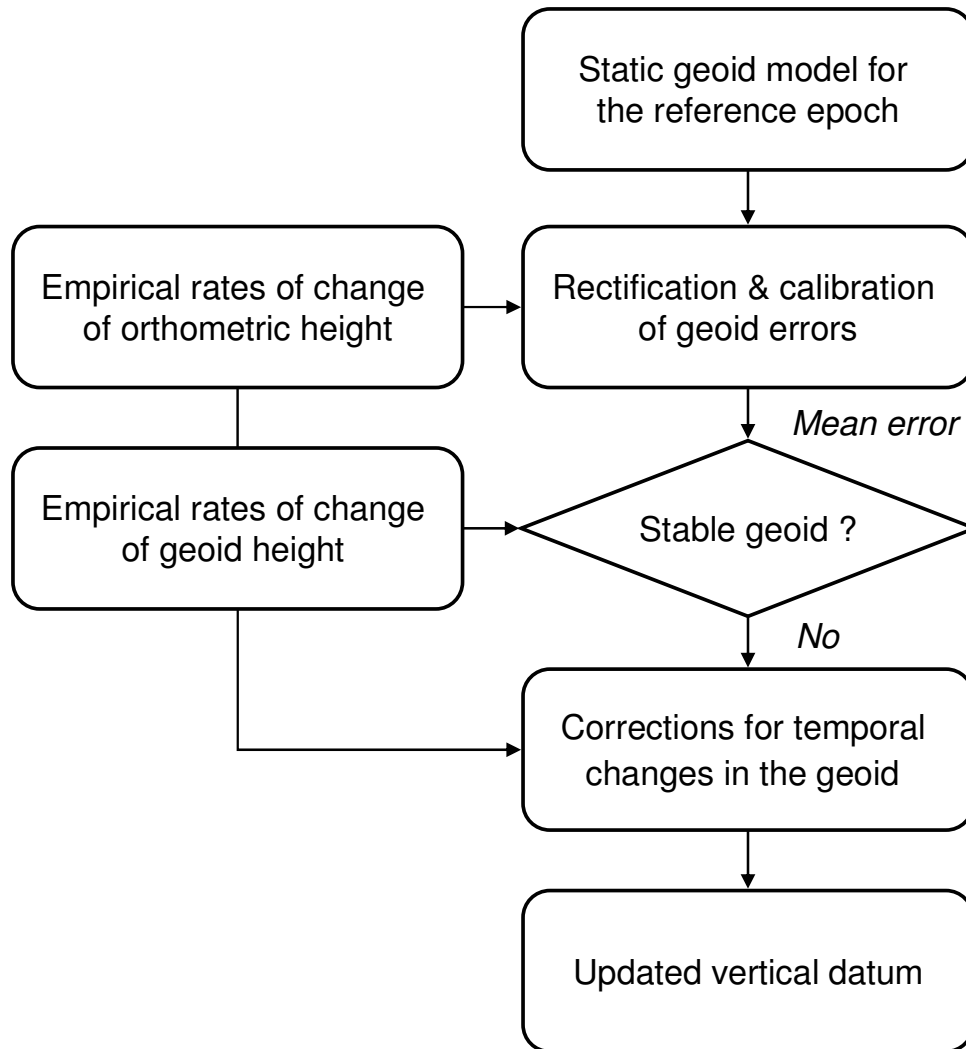


**Figure 8.2:** Steps for establishing a dynamic geoid-based vertical datum.

## Bibliography

- Abad J and Sesma J (1995): Computation of the Regular Confluent Hypergeometric Function. *Mathematica J.*, 5, pp. 74 - 76.
- Ali I (2006): A globally consistent and dynamic Canadian gravity reference frame for a modern heighting system and other applications. *MSc Thesis*, University of York, Toronto.
- Allis RG and Hunt TH (1986): Analysis of exploitation-induced gravity changes at Waiakei Geothermal Field. *Geophysics*, 51(8), pp. 1647 - 1660.
- Arge E and Floater M (1994): Approximating scattered data with discontinuities. *Numerical Algorithms*, 8, pp. 149 - 166.
- Argus D, Peltier R and Watkins M (1999): Glacial isostatic adjustment observed with VLBI and SLR. *J. Geophys. Res.*, 104(B12), pp. 29,077 - 29,094.
- Baarda W (1967): Statistical concepts in geodesy. 97 pp., *Netherlands Geodetic Commission, Publ. on Geodesy*, New series 2(4).
- Barthelmes F and Dietrich R (1991): Use of point masses on optimized positions for the approximation of the gravity field. In: *Determination of the Geoid: Present and future*, Springer, Berlin, pp. 484 - 493.
- Basu A and Paliwal KK (1989): Robust M-estimates and generalized M-estimates for autoregressive parameter estimation. *TENCON 89, Fourth IEEE Region 10 International Conference*, pp. 355 - 358.
- Becker S (2004): Smoothed spatial averaging in the interpretation of the time variable global gravity field. *Diploma Thesis*, Institut für Theoretische Geodäsie, Bonn, 2004.

- Benzi R, Deidda R and Marrocu M (1997): Characterization of temperature and precipitation fields over Sardinia with principal component analysis and singular spectrum analysis. *Int. J. Climatol.*, 17, pp. 1,231 - 1,262.
- Bettadpur S (2004): Gravity Recovery and Climate Experiment, Level-2 Gravity Field Product User Handbook, Center for Space Research, The University of Texas at Austin.
- Billings SD, Beatson RK and Newsam GN (2002): Smooth fitting of geophysical data using continuous global surfaces. *Geophysics*, 67(6), pp. 1,823 - 1,834.
- Biró P (1983): Time Variation of Heights and Gravity. Akademia Kiadó, Budapest.
- Biró P, Heck B and Thônq NC (1986): On a new approach into the solution of the three-dimensional geodetic-geodynamic boundary value problem. *AVN- Int. Edition*, 3, pp. 9 - 21.
- Björnsonn H and Venegas SA (1997): A manual for EOF and SVD analyses of climatic data. Department of Atmospheric and Oceanic Sciences and Centre for Climate and Global Change Research, McGill University, February, 1997.
- Blewitt G, Argus D, Bennett R, Bock Y, Calais E, Craymer M, Davis J, Dixon T, Freymueller J, Herring T, Johnson D, Larson K, Miller M, Sella G, Snay R and Tamisiea M (2005): A Stable North American Reference Frame (SNARF): First Release. Proceedings from *the Joint UNAVCO/IRIS Workshop*, Stevenson, WA, USA, 2005.
- Boedecker G (1991): IAGBN: Absolute Observations Data Processing Standards. *BGI-Bull. d'Information*, 1991, 69, 25.
- Breiman L (1993): Fitting additive models to regression data. Diagnostics and alternative views. *Computational Statistics and Data Analysis*, 15, pp. 13 - 46.
- Buhmann MD (2000): Radial Basis Functions. *Acta Numerica*, (2000), pp. 1 - 38.
- Bürgmann R, Hilley G, Feretti A and Novali F (2006): Resolving vertical tectonics in the San Francisco Bay area from permanent scatterer InSAR and GPS analysis. *Geology*, 34(3), pp. 221 - 224, doi: 10.1130/G22064.1.

- Carlson RE and Foley TA (1991): The parameter  $R^2$  in multiquadric interpolation. *Comp. Math. Appl.*, 24, pp. 29 - 42.
- Carrera G, Vaníček P and Craymer MR (1991): The compilation of the map of recent crustal movements in Canada. *Technical Report No 153*, Department of Surveying Engineering, University of New Brunswick.
- Cathles LM (1975): The viscosity of the Earth's mantle. Princeton University Press, Princeton – New Jersey.
- Cazenave A, Dominh K, Ponchaut F, Soudarin L, Cretaux JF and Le Provost C (1999): Sea level change from Topex-Poseidon altimetry and tide gauges, and vertical crustal motion from DORIS. *Geophys. Res. Lett.*, 26(14), pp. 2,077 - 2,080.
- Chambers DP (2006a): Observing seasonal steric sea level variations with GRACE and satellite altimetry. *J. Geophys. Res.*, 111, C03010, doi:10.1029/2005JG002914.
- Chambers DP (2006b): Evaluation of new GRACE time-variable gravity data over the ocean. *Geophys. Res. Lett.*, 33, L17603, doi:10.1029/2006GL027296.
- Chen S, Billings SA and Luo W (1989): Orthogonal least squares methods and their application to non-linear system identification. *Int. J. Control*, 50(5), pp. 1,873 – 1,896.
- Chen S, Cowan CFN and Grant PM (1991): Orthogonal Least Squares Learning Algorithm for Radial Base Function Networks. *IEEE Trans. Neural Networks*, 2(2), pp. 302 – 309.
- Chen F, Mitchell K, Schaake J, Xue Y, Pan H-L, Koren V, Duan QY, Ek M and Betts A (1996): Modeling of land surface evaporation by four schemes and comparison with FIFE observations. *J. Geophys. Res.*, 101(D3), pp. 7,251 – 7,268.
- Chen CS, Kuhn G, Li J and Mishuris G (2003): Radial basis functions for solving near singular Poisson problems. *Commun. Numer. Meth. Engng.*, 19, pp. 333 – 347.
- Chen JL, Wilson CR, Famiglietti JS and Rodell M (2005a): Spatial sensitivity of the Gravity Recovery and Climate Experiment (GRACE) time-variable gravity observations. *J. Geophys. Res.*, 110, B08408, doi:10.1029/2004JB00353.

- Chen JL, Rodell M, Wilson CR and Famiglietti JS (2005b): Low degree spherical harmonic influences on Gravity Recovery and Climate Experiment (GRACE) water storage estimates. *Geophys. Res. Lett.*, 32, L14405, doi:10.1029/2005GL022964.
- Chen JL, Tapley BD and Wilson CR (2006a): Alaskan mountain glacial melting observed by satellite gravimetry. *Earth and Planet. Sci. Lett.*, 248, pp. 368–378.
- Chen JL, Wilson CR, Blankenship DD and Tapley BD (2006b): Antarctic mass rates from GRACE. *Geophys. Res. Lett.*, 33, L11502, doi:10.1029/2006GL026369.
- Chen JL, Wilson CR and Seo KW (2006c): Optimized smoothing of Gravity Recovery and Climate Experiment (GRACE) time variable gravity observations. *J. Geophys. Res.*, 111, B06408, doi:10.1029/2005JB004064.
- Cianetti S, Giunchi C and Spada G (2002): Mantle Viscosity beneath the Hudson Bay: An Inversion Based on the Metropolis Algorithm. *J. Geophys. Res.*, 107, doi:10.1029/2001JB000585.
- CIRES (1993): Applications of absolute gravity measurements, Workshop, Boulder, Colorado, March 22-23, 1993.
- Clark JA, Haidle FE and Gunningham LN (2000): Comparison of satellite altimetry to tide gauge measurements of sea level: Predictions of glacio-isostatic adjustment. *J Climate*, 15, pp. 3,291 – 3,300.
- Crocetto N, Gatti M and Russo P (2000): Simplified formulae for the BIQUE estimation of variance components in disjunctive observation groups. *J. Geodesy*, 74, pp. 447 - 457.
- Danielsen JS (2001): A land uplift map of Fennoscandia. *Survey Review*, 36, pp. 282 - 290.
- Dermanis A (1985): Optimization problems in geodetic networks with signals. In *Optimization and Design of Geodetic Networks*, Springer-Verlag, pp. 220 - 256.
- Dermanis A and Rossikopoulos D (1991): Statistical Inference in integrated geodesy. *IUGG XXth General Assembly, IAG*, Vienna, 1991.

- Devaraji B (2006): Levelling Network Analysis for the Definition of a Kinematic Vertical Datum in Canada. *MSc thesis*, University of Calgary, Department of Geomatics Engineering, Report No 20244.
- Dickey JD et al. (1997): Satellite gravity and the Geosphere: Contributions to the study of the Solid Earth and Its Fluid Envelop. 112 pp., *Natl. Acad. Press*, Washington D.C., 1997.
- Douglas BC (2001): Sea Level Change in the Era of the Recording Tide Gauge. *Sea Level Rise: History and Consequences, International Geophysics Series, 75*, Academic Press.
- Dziewonski AM and Anderson DL (1981): Preliminary reference Earth model. *Phys. Earth Planet. Inter.*, 25, pp. 279 - 356.
- Egli R, Geiger A, Wiget A and Kahle H-G (2007): A modified least-squares collocation method for the determination of crustal deformation: first results in the Swiss Alps. *Geophys. J. Int.*, 168, pp. 1 - 12.
- Ekman M (1989): Impacts of geodynamics phenomena on systems for heights and gravity. *Bull. Geod.*, 63, pp. 281 - 293.
- Ekman M (1996): A consistent map of the postglacial uplift of Fennoscandia. *Terra Nova*, 8, pp. 158 - 165.
- Ekman M and Mäkinen J (1996): Recent postglacial rebound, gravity change and mantle flow in Fennoscandia. *Geophys. J. Int.*, 126, pp. 229 - 234.
- El-Fiky GS, Kato T and Fujii Y (1997): Distribution of vertical crustal movement rates in the Tohoku district, Japan, predicted by least-squares collocation. *J. Geodesy*, 71, pp. 432 - 442.
- Faller JE (2002): Thirty years of progress in absolute gravimetry: a scientific capability implemented by technological advances. *Metrologia*, 39, pp. 425 - 428.
- Fang M and Hager BH (2001): Vertical deformation and absolute gravity. *Geophys. J. Int.*, 146, pp. 539 - 548.
- Farrell WE and Clark JA (1976): On postglacial sea-level. *Geophys. J.*, 46, pp. 79 - 116.

Featherstone WE (1995): On the use of Australian geodetic datums in gravity field determination. *Geomatics Research Australasia*, 62, pp. 17 - 36.

Fengler MJ, Freedden W, Kohlhaas A, Michel V and Peters T (2007): Wavelet modeling of regional and temporal variations of the earth's gravitational potential observed by GRACE. *J. Geodesy*, 81, pp. 5-15, DOI 10.1007/s00190-006-0040-1.

Fielding EJ, Blom RG and Goldstein RM (1998): Rapid subsidence over oil fields measured by SAR interferometry. *Geophys. Res. Lett.*, 25(17), pp. 3,215 – 3,218.

Franke R (1982): Scattered data interpolation: tests of some methods. *Mathematics of Computation*, 38(157), pp. 181 – 200.

Franke R, Hagen H and Nelson GM (1994): Least square surface approximation to scattered data using multiquadric functions. *Advances in Computational Mathematics*, 2, pp. 81 - 99.

Fotopoulos G (2003): An analysis on the optimal combination of geoid, orthometric and ellipsoidal height data. *PhD thesis*, University of Calgary, Department of Geomatics Engineering, Report No 20185.

Fotopoulos G (2004): On the incorporation of sea surface topography in establishing vertical control. In: Proceedings IAG Symposia, Vol.129, *Gravity, Geoid and Space Missions*, Porto, Portugal August 30 – September 3, 2004, pp. 185 - 190.

Fotopoulos G (2005): Calibration of geoid error models via a combined adjustment of ellipsoidal, orthometric and gravimetric geoid height data. *J. Geodesy*, 79, pp. 111 - 123.

Fotopoulos G, Craymer M and Lapelle E (2007): Epoch rectification of GPS on benchmarks in Canada. *IUGG2007*, Perugia, Italy, July 2-13, 2007.

Fujii Y and Xia S (1993): Estimation of distribution of the rates of vertical crustal movements in the Tokai District with the aid of least squares prediction. *J. Phys. Earth*, 41, pp. 239 - 256.

Golub GH and van Loan CF (1996): Matrix computations. 3<sup>rd</sup> edition, The Johns Hopkins University Press, Baltimore and London.

- Gomm JB and Yu DL (2000): Selecting radial base function neural network centers with recursive orthogonal least squares training. *IEEE Trans. Neural Networks*, 11, pp. 306 - 314.
- Gottschalck J, Meng J, Rodell M and Houser P (2005): Analysis of Multiple Precipitation Products and Preliminary Assessment of Their Impact on Global Land Data Assimilation System Land Surface States. *J. Hydrometeorology*, 6, pp. 578 - 598.
- Groten E and Becker M (1995): Methods and experience of high precision gravimetry as a tool for crustal movement detection. *J. Geodynamics*, 19, pp. 141 - 157.
- Gunter B, Ries J, Bettadpur S and Tapley B (2006): A simulation study of the errors of omission and commission for GRACE RL01 gravity fields. *J. Geodesy*, 80, pp. 341 - 351.
- Györfi L, Kohler M, Krzyzak A and Wik H (2002): Springer Series in Statistics: A distribution-free theory of nonparametric regression, 647 pp., Springer-Verlag, New York.
- Han D and Wahr J (1995): The Viscoelastic Relaxation of a Realistically Stratified Earth, and a Further Analysis of Postglacial Rebound. *Geophys. J. Int.*, 120, pp. 287 - 311.
- Han SC, Shum SC and Braun A (2005a): High-resolution continental water storage recovery from low-low satellite-to-satellite tracking. *J. Geodynamics*, 39, pp. 11 - 28.
- Han SC, Shum SC, Jekeli C, Kuo CY, Wilson C and Seo KW (2005b): Non-isotropic filtering of GRACE temporal gravity for geophysical signal enhancement. *Geophys. J. Int.*, 163, pp. 18 - 25.
- Hardy RL (1971): Multiquadric equations of topography and other irregular surfaces. *J. Geophys. Res.*, 76, pp. 1,905 - 1,915.
- Hardy RL (1977): The application of multiquadric equations and point mass anomaly models to crustal movement studies. *Report, National Research Council, National Academy of Science*, Washington, D.C.
- Hardy RL and Nelson SA (1986): A multiquadric-biharmonic representation and approximation of disturbing potentials. *Geophys. Res. Lett.*, 13, pp. 18 - 21.

Hardy RL (1990): Theory and applications of the multiquadric-biharmonic method: 25 years of discovery 1968-1988. *Computers Math. Applic.*, 19(8/9), pp. 163 - 208.

Heck B (1982): Combination of levelling and gravity data for detecting real crustal movements. In: Proc. Int. Symp. *Geodetic Networks and Computation*, Munich 1981, VII. Deutsche Geodätische Kommission, B258/VII, pp. 20 - 30.

Heck B and Mälzer H (1983): Determination of vertical recent crustal movements by levelling and gravity data. *Tectonophysics*, 97, pp. 251 - 264.

Heck B (1984): Zur Bestimmung vertikaler rezenter Erdkrustenbewegungen und zeitlicher Änderungen des Schwerefeldes aus wiederholten Schweremessungen und Nivellements. *Deutsche Geodätische Kommission, Reihe C, Nr.302*, München 1984.

Heck B and Mälzer H (1986): On some problems connected with the determination of recent vertical crustal movements from repeated levelling and gravity measurements. *Tectonophysics*, 130, pp. 299 - 305.

Heck B and Rummel R (1989): Strategies for solving the vertical datum problem using terrestrial and satellite geodetic data. In: Proceedings IAG Symposium, Vol.104, Sünkel H and Baker T (Eds.), *Sea Surface Topography and the Geoid*, Springer-Verlag, pp. 116 - 128.

Heck B (1990): An evaluation of some systematic error sources affecting terrestrial gravity anomalies. *Bull. Geod.*, 64, pp. 88 - 108.

Hein GW and Kistermann R (1981): Mathematical foundation of non-tectonic effects in geodetic recent crustal movement models. *Tectonophysics*, 71, pp. 315 - 334.

Heiskanen H and Moritz H (1967): *Physical Geodesy*, 364 pp., Graz, Austria, (reprint 1999).

Hekimoğlu S (1997): Finite Sample Breakdown Points of Outlier Detection Procedures. *Journal of Surveying Engineering*, 123(1), pp. 15 - 31.

Hekimoğlu S and Berber M (2003): Effectiveness of robust methods in heterogeneous linear models. *J. Geodesy*, 76, pp. 706 - 713.

Henton JA, Liard JO, Craymer M, James T, Gagnon GG and Lapelle E (2004): Absolute gravity and global positioning system measurements of glacial isostatic adjustment in Eastern Canada. *Eos Trans., AGU* 85 (17), 2004.

Henton J, Craymer M, Liard J, Duval R and Klatt C (2005): Integration of the Canadian Gravity Standardization Network with the Canadian Spatial Reference System: Challenges and opportunities. AGU Fall Meeting, San Francisco, US, 2005.

Henton J, Craymer M, Ferland R, Dragert H, Mazzotti S and Forbes D (2006): Crustal motion and deformation monitoring of the Canadian landmass. *Geomatica*, 60, pp. 173 - 191.

Holdahl SR and Hardy RL (1979): Solvability and multiquadric analysis as applied to investigations of vertical crustal movements. *Tectonophysics*, 52, pp. 139 - 155.

Hon YC and Mao XZ (1997): A Multiquadric Interpolation Method for Solving Initial Value Problems. *Journal of Scientific Computing*, 12(1), pp. 51- 55.

Honkasalo T and Kukkamäki TJ (1964): On the use of gravity measurements for investigation of the land upheaval in Fennoscandia. *Fennia*, 89, pp. 21 - 24.

Horel JD (1981): A rotated principal component analysis of the inter-annual variability of the Northern hemisphere 500 mb height field. *M. Weather Rev.*, 109, pp. 2,080 – 2,092.

Huang J, Fotopoulos G, Cheng MK, Véronneau M and Sideris M (2006): On the estimation of the regional geoid error in Canada. In: Proceedings IAG Symposia , Vol.130, Tregoning P and Rizos C (Eds.), *Monitoring and Understanding a Dynamic Planet with Geodetic and Oceanographic Tools*, Cairns, Australia, August, 22-26, 2005.

(IERS – 2003) McCarthy D and Petit G (2003): IERS Conventions (2003), *IERS Technical Note* 32.

Ihde J and Augath W (2001): The European Vertical Reference System (EVRS), its relation to a World Height System and to the ITRS. In: Proceedings IAG Symposium, Vol. 125, Drewes H, Dodson A, Fortes LPS, Sánchez L and Sandoval P (Eds.), *Vistas for Geodesy in the New Millennium*, 2-7 September 2001, Budapest, Hungary, pp. 78 - 83. Springer Verlag, Berlin.

- Ishii H, Komukai Y and Takagi A (1981): Characteristics of vertical land movement and microearthquake activity in the Northeastern Japan Arc. *Tectonophysics*, 77, pp. 213 - 231.
- James TS and Lambert A (1993): A comparison of VLBI data with the ICE-3G glacial rebound model. *Geophys. Res. Lett.*, 20(9), pp. 871 – 874.
- James TS and Ivins ER (1998): Prediction of Antarctic crustal motions driven by present-day ice sheet evolution and by isostatic memory of the Last Glacial Maximum. *J. Geophys. Res.*, 103, pp. 4,993 – 5,017.
- Jekeli C (1981): Alternative methods to smooth the Earth's gravity field. *Rep. 327*, Dept. Geod. Sci. and Surv., Ohio State Univ., Columbus.
- Jekeli C (2000): Heights, the Geopotential, and Vertical Datums. *Rep. 459*, Dept. Geod. Sci. and Surv., Ohio State Univ., Columbus.
- Jekeli C and Dumrongchai P (2003): On monitoring a vertical datum with satellite altimetry and water-level gauge data on large lakes. *J. Geodesy*, 77, pp. 446 - 453.
- Johansson JM, Davis JL, Scherneck H-G, Milne GA, Vermeer M, Mitrovica JX, Bennett RA, Jonsson B, Elgered G, Elósegui P, Koivula H, Poutanen M, Rönnäng BO and Shapiro II (2002): Continuous GPS measurements of postglacial adjustment in Fennoscandia: 1. Geodetic results. *J. Geophys. Res.*, 107(B8), 2157, doi:10.1029/2001JB000400.
- Jolliffe IT (2002): Principal Component Analysis, *Springer Series in Statistics*, Springer, 2<sup>nd</sup> ed., 487 pp., New York.
- Jordan SK (1972): Self-consistent statistical models for the gravity anomaly, vertical deflections, and undulation of the geoid. *J. Geophys. Res.*, 77, pp. 3,660 - 3,670.
- Kakkuri J (1997): Postglacial deformation of the Fennoscandian crust. *Geophysica*, 33(1).
- Kanngieser E (1983): Application of least-squares collocation to gravity and height variations associated with a recent rifting process. *Tectonophysics*, 97, pp. 265 - 277.
- Kansa EJ (1990): Multiquadrics – a scattered data approximation scheme with applications to computational fluid-dynamics – I. *Computers Math. Applic.*, 19(8/9), pp. 127 - 145.

- Kansa EJ and Hon YC (2000): Circumventing the ill-conditioning problem with multiquadric radial basis functions: applications to elliptic partial differential equations. *Computers and Mathematics with Applications*, 39, pp. 123 - 137.
- Kearsley AHW, Ahmad Z and Chan A (1993): National Height Datums, Levelling, GPS Heights and Geoids. *Aust. J. Geod. Photogramm. Surv.*, 59, pp. 53 - 88.
- Kern M, Preimesberger T, Allesch M, Pail R, Bouman J and Koop R (2005): Outlier detection algorithms and their performance in GOCE gravity field processing. *J. Geodesy*, 78, pp. 509 - 519, doi:10.1007/s00190-004-0419-9.
- Koch K-R (1999): Parameter estimation and hypothesis testing in linear models. Springer-Verlag, 1999.
- Koch K-R and Kusche J (2002): Regularization of geopotential determination from satellite data by variance components. *J. Geodesy*, 76, pp. 259 - 268.
- Koohzare A, Vaníček P and Santos M (2007): The use of smooth piecewise algebraic approximation in the determination of vertical crustal movements in Eastern Canada. In: Proceedings IAG Symposia, Vol. 130, Tregoning Paul; Rizos Chris (Eds.), *Monitoring and Understanding a Dynamic Planet with Geodetic and Oceanographic Tools*, Cairns, Australia, August, 22 - 26, 2005.
- Korn T and Korn T (1968): Mathematical handbook for scientists and engineers. McGraw-Hill, 1968.
- Kotsakis K and Sideris MG (1999): On the adjustment of combined GPS/Levelling/geoid networks. *J. Geodesy*, 73(8), pp. 412 - 421.
- Krakiwsky E and Biacs Z (1990): Least squares collocation and statistical testing. *Bull. Géod.*, 64, pp. 73 - 87.
- Kuo CY, Shum CK, Braun A and Mitrovica JX (2004): Vertical crustal motion determined by satellite altimetry and tide gauge data in Fennoscandia. *Geophys. Res. Lett.*, 31, L01608, doi:10.1029/2003GL019106.

- Kuo CY (2006): Determination and characterization of 20<sup>th</sup> century global sea level rise. *Rep. 478*, Dept. Geod. Sci. and Surv., Ohio State Univ., Columbus.
- Kusche J (2007): Approximate decorrelation and non-isotropic smoothing of time-variable GRACE-type gravity field models. *J. Geodesy*, doi:10.1007/s00190-007-01433.
- Lambert A, Courtier N, Sasagawa GS, Klopping F, Winester D, James TS and Liard JO (2001): New constraints on Laurentide postglacial rebound from absolute gravity measurements. *Geophys. Res. Lett.*, 28, pp. 2,109 - 2,112.
- Lambert A, James TS, Courtier N, Simon K, Schmidt M, Lewis CFM and Mainville A (2005): An improved postglacial rebound model with applications to the Nelson drainage basin. *Geol. Surv. Can.*, Open File 4927.
- Lambert A, Courtier N and James TS (2006): Long-term monitoring by absolute gravimetry: Tides to postglacial rebound. *J. Geodynamics*, 41, pp. 307 - 317.
- Larsen C, Motyka R, Freymueller J, Echelmeyer K and Ivins E (2004): Rapid uplift of southern Alaska caused by recent ice loss. *Geophys. J. Int.*, 158, pp. 1,118 - 1,133.
- Larson K and van Dam T (2000): Measuring postglacial rebound with GPS and absolute gravity. *Geophys. Res. Lett.*, 27, pp. 3,925 – 3,928.
- Latychev K, Mitrovica JX, Tamisiea ME, Tromp J and Moucha R (2005): Influence of lithospheric thickness variations on 3-D crustal velocities due to glacial isostatic adjustment. *Geophys. Res. Lett.*, 32, L01304, doi:10.1029/2004GL021454.
- Lemoine FG, Kenyon SC, Factor JK, Trimmer RG, Pavlis NK, Chinn DS, Cox CM, Klosko SM, Luthcke SB, Torrence MH, Wang YM, Williamson RG, Pavlis EC, Rapp RH and Olson TR (1998): The development of the joint NASA GSFC and NIMA geopotential model EGM96. NASA/TP-1998-206861 GSFC, Greenbelt, MD.
- Leuliette EW and Wahr J (1999): Coupled pattern analysis of sea surface temperature and TOPEX/Poseidon sea surface height. *J. Phys. Oceanography*, 29, pp. 599 – 611.

- Li J, Miyashita K, Kato T and Miyazaki S (1999): GPS time series modeling by autoregressive moving average method: Application to the crustal deformation in central Japan. *Earth Planets Space*, 52, pp. 155 – 162.
- Lin J (2000): Correction of tide gauge measurements to absolute sea level by vertical land motion solution. *MSc Thesis*, The Ohio State University, August 2000.
- Liu QW and Chen YQ (1998): Combining the geodetic models of vertical crustal deformation. *J. Geodesy*, 72, pp. 673 - 683.
- Lodha SK and Franke R (1997): Scattered data techniques for surfaces. *Scientific Visualization Conference (dagstuhl'97)*, p. 181.
- Luthcke SB, Zwally HJ, Abdalati W, Rowlands DD, Ray RD, Nerem RS, Lemoine FG, McCarthy JJ and Chinn DS (2006): Recent Greenland Ice Mass Loss by Drainage System from Satellite Gravity Observations, *Science*, 314, pp. 1,286 - 1,289.
- Mainville A and Craymer M (2005): Present-day tilting of the Great Lakes region based on water level gauges. *GSA Bulletin*, 117(7 - 8), pp. 1,070 - 1,080.
- Mäkinen J and Saaranen V (1998): Determination of postglacial land uplift from the three precise levellings in Finland. *J. Geodesy*, 72, pp. 516 - 529.
- Mäkinen J, Koivula H, Poutanen P and Saaranen V (2000): Contemporary postglacial rebound in Finland: comparison of GPS results with repeated precise levelling and tide gauges. In: Proceedings IAG Symposia, Vol. 123, Sideris (Ed.), *Gravity, Geoid and Geodynamics*, Banff, Canada, 2000.
- Mautz R, Schaffrin B and Kaschenz J (2003): Biharmonic Spline Wavelets versus Generalized Multi-quadrics for Continuous Surface Representation. In: Proceedings IAG Symposia, Vol. 128, Sansò F (Ed.), *A Window on the Future of Geodesy*, IAG General Assembly Sapporo, Japan, June 30 – July 11, 2003.
- Meier S (1981): Planar Geodetic Covariance Functions. *Rev. Geophys. Space Phys.*, 19(4), pp. 673 - 686.

- Micchelli CA (1986): Interpolation of scattered data: distance matrices and conditionally positive definite functions. *Constructive Approximations*, 2, pp. 11 - 22.
- Milne GA and Mitrovica JX (1998): Postglacial sea-level change on a rotating Earth. *Geophys. J. Int.*, 133, pp. 1 - 19.
- Milne GA, Mitrovica JX and Davis JL (1999): Near-field hydro-isostasy: the implementation of a revised sea-level equation. *Geophys. J. Int.*, 139, pp. 464 - 482.
- Mitrovica JX and Peltier WR (1991): On Postglacial Geoid Subsidence over the Equatorial Oceans. *J. Geophys. Res.*, 96(B12), pp. 20,053 - 20,071.
- Mitrovica JX, Davis JL and Shapiro II (1993): Constraining proposed combinations of ice history and Earth rheology using VLBI determined baseline length rates in North America. *Geophys. Res. Lett.*, 20(21), pp. 2,387 - 2,390.
- Mitrovica JX and Peltier WR (1995): Constraints on Mantle Viscosity Based upon the Inversion of Post-Glacial Uplift Data from the Hudson Bay Region. *Geophys. J. Int.*, 122, pp. 353 - 377.
- Mitrovica JX (1997): Going Halves over the Hudson Bay. *Nature*, 390, pp. 444 - 446.
- Mitrovica JX, Milne GA and Davis JL (2001): Glacial isostatic adjustment on a rotating Earth. *Geophys. J. Int.*, 147, pp. 562 - 578.
- Mitrovica JX and Forte AM (2004): A new inference of mantle viscosity based upon joint inversion of convection and glacial isostatic adjustment data. *Earth Planet. Sci. Lett.*, 225, pp. 177 - 189.
- Miura S, Sato T, Fujimoto H, Sun W, Freymueller JT, Kaufman AM and Cross R (2006): ISEA (International geodetic project in SouthEastern Alaska) for rapid uplifting caused by glacial retreat: (1) Outline of the project. *EOS Trans. AGU* 87(52), Fall Meet. Suppl., Abstract G33B-0065.
- Moritz H (1980): *Advanced Physical Geodesy*, H. Wichmann Verlag, Karlsruhe, 1980.

Nakada M and Lambeck K (1991): Late Pleistocene and Holocene Sea-Level Change; Evidence for Lateral Mantle Viscosity Structure? In: Sabadini R, Lambeck K and Boschi E (Eds.) *Glacial Isostasy, Sea Level and Mantle Rheology*, Kluwer, pp. 79 - 94.

Nerem RS, Rachlin KE and Beckley BD (1997): Characterization of mean sea level variations observed by TOPEX/Poseidon using empirical orthogonal functions. *Surveys in Geophysics*, 18(2 - 3), pp. 293 - 302.

Nerem RS and Mitchum GT (2001): Observations of sea level change from satellite altimetry. In: Douglas BC, Kearney MS and Leatherman SP (Eds.), *Sea Level Rise: History and Consequences*, Academic Press, pp. 121 - 347.

North GR, Bell TL, Cahalan RF and Moeng FJ (1982): Sampling errors in the estimation of empirical orthogonal functions. *Mon. Weather Rev.*, 110, pp. 699 - 706.

Odijk D (2005): Integrated leveling and InSAR networks for the monitoring of subsidence due to gas extraction. *Fachbeiträge*, 130, Jg., pp. 1 - 12.

Pagiatakis SD and Salib P (2003): Historical relative gravity observations and the time rate of change of gravity due to postglacial rebound and other tectonic movements in Canada. *J. Geophys. Res.*, 108(B9), 2406, doi:10.1029/2001JB001676.

Park K-D, Nerem RS, Davis JL, Schenewerk MS, Milne GA and Mitrovica JX (2002): Investigation of glacial isostatic adjustment in northeast U.S. using GPS measurements. *Geophys. Res. Lett.*, 29(11), 1509, doi: 10.1029/2001GL013782.

Paulson A, Zhong S and Wahr J (2007): Limitations on the inversion for mantle viscosity from postglacial rebound. *Geophys. J. Int.*, 168, pp. 1195 - 1209.

Peltier WR (1974): The impulse Response of a Maxwell Earth. *Rev. Geophys.*, 12, pp. 649 - 669.

Peltier WR, Farrell WE and Clark JA (1978): Glacial isostasy and relative sea level: A global finite element model. *Tectonophysics*, 50, pp. 81 - 110.

Peltier WR and Wu P (1982): Mantle phase transitions and the free air gravity anomalies over Fennoscandia and Laurentia. *Geophys. Res. Lett.*, 9(7), pp. 731 - 734.

- Peltier WR and Andrews JT (1983): Glacial Geology and Glacial Isostasy of the Hudson Bay Region. In: Smith DE and Dawson AG (Eds.), *Shorelines and Isostasy*, Academic Press, London, pp. 285 - 319.
- Peltier WR (1985): The LAGEOS Constraint on Deep Mantle Viscosity: Results from a new normal mode method for the inversion of viscoelastic relaxation spectra. *J. Geophys. Res.*, 90(B11), pp. 9,411 - 9,421.
- Peltier WR (1994): Ice-age paleotopography. *Science*, 265, pp. 195 - 201.
- Peltier WR (1995): VLBI baseline variations from the ICE-4G model of postglacial rebound. *Geophys. Res. Lett.*, 22(4), pp. 465 – 468.
- Peltier WR (1996): Mantle viscosity and ice-age ice sheet topography. *Science*, 273, No 5280, pp. 1,359 – 1,365.
- Peltier WR (1998): The inverse problem for mantle viscosity. *Inverse Problems*, 14, pp. 441 - 478.
- Peltier WR (2004): Global Glacial Isostasy and the Surface of the Ice-Age Earth: The ICE-5G (VM2) Model and GRACE. *Annu. Rev. Earth Planet. Sci.*, 32, pp. 111 - 149.
- Poutanen M, Vermeer M and Mäkinen J (1996): The permanent tide in GPS positioning. *J. Geodesy*, 70(8), pp. 499 - 504.
- Preisendorfer RW (1988): Principal Component Analysis in Meteorology and Oceanography. *Developments in Atmospheric Science*, 17, Elsevier.
- Ramillien G, Cazenave A and Brunau O (2004): Global time variations of hydrology signals from GRACE satellite gravimetry. *Geophys. J. Int.*, 158, pp. 813 - 826.
- Ramillien G, Frappart F, Cazenave A and Güntner A (2005): Time variations of land water storage from an inversion of 2 year of GRACE geoids. *Earth Planet. Sci. Lett.*, 235, pp. 283 - 301.
- Rangelova E, van der Wal W, Sideris MG and Wu P (2006a): Numerical models of the rates of change of the geoid and orthometric heights over Canada. In: Proceedings IAG Symposia, Vol.130, Tregoning, P and Rizos, C (Eds.), *Monitoring and Understanding a*

*Dynamic Planet with Geodetic and Oceanographic Tools*, Cairns, Australia, August, 22 - 26, 2005.

Rangelova E and Sideris MG (2006b): Combination of GRACE, gravity, and GPS data for determination of long-term geoid changes in North America. *First International Symposium of IGFS*, Istanbul, August-September, 2006, pp. 437 – 442.

Rangelova E, van der Wal W, Braun A, Sideris MG and Wu P (2007a): Analysis of GRACE time-variable mass redistribution signals over North America by means of principal component analysis. *J. Geophys. Res.*, 112, F03002, doi: 10.1029/2006JF00615.

Rangelova E, Fotopoulos G and Sideris MG (2007b): Combined vertical motion model - case study for the Great Lakes. *IUGG2007*, Perugia, Italy, July 2-13, 2007.

Reigber C, Schmidt R, Flechtner F, König R, Meyer U, Neumayer KH, Schwintzer P and Zhu SY (2005): An Earth gravity field model complete to degree and order 150 from GRACE: EIGEN-GRACE02S. *J. Geodynamics*, 39, pp. 1 - 10.

Reigber C, Jochmann H, Wiunsch J, Petrovic S, Schwintzer P, Barthelmes F, Forste C and Neumayer K (2003): Low-degree temporal gravity field variations using CHAMP data. *EOS Trans.*, AGU Fall Meet. 2003, Abstract G31A-02.

Reilly WI (1979): Mapping of the local geometry of the Earth's gravity field. *Report No. 143*, Geophysics Division, Dept. of Scientific and Industrial Research, New Zealand.

Richman MB (1985): Rotation of principal components. *J. Climatology*, 6, pp. 293 - 335.

Robertson AW and Mechoso CR (1998): Interannual and Decadal Cycles in River Flows of Southeastern South America. *J. Climate*, 11, pp. 2,570 – 2,581.

Rodell M et al. (2004): The global land data assimilation system. *Bull. Am. Meteorol. Soc.*, 85(3), pp. 381 - 394.

Rousseeuw PJ and Leroy AM (1987): Robust regression and outlier detection. John Wiley and Sons.

Rousseeuw PJ and Croux C (1993): Alternatives to the median absolute deviation. *Journal of the American Statistical Association*, 88(424), pp. 1,273 – 1,283.

- Rowlands DD, Luthcke SB, Klosko SM, Lemoine FGR, Chinn DS, McCarthy JJ, Cox CM and Anderson OB (2005): Resolving mass flux at high spatial and temporal resolution using GRACE intersatellite measurements. *Geophys. Res. Lett.*, 32, L04310, doi:10.1029/2004GL021908.
- Rummel R (1996): Spherical spectral properties of the Earth's gravitational potential and its first and second derivatives. In: Lecture Notes in Earth Sciences, Sansò F and Rummel R (Eds.), *Geodetic boundary value problems in view of the one centimetre geoid*, Springer, pp. 359 - 401.
- Sansò F and Dermanis A (1982): A Geodynamic Boundary Value Problem. *ANNO XLI-Bollettino di Geodesia e Scienze Affini*, 1, pp. 65 - 87.
- Sansò F and Venuti G (2002): The height datum/geodetic datum problem. *Geophys J. Int.*, 149, pp. 768 - 775.
- Sasgen I, Martinez Z and Fleming K (2007): Wiener optimal filtering of GRACE data. *Stud. Geophys. Geod.*, 50(4), pp. 499 - 508, doi: 10.1007/s11200-006-0031-y.
- Scherneck HG, Johansson JM, Mitrovica JX and Davis JL (1998): The BIFROST project: GPS determined 3D displacement rates in Fennoscandia from 800 days of continuous observations in the SWEPOS network. *Tectonophysics*, 294, pp. 305 - 321.
- Schmidt M, Fengler M, Mayer-Gürr T, Eicker A, Kusche J, Sánchez L and Han SC (2007): Regional gravity modeling in terms of spherical base functions. *J. Geodesy*, 81, pp. 17 – 38.
- Schwarz KP, Sideris MG and Forsberg R (1987): Orthometric heights without leveling. *J. Surv. Eng.*, 113(1), pp. 28 - 40.
- Seeber G (2003): *Satellite geodesy* (2<sup>nd</sup> ed.). Walter de Gruyter, Berlin, New York, 2003.
- Sella GF, Stein S, Dixon TH, Craymer M, James TS, Mazzotti S and Dokka RK (2007): Observation of glacial isostatic adjustment in “stable” North America with GPS. *Geophys. Res. Lett.*, 34, L02306, doi:10.1029/2006GL027081.

- Seo K-W, Wilson CR, Famiglietti JS, Chen JL and Rodell M (2006): Terrestrial water mass load changes from Gravity Recovery and Climate Experiment (GRACE). *Water Resour. Res.*, 42, W05417, doi:10.1029/2005WR004255.
- Sharifi MA (2006): Satellite to satellite tracking in the space-wise approach. *Doctoral Dissertation*, Institute of Geodesy, University of Stuttgart.
- Shin N and Deng Z (2000): Space/time features of the secular variation in 1951  $\pm$  1998 northern 500-hpa height. *Meteorol. Atmos. Phys.*, 73, pp. 35 - 46.
- Shum CK, Kuo CY and Mitrovica JX (2002): Glacial isostatic adjustment in the Great Lakes region inferred by tide gauges and satellite altimetry. *EOS Trans.*, Spring AGU Meeting 2002.
- Sideris MG (1994a): Regional geoid determination. In Vaníček and Christou (Eds.): *Geoid and its geophysical interpretation*, CRC Press, pp. 77 - 110.
- Sideris MG (1994b): Geoid Determination by FFT Techniques. In: *International School for the Determination and Use of the Geoid*, Milan, October 10-15, 1994, pp. 165 - 224.
- Simons M and Hager B (1997): Localization of the gravity field and the signature of glacial rebound. *Nature*, 390, pp. 500 - 504, doi:10.1038/37339.
- Sjöberg LE (1982): Studies on the land uplift and its implications on the geoid in Fennoscandia. *Report. No.14*, Department of Geodesy, University of Uppsala.
- Sneeuw N (2000): A semi-analytical approach to gravity field analysis from satellite observations. *Reihe C 527*, DGK.
- Spada G, Antonioli A, Cianetti S and Giunchi C (2006): Glacial isostatic adjustment and relative sea level changes: the role of lithospheric and upper mantle heterogeneities in a 3-D spherical Earth. *Geophys. J. Int.*, 165(2), pp. 692 - 702.
- Sun W and Sjöberg L (2001): Permanent components of the crust, geoid and ocean depth tides. *J. Geodynamics*, 31, pp. 323 - 339.

Swenson S and Wahr J (2002): Methods for inferring regional surface-mass anomalies from Gravity Recovery and Climate Experiment (GRACE) measurements of time- variable gravity. *J. Geophys. Res.*, 107(B9), 2193, doi:10.1029/2001JB000576.

Swenson S and Wahr J (2006): Post-processing removal of correlated errors in GRACE data. *Geophys. Res. Lett.*, 33, doi:10.1029/2005GL025285.

Tamisiea ME, Leuliette EW, Davis JL and Mitrovica JX (2005): Constraining hydrology and cryospheric mass flux in southeastern Alaska using space-based gravity measurements. *Geophys. Res. Lett.*, 32, L20501, doi:10.1029/2005GL023961.

Tanner JG and Lambert A (1987): Gravity and crustal movements: the Canadian experience. *J. Geodynamics*, 7, pp. 329 - 338.

Tapley BD, Bettadpur S, Watkins M and Reigber C (2004a): The gravity recovery and climate experiment: Mission overview and early results. *Geophys. Res. Lett.*, 31, L09607, doi:10.1029/2004GL019920.

Tapley BD, Bettadpur S, Watkins M, and Reigber C (2004b): GRACE measurements of mass variability in the Earth system. *Science*, 305(5683), pp. 503 - 505.

Tapley BD, Ries J, Bettadpur S, Chambers D, Cheng M, Condi F, Gunter B, Kang Z, Nagel P, Pastor R, Pekker T, Poole S and Wnag F (2005): GGM02 – An improved Earth gravity field model from GRACE. *J. Geodesy*, 79, pp. 467 - 478.

Teunissen PJG (2000): Testing theory: an introduction. *Series on Mathematical Geodesy and Positioning*, Delft, University Press.

Timmen L et al. (2005): Observing Fennoscandian Gravity Change by Absolute Gravimetry. In: Proceedings IAG Symposia, Vol. 131, Sansò F and Gil AJ (Eds.), *Geodetic Deformation Monitoring: From Geophysical to Engineering Roles*, Jaén, Spain, 2005.

Torge W (2001): *Geodesy*. 3<sup>rd</sup> edition, 416 pp., De Gruyter, 2001.

Tosi NR, Sabadini R, Marotta AM and Vermeersen LLA (2005): Simultaneous inversion for the Earth's mantle viscosity and ice mass imbalance in Antarctica and Greenland. *J. Geophys. Res.*, 110, B07402, doi:10.1029/2004JB003236.

Tóth G (2004): The gradiometric-geodynamic boundary value problem. In: Proceedings IAG Symposia, Vol.129, Jekeli C, Bastos L and Fernandes J (Eds.), *Gravity, Geoid and Space Missions*, Porto, Portugal August 30 – September 3, 2004, pp. 352 - 357.

Tscherning CC, Arabelos D and Strykowski G (2000): The 1-cm geoid after GOCE. In: Proceedings IAG Symposia, Vol.123, Sideris M (Ed.), *Gravity, Geoid, and Geodynamics 2000*, Springer-Verlag, Berlin Heidelberg, 2001.

Tushingham AM and Peltier WR (1991): ICE-3G: a new global model of late Pleistocene deglaciation based upon geophysical predictions of post-glacial relative sea-level change. *J. Geophys. Res.*, B96, pp. 4,497 - 4,523.

Tushingham AM (1992): Postglacial uplift predictions and historical water levels of the Great Lakes. *Journal of Great Lakes Research*, 18(3), pp. 440 – 455.

Valle S, Weihua L and Qin SJ (1999): Selection of the number of principal components: the variance of the reconstruction error criterion with a comparison to other methods. *Ind. Eng. Chem. Res.*, 38, pp. 4,389 - 4,401.

van der Wal W, Rangelova E, Wu P and Sideris M (2006): Geoid rate from surface measurements as constraint for postglacial rebound modelling. *AGU Spring Meeting*, Baltimore, Maryland, May 23 - 26 2006.

van der Wal W, Rangelova E, Sideris M and Wu P (2007): Geoid rate in North America from GRACE with measurement and systematic errors. CMOS, CGU and AMS Congress “*Air, Ocean, Earth, and Ice on the Rock*”, May, 2007, St. John’s, Canada.

Vaníček P and Christodulidis D (1974): A method for the evaluation of vertical crustal movement from scattered geodetic re-levelling. *Canadian Journal of Earth Sciences*, 11(5), pp. 605 - 610.

Vaníček P and Nagy D (1981): On the compilation of the map of contemporary vertical crustal movements in Canada. *Tectonophysics*, 71, pp. 75 - 86.

Vaníček P and Krakiwsky E (1986): *Geodesy – the concepts*, 697 pp., 1986 (2<sup>nd</sup> edition).

- Vaníček P (1991): Vertical Datum and NAVD88. *Surveying and Land Information Systems*, 51, pp. 83 - 86.
- Vaníček P and Featherstone WE (1998): Performance of three types of Stokes's kernel in the combined solution from the geoid. *J. Geodesy*, 72, pp. 684 - 697.
- Vaníček P, Huang J, Novák P, Pagiatakis S, Véronneau M, Martinec Z and Featherstone WE (1999): Determination of the boundary values for the Stokes-Helmert problem. *J. Geodesy*, 73, pp. 180 - 192.
- Velicogna I and Wahr J (2002): Postglacial rebound and Earth's viscosity structure from GRACE. *J. Geophys. Res.*, 107(B12), 2376, doi:10.1029/2001JB001735.
- Vestøl O (2006): Determination of postglacial land uplift in Fennoscandia from leveling, tide-gauges and continuous GPS stations using least-squares collocation. *J. Geodesy*, 80, pp. 248 - 258.
- Véronneau M (2001): The Canadian vertical datum: A new perspective for the year 2005 and beyond. IAG Symposium 124 *Vertical Reference Systems*, Cartagena, Columbia, 2001.
- Véronneau M (2002): The Canadian gravimetric geoid model of 2000 (CGG2000). *Report, Geodetic Survey Division, Earth Sciences Sector*, Natural Resources Canada, Canada.
- Véronneau M (2006): Demystifying the vertical datum in Canada: A case study in the Mackenzie Delta, [http://www.geod.nrcan.gc.ca/hm/pdf/verticaldatumsdeltav10\\_e.pdf](http://www.geod.nrcan.gc.ca/hm/pdf/verticaldatumsdeltav10_e.pdf) (July 2007).
- Véronneau M, Duval R and Huang J (2006): A gravimetric geoid model as a vertical datum for Canada. *Geomatica*, 60(2), pp. 165 - 172.
- Viron O de, Panet I and Diament M (2006): Extracting low frequency climate signal from GRACE data. *eEarth*, [www.electronic\\_earth.net/1/9/2006](http://www.electronic_earth.net/1/9/2006) (July 2007).
- Visser PNAM et al. (2002): The European Earth Explorer Mission GOCE: Impact for Geosciences. In Mitrovica JX, Vermeersen, BLA (Eds.): *Ice Sheets, Sea Level and the Dynamic Earth*, Geodynamics Series, 29, AGU, pp. 95 - 107.
- Wahr J, DaZhong H and Trupin A (1995): Prediction of vertical uplift caused by changing polar ice volume on a viscoelastic Earth. *Geophys. Res. Lett.*, 22, pp. 977 - 980.

Wahr J, Molenaar M and Bryan F (1998): Time variability of the Earth's gravity field: Hydrology and oceanic effects and their possible detection using GRACE. *J. Geophys. Res.*, 103(B12), pp. 30,205 - 30,229.

Wahr J, Wingham D and Bentley C (2000): A method of combining ICESat and GRACE satellite data to constrain Antarctic mass balance. *J. Geophys. Res.*, 105(B7), pp. 16,279 - 16,294.

Wahr J and Davis J (2002): Geodetic Constraints on Glacial Isostatic Adjustment. In: Mitrovica JX and Vermeersen BLA (Eds.): *Ice Sheets, Sea Level and the Dynamic Earth, Geodynamics Series Vol.29*, AGU, 2002, pp. 3 - 32.

Wahr J, Swenson S and Velicogna I (2006): Accuracy of GRACE estimates. *Geophys. Res. Lett.*, 33, L06401, doi:10.1029/2005GL025305.

Wang H and Wu P (2006): Effects of lateral variations in lithospheric thickness and mantle viscosity on glacially induced surface motion on a spherical, self-gravitating Maxwell Earth. *Earth and Planetary Science Letters*, 244, pp. 576 - 589.

Wei M (1987): Statistical problems in collocation. *Manuscripta Geod.*, 12, pp. 282 - 289.

Wiehl M, Dietrich R and Lehmann A (2005): How Baltic Sea Water Mass Variations Mask the Postglacial Rebound Signal in CHAMP and GRACE Gravity Field Solutions. *Earth observation with CHAMP: Results from three years in orbit*. Springer, pp. 181- 186.

Wolf D, Klemann V, Wunsch J and Zhang FP (2006): A reanalysis and reinterpretation of geodetic and geological evidence of glacial-isostatic adjustment in the Churchill region, Hudson Bay. *Surveys in Geophysics*, 27, pp. 19 - 61.

Wood SN (2003): Thin plate regression splines. *J. R. Statist. Soc. B*, 65, pp. 95 - 114.

Wolf D, Shaw AGP and Tsimplis MN (2003): The influence of the North Atlantic Oscillation on sea-level variability in the North Atlantic Region. *The Global Atmosphere and Ocean System*, 9(4), December 2003, pp. 145 - 167.

Wu P and Peltier WR (1982): Viscous gravitational relaxation. *Geophys. J. R. Astron. Soc.*, 70, pp. 435 - 486.

Wu P and Peltier WR (1983): Glacial isostatic adjustment and the free air gravity anomaly as a constraint on deep mantle viscosity. *Geophys. J. R. Astron. Soc.*, 74, pp. 377 - 449.

Wu P and Peltier WR (1984): Pleistocene deglaciation and the Earth's rotation: A new analysis. *Geophys. J. R. Astron. Soc.*, 76, pp. 753 - 791.

Wu P and Hasegawa HS (1996): Induced stresses and fault potential in eastern Canada due to a disk load – a preliminary analysis. *Geophys. J. Int.*, 125(2), pp. 415 - 430.

## APPENDIX A: SIGNAL AUTO- AND CROSS-COVARIANCE FUNCTIONS

### A.1. Auto-covariance functions

#### *Rate of change of the geoid height*

$$\begin{aligned}
 \text{cov}(\dot{N}(P), \dot{N}(Q)) &= \text{cov}\left(\frac{1}{g_a} \dot{W}(P), \frac{1}{g_a} \dot{W}(Q)\right) \\
 &= \frac{1}{g_a^2} \text{cov}([\dot{W}_1(P) + \dot{W}_2(P)], [\dot{W}_1(Q) + \dot{W}_2(Q)]) \\
 &= \frac{1}{g_a^2} [C_{11}(P, Q) + C_{12}(P, Q) + C_{21}(P, Q) + C_{22}(P, Q)]
 \end{aligned} \tag{A.1}$$

$$\text{cov}(\dot{N}(P), \dot{N}(Q)) = \frac{1}{g_a^2} (C_{11}^1 + C_{12}^1 + C_{21}^1 + C_{22}^1) \tag{A.2}$$

#### *Rate of change of the terrestrial gravity*

$$\begin{aligned}
 \text{cov}(\dot{g}(P), \dot{g}(Q)) &= \text{cov}(St_P^{-1}[\dot{W}_1(P)], St_Q^{-1}[\dot{W}_1(Q)]) \\
 &= \frac{\partial^2 \text{cov}(\dot{W}_1(P), \dot{W}_1(Q))}{\partial r^2} + \frac{4}{R} \frac{\partial \text{cov}(\dot{W}_1(P), \dot{W}_1(Q))}{\partial r} + \frac{4}{R^2} \text{cov}(\dot{W}_1(P), \dot{W}_1(Q)) \\
 &= \frac{\partial^2}{\partial r^2} C_{11}(P, Q) + \frac{4}{R} \frac{\partial}{\partial r} C_{11}(P, Q) + \frac{4}{R^2} C_{11}(P, Q)
 \end{aligned} \tag{A.3}$$

$$\text{cov}(\dot{g}(P), \dot{g}(Q)) = C_{11}^3 - \frac{4}{R} C_{11}^2 + \frac{4}{R^2} C_{11}^1 \tag{A.4}$$

### ***Rate of change of orthometric height***

$$\begin{aligned}
\text{cov}(\dot{H}(P), \dot{H}(Q)) &= \text{cov}\left(\frac{R}{2g_a} St_P^{-1}[\dot{W}_2(P)], \frac{R}{2g_a} St_Q^{-1}[\dot{W}_2(Q)]\right) \\
&= \frac{R^2}{4g_a^2} \frac{\partial^2 \text{cov}(\dot{W}_2(P), \dot{W}_2(Q))}{\partial r^2} + \frac{R}{g_a^2} \frac{\partial \text{cov}(\dot{W}_2(P), \dot{W}_2(Q))}{\partial r} + \frac{\text{cov}(\dot{W}_2(P), \dot{W}_2(Q))}{g_a^2} \quad (\text{A.5}) \\
&= \frac{R^2}{4g_a^2} \frac{\partial^2}{\partial r^2} C_{22}(P, Q) + \frac{R}{g_a^2} \frac{\partial}{\partial r} C_{22}(P, Q) + \frac{1}{g_a^2} C_{22}(P, Q)
\end{aligned}$$

$$\text{cov}(\dot{H}(P), \dot{H}(Q)) = \frac{R^2}{4g_a^2} C_{22}^3 - \frac{R}{g_a^2} C_{22}^2 + \frac{1}{g_a^2} C_{22}^1 \quad (\text{A.6})$$

### ***Rate of change of ellipsoidal height***

$$\begin{aligned}
\text{cov}(\dot{h}(P), \dot{h}(Q)) &= \text{cov}(\dot{N}(P) + \dot{H}(P), \dot{N}(Q) + \dot{H}(Q)) \\
&= \text{cov}(\dot{N}(P), \dot{N}(Q)) + \text{cov}(\dot{N}(P), \dot{H}(Q)) + \text{cov}(\dot{H}(P), \dot{N}(Q)) + \text{cov}(\dot{H}(P), \dot{H}(Q)) \quad (\text{A.7})
\end{aligned}$$

$$\text{cov}(\dot{h}(P), \dot{h}(Q)) = \frac{1}{g_a^2} \frac{R^2}{4} C_{22}^3 + \frac{1}{g_a^2} \frac{R}{2} (C_{12}^2 + C_{21}^2) + \frac{1}{g_a^2} C_{11}^1 \quad (\text{A.8})$$

## **A.2. Cross-covariance functions**

### ***Rates of change of geoid height and terrestrial gravity***

$$\begin{aligned}
\text{cov}(\dot{N}(P), \dot{g}(Q)) &= \text{cov}\left(\frac{1}{g_a} \dot{W}(P), St_Q^{-1}[\dot{W}_1(Q)]\right) \\
&= \frac{1}{g_a} \text{cov}([\dot{W}_1(P) + \dot{W}_2(P)], St_Q^{-1}[\dot{W}_1(Q)]) \quad (\text{A.9}) \\
&= -\frac{1}{g_a} \frac{\partial}{\partial r} [C_{11}(P, Q) + C_{21}(P, Q)] - \frac{2}{g_a R} [C_{11}(P, Q) + C_{21}(P, Q)]
\end{aligned}$$

$$\text{cov}(\dot{N}(P), \dot{g}(Q)) = \frac{1}{g_a} (C_{11}^2 + C_{21}^2) - \frac{2}{g_a R} (C_{11}^1 + C_{21}^1) \quad (\text{A.10})$$

**Rates of change of geoid and orthometric heights**

$$\begin{aligned}
\text{cov}(\dot{N}(P), \dot{H}(Q)) &= \text{cov}\left(\frac{1}{g_a} \dot{W}(P), \frac{R}{2g_a} St_Q^{-1}[W_2(Q)]\right) \\
&= \frac{R}{2g_a^2} \text{cov}([\dot{W}_1(P) + \dot{W}_2(P)], St_Q^{-1}[W_2(Q)]) \\
&= -\frac{R}{2g_a^2} \frac{\partial}{\partial r} [C_{12}(P, Q) + C_{22}(P, Q)] - \frac{1}{g_a^2} [C_{12}(P, Q) + C_{22}(P, Q)]
\end{aligned} \tag{A.11}$$

$$\text{cov}(\dot{N}(P), \dot{H}(Q)) = \frac{R}{2g_a^2} (C_{12}^2 + C_{22}^2) - \frac{1}{g_a^2} (C_{12}^1 + C_{22}^1) \tag{A.12}$$

**Rates of change of terrestrial gravity and orthometric height**

$$\begin{aligned}
\text{cov}(\dot{g}(P), \dot{H}(Q)) &= \text{cov}(St_P^{-1}[\dot{W}_1(P)], \frac{R}{2g_a} St_Q^{-1}[W_2(Q)]) \\
&= \frac{R}{2g_a} \left[ \frac{\partial^2}{\partial r^2} C_{12}(P, Q) + \frac{4}{R} \frac{\partial}{\partial r} C_{12}(P, Q) + \frac{4}{R^2} C_{12}(P, Q) \right] \\
&= \frac{R}{2g_a} \frac{\partial^2}{\partial r^2} C_{12}(P, Q) + \frac{2}{g_a} \frac{\partial}{\partial r} C_{12}(P, Q) + \frac{2}{g_a R} C_{12}(P, Q)
\end{aligned} \tag{A.13}$$

$$\text{cov}(\dot{g}(P), \dot{H}(Q)) = \frac{R}{2g_a} C_{12}^3 - \frac{2}{g_a} C_{12}^2 + \frac{2}{g_a R} C_{12}^1 \tag{A.14}$$

**Rates of change of geoid and ellipsoidal heights**

$$\begin{aligned}
\text{cov}(\dot{N}(P), \dot{h}(Q)) &= \text{cov}(\dot{N}(P), \dot{N}(Q) + \dot{H}(Q)) \\
&= \text{cov}(\dot{N}(P), \dot{N}(Q)) + \text{cov}(\dot{N}(P), \dot{H}(Q))
\end{aligned} \tag{A.15}$$

$$\text{cov}(\dot{N}(P), \dot{h}(Q)) = \frac{1}{g_a^2} (C_{11}^1 + C_{12}^1) + \frac{R}{2} C_{12}^2 + \frac{R}{2} C_{22}^2 \tag{A.16}$$

**Rates of change of terrestrial gravity and ellipsoidal height**

$$\begin{aligned}
\text{cov}(\dot{g}(P), \dot{h}(Q)) &= \text{cov}(\dot{g}(P), \dot{N}(Q) + \dot{H}(Q)) \\
&= \text{cov}(\dot{g}(P), \dot{N}(Q)) + \text{cov}(\dot{g}(P), \dot{H}(Q))
\end{aligned} \tag{A.17}$$

$$\text{cov}(\dot{g}(\text{P}), \dot{h}(\text{Q})) = \frac{1}{g_a^2} (C_{11}^2 - C_{21}^2 - \frac{2}{R} C_{11}^1 + \frac{R}{2} C_{21}^3) \quad (\text{A.18})$$

***Rates of change of orthometric and ellipsoidal heights***

$$\begin{aligned} \text{cov}(\dot{H}(\text{P}), \dot{h}(\text{Q})) &= \text{cov}(\dot{H}(\text{P}), \dot{H}(\text{Q}) + \dot{N}(\text{Q})) \\ &= \text{cov}(\dot{H}(\text{P}), \dot{H}(\text{Q})) + \text{cov}(\dot{H}(\text{P}), \dot{N}(\text{Q})) \end{aligned} \quad (\text{A.19})$$

$$\text{cov}(\dot{H}(\text{P}), \dot{h}(\text{Q})) = \frac{1}{g_a^2} \left( \frac{R^2}{4} C_{22}^3 + \frac{R}{2} C_{21}^2 - \frac{R}{2} C_{22}^2 - C_{21}^1 \right) \quad (\text{A.20})$$

**APPENDIX B: OUTLIERS AND CALIBRATED ERRORS OF GPS AND TIDE  
GAUGE/ALTIMETRY DATA**

**B.1. Results from Baarda's data snooping in the combined case**

Steps	GPS		TGA	
	Data points	$\tilde{N}$ statistic	Data points	$\tilde{N}$ statistic
First iteration				
1	4, 29	2.27, -2.39	<b>3*</b> , 25, 39	<b>-2.60*</b> , 2.18, -2.54
2	4, 29	2.23, -2.36	25, <b>39</b>	2.00, <b>-2.67</b>
3	4, <b>29</b>	2.19, <b>-2.36</b>	-	-
4	4	2.16	-	-
Second iteration				
1	1, <b>6</b> , 43, 61	2.28, <b>3.01</b> , -2.03, 2.32	23, 24, 47	-2.22, 2.15, 2.16
2	<b>1</b> , 43, 61	<b>2.65</b> , -2.00, 2.27	23, 24, 47	-2.22, 2.15, 2.15
3	43, 61	-1.97, 2.18	23, <b>24</b> , 47	-2.16, <b>2.21</b> , 2.12
4	61	2.16	23, 47	-1.99, 2.10
5	-	-	23, <b>47</b>	-1.98, <b>2.18</b>
6	56	1.97	23	-2.03
7	56	1.98	-	-
Third iteration				
1	41	-1.98	24, <b>41</b> , 45	-2.07, <b>-2.11</b> , 1.99
2	8	-1.97	24	-2.12

3	8	-1.97	-	-
4	41	-1.98	45	-1.98
Fourth iteration				
1	63	-1.98	34	-2.02

\* Outliers removed at each step are printed in bold.

## B.2. Calibrated errors for GPS vertical velocities

$\varphi, ^\circ$	$\lambda, ^\circ$	$\dot{h}$ , mm/yr	$\sigma$ , mm/yr	$\hat{\sigma}^{DS}$ *, mm/yr	$\hat{\sigma}^{FMAD}$ **, mm/yr	$\hat{\sigma}^{FS}$ ***, mm/yr
266.30	41.90	-2.2	1.3	-	1.1	1.3
267.98	46.70	-2.0	0.8	0.5	0.5	0.6
268.10	44.30	-2.6	0.9	0.6	0.6	0.9
268.42	41.77	-1.2	0.6	-	0.5	0.7
269.47	43.23	-4.3	1.3	0.8	1.1	1.2
269.66	47.75	-1.0	1.9	1.2	1.6	1.6
269.77	42.01	-0.5	1.2	-	1.2	1.2
270.62	43.05	-5.0	2.4	1.6	2.8	2.2
270.78	48.47	3.8	2.4	1.6	2.3	2.2
271.38	47.23	0.6	0.8	0.5	0.3	0.6
271.56	46.75	-2.4	1.9	-	2.0	1.8
272.04	42.30	-1.9	1.6	1.0	0.8	1.2
272.11	43.00	-2.7	0.8	0.5	0.6	0.7
272.46	41.73	-3.5	2.1	1.4	1.9	1.8
272.48	48.83	3.8	1.9	1.2	1.6	1.7
272.69	44.8	-0.1	0.8	0.5	0.5	0.7
272.93	45.75	-0.4	1.6	1.0	1.1	1.3
274.33	42.99	-0.4	1.6	1.0	1.0	1.3

274.47	42.23	-1.2	1.5	1.0	0.7	1.1
274.49	46.3	0.8	1.6	1.0	1.1	1.3
274.56	44.26	-0.8	1.6	1.0	1.1	1.3
275.04	46.77	2.6	1.8	1.2	1.1	1.4
275.23	48.07	5.4	3.1	2.0	3.1	2.7
275.24	43.62	-0.6	1.7	1.1	1.0	1.3
275.32	44.99	-1.5	1.6	1.0	1.6	1.5
275.41	46.53	2.7	4.2	2.7	2.6	3.2
275.53	45.65	0.4	0.8	0.5	0.6	0.8
275.61	42.29	0.2	1.6	1.0	1.3	1.4
275.64	46.06	-1.6	1.3	-	1.6	1.4
275.87	44.65	-1.8	2.2	1.4	2.3	2.0
275.98	41.92	0.2	1.7	1.1	1.4	1.5
276.11	43.45	-0.2	1.6	1.0	0.8	1.2
276.24	42.52	-1.3	1.6	1.0	1.0	1.3
276.43	45.07	0.5	1.6	1.0	1.1	1.3
276.53	41.61	-2.0	2.2	1.4	1.7	1.8
276.66	42.28	-1.5	2.2	1.4	1.5	1.7
276.76	42.69	-0.7	1.6	1.0	0.8	1.2
276.76	42.17	0.9	1.9	1.2	1.7	1.7
276.84	43.60	-2.1	2.0	1.3	1.9	1.8
276.85	41.08	-0.9	1.6	1.0	0.9	1.2
276.91	42.30	-1.8	0.9	0.6	0.7	0.8
277.31	43.06	-2.0	2.1	1.3	1.9	1.8
277.36	43.85	-2.7	2.2	1.4	2.4	2.1
277.40	42.72	-2.0	2.4	1.5	2.1	2.0
277.41	42.91	-3.8	2.1	-	2.5	2.0
277.51	43.04	-2.5	2.1	1.4	2.1	1.9
278.39	41.42	-2.8	2.1	1.4	2.0	1.9

278.46	48.52	5.6	2.7	1.7	2.2	2.2
278.75	42.88	-0.4	4.3	2.8	2.3	3.1
278.81	46.45	3.9	4.5	2.9	3.1	3.5
279.28	41.46	-1.7	1.8	1.2	1.3	1.5
279.96	45.34	0.6	1.9	1.2	1.7	1.6
279.98	45.37	3.1	2.9	1.9	2.1	2.4
280.78	43.24	-1.7	1.9	1.2	1.7	1.7
280.84	48.78	6.6	1.8	1.2	1.7	1.6
280.91	46.72	4.5	2.2	1.4	1.6	1.8
281.03	43.23	0.3	0.9	0.6	0.5	0.7
281.11	42.88	-1.0	2.0	1.3	1.4	1.6
281.70	44.31	-2.6	4.7	3.0	6.4	4.1
281.93	45.96	3.1	0.5	-	0.3	0.5
282.11	45.04	-0.5	3.8	-	3.9	3.2
282.39	43.11	-1.3	2.3	1.5	1.9	1.9
282.44	48.10	7.8	1.7	-	2.0	1.7
282.75	45.84	3.4	5.3	3.4	3.6	4.1
282.81	44.23	-1.3	3.2	2.1	3.2	2.8
283.00	41.24	-1.3	2.3	1.5	1.5	1.8
283.48	44.22	0.7	1.9	1.2	1.1	1.4
283.49	43.47	-0.2	1.7	1.1	1.1	1.3
283.83	44.35	2.9	3.4	2.2	3.1	2.9
283.91	43.12	0.6	1.3	0.8	0.8	1.1
283.98	41.30	-2.3	1.1	-	1.0	1.1

\*  $\hat{\sigma}^{\text{DS}}$  - calibrated standard deviation from the IRLS with the data snooping procedure

\*\*  $\hat{\sigma}^{\text{FMAD}}$  - calibrated standard deviation from the IRLS with the Fair-MAD estimator

\*\*\*  $\hat{\sigma}^{\text{FS}}$  - calibrated standard deviation from the IRLS with the Fair-sigma estimator

**B.3. Calibrated errors for tide gauge/altimetry data**

$\varphi, ^\circ$	$\lambda, ^\circ$	$\dot{h}$ , mm/yr	$\sigma$ , mm/yr	$\hat{\sigma}^{\text{DS}}$ , mm/yr	$\hat{\sigma}^{\text{FMAD}}$ , mm/yr	$\hat{\sigma}^{\text{FS}}$ , mm/yr
281.11	42.88	0.4	0.2	0.4	0.4	0.5
279.92	42.15	-0.5	0.2	0.4	0.5	0.5
278.72	41.75	-1.4	0.2	-	0.6	0.6
278.36	41.54	0.1	0.2	0.4	0.4	0.5
277.27	41.54	0.1	0.2	0.4	0.4	0.5
276.53	41.69	-0.3	0.2	0.4	0.4	0.4
276.74	41.96	-0.1	0.2	0.4	0.4	0.5
276.88	42.15	0.2	0.2	0.4	0.4	0.5
276.88	42.05	-1.0	0.2	0.4	0.5	0.6
277.27	42.03	-0.3	0.2	0.4	0.4	0.5
278.08	42.27	-0.1	0.2	0.4	0.4	0.5
278.78	42.67	-0.3	0.2	0.4	0.5	0.5
279.80	42.78	0.3	0.2	0.4	0.4	0.4
280.75	42.87	0.2	0.2	0.3	0.4	0.5
277.36	43.85	1.2	0.1	0.2	0.3	0.3
276.15	43.64	0.6	0.1	0.3	0.3	0.2
275.28	45.78	2.1	0.1	0.2	0.3	0.2
276.10	45.99	2.7	0.1	0.2	0.3	0.2
276.45	46.25	3.2	0.1	0.2	0.3	0.3
278.07	45.98	3.1	0.1	0.2	0.3	0.2
279.97	45.33	3.1	0.1	0.2	0.3	0.3
279.74	44.50	2.0	0.1	0.2	0.2	0.3
278.33	45.27	2.8	0.1	0.2	0.3	0.3
278.27	43.75	0.4	0.1	-	0.3	0.3
277.51	43.14	0.8	0.1	-	0.3	0.3
276.71	44.66	1.7	0.1	0.2	0.2	0.2

273.56	43.95	-1.2	0.3	-	1.1	0.8
272.46	41.73	-0.6	0.3	0.6	0.8	0.8
272.11	43.00	-1.3	0.3	0.6	0.6	0.7
272.69	44.60	-0.2	0.3	0.6	0.8	0.7
271.99	44.54	-1.0	0.3	0.6	0.8	0.8
274.13	45.97	1.0	0.3	0.6	0.9	0.8
273.80	42.77	-0.7	0.3	0.6	0.6	0.7
272.50	44.46	-0.4	0.3	0.6	0.6	0.7
283.66	44.13	1.5	0.1	0.3	0.3	0.2
283.49	43.46	1.3	0.1	0.3	0.3	0.3
282.37	43.27	1.2	0.1	0.3	0.3	0.3
280.78	43.23	0.4	0.1	-	0.3	0.3
280.23	43.33	-0.1	0.1	-	0.4	0.3
280.62	43.63	1.0	0.1	0.3	0.3	0.2
281.83	43.95	1.3	0.1	0.3	0.3	0.2
283.48	44.22	1.7	0.1	0.3	0.3	0.2
275.37	46.48	2.5	0.2	0.4	0.5	0.5
272.62	46.54	1.3	0.2	0.4	0.4	0.5
270.68	46.88	0.1	0.2	-	0.4	0.5
267.91	46.78	-0.7	0.2	0.4	0.4	0.5
269.66	47.75	1.3	0.2	0.4	0.4	0.5
270.78	48.42	2.1	0.2	0.4	0.4	0.4
272.48	48.83	4.2	0.2	-	0.7	0.6
275.10	47.97	4.3	0.2	0.4	0.5	0.6
275.42	46.53	2.2	0.2	-	0.5	0.5